Euskal Herriko Unibertsitatea
Universidad del País Vasco

UNIVERSIDAD DEL PAÍS VASCO
EUSKAL HERRIKO UNIBERTSITATEA

FACULTAD DE CIENCIA Y TECNOLOGÍA/ZIENTZIA ETA TEKNOLOGIA FAKULTATEA
DEPARTAMENTO DE INGENIERÍA QUÍMICA INGENIERITZA KIMIKOKO SAILA

CIC ENERGIGUNE

Na-ion battery development: from electrode processing studies to heat generation model of a monolayer pouch cell

By

Jaione Martínez de Ilarduya Martínez de San Vicente

Thesis supervisors:

Dr. Laida Otaegui Ameztegui

Dr. Monika Ortueta Aldama

Vitoria-Gasteiz, Octubre de 2019

(c)2019 JAIONE MARTINEZ DE ILARDUYA MARTINEZ DE SAN VICENTE

RESUMEN

Un sector energético sin carbón, dominado por fuentes de energía renovables, ocupa un rol trascendental en la transición hacia un futuro energético sostenible, principalmente, a través del crecimiento de la generación de energía solar y eólica. Entre la variedad de sistemas de almacenamiento de energía, la inclusión de baterías en las redes eléctricas balancearía el equilibrio del suministro y la demanda de electricidad. Por ejemplo, la tecnología de iones de sodio podría ser una opción viable para una próxima generación de baterías para aplicaciones estacionarias, debido a diversos aspectos, como su potencial para alcanzar un coste global menor debido a la abundancia y distribución geográfica de las fuentes de sodio en comparación con las de litio. Además, su fabricación sigue las pautas técnicas y de procesado de la tecnología de iones de litio actualmente implementados a escala industrial y, por lo tanto, su escalado sería más fácil y sin inversiones significativas en comparación otro tipo de tecnologías más novedosas. Sin embargo, el desarrollo de baterías de iones de sodio presenta aun desafíos críticos que deben superarse. Es por ello necesario impulsar la investigación en los procesos de escalado, procesado de electrodos y diseño de celdas para aproximar esta tecnología a los requerimientos de una tecnología madura.

Esta tesis doctoral incluye el trabajo realizado en el desarrollo de una batería con tecnología Na-ion. Es un trabajo diferenciado del estado del arte de este tipo de tecnología, y centrado en una perspectiva ingenieril de su desarrollo, empezando desde la fabricación de celdas de botón y acabando con el desarrollo de una celda de tipo pouch-cell de iones de sodio monocapa. Este trabajo representa un informe completo de la mencionada tecnología en términos de procesado de electrodos, estrategias encaminadas a superar las limitaciones de esta tecnología y fabricación de una celda completa con sus respectivas caracterizaciones electroquímicas y térmicas.

Con respecto al inicio del desarrollo de la tesis, en el Capítulo 1, se ha descrito el estado del arte de las baterías recargables con especial énfasis en la tecnología de baterías de iones de sodio objetivo de la tesis. En base al estado del arte, se han establecido los objetivos de la Tesis. En el

Capítulo 2, se proporciona la caracterización estructural y morfológica de los materiales activos de los electrodos junto con los procedimientos experimentales generales utilizados para preparar los componentes de las celdas, a nivel de electrodo y celdas completas. Además de esto, también se describen las técnicas experimentales utilizadas para la caracterización de las propiedades estructurales, morfológicas y mecánicas de los componentes procesados de la celda. Los siguientes capítulos comprenden los resultados experimentales y la discusión de los diferentes temas evaluados en esta Tesis.

Centrándose en estudios relacionados con el cátodo, el Capítulo 3 explora la utilización de 2 sales de sacrificio diferentes para superar la deficiencia de sodio característica de los cátodos de óxido laminares de sodio de tipo P2. Los óxidos laminares de tipo P2 representan una de las opciones más prometedoras para su uso como cátodos. Sin embargo, este tipo de estructuras son deficientes en sodio y dan lugar a una reducción significativa de la capacidad y densidad energética de las celdas cuando se combinan con ánodos que no contienen sodio. En este trabajo se han evaluado los compuestos NaN_3 y $Na_2C_4O_4$ como sales de sacrificio para compensar esa deficiencia en formato de celda completa, usando P2-$Na_{0.67}Mn_{0.5}Fe_{0.5}O_2$ como cátodo y un hard-carbon como ánodo. La adición de las dos sales ha dado lugar a un incremento de la capacidad reversible habiéndose comprobado mediante técnicas de microscopía y análisis estructural que NaN_3 y $Na_2C_4O_4$ se descomponen electroquímicamente en el rango de voltajes de interés (3.5-4.1 V) y que los iones de Na^+ generados debido a la descomposición de las dos sales se insertan reversiblemente en la estructura del cátodo. Sin embargo, se ha observado un comportamiento de ciclado más estable al usar $Na_2C_4O_4$ como sal de sacrificio. Siendo esta sal fácil de sintetizar y más segura de manipular que el NaN_3, se ha concluido que el $Na_2C_4O_4$ representa una solución estable, segura y rentable para posibilitar el uso de cátodos deficientes en sodio de tipo P2 en baterías de iones de sodio.

Los trabajos correspondientes al desarrollo de cátodos de tipo óxido laminar de tipo O3 se han llevado a varios niveles, en el Capítulo 4 y el Capítulo 5, a menor y a mayor escala de material procesado, respectivamente. Los resultados obtenidos de los estudios de formulación tanto a pequeña como a mayor escala, ponen de manifiesto la importancia de la cooperación óptima entre los materiales inactivos de la formulación del cátodo, aditivo conductor y aglutinante, así

como la necesidad de la combinación óptima entre materiales inactivos y contenido de material activo. En ambos casos, se han alcanzado porcentajes de material activo de ca. 87-88% con una pérdida de rendimiento mínima.

En el Capítulo 4, se ha evaluado el O3-$Na_{1-\delta}Ni_{0.32}Ti_{0.32}Mg_{0.16}Mn_{0.20}O_2$ como material activo del cátodo para el desarrollo de celdas de iones de sodio. Por un lado, se han identificado los parámetros óptimos de síntesis en estado sólido del material O3-$Na_{1-\delta}Ni_{0.32}Ti_{0.32}Mg_{0.16}Mn_{0.20}O_2$ variando la temperatura y tiempo de calcinación además de las condiciones de molienda de los precursores. La ruta de síntesis en estado sólido optimizada ha permitido la síntesis del material activo con un mínimo de impurezas de $Mg_{1-x}Ni_xO$. Se ha concluido que el tiempo de calcinación y la temperatura promueven la formación de la fase con impurezas y que la mezcla/molienda de los precursores en húmedo permite reducir la temperatura y el tiempo de calcinación. Una vez optimizada la ruta de síntesis se han llevado a cabo estudios preliminares a pequeña escala (ca. 0.5 g) del efecto de la formulación en la respuesta electroquímica, observando que es posible aumentar la cantidad de material activo en la composición del electrodo del 75% al 88% con resultados comparables (100 mAh g^{-1} después de 40 ciclos y una retención de la capacidad cercana al 70%). Los cátodos con un contenido de material activo de 88% en peso se han ensamblado y caracterizado electroquímicamente en formato de celdas completas de tipo botón usando un hard-carbon como ánodo. Se han tomado como base de estudio cátodos con dos cargas de material activo y se han emparejado con ánodos de diferentes cargas de material activo con el objetivo de optimizar el balance de masas, habiéndose obtenido una densidad energética máxima a nivel de materiales de 111 Wh kg^{-1}.

En el Capítulo 5, ya a mayor escala (ca. 10-30 g), se han llevado a cabo estudios de formulación y procesado de electrodos usando O3-$NaFe_{0.4}Mn_{0.3}Ni_{0.3}O_2$ como material activo de cátodo. En este capítulo, se ha analizado el efecto de diferentes parámetros de procesado de los electrodos de cátodo en sus características reológicas, morfológicas, mecánicas y electroquímicas. Se ha analizado el efecto del ratio entre el aditivo conductor y el aglutinante y con el objetivo de avanzar hacia mayores cargas de material activo y, por lo tanto, mayores capacidades/densidades de energía, el contenido de material activo se ha incrementado con respecto a las formulaciones con un 75-80%, generalmente empleadas en el desarrollo de

nuevos materiales activos de electrodos. Es importante resaltar que, además de aumentar la carga de material activo, el procedimiento de preparación de las suspensiones con contenidos de aditivo conductor más bajos es más fácil, se pueden usar contenidos en sólido más altos y la viscosidad es menor. Además, los electrodos resultantes muestran una microestructura más homogénea que aquellos con altos contenidos de aditivo conductor. Se han obtenido rendimientos de ciclo similares (90 mAh g^{-1} después de 50 ciclos) a intensidades bajas de corriente para los electrodos con 75%, 87% y 90% de material activo y cargas de material activo en el rango de 8 mg cm^{-2}. Sin embargo, la capacidad reversible a corrientes altas es significativamente menor para los electrodos con 90% de material activo debido al bajo contenido de aditivo conductor, C65 y la pérdida de integridad mecánica de los electrodos. Por lo tanto, se ha seleccionado un contenido de material activo del 87% como la composición de electrodo óptima que proporciona 105 Wh kg^{-1} a nivel de materiales.

En este apartado, se han explorado también varias estrategias para mejorar la microestructura de los electrodos de cátodo de O3-$NaFe_{0.4}Mn_{0.3}Ni_{0.3}O_2$, como el uso de diferentes equipos para la preparación de las suspensiones, el uso de agentes dispersantes o surfactantes o la variación de la morfología del material activo. Se ha seleccionado un mezclador con discos dentados como mejor opción para la mezcla de los componentes del cátodo, puesto que presenta el mejor compromiso entre la dispersión de los componentes, la microestructura del electrodo y el rendimiento electroquímico. Sin embargo, el tamaño de los aglomerados presentes en las suspensiones preparadas usando este equipo, impide la preparación de laminados en continuo a mayor escala mediante un equipo de deposición con cabezal de tipo comma bar. No se ha observado ninguna mejora con respecto al tamaño de los aglomerados mediante el uso de agentes dispersantes o surfactantes, mientras que la modificación de la morfología del material activo mediante un tratamiento de spray drying (material con morfología esférica) ha dado como resultado electrodos con un tamaño de aglomerados más pequeños que permiten la preparación de laminados mediante un proceso en continuo. Finalmente, se ha analizado el efecto de la temperatura de secado de los electrodos de O3-$NaFe_{0.4}Mn_{0.3}Ni_{0.3}O_2$, habiéndose observado un máximo del coeficiente de difusión y mejor respuesta electroquímica de las celdas, al emplearse una temperatura de secado de 60-80 °C.

El Capítulo 6 se centra en el electrodo negativo de hard carbon. El desarrollo del ánodo se ha centrado en el análisis del efecto del contenido y carga de material activo mediante análisis reológico, mecánico, morfológico y electroquímico de los electrodos. Se ha observado que la viscosidad en las suspensiones del ánodo varía en función del contenido de aditivo conductor. Además, el contenido de aditivo conductor también afecta a la capacidad irreversible del primer ciclo. A este nivel de estudio, no se ha observado una justificación clara para el uso de aditivo conductor en base a los datos experimentales obtenidos. Es por ello que en base a factores de facilidad de procesado y ahorro de tiempo, la formulación de ánodo seleccionada para posteriores análisis es de 95% de material activo y 5% de aglutinante.

En este capítulo se ha estudiado también el efecto de las condiciones de calandrado en la microestructura y respuesta electroquímica de los electrodos de hard-carbon mediante Diseño de Experimentos. Los parámetros estudiados han sido la distancia entre los rodillos del equipo de calandrado, la temperatura de calandrado, la velocidad de los rodillos y el número de repeticiones de dichos procesos de calandrado. Las respuestas evaluadas son el espesor y la porosidad del electrodo, la capacidad irreversible del primer ciclo y la capacidad reversible. Los resultados obtenidos muestran que son la distancia entre los rodillos y la temperatura de calandrado, así como la interacción entre estos dos factores los que, en mayor medida, afectan a las propiedades de los electrodos. Además, la combinación de distancias entre los rodillos pequeñas (40 µm) y temperaturas altas (100 °C) da como resultado condiciones de calandrado demasiado agresivas y el consiguiente daño de la microestructura del electrodo. Dependiendo de las condiciones de prensado, los valores de porosidad obtenidos varían entre 32 y 39%. Sin embargo, se concluye que además de la porosidad de los electrodos, otros parámetros como el tamaño de poro, la microestructura del electrodo, la integridad mecánica y la adhesión al colector de corriente determinarán la respuesta electroquímica de las celdas.

Finalmente, en el Capítulo 7, se ha ensamblado una celda completa monocapa de iones de sodio, pouch-cell, usando los componentes de cátodo y ánodo descritos y optimizados en los capítulos anteriores, Capítulo 5 y Capítulo 6, respectivamente; es decir, O3-$NaFe_{0.4}Mn_{0.3}Ni_{0.3}O_2$ y hard-carbon. Las variables que se han seleccionado para optimizar el comportamiento electroquímico de la celda completa de iones de sodio son el balance de masas (ratio entre la capacidad del

ánodo y la capacidad del cátodo, $R_{N/P}$ (Q)) entre el electrodo negativo y positivo, la morfología del material activo del cátodo y el voltaje límite de carga, partiendo de un estudio a nivel de celda de botón e implementando los resultados a nivel de pouch-cell.

La relación de la capacidad entre el electrodo negativo y positivo debe definirse correctamente al configurar una nueva celda a nivel de pouch-cell ya que la optimización de esta relación ayudará a mejorar la eficiencia de los procesos de carga y descarga y la seguridad de este tipo de celdas de iones de sodio. En base a los estudios realizados a pequeña escala, a nivel de celda botón de 2 electrodos y celda Swagelok de 3 electrodos, se ha seleccionado un rango óptimo de $R_{N/P}$ (Q) entre 1.5-1.2. Ya en base a estudios a nivel de pouch cell, se descarta la celda con $R_{N/P}$ (Q) = 1 debido a que se detecta un proceso de recubrimiento de sodio metálico en la superficie del ánodo, que los valores de capacidad reversible son bajos, precisamente debido al hecho mencionado anteriormente y especialmente, que el rendimiento es bajo a intensidades de corriente mayores. En el caso de $R_{N/P}$ (Q) = 1.6, no existe un riesgo de recubrimiento del ánodo con sodio, pero los valores de capacidad reversible se reducen debido a que no se hace un uso efectivo de la capacidad del ánodo y únicamente se obtiene la capacidad correspondiente a la región en pendiente del perfil de voltaje del electrodo negativo. La relación $R_{N/P}$ (Q) = 1.3 representa un compromiso entre los dos ratios anteriormente mencionados y se convierte en la mejor opción para el desarrollo de una pouch-cell optimizada, mostrando valores adecuados de capacidad reversible y retención de capacidad a 13 mA g^{-1}, además de valores superiores de capacidad a mayores densidades de corriente. Se ha concluido también que reducir la condición de límite de carga de 4.0 a 3.9 V en ensayos de mayor duración, permite evitar el recubrimiento con sodio metálico de la superficie del ánodo al limitar el voltaje del ánodo a valores por encima de 0 V mejorando la retención de capacidad de las celdas. Por último, aunque el uso del material con morfología de tipo esférico obtenido mediante el proceso de spray drying permite preparar electrodos mediante un proceso en continuo, presenta capacidades reversibles ligeramente más bajas y un rendimiento electroquímico ligeramente peor a corrientes altas que el cátodo con morfología original. El análisis post-mortem realizado tras los ensayos de ciclabilidad a nivel de pouch-cell, indica que la degradación del ánodo es la principal causa de la degradación de las celda completas.

Por último, se ha llevado a cabo la determinación, por primera vez, de los parámetros térmicos de la celda de tipo pouch-cell monocapa de iones de sodio. Concretamente, se han cuantificado la resistencia interna, el calor entrópico, el calor específico y la conductividad térmica de las celdas desarrolladas en esta Tesis. En referencia a la resistencia interna, aumenta al disminuir la temperatura, por lo que estos dos factores tienen una relación inversamente proporcional. Sin embargo, está más influenciada por el estado de carga (SOC) al cual se lleva a cabo la medida que por la temperatura. Por otro lado, el calor entrópico mantiene valores negativos para todo el rango de SOC estudiado, tanto en los procesos de carga como en descarga.

La obtención de dichos parámetros ha permitido el desarrollo de un modelo de generación de calor que ofrece una valiosa estimación del incremento de temperatura durante los procesos de carga y descarga de la celda desarrollada en esta Tesis. Al desarrollar el modelo de generación de calor de la celda monocapa de iones de sodio, se ha concluido que el calor irreversible, que está relacionado con la polarización y la resistencia óhmica, es el factor principal que contribuye a la generación de calor total. Es decir, a medida que se genere menos calor en una celda, será más eficiente en el proceso de transferencia de energía eléctrica.

Aunque la validación del modelo de generación de calor no ha podido desarrollarse debido al tamaño y espesor limitado de la celda de iones de sodio, ya que calor total generado es menor que el que es capaz de medir el equipamiento disponible para la validación, el modelo calculado ofrece una idea sobre el calor generado durante el procesos de carga y descarga en este tipo de tecnología, para los materiales específicos de cátodo y el ánodo seleccionados en esta Tesis, en condiciones isotérmicas y no adiabáticas refrigeradas. Este modelo ayuda a identificar mejoras adicionales que deberían realizarse en la tecnología de iones de sodio, con óxidos laminares de sodio como material activo de cátodo y hard-carbon como material activo de ánodo y la implementación en una pouch-cell multicapa de iones de sodio.

Sólo los valientes son felices.

CONTENTS

ABSTRACT/RESUMEN……I-VIII

ACKNOWLEDGEMENTS……IX-XII

CHAPTER 1. INTRODUCTION 1

1.1 THE ENERGY OF LIFE 3
1.1.1 Energy demand & production scenario 3
1.1.2 Energy storage systems 5
1.2 RECHARGEABLE BATTERIES 6
1.2.1 Mature technologies 6
1.2.2 Emerging technologies 15
1.3 NA-ION BATTERIES 18
1.3.1 Cathode materials 20
1.3.2 Anode materials 27
1.3.3 Electrolyte 31
1.3.4 Full-cell prototype fabrication 33
1.4 PROCESSING AND MANUFACTURING OF METAL-ION BATTERIES 34
1.4.1 Slurry mixing 36
1.4.2 Electrode coating 39
1.4.3 Stacking / Packaging 40
1.5 SCOPE OF THIS THESIS 43

CHAPTER 2. EXPERIMENTAL PROCEDURE 45

2.1 SYNTHESIS AND CHARACTERIZATION OF ELECTRODE ACTIVE MATERIALS 47
2.1.1 Cathode active materials 48
2.1.2 Anode active material 52
2.2 ELECTRODE PREPARATION 53
2.2.1 Slurry formulation 54
2.2.2 Electrode coating and drying 59
2.2.3 Electrode calendering 61
2.3 ELECTROLYTE PREPARATION 61
2.4 CELL ASSEMBLY 63
2.4.1 Coin cell assembly 63
2.4.2 Swagelok cell assembly 65
2.4.3 Monolayer pouch cell assembly 66
2.4.4 3-electrode pouch cell assembly 69

2.5 CHARACTERIZATION TECHNIQUES 71
2.5.1 Electrochemical characterization 71
2.5.2 Rheological analysis 76
2.5.3 Peel tests 80
2.5.4 Scanning Electron Microscopy (SEM) 82
2.5.5 X-Ray Diffraction (XRD) 85
2.5.6 Solid State Nuclear Magnetic Resonance (NMR) 88
2.6 EXPERIMENTAL DETERMINATION OF THERMAL PARAMETERS 89
2.6.1 Selected Na-ion battery description 89
2.6.2 Heat Capacity 90
2.6.3 Thermal Conductivity 93
2.6.4 Internal Resistance 96
2.6.5 Entropic Heat Coefficient 99

CHAPTER 3. NaN_3 AND $Na_2C_4O_4$ AS SACRIFICIAL SALTS IN P2-TYPE Na_xMO_2 CATHODES. 103

3.1 INTRODUCTION 105
3.2 EXPERIMENTAL PROCEDURE 107
3.3 ELECTROCHEMICAL PERFORMANCE OF INDIVIDUAL CELL COMPONENTS 108
3.3.1 $Na_{0.67}Fe_{0.5}Mn_{0.5}O_2$ as cathode active material 108
3.3.2 Hard carbon as anode active material 109
3.3.3 NaN_3 and $Na_2C_4O_4$ as sacrificial salts 110
3.4 USE OF NaN_3 AS SACRIFICIAL SALT 111
3.4.1 Electrochemical performance 111
3.4.2 Post-test morphological and structural analysis 116
3.5 EFFECT OF THE USE OF $Na_2C_4O_4$ AS SACRIFICIAL SALT 120
3.5.1 Electrochemical performance 120
3.5.2 Post-test morphological and structural analysis 123
3.5.3 Ex-situ morphological and structural analysis of 31-$Na_2C_4O_4$ 125
3.6 COMPARATIVE OF NaN_3 AND $Na_2C_4O_4$ AS SACRIFICIAL SALTS 128
3.7 CONCLUSIONS 132

CHAPTER 4. $Na_{1-\Delta}Ni_{0.32}Ti_{0.32}Mg_{0.16}Mn_{0.20}O_2$ AS CATHODE ACTIVE MATERIAL FOR SIBS.... 133

4.1 OPTIMIZATION OF $Na_{1-\Delta}Ni_{0.32}Ti_{0.32}Mg_{0.16}Mn_{0.20}O_2$ SYNTHESIS CONDITIONS 135
4.2 HALF-CELL STUDIES ON CATHODE FORMULATION 142
4.3 FULL-CELL STUDIES 148
4.3.1 General overview 148
4.3.2 Electrochemical performance of selected half-cell electrodes 151
4.3.3 Cycling stability of full-cells 153

4.4 CONCLUSIONS 156

CHAPTER 5. ANALYSIS OF THE $NaFe_{0.4}Mn_{0.3}Ni_{0.3}O_2$ PROCESSING PARAMETERS FOR SIBS CATHODE APPLICATIONS 159

5.1 INFLUENCE OF THE C65: PVDF RATIO 161
5.1.1 Slurry preparation 161
5.1.2 Slurry characterization 162
5.1.3 Electrode characterization 166
5.2 INFLUENCE OF THE AM CONTENT AND LOADING 172
5.2.1 Slurry preparation 173
5.2.2 Slurry characterization 174
5.2.3 Electrode characterization 176
5.3 EFFECT OF MIXING EQUIPMENT IN SLURRY AND ELECTRODE PROPERTIES 187
5.3.1 Slurry preparation 187
5.3.2 Slurry characterization 191
5.3.3 Electrode characterization 193
5.4 STRATEGIES TO IMPROVE ELECTRODE MICROSTRUCTURE 197
5.4.1 Use of dispersing additives 198
5.4.2 Effect of the active material morphology 202
5.5 DRYING PROCESS INFLUENCE 205
5.5.1 Electrode preparation 206
5.5.2 Electrode characterization 206
5.6 CONCLUSIONS 212

CHAPTER 6. ANALYSIS OF THE HARD CARBON ANODE PROCESSING PARAMETERS FOR SIBS 215

6.1 INFLUENCE OF THE AM CONTENT AND LOADING 217
6.1.1 Slurry preparation 217
6.1.2 Slurry characterization 218
6.1.3 Electrode characterization 221
6.2 EFFECT OF CALENDERING IN ELECTRODE PROPERTIES 237
6.2.1 Thickness and porosity 241
6.2.2 1^{st} cycle irreversibility 246
6.2.3 Reversible capacity 246
6.3 CONCLUSIONS 252

CHAPTER 7. DESIGN, ELECTROCHEMICAL CHARACTERIZATION AND THERMAL MODEL OF A Na-ION MONOLAYER POUCH-CELL PROTOTYPE 255

7.1 EXPERIMENTAL PROCEDURE 257

7.2 FULL-CELL ASSEMBLY AT COIN CELL LEVEL 257
7.2.1 Influence of the N/P ratio in 3-electrode cells 257
7.2.2 Influence of the N/P ratio in 2-electrode cells 262
7.3 FULL-CELL ASSEMBLY AT POUCH CELL LEVEL 264
7.3.1 3-electrode cell 264
7.3.2 Cycling stability of monolayer pouch cells 272
7.4 THERMAL MODEL FOR SODIUM-ION BATTERY 289
7.4.1 Determination of thermal parameters 292
7.4.2 Heat generation model 312
7.5 CONCLUSIONS 323

CHAPTER 8. GENERAL CONCLUSIONS AND FUTURE WORK 327

8.1 GENERAL CONCLUSIONS 329
8.2 FUTURE WORK 332

CHAPTER 9. BIBLIOGRAPHY 335

APPENDIX 357

A.1. LIST OF ABBREVIATIONS AND SYMBOL 359
A.2 LIST OF CONTRIBUTIONS 363
A.2.1 Publications 363
A.2.2 Conferences 363

ABSTRACT

A decarbonized energy sector, dominated by renewable energy sources, is at the core of the transition to a sustainable energy future, mostly through growth in solar and wind power generation. Among the several types of energy storage systems, the inclusion of banks of batteries into the electricity grids would enable the balance of the supply and the demand of electricity. For instance, sodium-ion technology is aimed to become a next generation viable technology for stationary applications, based on some aspects such as their potential to be cheaper due to the abundance and geographical distribution of sodium sources in comparison to lithium ones. Moreover, their fabrication is similar of that of lithium-ion technology which is already implemented at industrial level; thus, its up-scale should be easier and with no significant investments compared to other emerging technologies. However, the development of sodium-ion batteries presents critical challenges which still need to be overcome. Therefore, research in the scale-up, electrode processing and cell design aspects should be boosted in order to approximate this technology to the demands of a mature technology.

P2-type layered oxides are some of the most promising cathode active material options. However, this type of structures are sodium deficient and show low capacity and energy density when coupled with non-sodium containing anodes. In this work NaN_3 and $Na_2C_4O_4$ were evaluated as sacrificial salts using P2- $Na_{0.67}Mn_{0.5}Fe_{0.5}O_2$ cathode and hard carbon anode. An increment of the reversible capacity was observed with the addition of the two sacrificial salts and it was confirmed by morphological and structural analysis that the Na^+ ions generated during the decomposition of the salts are reversibly inserted in the cathode structure. More stable cycling behavior was observed when $Na_2C_4O_4$ was used as the sacrificial salt. Being this salt easy to synthesize and safer to manipulate than NaN_3,$Na_2C_4O_4$ represents a stable, safe and cost effective solution to enable the use of sodium deficient P2-type layered oxide cathodes in sodium-ion batteries.

The works focused in the development of O3-type layered oxides were carried out at different levels. On the one hand, the optimized synthesis parameters were determined for the solid state

synthesis of O3- O3-$Na_{1-\delta}Ni_{0.32}Ti_{0.32}Mg_{0.16}Mn_{0.20}O_2$ by tuning the temperature and time of calcination as well as precursors milling conditions. Once the synthesis route was optimized, preliminary formulation studies were performed at small scale (ca. 0.5 g) to evaluate the effect of the formulation in the electrochemical performance of the electrodes. Moreover, full-cells in coin cell format were also assembled using hard carbon as the anode material and energy densities of 111 Wh kg^{-1} were obtained at materials level. At a higher scale (ca. 10-30 g), formulation studies were also performed using O3-$NaFe_{0.4}Mn_{0.3}Ni_{0.3}O_2$ as cathode active material. The results obtained at small and large scale reveal the importance of optimal cooperation between both inactive materials of the cathode slurry, carbon black and binder, as well as the optimal combination between the inactive materials and the active material content. For both the cathode active material components, active material contents of ca. 87-88% were reached with minimum loss of performance. Several approaches were also followed in order to enhance the microstructure of O3-$NaFe_{0.4}Mn_{0.3}Ni_{0.3}O_2$ electrodes, such as the use of different mixing devices for the slurry preparation, the use of dispersing agents and surfactants and the variation of the active material morphology. Finally, the effect of the drying temperature was also studied which showed a maximum diffusion coefficient when electrodes are dried at 60-80 °C.

The anode development was focused in the analysis of the active material content and loading by means of rheological, mechanical, morphological and electrochemical studies. Moreover, the effect of the calendering conditions in the hard carbon electrode microstructure and electrochemical response was also evaluated by Design of Experiments. Based on the obtained results, the gap between the rollers and the calendering temperature, as well as the interaction between these two variables are the factors that most significantly to the electrode properties.

The fabrication of a monolayer pouch cell was done using the O3-$NaFe_{0.4}Mn_{0.3}Ni_{0.3}O_2$ cathode coupled with a hard carbon anode. The variables selected to optimize the electrochemical performance of the full-cell are the mass balance, the cathode active material morphology and the end of charge voltage, the study being started at coin cell level and being concluded at monolayer pouch cell level. The cycling stability studies indicate that the degradation of the anode is the main cause for cell degradation. Finally, the thermal parameters of the monolayer

Na-ion pouch cell are determined. The obtainment of these parameters enabled the development of a heat generation model which provides a valuable estimation of the temperature increase during the charge and discharge processes for the cell developed in this Thesis.

RESUMEN

Un sector energético sin carbón, dominado por fuentes de energía renovables, ocupa un rol trascendental en la transición hacia un futuro energético sostenible, principalmente, a través del crecimiento de la generación de energía solar y eólica. Entre la variedad de sistemas de almacenamiento de energía, la inclusión de baterías en las redes eléctricas posibilitaría el equilibrio entre el suministro y la demanda de electricidad. Por ejemplo, la tecnología de iones de sodio podría ser una opción viable para una próxima generación de baterías para aplicaciones estacionarias, debido a diversos aspectos, como su potencial para alcanzar un coste global menor debido a la abundancia y distribución geográfica de las fuentes de sodio en comparación con las de litio. Además, su fabricación sigue las pautas técnicas y de procesado de la tecnología de iones de litio actualmente implementados a escala industrial y, por lo tanto, su escalado sería más fácil y sin inversiones significativas en comparación otro tipo de tecnologías más novedosas. Sin embargo, el desarrollo de baterías de iones de sodio presenta aun desafíos críticos que deben superarse. Es por ello necesario impulsar la investigación en los procesos de escalado, procesado de electrodos y diseño de celdas para aproximar esta tecnología a los requerimientos de una tecnología madura.

Los óxidos laminares de tipo P2 representan una de las opciones más prometedoras para su uso como cátodos. Sin embargo, este tipo de estructuras son deficientes en sodio y dan lugar a una reducción significativa de la capacidad y densidad energética de las celdas cuando se combinan con ánodos que no contienen sodio. En este trabajo se han evaluado los compuestos NaN_3 y $Na_2C_4O_4$ como sales de sacrificio para compensar esa deficiencia en formato de celda completa, usando P2-$Na_{0.67}Mn_{0.5}Fe_{0.5}O_2$ como cátodo y un hard carbon como ánodo. La adición de las dos sales ha dado lugar a un incremento de la capacidad reversible habiéndose comprobado mediante técnicas de microscopía y análisis estructural que los iones de Na^+ generados debido a la descomposición de las dos sales se insertan reversiblemente en la estructura del cátodo. Sin embargo, se ha observado un comportamiento de ciclado más estable al usar $Na_2C_4O_4$ como sal de sacrificio. Siendo esta sal fácil de sintetizar y más segura de manipular que el NaN_3, se ha

concluido que el $Na_2C_4O_4$ representa una solución estable, segura y rentable para posibilitar el uso de cátodos deficientes en sodio de tipo P2 en baterías de iones de sodio.

Los trabajos correspondientes al desarrollo de cátodos de tipo óxido laminar de tipo O3 se han llevado a varios niveles. Por un lado, se han identificado los parámetros óptimos de síntesis en estado sólido del material O3-$Na_{1-\delta}Ni_{0.32}Ti_{0.32}Mg_{0.16}Mn_{0.20}O_2$ variando la temperatura y tiempo de calcinación además de las condiciones de molienda de los precursores. Una vez optimizada la ruta de síntesis se han llevado a cabo estudios preliminares a pequeña escala (ca. 0.5 g) del efecto de la formulación en la respuesta electroquímica y se han ensamblado y caracterizado electroquímicamente celdas completas de tipo botón usando un hard carbon como ánodo y habiéndose obtenido una densidad energética a nivel de materiales de 111 Wh kg^{-1}. Ya a mayor escala (ca. 10-30 g), se han llevado a cabo estudios de formulación usando O3-$NaFe_{0.4}Mn_{0.3}Ni_{0.3}O_2$ como material activo de cátodo. Los resultados obtenidos de los estudios de formulación tanto a pequeña como a mayor escala, ponen de manifiesto la importancia de la cooperación óptima entre los materiales inactivos de la formulación del cátodo, aditivo conductor y aglutinante, así como la necesidad de la combinación óptima entre materiales inactivos y contenido de material activo. En ambos casos se han alcanzado porcentajes de material activo de ca. 87-88% con una pérdida de rendimiento mínima. En este apartado, se han explorado también varias estrategias para mejorar la microestructura de los electrodos de cátodo de O3-$NaFe_{0.4}Mn_{0.3}Ni_{0.3}O_2$, como el uso de diferentes equipos para la preparación de las suspensiones, el uso de agentes dispersantes o surfactantes o la variación de la morfología del material activo. Finalmente, se ha analizado el efecto de la temperatura de secado de estos electrodos habiéndose observado un máximo del coeficiente de difusión a 60-80 °C.

El desarrollo del ánodo se ha centrado en el análisis del efecto del contenido y carga de material activo mediante análisis reológico, mecánico, morfológico y electroquímico de los electrodos. Además, se ha estudiado el efecto de las condiciones de calandrado en la microestructura y respuesta electroquímica de los electrodos de hard carbon mediante Diseño de Experimentos. Los resultados obtenidos muestran que son el espacio entre los rodillos y la temperatura de calandrado, así como la interacción entre estos dos factores los que en mayor medida afectan a las propiedades de los electrodos.

La fabricación de una pouch cell de tipo monolayer se ha llevado a cabo usando el ya mencionado cátodo O3-$NaFe_{0.4}Mn_{0.3}Ni_{0.3}O_2$ en combinación con un ánodo de hard carbon. Las variables que se han seleccionado para optimizar el comportamiento electroquímico de la celda completa de iones de sodio son el balance de masas, la morfología del material activo del cátodo y el voltaje límite de carga habiéndose iniciado el estudio a nivel de celda de botón y habiéndose finalizado el mismo a nivel de pouch cell. El estudio de ciclabilidad indica que la degradación del ánodo es la principal causa de la degradación de la celda. Por último, se ha llevado a cabo la determinación de los parámetros térmicos de la celda de tipo monolayer pouch cell de iones de sodio. La obtención de dichos parámetros ha permitido el desarrollo de un modelo de generación de calor que ofrece una valiosa estimación del incremento de temperatura durante los procesos de carga y descarga de la celda desarrollada en esta Tesis.

ACKNOWLEDGEMENTS

El fin de una etapa. Es hora de cambiarse los zapatos y seguir hacia delante. Con estos zapatos, he crecido tanto personal como profesionalmente, he tomado decisiones importantes, he hecho caso a lo que me dictaba el corazón, he tenido el placer de conocer a gente de todo menos corriente y he llegado hasta aquí. ¿Cómo resumo mis agradecimientos?

Muchas gracias a CICenergigune por darme la oportunidad de iniciarme en el camino de la investigación, a toda la gente que hace que cada día este centro se mueva y siga en constante mejora y crecimiento. Thank you very much to the Lawrence Berkeley National Laboratory for hosting me during 3 amazing months. Thank you Vince for giving me the opportunity to discover a great lab and team, and for your advices. Yanbao, thank you for your patient and help at every step during those months as I learnt a lot from you. Y así mismo, gracias a Ikerlan por ayudarme a iniciarme en otro ámbito en el área del almacenamiento electroquímico. A ti Jon, por hacer que mi pequeña estancia allí fuera de lo más provechosa, de ponerme los medios y de estar hasta el final.

Con estos zapatos, me ha acompañado mucha gente. Gente que dejó de caminar a mi lado, gente que me pilló en un cruce y se fue, gente que se cruzó y siguió, y gente que sigue dándome la mano desde el primer día.

Primeramente, a todos los que me acompañaron en determinadas etapas de mi tesis, y que tuvieron que dejar de caminar conmigo, por circunstancias ajenas, propias o simplemente, circunstancias, gracias. No es un gracias pequeño, aunque plasmado en un escrito parezca que sí. Es un agradecimiento que alcanza a todos los recuerdos que siguen conmigo, por un tiempo, o para siempre. Gracias por aguantar todo lo que vino de la mano con mi decisión de iniciar una tesis.

Mis zapatos nuevos, aquel 23 de Marzo de 2015, en el que empecé a entrar por la puerta del CIC, estaban ansiosos por caminar con un montón de gente nueva. Y así fue. Aquí he conocido a gente, que tanto a nivel profesional como personal, me han hecho cambiar y crecer.

No puedo menos que acordarme de Gurpreet. Gracias por iniciarme en el camino de la investigación, las primeras lecciones que aprendí llevan tu nombre. Espero que algún día tengamos la oportunidad de ponernos al día con una buena cerveza. Me acuerdo de nuestro primer pequeño grupo de prototipado, donde todo se empezó a cocer. Primeras jornadas en la sala seca, y todo lo que vendría después. Problema, solución, problema, solución, hasta hoy. Laida, gracias por enseñarme, por tenerme alerta, y por ser exigente en lo que hemos hecho. He aprendido mucho de ti y espero que lo pueda seguir haciendo. Aitor, gracias por tenerme en cuenta, por luchar y creer en mí. Y por darme oportunidades de crecer. Eres todo un referente de buen líder, de currante y de buena persona. Gracias de nuevo por todo.

A las personas increíbles que he ido conociendo en el CIC, a los doctorandos que empezamos, con aquellos que he podido compartir pintxo-potes que se alargan horas, planes y confidencias, a los que se han convertido en amigos, y compañeros de viaje, gracias por formar parte de este todo tan grande. No han sido pocas las horas de comidas en el CIC, los ratos de cerveceo, conversaciones de pasillo, cotilleos infinitos, y un largo etcétera de momentos que me llevo para siempre. No puedo más que desear que nos sigamos encontrando en nuestra vida profesional, pero sobre todo personal. Tengo muchísima suerte de llevarme un montón de soles en los bolsillos.

Aquí dentro también queda un huequito para toda la gente de Berkeley que hizo que mi aventura fuera excepcional y única. Sobre todo a ti Leti, por contribuir a que Berkeley fuera mi hogar (con todas las letras) durante aquellos meses. Sin duda, me llevo en el corazoncito a una de las mejores personas que he conocido nunca. Gracias por aparecer allí y seguir en mi vida, siempre tendrás otra casa aquí, en Vitoria.

Y a ti. “Menos mal que existes, porque si no tendría que imaginarte…”. Mi etapa doctoral, en lo personal, ha estado marcada sobre todo por ti. Porque si un día no hubiera tomado la decisión de iniciar el doctorado, y tú no habrías aterrizado aquí, nunca te hubiera conocido. Nunca hubiera conocido a la persona que más me ha cuidado, más paciencia ha tenido conmigo, la que nunca, y digo nunca, ha soltado mi mano, en los malos tiempos. Eres mi persona, mi terrón, la que quiero que me dé la mano siempre, al que quiero ver al iniciar y al acabar el día, con la que me relajo, con la que soy del todo yo. Nunca sabré agradecerte todo lo que has hecho, haces, y

espero, harás por mí en nuestro camino. Estoy locamente enamorada de nuestro “nosotros” y eres casa.

Y no podría estar cerrando este capítulo, sin ellas, sin mis compañeras de camino. Porque abro y cierro capítulos, y ellas siempre están. Ríen y lloran conmigo. Parece simple, pero encontrar personas como ellas, es difícil de narices. Os merecéis un capítulo, un libro o una jodida enciclopedia para contar lo que significáis para mí. Que sigamos cuidándonos por toda una vida. Ane, Karla, Sil, Agur, Yuly, Amaia, Lore, Cori, Karime, Lei, sois movimiento, admiración, caos y vida.

Y sobre todo, todo este gran agradecimiento está dedicado a mi familia. La definición de valientes es inherente a ellos. Porque yo no sería una luchadora, si ellos no me hubieran sentado las bases. A ti, mamá. Eres la persona más incondicional, leal, y valiente que conozco, junto a papá. Y siempre estás. Has tenido que aguantar mis, y nuestros, ratos de frustración, de enfado, las ganas de tirarlo todo por la ventana, y nunca has fallado. A ti papá. Has sido y serás ejemplo de luchador para mí. Has encontrado tus razones y las has hecho vivir. Sigue dando guerra, por favor. A ti, hermano. Siempre he tenido un buen referente en mi vida. Concienzudo, valiente e impaciente por naturaleza, y no sabes todo lo que te admiro. A mi cuñada, por ser ejemplo de paciencia y de unión. Y a mis pequeñas sobris, pequeñas grandes revoluciones que algún día se comerán la vida a manos llenas. Ellas son luz. Sois el mejor ejemplo de familia que podría tener, de verdad, con nuestros más y nuestros menos, pero siempre como una piña. Estoy orgullosa de vosotros.

Partiendo de que “La vida es un ir y venir de girar pomos”, no queda más que descalzarse y buscarse unos nuevos zapatos, un nuevo horizonte, una nueva meta. O una nueva terraza donde echarse una buena cerveza, que está claro que la vida son dos días, y tengo que recordármelo cada instante.

Chapter 1. Introduction

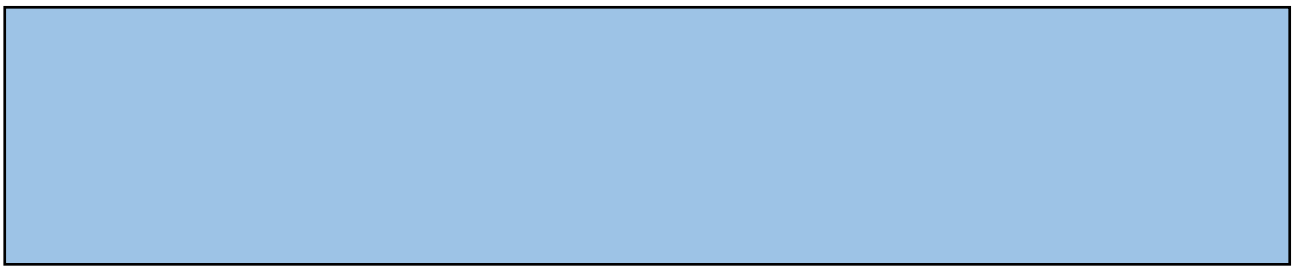

1.1 The energy of life

1.1.1 Energy demand & production scenario

The global energy consumption should move from a fossil fuel-based system to a complete renewable energy-based system [1]. The utilization of fossil fuels based energy sources, as coal and oil, has increased the concentration of carbon dioxide, CO_2 (**Figure 1.1**), as well as other gases. As a consequence of the accumulation of greenhouse gases, such as water vapor (H_2O), methane (CH_4), carbon dioxide (CO_2) and nitrous oxide (N_2O), the Earth is currently suffering a global warming trend. This global warming process will likely melt glaciers, increase the sea level, shift current climate patterns making that some regions will become drier and others wetter and affect to food production among other consequences [2]. Fossil fuels, as oil, natural gas or coal continue dominating the global energy system; and although many governments have strengthened efforts to reduce national emissions, cumulative emissions must be reduced by a further 470 Gt, compared to what is expected with current and planned policies by 2050 to limit the global temperature increase to below 2 °C according to the International Renewable Energy Agency (IRENA) [1]. Based on the same source, the implementation of renewable energy sources will need to be scaled up, at least six times faster to meet the goals which were fixed in the Paris Agreement [3].

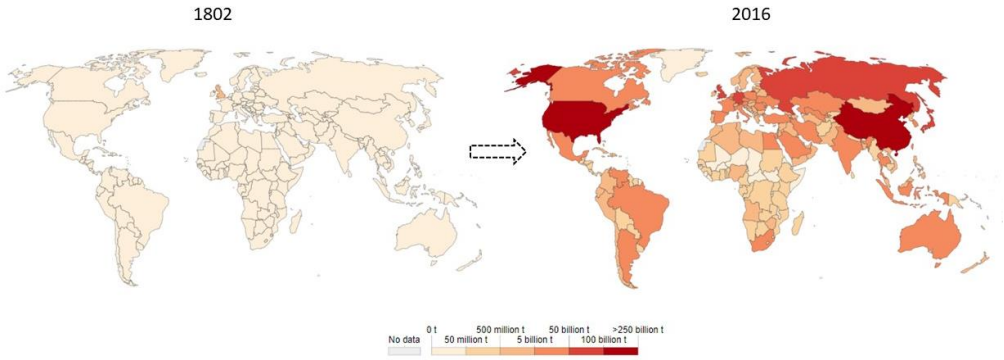

Figure 1.1. Cumulative CO_2 emissions (in tons) representing the total sum of emissions in 1802 and 2016 [4].

Energy transformation will require new approaches to power system planning, system and market operations, and regulation and public policy [1]. Energy transition should be based on the development of renewable energies and the improvement of energy efficiency, in addition to the reduction of the carbon emissions and the decrease of greenhouse gas emissions in global production. **Figure 1.2** shows a predicted energy demand scenario from the International Energy Agency from 2000 to 2040, which incorporates existing energy policies and the implementation of the announced policy intentions.

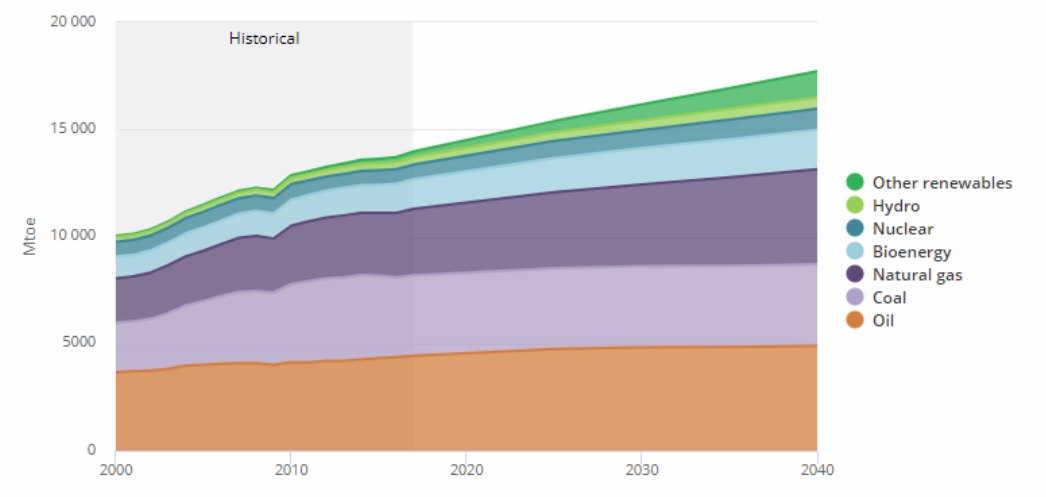

Figure 1.2. Global total primary energy demand (1 toe = 11.63 MWh) [5].

If renewable energy sources want to be integrated as power supplies in the electrical grids, they will need to present a continuous balance between the supply and demand of electricity. That is, as the energy generated by the renewable sources, such as solar plants or wind farms, is intermittent, they will need to operate coupled with energy storage systems in order to be able to respond to high demand peaks when the generation is low. At this point, the energy storage systems gain tremendous importance.

Worldwide, the power sector has added 167 GW of renewable capacity, with a growth rate per year of 8% from 2010. The renewable power generation sector is quantified as one quarter of the global power generation [1]. According to the DOE Energy Storage Database, USA, Germany, Japan, South Korea and China are nowadays the countries with the highest capacity of electric storage, with new projects under development, capable to generate more than 50 MW [6]. In

Spain, according to the World Energy Council [7], there is a remarkable investment for different energy storage systems. Pumped hydro storage systems suppose 5268 MW. Thermal storage encompasses 26 projects, especially in molten salt projects associated with solar plants which suppose 1132 MW. In addition to this, there are 14 electrochemical storage system projects running which suppose 8 MW and 2 electro-mechanical storage projects which suppose 2 MW. In the Basque Country there are currently 30 companies dedicated to the energy storage sector with an estimation of investment budget of 16.2M€ [8]. According to the Vice-ministry of Industry and Basque Energy Entity, hydro-electrical and eolic renewable sources maintain similar levels of power generation, 173 and 153 MW, respectively, while solar renewable sources keep growing [9].

1.1.2 Energy storage systems

Energy storage systems are used to store the energy to be used on demand. Energy storage systems can be classified in five main categories in which the way the energy is converted is the main differentiation: mechanical, chemical, electrical, thermal and electrochemical storage systems [7,10] (**Figure 1.3**).

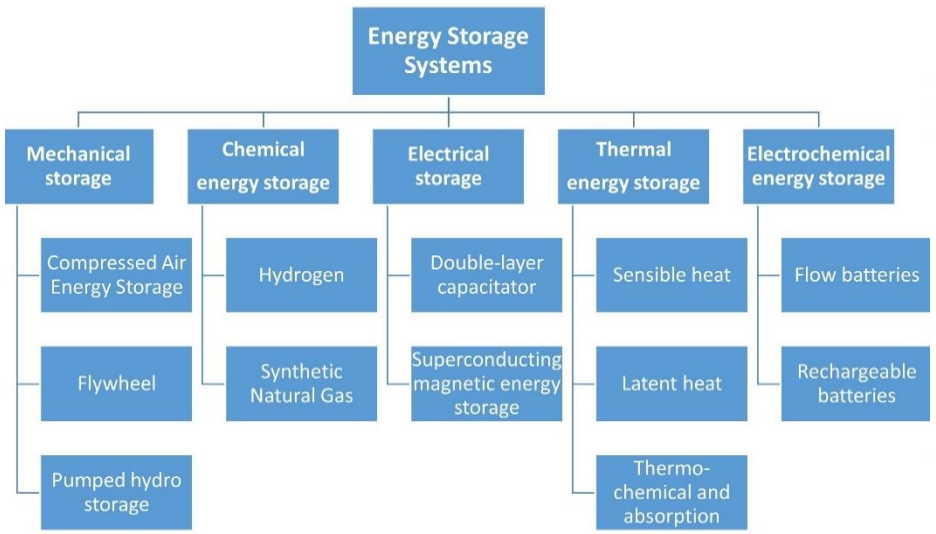

Figure 1.3. Classification of energy storage systems.

Each energy storage system is selected depending on the application. Electrochemical energy storage systems have higher efficiencies than the rest of technologies and are usually oriented to short-term energy storage applications. However, they present higher costs. In the case of mechanical energy storage systems, high power and capacity, as well as long lifetime, are the main characteristics. Fulfilling the requirements of applications such as arbitrage, black start and off-grid are the goals of this type of technology. Electrical and chemical energy storage are less efficient but more durable systems, and therefore, they are used for seasonal storage.

1.2 Rechargeable batteries

Among the different types of electrochemical energy storage systems, rechargeable batteries are becoming a promising technology. As there are a wide range of options and some of them are technologically mature enough to be massively used, they are the most suitable option for some specific energy storage applications. By definition, rechargeable batteries are devices capable to produce electricity from a reversible electrochemical reaction. In this section, seven types of batteries are described, lead-acid, nickel-cadmium, nickel-metal hydride, redox flow, metal-sulfur (Na-S and Li-S), metal-air and metal-ion batteries (Li-ion and Na-ion). The working principle, chemical composition of the cell components and electrochemical reaction will be provided together with the characteristic advantage and disadvantages of each technology, making a difference between mature and emerging systems.

1.2.1 Mature technologies

1.2.1.1 Lead-acid batteries

Lead-acid batteries were invented by Planté in 1859, and they became the first commercially used rechargeable battery. Lead-acid batteries are composed by lead alloy in combination with other additives, such as antimony, calcium, tin and selenium. At charged state, the positive active material is porous PbO_2 while the negative active material is highly porous Pb. At the discharge state, both electrodes are made of $PbSO_4$. The electrolyte in these types of batteries is an aqueous H_2SO_4 solution [11]. The overall discharge reaction (1.1) and cell voltage are,

$$PbO_2 + Pb + 2H_2SO_4 \leftrightarrow 2PbSO_4 + 2H_2O\ (2.05\ V) \quad (1.1)$$

Lead-acid technology is commonly categorized in three main fields of application: automotive (starter battery), motive power and stationary applications (uninterruptible power supply) [12]. Currently, this technology shares rechargeable batteries market with lithium-ion batteries. Main advantages and drawbacks of the lead-acid technology are summarized in **Table 1.1**.

Table 1.1. Advantages and disadvantages of lead-acid batteries [13,14].

Advantages	Disadvantages
Low self-discharge rate (5%/month)	Not environmentally friendly (lead and sulphuric acid)
High specific power (180 W kg^{-1})	Heavy and low durability (< 350 cycles)
Good performance at high rates and low internal impedance	Danger of overheating during charging (thermal management is critical – maximum 45 °C)
Low cost	Maximum shelf life of 2 years
Robust	Need for maintenance
Lead is most recycled product	

1.2.1.2 Nickel-Cadmium batteries

This type of technology was invented by Waldemar Jungner in 1899 being an alternative for the lead-acid, as the second rechargeable battery that was developed and successfully commercialized. The current nickel-cadmium battery configuration was developed in 1947 by implementing the absorption of gases during charge. This type of batteries are widely used in the aviation industry. They are composed of a positive electrode made by nickel-hydroxide and a negative electrode with cadmium-hydroxide, both deposited over similar sintered porous plaques. The electrolyte is a potassium hydroxide solution in water [15]. The overall net reaction and cell voltage for nickel-cadmium batteries are described in reaction (1.2) [16]. Nickel-cadmium technology presents some remarkable advantages and disadvantages summarized in **Table 1.2**.

$$2NiO(OH) + Cd + 2H_2O \leftrightarrow 2Ni(OH)_2 + Cd(OH)_2\ (1.2\ V) \quad (1.2)$$

Table 1.2. Advantages and disadvantages of nickel-cadmium batteries [17, 15].

Advantages	Disadvantages
Completely sealed construction	Memory effect (periodic full discharges required)
Good load performance (if it is not abused)	Toxicity of cadmium metal
Long storage life and long service life (> 2000 cycles)	High self-discharge (10-15%/month and 10-15% in the first 24 h)
Simple storage and transportation	Low cell voltage (1.20 V)
Wide range of sizes and performance options	
Wide operating range (-20°C - 45°C)	

1.2.1.3 Nickel-metal hydride batteries

Nickel-metal hydride batteries emerged as an evolution of the nickel-cadmium battery technology with the aim of replacing the cadmium-based electrode. On the one hand, toxic cadmium is avoided in this type of batteries and on the other hand, higher capacities are obtained. This technology is mainly used in portable electronic products which demand a notable battery performance [18] but they are also being used in stationary energy storage applications and transportation usages [19]. As it can be observed in **Table 1.3**, some disadvantages associated to the nickel-cadmium batteries have been overcome by nickel-metal hydride batteries.

In the case of nickel-metal hydride batteries, the positive electrode is nickel oxy-hydroxide, while the negative electrode is made of hydrogen absorbing alloys [20]. Both electrodes are separated by the separator, which is a non-woven polyolefin [18]. As in the case of nickel-cadmium batteries, the electrolyte is an alkaline potassium hydroxide solution [20]. The overall reaction (1.3) that takes place in nickel-metal hydride batteries is,

$$\mathrm{M} + \mathrm{Ni(OH)_2} \leftrightarrow \mathrm{MH} + \mathrm{NiO(OH)}\ (1.35\ \mathrm{V}) \qquad (1.3)$$

Table 1.3. Advantages and disadvantages of nickel-metal hydride batteries [21,18,19].

Advantages	Disadvantages
High specific energy (60-120 Wh kg^{-1})	High rate of self-discharge (up to 70% at room temperature)
Environmentally friendly	Limited service life and discharge current
Less memory effect than nickel-cadmium batteries	Detrimental effect at elevated temperatures
Simple storage and transportation	High maintenance
	Battery life (< 2000 cycles)
	Low cell voltage (1.20 V)

1.2.1.4 Redox flow batteries

The redox flow batteries convert chemical energy into electrical energy through reversible oxidation and reduction of working fluids. These types of batteries have been investigated since the 1970s [22] and first studies were focused on simple metal-based redox species, such as Fe/Cr, Fe/V or Zn/Br. Among the various flow batteries, the vanadium redox flow battery is the most developed one [23] and large commercial-scale batteries are currently in construction [22].

This technology is based on two vanadium redox couples, V^{2+}/V^{3+} and V^{4+}/V^{5+}, in two electrolytic tanks [24] as it can be observed in **Figure 1.4**. The cell voltage of V/V redox flow batteries is 1.26 V, while the overall reaction that occurs in the cell is (1.4) [22],

$$V^{2+} + VO_2{}^{+} + 2H^{+} \leftrightarrow VO^{2+} + V^{3+} + H_2O\ (1.26\ V) \qquad (1.4)$$

The benefits and drawbacks associated to vanadium redox flow batteries are summarized in **Table 1.4**.

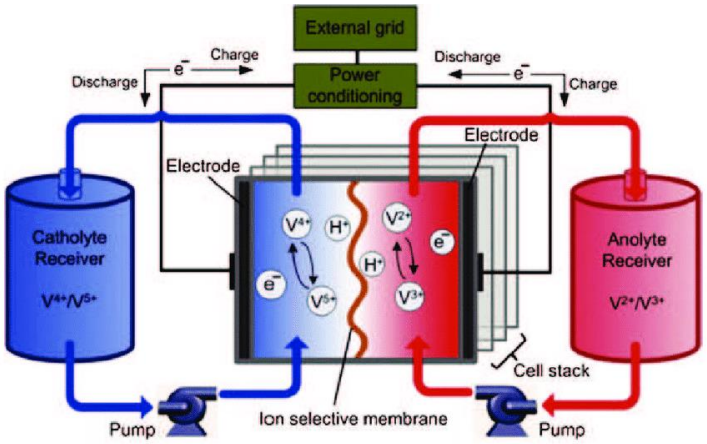

Figure 1.4. Basic scheme of vanadium redox flow battery [25].

Table 1.4. Advantages and disadvantages of redox-flow batteries [26,22].

Advantages	Disadvantages
No self-discharge	Low energy density in comparison to other energy storage systems (10-20 Wh kg^{-1})
Electrolytes are recyclable	Good temperature control system
Scalability of power and energy	Many system requirements (pumps, sensors, flow and power management)
Large scale storage application	Electrical current leakage
Low environmental impact	
Instant recharge	
Time durability (20-30 years)	

1.2.1.5 Sodium-sulfur batteries

Sodium-sulfur batteries were firstly developed by Ford Motor Company in the 1960s. After that, this technology was sold to NGK, which is a Japanese company dedicated to the manufacturing of electrical insulators [27]. Although new research is currently being performed with the aim to develop room temperature sodium-sulfur batteries [28,29 ,30], mature concepts operate at temperatures above 300 °C with a round trip efficiency close to 90%. The largest installation of sodium-sulfur technology is located in Northern Japan with 34 MW and 245 MWh [27].

The positive electrode is sulfur while the negative electrode is sodium and at such operating temperature, both electrodes are in the molten state [28]. As a separator and solid electrolyte, β-alumina which selectively conducts sodium ions and it is a poor electronic conductor is used; therefore, it avoids self-discharge problems. The battery is based on the reversible reaction between sodium and sulfur and the formation of sodium polysulfides (Na_2S_x) (1.5) [28].

$$2Na + xS \leftrightarrow Na_2S_x\ (2.0\ V) \qquad (1.5)$$

This type of technology is mainly fabricated in cylindrical configuration. A scheme of a sodium-sulfur battery is shown in **Figure 1.5** and **Table 1.5** summarizes some of the advantages and drawbacks of the Na-S battery technology.

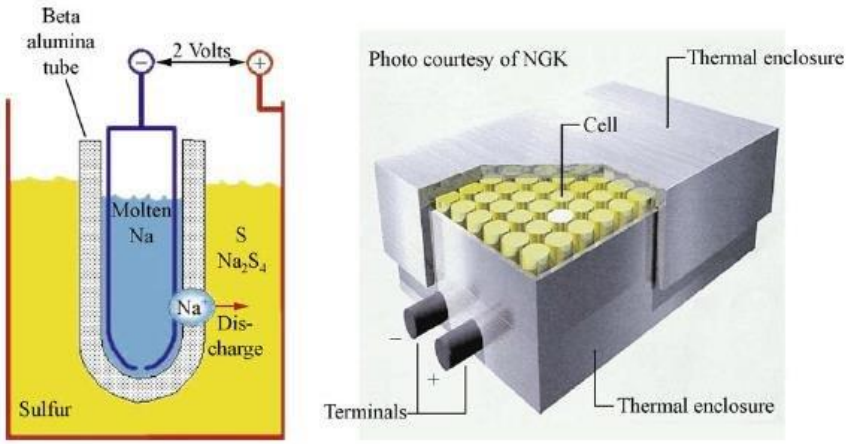

Figure 1.5. Schematic drawing of a sodium-sulfur battery [31].

Table 1.5. Advantages and disadvantages of sodium-sulfur batteries [12,32,24].

Advantages	Disadvantages
Low cost and availability of sulfur	Heat source requirement (300 – 350 °C)
High power and energy density (150-230 W kg^{-1} and 150-240 Wh kg^{-1}, respectively)	High capacity fading (0.1% or 0.4% per cycle)
Non-toxic	Dendrite formation on, i.e. sodium metal anode (room-temperature Na-S)
Long term cycling (> 4000 cycles) and cycle life (15-20 years)	High production costs
No self-discharge	Insulating character of sulfur and polysulfides

1.2.1.6 Lithium-ion batteries

Li-ion batteries have been commercialized since the 1970s. Nowadays, the system which combines graphite and $LiCoO_2$ is the most common technology in portable electronic devices such as mobile phones, laptops, etc. [33]. Li-ion batteries represent very good combination of high energy and power density, and therefore they became the selected technology for power devices, portable electronics and electric vehicles [34]. However, Li-ion batteries are more expensive than other technologies for grid applications. Some of the main advantages/disadvantages associated to Li-ion batteries are shown in **Table 1.6**.

Table 1.6. Advantages and disadvantages of Li-ion batteries [35,36].

Advantages	Disadvantages
High nominal cell voltage (> 3.5 V)	Shortage of lithium compounds
High gravimetric and volumetric capacity	High costs
High power and energy density (up to 1000 W kg^{-1} and 160-200 Wh kg^{-1}, respectively)	Protection circuitry requirement
Wide temperature range operation (0-45 °C)	Ageing
Low self-discharge (1-2% per month)	Transportation safety requirements
Low maintenance	
Low weight	

Li-ion batteries are composed of three main components, the negative electrode (anode), a non-aqueous liquid electrolyte and the positive electrode (cathode). **Figure 1.6** shows the working principle of a Li-ion battery. The system is based in the movement of Li^+ ions between cathode and anode across the liquid electrolyte. During charging Li^+ ions are extracted from the cathode and move to the anode through the electrolyte. During the discharge the reverse process happens. The electrons that are released during the electrochemical reaction are conducted through an external circuit. Both the electrodes are physically separated by a porous polymer separator which allows the ion movement [33].

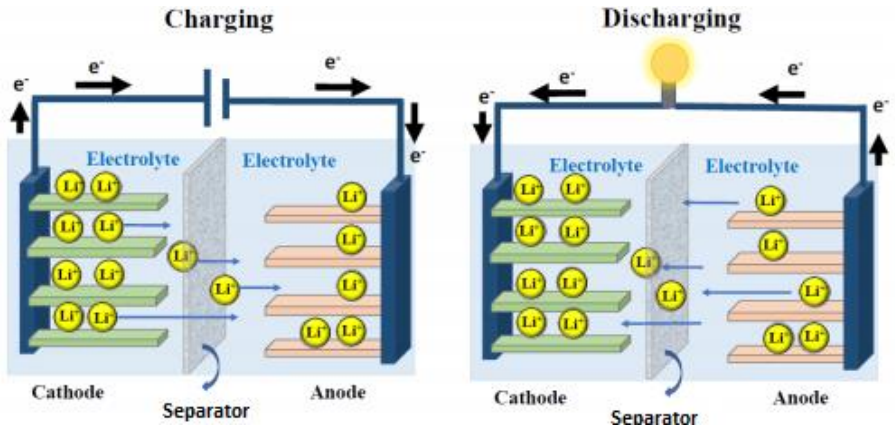

Figure 1.6. Schematic representation of the working principle of Li-ion batteries [33] during charge and discharge processes.

The overall reaction which happens in a graphite//layered oxide Li-ion battery is the following one (1.6),

$$\mathrm{LiMO_2 + C_y \leftrightarrow Li_{1-x}MO_2 + C_yLi_x\ (> 3.5\ V)} \qquad (1.6)$$

Intercalation cathode compounds can be divided in layered, spinel, olivine or tavorite, crystal structures. The layered structure is the easiest form of intercalation for the Li-ion cathode materials. Most of the intercalation cathode materials are, mainly, transition metal oxides and polyanion compounds due to their higher operating potentials and specific energies [35]. Among the transition metal oxides, the first commercialized cathode was $LiCoO_2$ (LCO) introduced by J.B. Goodenough [37]. It has a high theoretical specific capacity of 274 mAh g^{-1}, low self-discharge

and good cycling performance. However, this cathode represents an expensive option because of the use of Co which has a high cost.

Several types of substitutions or transition metal combinations have been proposed since the starting $LiCoO_2$ [38]. $LiNi_{0.33}Co_{0.33}Mn_{0.33}O_2$, known as NMC, has similar properties as $LiCoO_2$ and it shows a reduction of the costs because of the lower Co content. $LiNi_{0.8}Co_{0.15}Al_{0.05}O_2$ (NCA) cathode was also proposed as an alternative to improve the electrochemical performance of Li-ion batteries through higher specific energy values [39]. This compound has found relatively widespread commercial use, for example, in Panasonic batteries for Tesla EVs. $Li(Ni_{0.5}Mn_{0.5})O_2$ (NMO) cathode emerged as a cheaper alternative for LCO due to the lower cost of the transition metals used in its composition; however the low Li ion diffusivity limited its practical use.

Among the polyanionic compound family, the olivine $LiFePO_4$ (LFP) is the most common material, known for its thermal stability and high power capability. However, this material has relatively low average potential and low electrical and ionic conductivity [40]. $LiMnPO_4$ (LMP) represents other olivine structure with higher average potential, + 0.4 V [41]. The vanadium-containing material, $LiVPO_4F$, cycles well, and has high voltage and capacity [42]; however, the use of vanadium implies further environmental pollution.

Table 1.7 shows a list of Li-ion battery cathode active material compounds together with their voltage and capacity values and their level of maturity.

Table 1.7. Representative intercalation cathode compounds for Li-ion technology [35].

Crystal structure	Compound	Specific capacity (mAh g^{-1}) (experimental in commercial cells)	Volumetric capacity (mAh cm^{-3}) (theoretical/typical in commercial cells)	Average voltage (V)
Layered	$LiTiS_2$	210 [43]	697	1.9
	$LiCoO_2$	148 [44]	1363/550	3.8
	$LiNiO_2$	150 [45]	1280	3.8
	$LiMnO_2$	140[46]	1148	3.3
	$LiNi_{0.33}Mn_{0.33}Co_{0.33}O_2$	160[47]	1333/600	3.7
	$LiNi_{0.8}Co_{0.15}Al_{0.05}O_2$	199[48]	1284/700	3.7
	Li_2MnO_3	180[49]	1708	3.8
Spinel	$LiMn_2O_4$	120[50]	596	4.1
	$LiCo_2O_4$	84[51]	704	4.0
Olivine	$LiFePO_4$	165[40]	589	3.4
	$LiMnPO_4$	168[51]	567	3.8
	$LiCoPO_4$	125[52]	510	4.2
Tavorite	$LiFeSO_4F$	120[53]	487	3.7
	$LiVPO_4F$	129[42]	484	4.2

Li-ion battery anode options are carbons [54], lithium titanium oxides [55] and conversion materials such as, $LiMn_3O_4$ [56]. Among them, graphite is the most widely used material as carbon is abundant and low cost and it has a low voltage and relatively low volume change over cycling.

1.2.2 Emerging technologies

1.2.2.1 Metal-air batteries

In 1878, first metal-air battery was developed by Maiché. Some years later, non-rechargeable zinc-air batteries started to compete in the market [57] and currently, are a mature technology in which efforts are being done to make them rechargeable. Afterwards, secondary metal-air batteries such as iron-air, aluminum-air and magnesium-air were developed [58,59]. Lithium-air, sodium-air and potassium-air are the first metal batteries containing non-aqueous electrolytes [60,61]. Huge progress has been developed in recent years in the field of the alkali metal-air batteries lead by the potential high energy density of these types of batteries. Metal-air batteries are composed by metal anodes, aqueous and/or non-aqueous or solid electrolytes and air cathodes. The chemistry of metal-air batteries is based on the metal dissolution and deposition

on the metal anode, while the oxygen reduction and evolution reactions (ORR and OER, respectively) take place in the air cathode [62].

Target applications for metal-air batteries are large-scale stationary energy storage applications, renewable generation and transportation, due to their high energy density which could enhance the autonomy of the electric vehicles [63]. The main advantages and disadvantages of Li-air batteries are gathered in **Table 1.8**.

Table 1.8. Advantages and disadvantages of metal-air batteries [64].

Advantages	Disadvantages
High energy density (> 1000 Wh kg^{-1})	Limited power density
Flat discharge voltage	Limited operating temperature range
Long shelf life	Poor reversible reactions (depend on the metal type)
Non-toxic	Non-moisture stability (depend on the metal type)
Low cost (depend on metal type)	Formation of dendrites
Relatively high average voltage (2.9 V in the case of Li-O_2)	Volatility of electrolytes

Although Na-air batteries are expected to reach 1700 Wh kg^{-1}, half of the specific energy density of Li-air batteries, those values are still close to gasoline [65]. Na-O_2 systems started to be explored around 2010 [66] and are composed by a porous carbonaceous material as a cathode, sodium metal as the anode and a separator which contains an aprotic electrolyte placed between the two electrodes. The carbonaceous material allows the air to pass through the electrode [65]. The overall conversion reaction describing the process in sodium-air batteries and expected cell voltage are (1.7),

$$O_2 + 2e^- + 2Na^+ \leftrightarrow Na_2O_2\ (2.3\ V) \qquad (1.7)$$

1.2.2.2 Li-sulfur batteries

The lithium-sulfur system has an enormous potential as high energy density energy storage device; however, the reaction involved in the charge/discharge process is complex and still needs

to be fully understood. In spite of this, a 21 Ah prototype has been developed by OXIS Energy Ltd. [67].

The electrochemical reaction that takes place in Li-sulfur batteries is very different from the cation redox chemistry of the lithium-ion technology. In this case, the redox active element of the cathode is non-metallic and the electrode reaction is based on the anion redox reaction (1.8) [12]. The main advantages and disadvantages associated to Li-S batteries are summarized in **Table 1.9**.

$$S_8 + 16e^- + 16Li^+ \leftrightarrow 8Li_2S\ (2.8\ V) \qquad (1.8)$$

Table 1.9. Advantages and disadvantages of Li-sulfur batteries [12,67,32].

Advantages	Disadvantages
Sulfur is cheap, abundant and non-toxic	Low practical energy density (25-33% of theoretical energy density, 600 Wh kg^{-1})
High cell voltage (up to 2.8 V)	High capacity fading (0.1% or 0.4% per cycle)
Very high theoretical energy density (> 2000 Wh kg^{-1})	High self-discharge rates (8-15% per month)
Ability to be discharged to 0% of SOC	Complex reaction mechanism, insulating character of sulfur and polysulfides
Neutral buoyancy (submarine and aeronautical applications)	High production costs
Long term cycling (> 4000 cycles)	Electrolyte degradation because of Li metal reaction
	Limited power capability

1.2.2.3 Na-ion batteries

Sodium-ion batteries are currently under development. Since 2010, a lot of research in the development of new cathodic and anodic materials have been performed. Nowadays, efforts are being done with the aim to enable the practical use and commercialization of this type of batteries**. Table 1.10** summarizes the main advantages and disadvantages of Na-ion batteries.

Table 1.10. Advantages and disadvantages of Na-ion batteries [68].

Advantages	Disadvantages
Sodium abundancy	Lower power and energy density than Li-ion batteries
Processing similar to Li-ion technology	Difficulty of stable SEI formation
Potentially cheaper than Li-ion batteries	Protection circuitry requirement
High working voltage (3.0 V)	

This Thesis is focused in the study of the effect of several cell fabrication parameters in the electrochemical performance of Na-ion batteries; therefore, additional information related to this technology will be provided in the following sections on the basics and more innovative investigations together with some insights in the processing and fabrication of Na-ion batteries.

1.3 Na-ion batteries

Sodium based rechargeable batteries have recently regained the attention of the scientific community, as an alternative to Li-ion batteries. The history of Na battery research started in the 1980s, when Delmas et al. started evaluating characteristics of sodium layered oxides as cathode materials combined with metallic Na as the anode component [69]. However, as Li-ion technology emerged at that time, research in sodium insertion materials for energy storage was set aside until the 2000s. In 2010, J.M. Tarascon [70], published an article showing serous concern about the Li dependency if future energy storage systems are only based in Li-containing systems and forecasted a growing interest in non-Li containing technologies, boosting the research in Na-ion batteries, mainly for stationary applications.

Na-ion batteries present similar chemistry and electrode processing and cell assembly routes than well-known Li-ion technology; therefore, it is expected that part of the 'know-how' will be directly implemented from one technology to the other. However, some challenges have still to be overcome to reduce costs and improve the electrochemical performance of Na-ion batteries in order to be competitive in the stationary applications market.

The main differences between Li-ion and Na-ion technology are described in **Table 1.11.** The larger size of sodium ions has a great influence in the host structures and the volumetric capacity. Besides, the phase behavior, which includes coordination, lattice constants or crystal structure and diffusion properties are affected by the difference in the ionic radius of lithium and sodium. Higher voltages than those obtained in Li-ion batteries are also difficult to reach in Na-ion batteries as the intercalation of Na^+ in a given positive electrode is energetically less favorable than the Li^+ intercalation and consequently lower nominal cell voltage and energy density are expected for Na-ion technology. Finally, it is also remarkable that the utilization of metallic electrodes, Li or Na metal, derives in differences in the surface passivation processes [71].

Table 1.11. Comparison of Li-ion and Na-ion battery technologies [72,71,73,74].

	Lithium	**Sodium**
Ion radius	0.76 Å	1.02 Å
Atomic weight	6.9 g mol^{-1}	23 g mol^{-1}
Standard potential vs. SHE	-3.05 V	-2.71 V
Anode current collector	Copper	Aluminum
Abundance in the Earth Crust	0.0017% w/w	2.3% w/w
Distribution in the Earth Crust	Located in Chile, Argentina, Bolivia, Australia, China	Widely distributed

The working principle of Na-ion batteries is similar to that described for Li-ion technology. **Figure 1.7** shows the scheme of a Na-ion battery which describes the system presented in this Thesis. The different cathode, anode and electrolyte components used in Na-ion technology are described in the following sections.

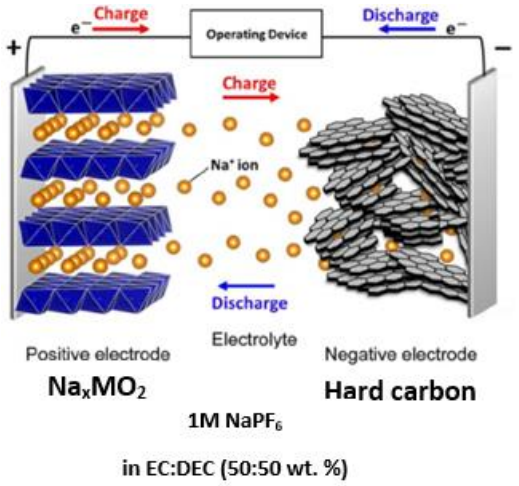

Figure 1.7. Illustration of the Na-ion battery presented in this Thesis [68].

1.3.1 Cathode materials

The reported cathode active materials for sodium-ion technology are mainly transition metal layered oxides and polyanionic compounds [72] (**Figure 1.8**). However, Prussian Blue analogues and a variety of organic compounds have also been reported.

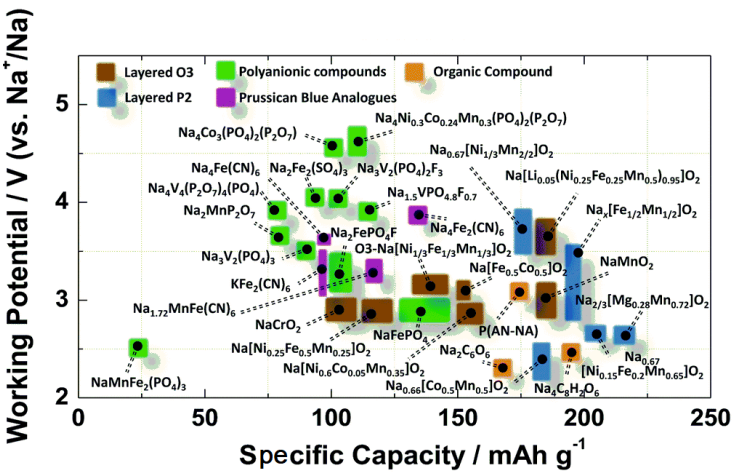

Figure 1.8. Representation of reported Na-ion battery cathode materials ordered with respect to their working potential and specific capacity [72].

1.3.1.1 Layered oxides

Transition metal layered oxides with the general formula Na_xMO_2 (M = one or several transition metals) are attractive cathode materials due to their ease of synthesis, good tap density, high energy density and reversibility of the sodium insertion/deinsertion process [75]. Oxide electrode materials distinguish themselves from other families such as phosphates, Prussian blue/white analogues, sulfates, etc. because of their high tap density. This leads to high packing density of the material on a given area and hence high energy density. $NaCrO_2$, Na_xCoO_2, Na_xMnO_2, and $Na_xMn_{0.5}Fe_{0.5}O_2$ are examples of oxide materials, which show capacity values about 100-150 mAh g^{-1} in the voltage range from, i.e. 2.0 to 4.0 V, vs. metallic sodium [76]. Moreover, a careful combination of the transition metals can help to tune their electrochemical properties and avoid undesired phase transitions during cycling [77].

Typical sodium layered oxide cathodes can be categorized in the P2- and O3-type structures according to Delmas' notation [78]. P and O indicate the prismatic and octahedral sites for the sodium ions and the numbers 2 and 3 indicate the number of MO_2 slabs in the hexagonal cell [79] (**Figure 1.9**). According to Keller et al. P-type cathodes present more powerful performance, while O-type ones, present more energetic performances. O3-type phases have higher sodium content and hence, they provide high initial specific capacities. In contrast, P2- and P3-types provide better rate capabilities because of the easy and faster sodium ion movement between face-sharing prismatic sites and large inter-slab distance. In addition to this, they present better high-voltage stability [80,79].

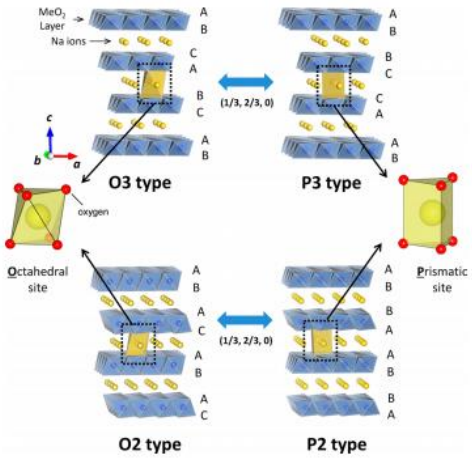

Figure 1.9. Classification of sodium layered oxides depending on the type of sites, prismatic or octahedral and the number of MO_2 slabs in the hexagonal cell (Delmas' notation) [81].

Na-batteries started with the development of TiS_2 and Na_xCoO_2 materials. The group of Komaba started to develop research in Na-ion batteries in 2004 [68]. After that, Okada's group reported α-$NaFeO_2$ as cathode active material, which became in one of the most common layered oxides [82].

Sodium layered oxides can be synthesized by means of different methods. According to Ma et al., the crystallization properties of layered oxides such as the P2- and P'2-$Na_{2/3}MnO_2$ are highly dependent on the synthesis parameters as the heating conditions and the Na/Mn ratio. They remarked the great importance of understanding the crystal structure formation mechanism as well as the need to control the Na_2CO_3 content in the synthesis of this compound [79]. Until date, the most spread synthesis route is the solid state synthesis due to its versatility to easily prepare different compositions. Nguyen et al. studied the effect of calcination temperature in the particle morphology, size, crystallinity and electrochemical properties using co-precipitation and solid state reactions for P3 and P2 sodium layered oxides [83]. Keller et al. also synthesized P2, O3 and P3/P2/O3 phases of a quaternary layered oxide by tuning the solid state reaction conditions and concluded that there are synergetic effects attributed to the simultaneous presence of the P- and O-type phases that enabled the achievement of improved electrochemical performance [80].

3 different layered oxides were selected in this Thesis to be used as cathode active materials. In the following paragraphs the state of art on related compounds will be provided for each of the three compositions.

1.3.1.1.1 P2-$Na_{0.67}Fe_{0.5}Mn_{0.5}O_2$ layered oxide

P2-type structures are usually sodium deficient compounds and this sodium deficiency gives a significant reduction in the delivered capacity when assembled together with sodium-free anode materials such as hard carbons. In this Thesis, P2-$Na_{0.67}Fe_{0.5}Mn_{0.5}O_2$ was selected to develop a strategy to overcome the sodium deficiency issue of P2-type layered oxides.

P2-$Na_{0.67}Fe_{0.5}Mn_{0.5}O_2$ was firstly reported by Yabuuchi et al. This Mn and Fe containing compound attracted much interest due to the use of low-cost and non-toxic precursors. They reported 190 mAh g^{-1} as delivered capacity due to its electrochemically active Fe^{3+}/Fe^{4+} and Mn^{3+}/Mn^{4+} redox couples [84,85]. After this first publication, Zhu et al. also reported the same material tested as a free-standing composite electrode with graphene following an aqueous scalable fabrication process for the electrode preparation [86]. Bai et al. studied the synthesis of P2-$Na_{0.67}Fe_{0.5}Mn_{0.5}O_2$ by means of a sol-gel method assisted by a chelating agent with $NH_3 \cdot H_2O$ and calcined at 900 °C, reaching 92 mAh g^{-1} after 40 cycles with 100% of Coulombic efficiency [87]. Other authors as Talaie et al. and Park et al. based their research on the substitution of P2-$Na_{0.67}Fe_{0.5}Mn_{0.5}O_2$ with Ni and Ti, respectively. Ti substitution improves the rate capability and cycling stability, while Ni substitution increases the specific energy density [88,85].

1.3.1.1.2 O3-$Na_{1-\delta}Ni_{0.32}Ti_{0.32}Mg_{0.16}Mn_{0.20}O_2$ layered oxide

For preliminary formulation and full-cell studies at small scale (ca. 0.5 g), a composition that was reported to show high energy density such as $Na_{1-\delta}Ni_{0.32}Ti_{0.32}Mg_{0.16}Mn_{0.20}O_2$ was selected. Ni-based sodium layered oxides are very attractive materials due to the high potential of $Ni^{2+}/Ni^{3+}/Ni^{4+}$ redox couples [89] and good electrochemical performance in terms of capacity and thermal properties [90]. However, $NaNiO_2$ shows a multiple plateau voltage profile [91]. Incorporating a small mole fraction of an electrochemically inactive element, as Mn^{4+} and Ti^{4+}, into an oxide layer can stabilize oxide layers, resulting in better long term cycling performance

although the amount of Na de/intercalation is reduced by this substitution [92,77,93]. Therefore, nickel ions are the redox active elements which contribute to the reversible specific capacity and the manganese and titanium ions play the role of a structure stabilizer. Moreover, if Mg is incorporated in the compound, it also helps to smoother the voltage profile, to enhance the capacity retention and improving the rate performance.

1.3.1.1.3 O3-$NaFe_{0.4}Mn_{0.3}Ni_{0.3}O_2$ layered oxide

A composition which has already been reported to show good cycling properties in half and full-cell configuration such as $NaFe_{0.4}Mn_{0.3}Ni_{0.3}O_2$ was selected in order to perform formulation and full-cell development studies at a larger scale (ca. 10-30 g). It is remarkable to mention that among the group of transition metals, manganese and iron are a representation of abundant and low-cost materials, while nickel allows improved electrochemical performances due to the $Ni^{2+/4+}$ redox process [77]. On the other hand, the inclusion of high redox potential couples, as $Fe^{3+/4+}$, are expected to have a positive effect in order to increase the operating voltage, although the amount of Fe should be limited to avoid structure instability issues [77].

Back in 2012, Yabuuchi et al. proposed as a strategy to solve the problem of irreversible iron migration which happens when α-$NaFeO_2$ is charged above 3.5 V, the partial substitution of Fe with $Ni_{1/2}Mn_{1/2}$ to form the $NaFeO_2$-$NaNi_{1/2}Mn_{1/2}O_2$ solid solution [94]. Later in 2015, the addition of Fe to $NaNi_{1/2}Mn_{1/2}O_2$ was reported to be beneficial for cycling stability. The results obtained by Yuan et al. revealed that the O3-$NaFe_x(Ni_{1/2}Mn_{1/2})_{1-x}O_2$ lattices with Fe substitution undergo different phase transformation at high charging potentials and that the Fe substitution can lead to a decreased interlayer distance, which might suppress insertion of the solvent components and therefore enhance the cycling stability of the material [95]. Both the studies [94,95] show good cycling stabilities for the same composition as that selected for this study, i.e. $NaFe_{0.4}Mn_{0.3}Ni_{0.3}O_2$.

In addition to these studies based in half-cell configuration, the feasibility of full-cells utilizing slightly lower Fe content compound, i.e. O3-$NaFe_{1/3}Mn_{1/3}Ni_{1/3}O_2$, has also been demonstrated by Kim et al. using hard carbon as an anode. This material showed good cyclability, starting from

120 mAh g^{-1} in the first cycle and delivering ~100 mAh g^{-1} after 150 cycles [96]. Furthermore, Kuze et al. also studied the $NaFe_xMn_{1/2-x/2}Ni_{1/2-x/2}O_2$ phase for x = 0.2, 0.33 and 0.4, but no clear differences were found in terms of 1st cycle capacity. Therefore, the composition with the highest iron content (x = 0.4), for which resources are abundant, was selected as the most appropriate for full-cell assembly. In this report 500 cycles at coin cell level and 20 cycles at pouch cell level were shown using this cathode composition combined with hard carbon as the anode material [76].

1.3.1.2 Polyanionic compounds

Polyanionic compounds include a variety of phosphates, sulphates, silicates, borates and some other oxysalts. As it was reported by Barpanda et al., as there is an essential lack of high-voltage cathode materials, these compounds look for Na-ion systems operating at voltages over 3.5 V in Na batteries [97]. Moreover, polyanion-type compounds present high thermal stability, oxidation stability during the charging process and non-significant volume change among other characteristics. However, they present poor electrochemical performances in combination with des-stabilization of the electrolyte [98].

Among phosphates, the most investigated compounds are ortho-, pyro- and fluoro- phosphates [98]. For instance, olivine $NaFePO_4$, $Na_3V_2(PO_4)_3$, pyrophosphate $Na_2MP_2O_7$ (M = Fe, Co, Mn), pyrophosphate $Na_4M_3(PO_4)_2P_2O_7$ (M = Co, Fe), fluorophosphate Na_2MPO_4F (M = Fe, Co, Mn) have been widely studied.

$NaFePO_4$ has a theoretical capacity of 154 mAh g^{-1} with an average voltage of 2.9 V vs. Na, based in the $Fe^{3+/2+}$ redox reaction [99]. However, the practical capacity of the olivine phase of this compound is lower because of its poor electron conductivity. Some strategies have been followed in order to overcome this issue, as carbon coating or synthesis of $NaFePO_4$ nanoparticles. The nanosized maricite $NaFePO_4$ phase shows a practical reversible capacity of 142 mAh g^{-1} with a high capacity retention after 200 cycles of 95% [100], and also, Li et al. reported a highly reversible capacity of 144 mAh g^{-1} after 300 cycles [101].

The reversible redox reaction of $V^{4+/3+}$ and its optimal ionic diffusion in $Na_3V_2(PO_4)_3$ are attractive characteristics to consider this compound as good cathode active material candidate for sodium-ion batteries. In this polyanion-type compound, only two of the three Na ions can be extracted from the structure below 4.5 V [102]. As well as in the case of $NaFePO_4$, strategies as carbon coating have been used in order to enhance the electrochemical performance [103,104]. For instance, carbon-coated $Na_3V_2(PO_4)_3$ presents a reversible capacity of 114 mA h g^{-1} at 1C rate [105]. In addition to this, cationic substitution strategies can be used to improve the electrochemical performance. As an example, Aragón et al. developed a series of compounds based on Fe substitution of V, i.e. $Na_3V_{2-x}Fe_x(PO_4)_3/C$ ($0 \leq x \leq 0.5$), in order to study the influence of Fe in the unsubstituted compound [106]. Moreover, this material can also be used as anode in sodium-ion batteries with the potential to accommodate five Na ions in the $V_2(PO_4)_3$ host. As anode, it delivers 100 mAh g^{-1} at 1C [107].

The family of pyrophosphate compounds, $Na_2MP_2O_7$ (M = Fe, Co, Mn), presents some desirable characteristics related to its stability and its optimal ionic pathways for Na [108]. This family of compounds comprises different polymorphic forms, as triclinic, orthorhombic or tetragonal structures. While the triclinic phase is considered as the most thermodynamically stable for Na_2FeP_2O and Na_2MnP_2O, the orthorhombic phase is better for Na_2CoP_2O. For instance, triclinic $Na_2FeP_2O_7$ exhibits a theoretical capacity of 90 mAh g^{-1} and an average operating potential of 3.0 V [109], while triclinic $Na_2MnP_2O_7$ offers a similar capacity of 80–90 mAh g^{-1} and an average operating potential of 3.7 V [110].

Among the Na_2MPO_4F (M = Fe, Co, Mn) family compounds, orthorhombic Na_2FePO_4F and Na_2CoPO_4F are the most relevant. For example, carbon coated Na_2FePO_4F and Na_2CoPO_4F have been reported to reach a reversible capacity of 100 mAh g^{-1} and an average potential of 3.0 V [111] and 4.3 V, respectively. In the case of Na_2CoPO_4F, the energy density is largely enhanced because of the high average voltage [112]. The electrochemical performance of Na_2MnPO_4F is improved by means of the nanosized particles and carbon coating strategies, delivering a reversible capacity of 120.7 mAh g^{-1} [113].

Alluaudite-type ($Na_2Fe_2(SO_4)_3$) and Kröhnkite-type ($Na_2Fe(SO_4)_2 \cdot 2H_2O$) are 2 of the examples of suitable sulphate Na-ion cathode active materials. In both cases, reversible capacities over 70 mAh g^{-1} with an average working potential of 3.8 and 3.25 V, respectively were reported by Yamada et al. [114,115].

1.3.2 Anode materials

Metallic sodium is widely used in the academic field to assemble half-cells with the aim to evaluate novel cathode active materials; however, it is not the preferred choice as an anode active material for high capacity/energy density batteries because of the formation of dendrites, nano-sized metal with a tree like growth which penetrate through the separator and lead to short circuits. Moreover, Na metal is highly reactive and continuously growing polarization is caused due to dendrite deposition [116]. Alternative, anode materials for sodium-ion batteries comprise a wide range of carbonaceous, metal alloys, organic and transition metal materials (**Figure 1.10**).

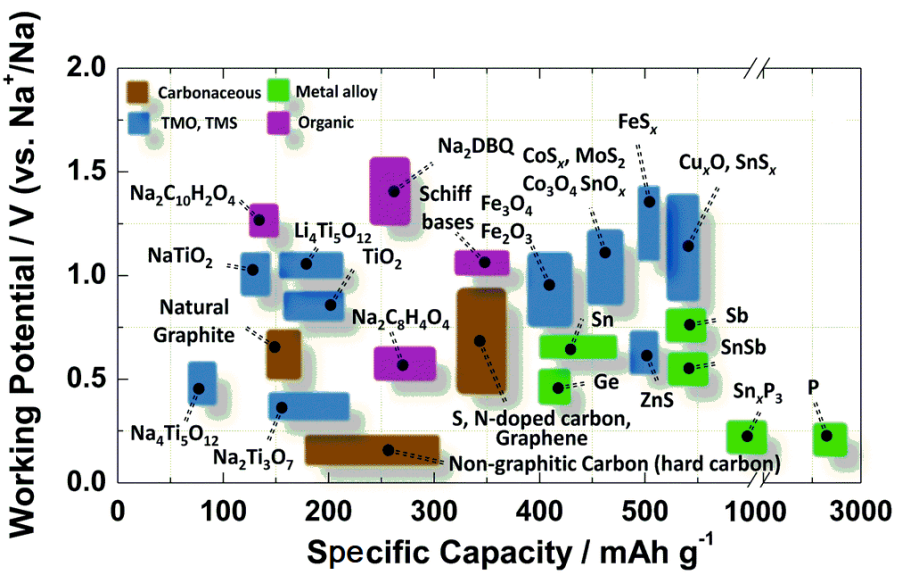

Figure 1.10. Reported Na-ion battery anode materials ordered with respect to their working potential and specific capacity [72].

1.3.2.1 Carbons

Carbons, and more commonly, graphite is used as the intercalation host for lithium-ion batteries. Although, in the previous years, graphite was known to be a non-suitable host for Na^+ ions because of its low inter-planar spacing of 0.34 nm (Na^+ ion has an ionic radius of 95 pm and Li^+ ion has a ionic radius of 68 pm), it has recently been reported that Na+ ions can be reversibly intercalated in graphite. Back in 2000, Thomas et al. proved the ability of carbon structures to host sodium ions. For instance, they can be tuned by means of mechanical grinding, to improve the reversible capacity from 16 to 187 mAh g^{-1} after grinding [117]. According to Wen et al. a minimum interlayer distance of 0.37 nm is required for the insertion of Na^+ ions and they proposed an expanded graphite with an interlayer distance of 40.34 nm as a Na-ion battery anode. The manipulation of the interlayer spacing was performed by controlled oxidation and partial reduction [118]. In addition to this, Jache et al. also proved that sodium ions can be intercalated in the graphite structure by means of co-intercalation using a diglyme-based electrolyte [119]. In spite of this, disordered carbons, as hard carbon, are preferred as sodium-ion battery anodes because of their large reversible capacity at low voltages.

Disordered carbons have been deeply studied to be used as sodium-ion battery anodes [120,121,122,123]. Specifically, hard carbon is the most common anode material with a high reversible capacity in the range of 200-300 mAh g^{-1} at low operating potential, which are both key factors in its use [124,123]. According to Bommier et al., as porosity and surface area decreases, the obtained reversible capacity increases [125].A representative curve corresponding to the cycling behavior of the hard carbon *versus* Na used in this Thesis, with an approximate active material loading of 5 mg cm^{-2} is shown in **Figure 1.11.** Three regions can be differentiated in the discharge profile. Firstly, a flat plateau that runs from 0.01 V to ca. 0.2 V is observed (I). This low-voltage plateau can be attributed to the insertion of the sodium ions in the porosity of the structurally disordered carbon material. The plateau is followed by a slopping region from ~ 0.2 V to 1.0 V (II), which is related to the insertion of the sodium-ions on both sides of the single graphene layers [126]. The last region (III) corresponds to a sharp potential decrease at the beginning of the reduction.

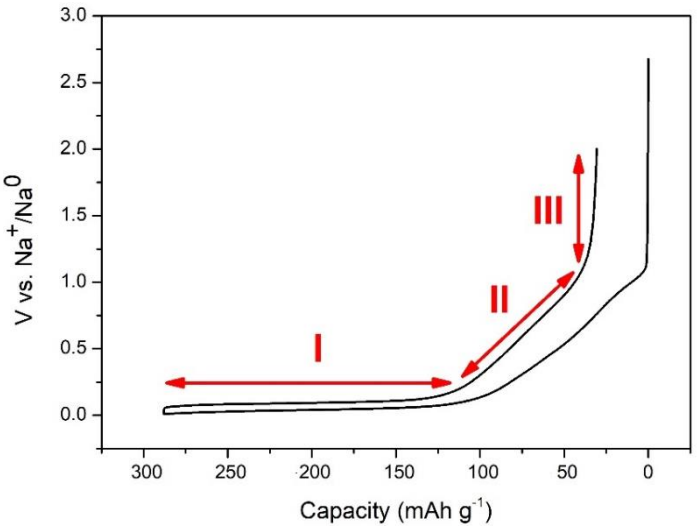

Figure 1.11. First galvanostatic charge/discharge cycle of hard carbon at 0.1C within 0.01-2 V.

This disordered carbon can be derived from diverse biomass sources which are being investigated by several researchers. These sources include among others macadamia shell [123], old-loofah [127], rape seed shuck [128], etc. In operation as Na-ion battery anode, hard carbon is discharged to voltages close to 0.0 V vs. Na/Na^+. At this voltage the electrolyte is expected to be reduced to form the Solid Electrolyte Interphase (SEI). Some authors have studied the formation of the SEI in the hard carbon anodes by means of different techniques [122]. As well, many authors have investigated the importance of the electrolyte choice when using hard carbon as anode. The electrolyte formulation should promote the formation of a protective SEI layer on the surface of the electrode which should enable an optimal path for Na^+ ion conduction. Regarding this, additives such as fluoroethylene carbonate (FEC) [129] or $RbPF_6/CsPF_6$ [124] have been studied in the literature.

Hard carbons have a random alignment of small-dimensional graphene layers [130]. The X-ray diffraction pattern of hard carbon presents two broad peaks approximately at 24 and 43 degrees (**Figure 1.12** (a)). These patterns provide useful information about the interlayer spacing between graphene sheets, in which low angles for (002) mean that there are distorted graphitic

planes in the material [131,132]. Besides, the width ratio of the (100)/(110) and (002) diffraction peaks provide information about the number of stacked graphene sheets [133].

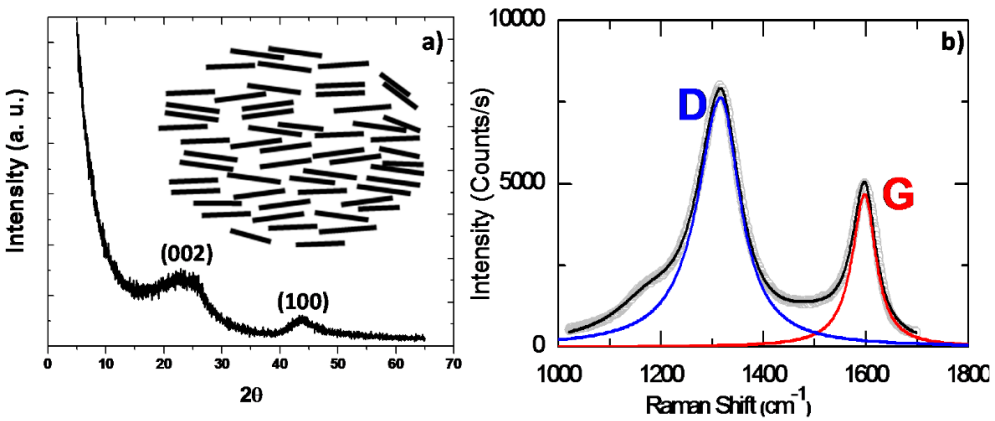

Figure 1.12. (a) X-ray diffraction pattern and (b) Raman Spectra of Hard Carbon [118].

Dahn et al., explained that the ordering of the hard carbon corresponds to the "falling cards model" [132].An estimation of the graphitization of the hard carbon can be done based on Raman spectroscopy (**Figure 1.12** (b)). Two characteristic bands are related to carbon materials, D and G-bands, at ca. 1350 cm^{-1} and 1580 cm^{-1}. The D-band corresponds to the defect-induced mode, while the G-band is related to the graphitic character. The ratio between both bands indicates the degree of graphitization, which can be improved by increasing the pyrolysis temperature [134].

1.3.2.2 Titanium-based components

Titanium-based components are interesting compounds for anode materials due to their reasonably low operation voltage, low cost and non-toxic nature [135,136]. In this group, titanium dioxides, spinel-lithium titanate and sodium titanate compounds can be included [137,138]. The redox couple of these compounds is Ti^{4+}/Ti^{3+}. Most of the discoveries have been performed using anatase TiO_2, which can properly accommodate the large ionic radius of the Na^+ ions [139], being the sodium ions insertion into the anatase lattice, comparable to that of lithium ions. Xu et al., reported the improvement of the electrochemical activity of TiO_2 by reducing its particle size to

nanometers and shortening the migration paths for sodium ions [140]. The influence of the electrolyte composition and the cut-off potential was also studied by Wu et al. [141]. Nb Doped TiO_2, $Ti_{0.94}Nb_{0.06}O_2$, was reported to reach 160 mAh g^{-1} after 50 cycles. Zhang et al. also proposed rutile TiO_2 with a capacity retention of 83.1% after 200 cycles at a current density of 0.1C rate [142]. Strategies such as structure modification or conductivity improvement by means of carbon additives in order to enhance sodium kinetics because of its large ionic radius need still to be explored. As an example, Kim et al. developed carbon coated anatase TiO_2 nanorods, exhibiting a capacity of 193 mAh g^{-1} [100].

1.3.3 Electrolyte

The electrolyte plays an important role in the cell performance as it can affect to the electrochemical response of the electrodes. In fact, the choice of the electrolyte has been controversial as different results have been obtained for similar electrode compounds. Ponrouch et al. listed some of the important properties required for electrolytes to be used in sodium-ion cells [143]. High ionic conductivity and electronic insulating character are two of the most important requirements in order to maximize the sodium ion transport and minimize the self-discharge issue [143]. In addition to this, the chemical stability is related to the suppression of the chemical reactions during charge and discharge processes. Thermal stability is also required in order to maximize the operation temperature range and minimize the safety hazards. Finally, the environmental impact has to be minimized and electrolyte components should present sustainable, abundant and low-cost precursors as well as synthesis and production routes.

Most of the electrolyte compositions reported in the literature are the Na analogues of those reported for Li-ion technology. Lithium and sodium-ion battery electrolytes consist in Li/Na salts dissolved in a carefully selected combination of organic solvents. However, some considerations must be beard in mind since analogue Li and Na electrolyte solutions show different electrochemical behavior in operation and the created interphases are highly dependent on the electrode and electrolyte nature. For example, sodium salts present higher solubility than lithium salts, so batteries can suffer a failure, because of SEI dissolution deriving in unstable interface

layer [144]. In addition, stable SEI formation is more complicated since it usually suffers from ruptures and it allows new areas to be exposed to the electrolyte. As well, due to the high reactivity of sodium metal, it causes higher electrolyte degradation and self-discharge effect than lithium metal. Associated to this issue, the use of FEC electrolyte additive has been proposed [145].

The upper voltage of the cells is limited by the anion part of the salt which oxidizes at high voltages, while the lower voltage limit is usually selected to avoid the solvent reduction. The most common Na salt anions used for Na-ion batteries are $-ClO_4^-$, $-BF_4^-$, $-PF_6^-$, $-CF_3SO_3^-$ (Tf), $-[N(SO_2F)_2]^-$ (FSI) and $-[N(CF_3SO_2)_2]^-$ (TFSI), all of them widely reported for Li-ion batteries. $-ClO_4^-$ is a strong oxidizing agent and it is not recommended for practical cell development. $-PF_6^-$ is regularly used but, it can present safety issues related to cell temperature raise or the presence of moisture, leading to PF_5, POF_3 or HF formation. $-BF_4^-$ produces less conductive electrolytes, as in the case of Tf, which also corrodes Al current collectors [143]. FSI and TFSI anions also produce Al current collector corrosion when used coupled to carbonate solvents [146].

It is remarkable that sodium salts present higher melting points and better thermal stability than their lithium analogues, which is an advantage in terms of safety [143].

In addition to present non-toxic and low-cost characteristics, Na-ion battery electrolyte solvents must have polar groups in order to dissolve the salts. The solvent has also a great influence on the thermal stability and the ion mobility, which is inversely proportional to the electrolyte viscosity [143]. The choices of electrolyte solvents are mainly organic carbonates such as ethylene carbonate (EC), propylene carbonate (PC), dimethyl carbonate (DMC) or diethyl carbonate (DEC). The use of ionic liquids in the sodium ion battery field is also growing [147] as they fulfill most of the requirements to be used as electrolyte solvents. However, they are still not competitive in terms of cost [143].

The combination of $NaClO_4$ or $NaPF_6$ as sodium salts and carbonate ester solvents, as PC, DEC or EC are the most common electrolytes for sodium ion technology. As a reference, **Figure 1.13**

shows the electrochemical stability window and the thermal stability of several $NaClO_4$ based electrolytes.

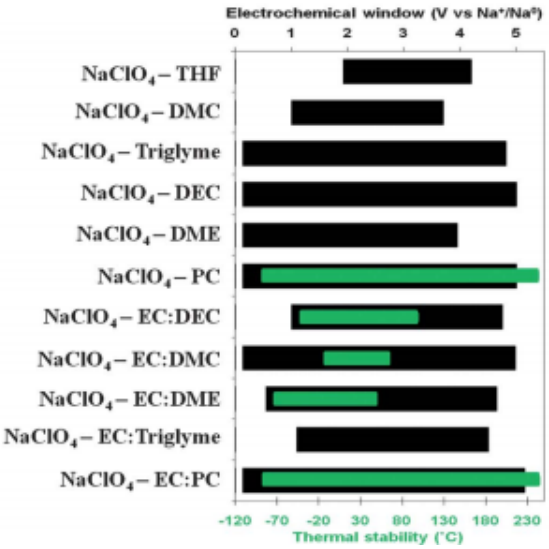

Figure 1.13. The electrochemical potential stability window (black bars) and thermal stability range (green bars) of different 1 M $NaClO_4$ electrolytes [148].

1.3.4 Full-cell prototype fabrication

Several authors have reported Na-ion full-cells in coin cell configuration. Raj. K. et al. have developed a bio-derived mesoporous disordered carbon which delivers 146 mAh g^{-1} at 0.2 A g^{-1} after 100 cycles. They used it in combination with a sodium vanadium phosphate cathode in order to assemble a full-cell with a reversible capacity of 266 mAh g^{-1} for 50 cycles at 0.1 A g^{-1} [149]. As well, P2/P3-$Na_{0.7}Li_{0.06}Mg_{0.06}Ni_{0.22}Mn_{0.67}O_2$ composite cathode was tested by Zhou et al. in full-cell configuration showing excellent performance with an average cell voltage of 3.36 V and energy density of 218 W h kg^{-1} [150].

Other research groups are also developing different sodium secondary battery prototypes. Barker et al. assembled a full-cell containing $NaVPO_4F$ as cathode active material and hard carbon as anode, having a high average voltage of 3.7 V and reversible capacity of approximately 80 mAh g^{-1} [151]. Nose et al. used $Na_4CO_3(PO_4)_2P_2O_7$ as a cathode and hard carbon as an anode in

their full-cells [152]. Among the groups that have selected sodium layered oxides as the cathode active material, Komaba et al. fabricated a full-cell containing a O3-type sodium layered oxide, $Na[Ni_{0.5}Mn_{0.5}]O_2$, with an operating voltage of 3.0 V and a specific capacity of around 200 mAh g^{-1} based on the negative electrode mass [153]. Kim et al. used O3-$Na[Ni_{0.33}Fe_{0.33}Mn_{0.33}]O_2$ cathode coupled to carbon anode and reported an average voltage of 2.75 V and 100 mAh g^{-1} after 150 cycles [154].

Going one step further, several institutes have addressed the challenge of fabricating sodium-ion batteries in the range of few Ah [155,156,157]. For instance, the French National Center for Scientific Research (CNRS) and the French Alternative Energies and Atomic Energy Commission (CEA) developed the first cylindrical sodium-ion battery which claims an energy density close to 90 Wh kg^{-1} and stable cycling behavior over 2000 cycles [158]. Also, new start-up companies are developing new sodium ion batteries for large scale applications, as Novasis Energies, Inc., Faradion Limited, Natron Energy, etc. [159,160]. Anyway, there is still the need to perform further research in the design of the full-cells, electrode balancing, definition of the suitable cycling voltage ranges, development of new electrolytic solutions, etc. to make this technology viable for commercialization [72].

1.4 Processing and manufacturing of metal-ion batteries

Innovation is a continuous demand of the final battery users to the manufacturers in order to meet the energy density, cycling stability, safety and cost targets of their applications which are not fulfilled with the technologies that are currently available in the market. This innovation should not be limited only to new material development and it should also include better engineering strategies. Therefore, research in component processing and cell manufacturing are necessary to elucidate possible paths for improvement. According to Wolter et al. [161], the mixing, coating and calendering steps of the Li-ion battery processing, i.e. electrode manufacturing steps, are very relevant processes that determine the quality of the product,

including battery performance and lifetime. In fact, most of the battery failures usually have their origin in the electrode manufacturing processes.

The bases for Na-ion cell manufacturing process have been stablished by the Li-ion cell manufacturing technology. However, there are some particularities specific for Na-ion electrode processing, such as moisture sensitivity, which need to be taken into consideration. In fact, the amount of information available in the literature dealing with Na-ion battery electrode processing is far away from the amount of studies dealing with Li-ion technology. Therefore, Na-ion battery processing related studies are of especial interest for the development of this technology.

The general Li/Na-ion pouch cell manufacturing process steps are represented in **Figure 1.14**. First, the electrode components are mixed with the proper solvent and casted on top of the current collectors. In order to finely control the thickness and porosity of the electrodes, laminates are calendered at selected pressure and temperature conditions. After cutting the electrodes to the desired size, those are stacked together with the porous separator. Then, electrical connector tabs are welded to the current collectors, usually by ultrasonic welding. Once the cavity of the pouch bag is made and the electrodes/separator stack is placed, 3 of its 4 sides are sealed with the action of temperature and pressure. The electrolyte dosage and 4^{th} side sealing are done under vacuum conditions and once the formation cycles are performed under carefully selected cycling regime the gases are extracted and the cells are definitely sealed. Additional details on some of the cell processing steps are provided in the following sections.

Figure 1.14. Illustration of Li/Na-ion cell manufacturing steps.

1.4.1 Slurry mixing

In addition to the chemical composition of the active material, an effective mixture of this compound with the conductive agent and the binder, combined with an optimum slurry composition (ratio between the active material, conductive additive and binder) are needed in order to obtain good electrochemical cell performances. Moreover, an optimized mixing process should allow to obtaining slurries with the properties suitable to be properly coated on top of the current collectors, with no defects in the resulting electrodes. The electrode slurry preparation is the first step of the cell manufacturing sequential process and it determines its final properties; therefore, especial care needs to be taken in this process which includes the selection of the most adequate mixing sequence and equipment. It is remarkable to mention that cathode slurry mixing presents more challenges than anode slurry mixing according to Liu et al. [162], as they said that it is more complicated to disperse Li complex compounds than graphite powder. The main processes that take place during the slurry mixing step are the wetting of the solid components with the selected solvent, their homogenization, the de-agglomeration of the active material and the conductive agents, the adjustment of the solid

content and the rheological properties, the stabilization of the slurry and the elimination of air bubbles to avoid the creation of defects in the casted electrodes [163].

The stability of Li-ion battery electrode slurries has been studied in the literature by means of rheological analysis. The rheological properties of slurries are influenced by the particle shape, surface chemistry and solvent nature and concentration among other parameters. Ligneel et al. [164] observed that with 0.004 ml mg^{-1} of solvent concentration there was almost no settling in $Li_{1.1}V_3O_8$ containing electrodes, for instance. Moreover, the morphology and the electrochemical performance of the composite electrodes were also strongly affected by the solid content. Bauer et al. [165] also studied the colloidal stability of the cathode slurries. According to them, the addition of electrochemically inactive components such as the binder and the carbon black, in addition to be necessary for the proper electrochemical performance of the electrodes, affect to the stability of the slurries. Kwon et al. [166] also studied the effect of storage time and agitation on the rheological properties and the electrode microstructure. More concretely, the effect of the storage time and agitation in the required stress to break the structure and the flow to start, i.e. the yield stress, was analyzed.

Focusing more on the electrochemical performance of the electrodes, Liu et al. [167] concluded that the optimization of the carbon black and binder ratio leads to the maximization of the active material loading and a minimization of the impedance of the cell. They found in their research that the most conductive electrodes with 78%–95% active material content were obtained with a carbon black:binder ratio of 0.6:1.

The slurry formulation has also an influence on the mechanical strength and flexibility of the electrodes. Gaikwad et al., [168] for instance, emphasized the binder selection in order to reach better adhesion and cohesion properties. Furthermore, Despotopoulou et al., [169] working also in Li-ion batteries, showed in their work the importance of the polymer selection, solvent effects and slurry formulation and preparation procedure among other parameters in the adhesion and cyclability properties of the electrodes.

The use of additives has also been reported in the literature. Zhang et al. [170] observed that by using Triton X surfactant as a dispersant agent, all the components are better distributed and the electrodes show less polarization.

In addition to the slurry formulation, it has been reported that the selected mixing procedure has a huge impact in the microstructure of the resulting electrodes. For example, variations in the mixing sequence and/or mixing equipment can produce a change in the morphology of carbon black particles [171]. As a consequence, the final electrochemical behavior is also affected [172,173,162]. Lee et al. [173] compared two different mixing processes, one-step and multi-step mixing, by means of rheological measurements and evaluation of the solid dispersion, electrode resistance and capacity retention characteristics among others. The network created following the multi-step processing route resulted to be more uniform resulting in better electrochemical performance.

For small scale slurry preparation in the range of few milliliters, simple mixing equipment such as manual mortar and pestle or magnetic stirrers are typically used. Other devices identified by Kraytsberg et al. for powder dispersion include hydrodynamic shear-based mixers (dissolvers), ball-milling, kneaders, 3-roller mills, disc mills and ultrasonic homogenizers [174] (**Figure 1.15**).

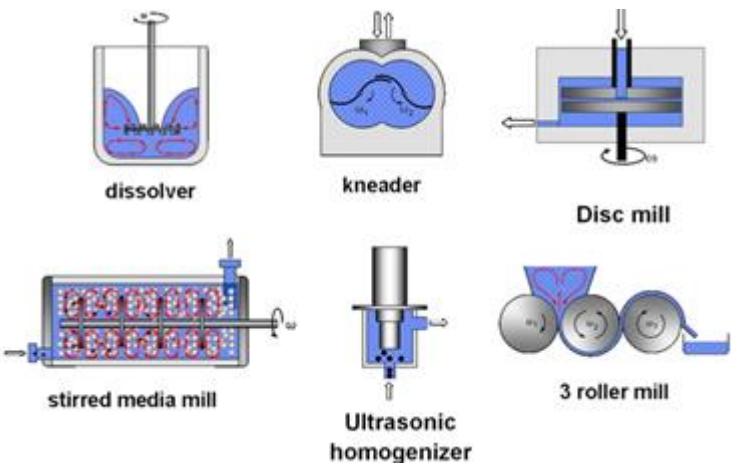

Figure 1.15. Schematics drawings of different mixing equipment [175].

In the case of the ball-milling process, in addition to the dispersing effect, the grinding effect has also a big influence in the way that the dry powders are dispersed [175]. Zirconia balls with different diameters are used to promote the grinding step during the rotational movement [176,177]. This milling action has usually an influence on the temperature that is reached in the milling tank. In the rest of the mixing devices proposed by Kraytsberg et al., [174] the dispersion and homogenization of the materials is done by applying a shear stress through a liquid. Kneaders and 3-roller mills, are considered when the slurry presents a high solid content close to 75% w/w and hence, large viscosity [178,179]. Finally, disc mills, are rarely used for electrode slurry preparation [180]. The combination of more than one of these mixing devices is an approach that has been usually followed in order to obtain better dispersing efficiency.

1.4.2 Electrode coating

Once the electrode slurries are prepared, the second electrode manufacturing step consists in the coating process, which as it has already been mentioned earlier, is one of the crucial steps since it determines the thickness, active material loading and quality of the electrodes. Moreover, including equipment investments and operating costs, it constitutes the highest contribution to the whole process cost [161].

The coating process methods can be categorized into self-metered and pre-metered processes [181] (**Figure 1.16**). The main advantages of self-metered methods are their simplicity and robustness. However, they can suffer from low accuracy and coating precision. Roll coating, gravure coating, dip coating, comma bar or doctor blade coating are classified as self-metered coating methods. As the quality of the coated layer can be affected by the environmental conditions, this type of equipment must be often recalibrated [182,183].

In the case of the pre-metered coating methods, the control of the coating thickness is via the coating width, web speed and volume flow. These methods allow multilayer coatings. However, one of the disadvantages of these methods is the strict control of the slurry rheology [181]. The

most common pre-metered coating method used for electrode fabrication is the slot die coating method [184,185].

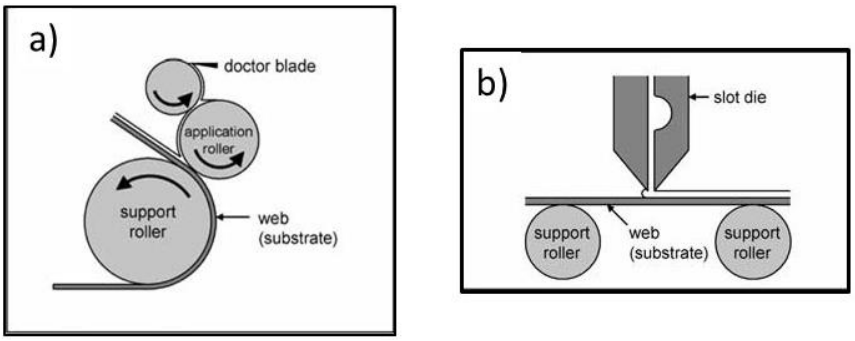

Figure 1.16. Self-metered and pre-metered coating method examples (a) Comma bar coating method and (b) Slot die coating method [186].

1.4.3 Stacking / Packaging

In the batteries for commercial use, i.e. lithium-ion batteries, electrodes are coated in both sides of the current collector in order to layer multiple elements in a single casing and increase the capacity of the cells. Several architectures and cell designs, such as cylindrical or flat cells which include pouch cells, with a variety of positions for the tabs [187] exist in the market. The outer design is selected based on the final application of the cell and the battery pack.

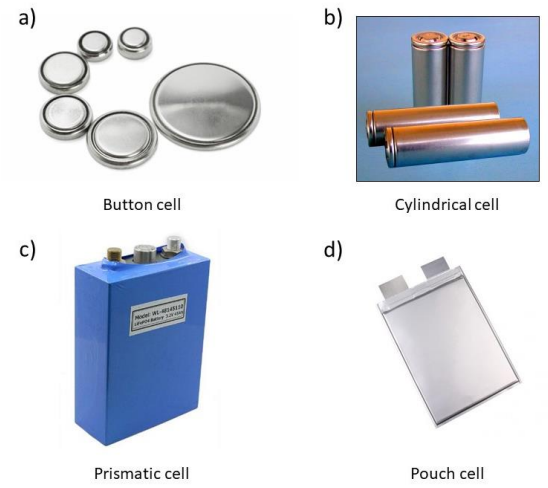

Figure 1.17. Typical available lithium-ion battery cell designs [188,189,190] (a) coin cell, (b) cylindrical cell, (c) prismatic cell and (d) pouch cell.

The smallest cell size is the button cell, also called coin cell (**Figure 1.17** (a)). It consists in a compact design that includes small size electrodes. However, they have the risk of swelling and have no safety vent. This configuration has usually been used for non-rechargeable cells and for research purposes in Li-ion and Na-ion battery development.

Among the high capacity cell designs, some of the most typical ones have cylindrical geometry with jelly roll configuration (**Figure 1.17** (b)). This type of cylindrical cells is widely used, as it presents good mechanical stability and the manufacturing process is easy. Moreover, this type of packaging allows to standing high internal pressures without suffering any deformation. However, the internal space of the cell is not used at all and the risk of lack of pressure exists when the electrodes are too thin since the metal wrap cannot ensure the pressure to maintain the desired electrochemical performance over cycling. Cylindrical cells can be manufactured using different dimensions, 20700, 21700 or 22700, in which the first two numbers correspond to the diameter and the last three to the height of the cells measured in mm are some examples. The 18650 model is the most optimized cell, which has higher energy density than prismatic or pouch cell Li-ion batteries. However, the demand for this type of cells is fading over the years, as the market is moving towards lighter and more flat designs.

The prismatic cell (**Figure 1.17** (c)) was firstly developed in the early 1990s and it accomplishes with the demands of thin size and makes a good use of the space. In this type of cells, flat stacks are encased in welded aluminum housing and some swelling due to the gas formation inside the cell is considered as normal.

In order to overcome the problem of the lack of enough pressure, flat design geometries are developed and selected for many battery manufacturers. Some of the advantages detected for the flat plate designs are: the maintenance of the homogeneity and the uniformity in the whole battery, the minimization of the outer container of the cell which maximize the energy density and the minimization of the impedance related to the many electrical contacts through the electrode tabs detected in the jelly roll geometry. Moreover, stacked cell design minimizes risk for safety issues [191].

5 years after the development of the first prismatic cells, pouch cell design emerged (**Figure 1.17** (d)). Conductive metal tabs welded to the electrodes and a fully sealed non-metallic package are its main characteristics. One of its most relevant features is the 90-95% of packaging efficiency, which is the highest among different battery pack designs. Moreover, the absence of a metal container reduces the loss weight of the battery. There is not a standard pouch cell design, as the manufacturers are the ones designing their own cells. Similar to what happens in prismatic cells, swelling is typical in this type of formats. Therefore, it is important to leaving free space in between the cells when stacking them in a battery pack. If the pressure inside the container is too high it can crack the casing, break the device and the electronic circuit boards. Most of the gas generation reactions take place during the formation cycles due to the decomposition of the electrolyte and SEI formation. The gases generated during these formation cycles are released in a controlled way before the final sealing of the cell is done. However, the gas generation issue cannot be totally be avoided, as electrolyte decomposition accompanied with gas release continues occurring over cycling.

1.5 Scope of this Thesis

This doctoral thesis encompasses the work done in the development of a sodium-ion battery. Different from many of the bibliography available in the topic, dealing with novel materials synthesis and structural characterization, this work aims to focus more on the engineering perspective of Na-ion battery development, starting from the development of button type cells and ending in the development of a monolayer sodium-ion pouch cell. This work represents a complete report in terms of electrode processing, strategies to overcome the limitations of this technology and Na-ion full-cell fabrication and electrochemical/thermal characterization.

Considering this scenario, the main objectives of the present Thesis are:

- The evaluation of NaN_3 and $Na_2C_4O_4$ sacrificial salts as a strategy to overcome the sodium deficiency issue on P2-type sodium layered oxide cathodes.
- The realization of anode and cathode formulation studies at small (< 1 g) and larger scale (10-30 g) to understand the interactions between the electrode components and with the aim to increase the active material content and loading of the resulting electrodes.
- The analysis of rheological, morphological, mechanical and electrochemical characteristics of the $NaFe_{0.4}Mn_{0.3}Ni_{0.3}O_2$ cathodes and hard carbon anodes processed at larger scale.
- The realization of systematic studies to improve specific cathode and anode electrode characteristics, including strategies to improve of the cathode microstructure or determination of the anode calendering conditions among others.
- The assembly and electrochemical characterization of a Na-ion cell, progressing from coin cell to monolayer pouch cell level, including the optimization of the mass balance and cycling regime.
- The determination of the thermal parameters of the developed monolayer Na-ion pouch cell and the development of a heat generation model for that system.

In this chapter (**Chapter 1**), the state-of-art of rechargeable batteries with special emphasis in Na-ion battery technology and the aim of the Thesis have been described. In **Chapter 2**, the structural and morphological characterization of the electrode active materials together with the experimental procedures utilized to prepare the individual cell components and the cells itself are provided. In addition to this, the experimental techniques used for the characterization of the structural, morphological and mechanical properties of the raw materials and the processed components of the cell are also described. The next 5 chapters comprise the experimental results and the discussion of the different topics assessed in this Thesis. Focusing in cathode related studies, **Chapter 3** explores the utilization of 2 different sacrificial salts in order to overcome the sodium deficiency characteristic of P2-type sodium layered oxide cathodes. In the **Chapter 4**, $Na_{1-\delta}Ni_{0.32}Ti_{0.32}Mg_{0.16}Mn_{0.20}O_2$ is evaluated as cathode active material. Material synthesis conditions are optimized, formulation studies are performed at small scale and the full-cell is assembled and electrochemically characterized at coin cell level. The **Chapter 5** includes the electrode processing studies performed at a larger scale using $NaFe_{0.4}Mn_{0.3}Ni_{0.3}O_2$ as the active material which deals with slurry formulation and drying process studies. **Chapter 6** is focused on the negative electrode. It describes the effects of the formulation, the active material loadings or calendaring conditions on the final characteristics of the electrodes. Finally, in the **Chapter 7,** a monolayer pouch cell is assembled using the cathode and anode components described and optimized in the previous chapters, Chapter 5 and Chapter 6, respectively. In this last chapter, the thermal parameters of a Na-ion full-cell prototype are described and a heat generation model prepared to be implemented at a multilayer Na-ion pouch cell level is developed.

Chapter 2. Experimental procedure

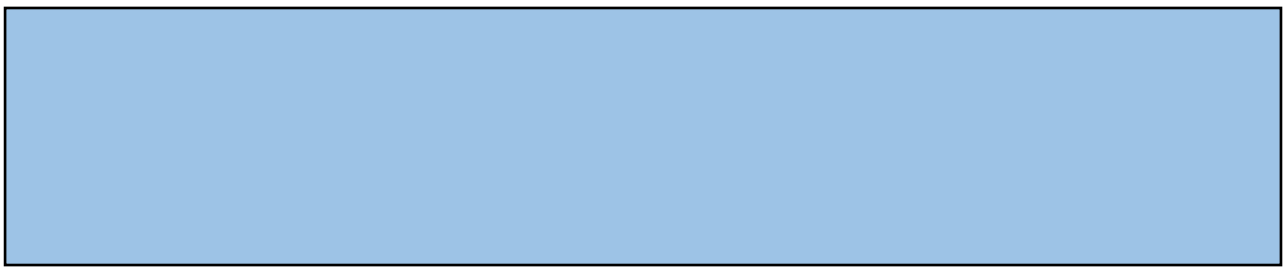

2.1 Synthesis and characterization of electrode active materials

Table 2.1 displays the materials used in the execution of this Thesis. In the following sections the synthesis procedure and some relevant properties of these materials will be provided.

Table 2.1 Summary of the materials used in this Thesis

Material	Source	Function
$Na_{0.67}Fe_{0.5}Mn_{0.5}O_2$	Synthesized for this Thesis	Cathode active material
$Na_{0.95}Ni_{0.32}Ti_{0.32}Mg_{0.16}Mn_{0.20}O_2$	Synthesis optimized in this Thesis	
$NaFe_{0.4}Mn_{0.3}Ni_{0.3}O_2$	Custom made synthesis by External Company	
Hard carbon, Kuranode	Kuraray Ltd.	Anode active material
Carbon black, C65	Timcal	Conductive additive
Polyvinylidene fluoride, Solef 5130	Solvay	Binder
N-methyl-2-pyrrolidone (C_5H_9NO)	Sigma Aldrich	Electrode slurry solvent
Sodium azide (NaN_3)	Sigma Aldrich	Sacrificial salt
Disodium squareate ($Na_2C_4O_4$)	Synthesized for this Thesis	Sacrificial salt
Sodium hexafluorophosphate ($NaPF_6$)	Acros Organics	Electrolyte salt
Ethylene carbonate	Sigma Aldrich	Electrolyte solvent
Diethyl carbonate	Sigma Aldrich	Electrolyte solvent
Sodium dodecyl sulfate ($NaC_{12}H_{25}SO_4$)	Sigma Aldrich	Electrode slurry surfactant
Polyvinylpyrrolidone ($(C_6H_9NO)_n$)	Sigma Aldrich	Electrode slurry dispersant
Al foil	Hohsen	Anode/Cathode current collector
Glass fiber, GF/D	Whatman	Separator
Celgard, 2325	Celgard	Separator

2.1.1 Cathode active materials

2.1.1.1 $Na_{0.67}Fe_{0.5}Mn_{0.5}O_2$

$Na_{0.67}Fe_{0.5}Mn_{0.5}O_2$ was synthesized by conventional solid-state synthesis route. Stoichiometric amounts of Na_2CO_3 (99.5%, Sigma Aldrich), Fe_2O_3 (99%, Alfa Aesar) and Mn_2O_3 (98%, Alfa Aesar) were mixed by wet ball milling (classic line Planetary Mill Pulverisette 5) in ethanol. Balls to powder mass ratio was fixed at 30:1 and other ball milling parameters such as speed and time were set at 300 rpm and 30 minutes, respectively. The powder mixture was compressed in the form of pellets using a uniaxial hydraulic press (Specac, max. 15 tons) under a load of 4 ton in^{-2}. Then, the pellets were calcined in a box furnace, at a temperature of 900 °C for 12 hours. After the calcination in air, the reaction product was quenched to room temperature and stored under dry conditions in an argon filled glove box (< 0.5 ppm H_2O and O_2) to avoid any moisture contamination.

The XRD pattern of $Na_{0.67}Fe_{0.5}Mn_{0.5}O_2$ in **Figure 2.1** shows the formation of a single phase P2-type layered structure in a hexagonal system with *$P6_3/mmc$* space group [192]. The layered P2-type structure is formed by MO_6 (M = Fe, Mn) octahedral and sodium cations located in the prismatic sites, coordinated with six oxygen atoms and positioned in between the layers. The lattice parameters were calculated using profile matching technique and are observed to be a = b = 2.9327(3) Å and c = 11.226(3) Å [193].

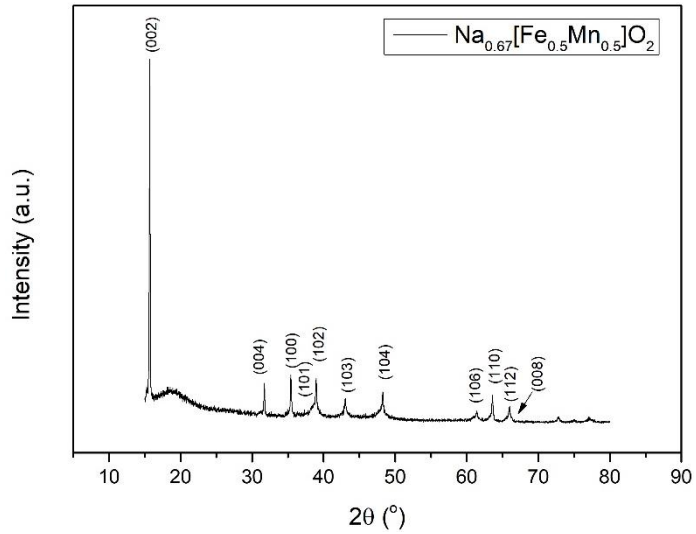

Figure 2.1 XRD pattern of $Na_{0.67}Fe_{0.5}Mn_{0.5}O_2$ powder.

2.1.1.2 $Na_{1-\delta}Ni_{0.32}Ti_{0.32}Mg_{0.16}Mn_{0.20}O_2$

$Na_{1-\delta}Ni_{0.32}Ti_{0.32}Mg_{0.16}Mn_{0.20}O_2$ was synthesized using the stoichiometric amounts of Na_2CO_3 (99.5%, Sigma Aldrich), NiO (Ni 78.5%, Alfa Aesar), TiO_2 (99.9%, Alfa Aesar), MgO (99%, Alfa Aesar) and MnO_2 (98%, Alfa Aesar). Material was synthesized by conventional solid state synthesis route and the determination of the optimum synthesis parameters such as calcination time and temperature and the ball milling media will be described in the Chapter 4 of this Thesis. Balls to powder mass ratio was fixed at 30:1 (by wt. %) and ball-milling parameters such as speed and time were set at 300 rpm and 45 minutes, respectively. The powder mixture was compressed in the form of pellets using a uniaxial hydraulic press (Specac, max. 15 tons) under a load of 4 ton in^{-2}. The pellets were calcined in a box furnace (optimized calcination temperature and time of 900 °C and 8 hours determined in Chapter 4, section 4.1, page 135) and after the calcination in air, the reaction product was quenched to room temperature and stored in an Ar filled glove box (< 0.5 ppm H_2O and O_2) in order to avoid any moisture contamination.

The XRD pattern of $Na_{1-\delta}Ni_{0.32}Ti_{0.32}Mg_{0.16}Mn_{0.20}O_2$ is presented in **Figure 2.2** (the XRD pattern corresponds to the material synthesized using the optimized synthesis conditions determined in

Chapter 4). Most of the peaks can be indexed to α-$NaFeO_2$ type crystal structure. However, an impurity peak attributed to $Mg_{1-x}Ni_xO$ can be observed in the diffraction pattern marked with an asterisk. In order to minimize the amount of impurities, a reduction of the amount of the alkali metal has been proposed, always maintaining an optimal amount of alkali metal to ensure the formation of the O3-type crystal structure [194]. In this work, the amount of Na^+ ions was fixed to $1-\delta = 0.95$.

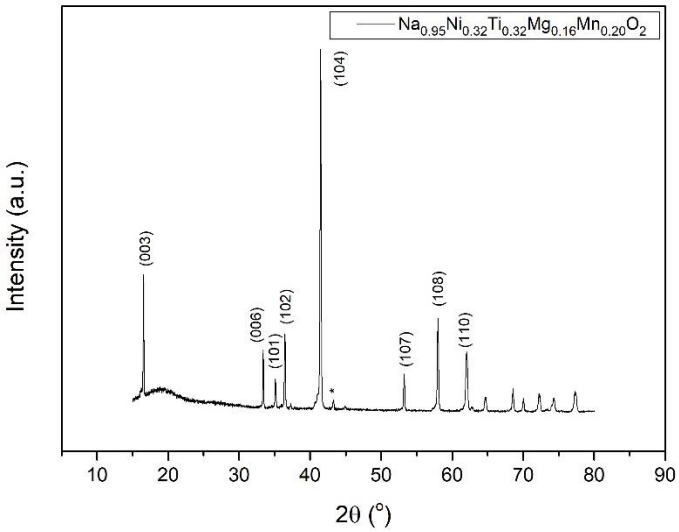

Figure 2.2. XRD pattern of $Na_{1-\delta}Ni_{0.32}Ti_{0.32}Mg_{0.16}Mn_{0.20}O_2$ powder. $Mg_{1-x}Ni_xO$ impurity is marked with an asterisk.

The microstructural analysis of the active material done by SEM (**Figure 2.3**) shows the well-defined morphology typical of layered structures characterized by a series of planes forming single particles. The primary particles have a particle size of ca. 3 µm showing platelets-shaped morphology.

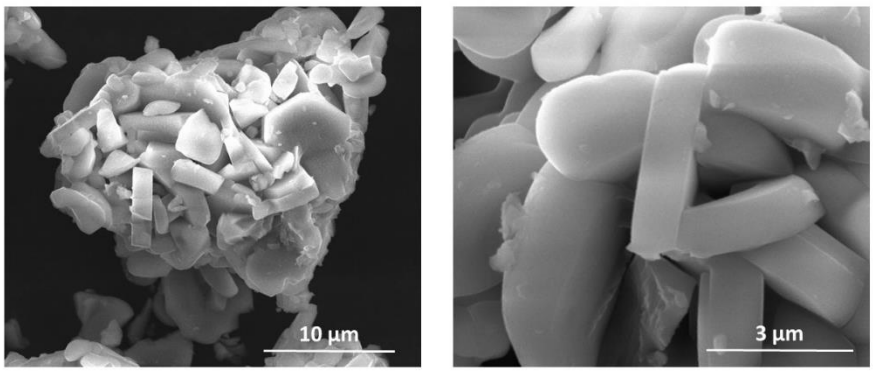

Figure 2.3. SEM images of $Na_{1-\delta}Ni_{0.32}Ti_{0.32}Mg_{0.16}Mn_{0.20}O_2$ powder.

2.1.1.3 $NaFe_{0.4}Mn_{0.3}Ni_{0.3}O_2$

This cathode active material was custom made for this work by External Company. The specifications provided by the supplier are summarized in **Table 2.2**.

Table 2.2. Supplier specifications for $NaFe_{0.4}Mn_{0.3}Ni_{0.3}O_2$ active material.

Composition	Particle size d_{50} (µm)	Specific Surface Area ($m^2\ g^{-1}$)
Na = 1.08 ± 0.03 Fe = 0.37 ± 0.01 Mn = 0.28 ± 0.01 Ni = 0.27 ± 0.01	1.1 ± 0.1	1.2 ± 0.1

The X-ray diffraction patterns of $NaFe_{0.4}Mn_{0.3}Ni_{0.3}O_2$ (**Figure 2.4**) can be indexed to a hexagonal O3-type structure with $R\bar{3}m$ space group.

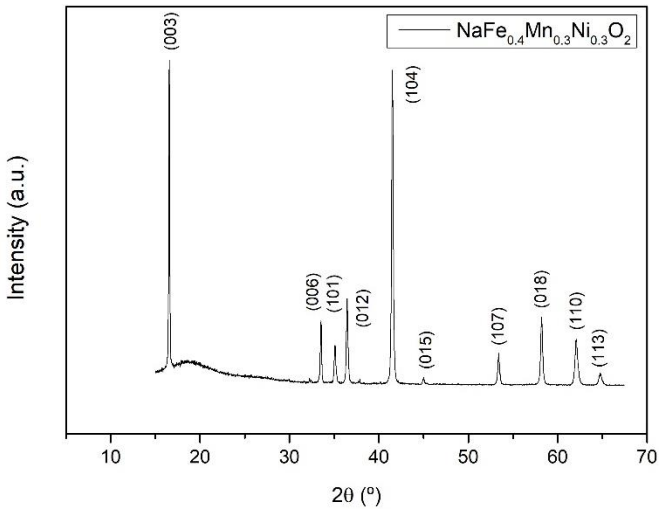

Figure 2.4. XRD pattern of $NaFe_{0.4}Mn_{0.3}Ni_{0.3}O_2$ powder.

According to the SEM images shown in **Figure 2.5**, $NaFe_{0.4}Mn_{0.3}Ni_{0.3}O_2$ pristine material presents primary particles in the range of 1 µm, which form agglomerates of approximately 30 µm.

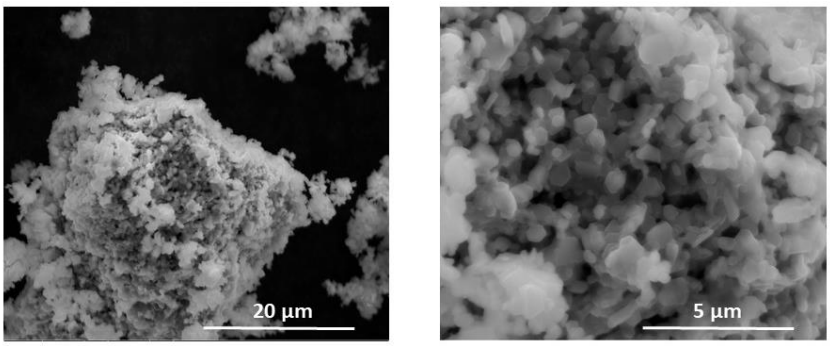

Figure 2.5. SEM images of $NaFe_{0.4}Mn_{0.3}Ni_{0.3}O_2$ powder.

2.1.2 Anode active material

Kuranode hard carbon has been supplied by Kuraray, Ltd. **Table 2.3** shows the specifications of this carbon provided by the material supplier. Kuranode hard carbon powder particles have an irregular shape and size according to the SEM image shown in **Figure 2.6**. In order to commit

with a non-disclosure agreement signed with the hard carbon supplier no additional physico-chemical, structural and morphological characterization will be provided in this document.

Table 2.3 Kuranode hard carbon properties provided by the material supplier.

Bulk density (g cm^{-3})	d50 (µm)	Specific surface area (m^2 g^{-1})
1.48	9	4

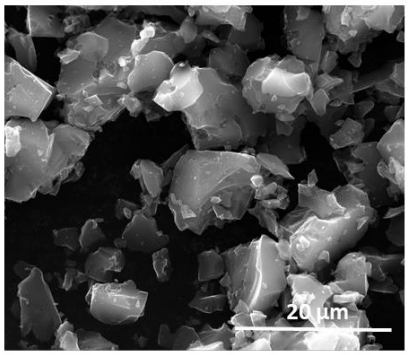

Figure 2.6 SEM image of Kuranode hard carbon powder

2.2 Electrode preparation

Electrode processing is done in dry room environment (**Figure 2.7**) to avoid moisture contamination of the components. The dry room at CIC energigune has a constant temperature of 21 °C ± 1 °C and a dew point of ca. -60 °C, which is equivalent to 11 ppm of H_2O.

Figure 2.7. Dry Room at CIC energigune.

2.2.1 Slurry formulation

The slurry formulation in this Thesis consists in the mixing of the electrode active material components with the C65 conductive additive and the PVDF binder in the optimum composition using NMP as a solvent.

2.2.1.1 Equipment for slurry preparation

Different mixing equipment have been used in this Thesis for electrode preparation depending on the amount of material available to perform the experiments and the nature of the active material. Moreover, a dedicated study on the slurry characteristics depending on the employed mixing device has been also performed in Chapter 5. The mixing devices used in this Thesis are: a mortar & pestle (**Figure 2.8** (a)), an overhead stirrer with a paddle type impeller (R18 model, CAT) (**Figure 2.8** (b)), a planetary centrifugal vacuum mixer (ARV-310 model, Thinky) (**Figure 2.8** (c)), a disperser with a dissolver type impeller (Dissolver DISPERMAT$^{(R)}$ LC30, VMA Getzmann) (**Figure 2.8** (d)) and a planetary ball-milling (Pulverisette 4/5, Fristsch) (**Figure 2.8** (e)). In the following paragraphs some details on these mixing equipment will be provided.

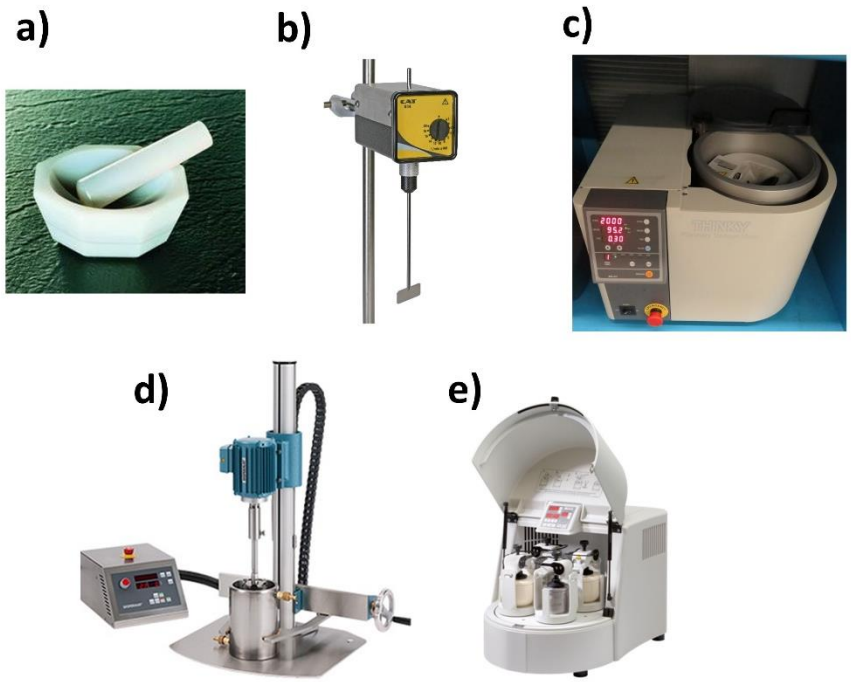

Figure 2.8. (a) Mortar & pestle, (b) Mixer with a paddle type impeller, (c) Planetary centrifugal vacuum mixer, (d) Disperser with a dissolver type impeller and (e) Planetary ball mill.

- *Mortar and pestle* (**Figure 2.8** (a)): It is a simple and easy grinding technique widely used at lab-scale for slurry preparation for preliminary electrochemical characterization of novel electrode compositions. In this Thesis, it has been used when the amount of active material available for slurry preparation is less than 5 g.

- *Overhead stirrer with the paddle type impeller* (**Figure 2.8** (b)): It has a centrifugal tip which allows an axial flow in the slurry. The effect is similar to a 4-bladed stirrer. Axial stirrers are effective to produce a movement in the tank from the top to the bottom.

- *Planetary centrifugal vacuum mixers* (**Figure 2.8** (c)): This type of devices can mix, disperse and degas materials in seconds to minutes. The material container is tilted at 45˚ and this equipment uses a planetary mixing action, combining the rotation and revolution movements [195]. Depending on the used rotation and revolution speeds and

mixing times different mixing results are obtained. According to Adachi et al. when revolution and rotation are combined, the slurry in the container is mixed by whirling in the direction of the circumference and moving upwards and downwards along the rotation shaft [196]. The ratio between rotation and revolution in this equipment is set at 1:2.5 and a typical rotation:revolution speed ratio is 800 rpm:2000 rpm, which provides 400 G of mixing force. In this type of equipment, the speed changes from slow to fast, or vice versa, provide "shaking" effect to the materials which can result in better mixing quality. The main advantages of this device are the fast processing, the versatility in terms of processing capacity (containers are available in the range from 10 to 300 ml) and that if specific containers are used for each composition, it allows to avoid contamination issues. In addition to this, it is a simple and clean device that avoids material damage because of the absence of rollers, mixing blades or propellers in the mixing tank. Moreover, it saves time and cost and can improve slurry production yield rate because minimum amount of material is lost in the process [195].

- *Mixer with the dissolver type impeller* (**Figure 2.8** (d)): It produces high consistency slurries by applying high turbulence and high shearing forces. The best dispersion results with a DISPERMAT® are obtained when the geometry of the dispersion container, the diameter, the peripheral velocity and the height of the dissolver disc above the bottom of the vessel as well as rheological millbase properties are matched to one another. After adding the mixing components, the millbase is brought into a laminar rolling flow pattern by increasing the speed of the shaft until no standing material can be seen at the wall of the container. At the correct speed, a channel begins to form around the shaft and a part of the dissolver disc becomes visible. At this point, the millbase will form a doughnut-like flow pattern. This doughnut-like flow pattern is a signal that the maximum mechanical power possible is being transferred into the millbase and furthermore that the millbase is being agitated so that all the agglomerates will eventually reach the dissolver disc. The doughnut effect develops because the millbase is accelerated outwards from the tip of the dissolver disc. When it hits the wall of the vessel, the stream is divided into two parts. The one going downwards flows back to the

middle of the dissolver disc along the bottom of the dispersion vessel and rises up to hit the disc once again. The second part flowing upwards has the same circular path, which is limited in by the force of gravity and the rheological properties of the millbase [197].

- *Planetary ball milling* (**Figure 2.8** (e)): It consists in 4 jars that are attached to a disk that rotates around a common central axis, while the pots simultaneously rotate around their own axis. Comminution and mechano-chemical processes in planetary ball mills are complex and strongly dependent on the properties of the processed material. Thus, the optimum milling conditions must be assessed for each individual system. High impact energies are obtained as a consequence of the impacts of the milling balls against the walls of the pots. The motion of the balls influences the number of collisions, the ball velocity and therefore the impact intensity which contributes to the energy input to the powder charge. Due to the impact and frictional forces inside the planetary jars, in addition to the mixing process, powder particles are also ground. The processing parameters to take into account in the planetary ball-milling are the revolution speed and rotational speed (the rotation:revolution speed ratio is usually maintained constant), the milling time, the size and composition of the milling media and the balls to powder ratio [177]. During ball milling process, up to 80 % of the energy that is generated in the mill is dissipated as heat. Measuring the temperature inside of the milling jar is a tricky issue, as the temperature on the surface is not necessarily the same as the temperature inside the milling jar. As an example, a temperature difference between the milling jar and the balls of 25 K has been reported [176]. Therefore, it is important to intercalate resting periods between the milling sequences in order to avoid the overheating of the materials inside the jar.

2.2.1.2 Slurry preparation procedure

A mortar and pestle are used for slurry preparation in this Thesis when the amount of active material to perform the experiments is < 5 g, i.e. when the active material is synthesized in the laboratory. In this case, the slurry preparation procedure is different from that described below.

The desired amount of active material, conductive additive and binder are mixed for 30 minutes using the mortar, then the NMP solvent is added (0.5 ml of NMP per 0.5 g of total dry powder) and gently mixed with the powder components, forming a highly viscous slurry.

When the slurry preparation is performed at larger scale, the preparation procedure is usually a multi-step type process. The first step is the preparation of the binder solution which consists in the dissolution of the PVDF binder in the NMP solvent. PVDF supplier recommends a concentration from 5 to 12% wt. Following this recommendation, cathode slurries were prepared with 8% wt. binder solution, while anode slurries were prepared with 5.5% wt. binder solution in this Thesis. By using this initial concentration, in case the viscosity of the final slurry being too high, the addition of extra NMP is possible without the PVDF concentration in NMP going below 5% wt. More diluted binder solutions are selected for anode formulations due to the higher surface area of the hard carbon compared to the layered oxide cathode used in this Thesis.

The binder solution is prepared using the disperser with the dissolver type impeller at a mixing speed of 1500 rpm for 2 hours. **Figure 2.9** shows the flow curves of the cathode and anode binder solutions. Due to the lower PVDF concentration, the viscosity of the anode binder solution is lower.

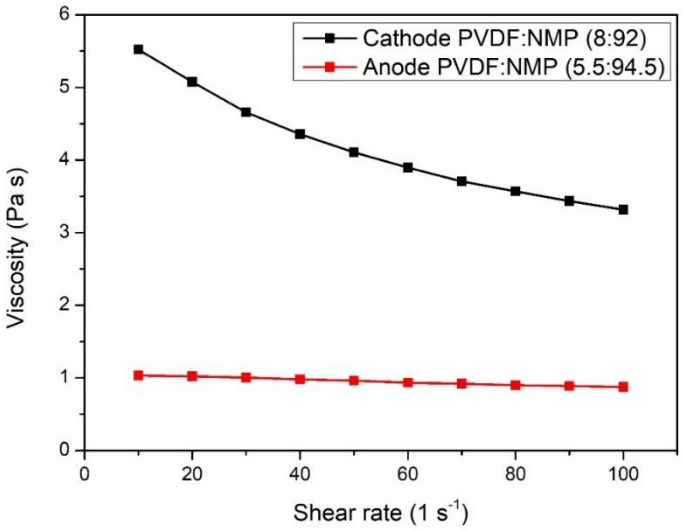

Figure 2.9. Flow curve of the binder solution for cathode and anode slurry preparation.

Once the binder solution is ready, desired amounts of the conductive additive first and active material secondly are added as a standard slurry preparation procedure. Detailed information on the mixing equipment, mixing procedure and slurry composition employed for each specific experiment are provided in the corresponding chapters.

2.2.2 Electrode coating and drying

The coating process of the slurries on top of the current collector is done by means of two equipment in this Thesis: (1) a K Control Coater (RK PrintCoat Instruments) coupled to a micrometer adjustable Doctor Blade applicator (**Figure 2.10**) and (2) a continuous coating machine (B&W Megtec) (**Figure 2.11**). In this case, the current collector is a 16 µm thick aluminum foil in both cathode and anode electrodes. The continuous coating machine also allows to perform the drying process in the same equipment.

- *Doctor Blade* (**Figure 2.10**): The Doctor Blade applicator consists on an adjustable blade from 0-10 mm (10 µm accuracy). It allows a coating width of 100 mm and produces a wet film thickness of 50-80% of the doctor blade gap. The speed of the slurry deposition can be controlled in the range between 2 and 15 m min^{-1}. The smooth aluminum faced

bed with vacuum applied via multiple holes over the entire substrate surface holds the current collector appropriately.

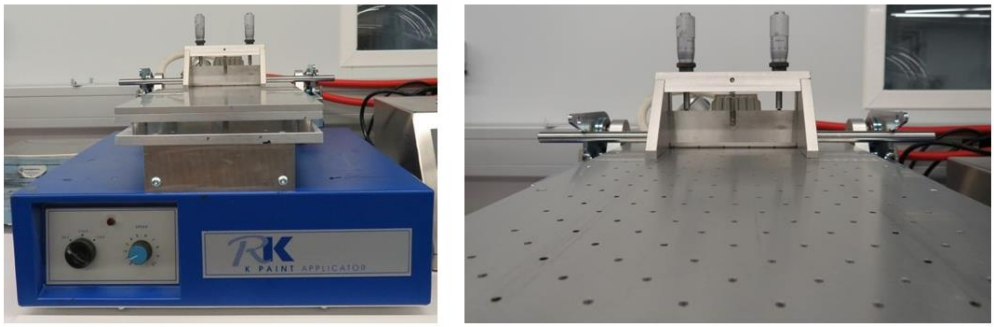

Figure 2.10. K Control Coater.

- *Continuous coating machine* (**Figure 2.11**): It has a reverse comma bar coating head and 2 drying zones. The adjustable gap allows a thickness control up to 300 µm, with an accuracy of 2 µm. It is possible to perform single side or double side coating.

Figure 2.11. Continuous coating machine.

If otherwise is not stated, the electrodes used in this Thesis are prepared using the Doctor Blade coating. Depending on the gap of the Doctor Blade, electrodes with different active material loadings are obtained. The active material loadings utilized in each experiment are included in the corresponding chapters.

The drying process of the electrodes prepared using the Doctor Blade is performed at 120 °C for 2 hours under vacuum (50 mbar) if otherwise is not stated.

2.2.3 Electrode calendering

The dried electrodes are calendered using two different equipment in this Thesis depending on the size of the electrodes and the purpose of the study. 12 mm discs used for coin cell assembly are pressed applying 4 and 6 ton in^{-2} of uniaxial pressure in a hydraulic press (Specac, max. 15 tons), respectively for the cathode and anode electrodes.

The electrodes used for pouch cell assembly, to perform peel tests and the ones used for anode calendering condition optimization are calendered using dedicated calendering equipment (**Figure 2.12**) (Mediatech). This equipment applies a maximum load of 40 ton and consists in 2 rolls with an adjustable gap, temperature and speed. If otherwise is not stated, electrodes are calendered at 80 °C, at a calendering speed of 1.2 cm s^{-1} and targeting a thickness reduction of 10%.

Figure 2.12. Calendering equipment.

2.3 Electrolyte preparation

1 M $NaPF_6$ in EC:DEC (50:50 wt. %) has been used as the electrolyte in this Thesis for the electrochemical characterization of the cells. The solvents and the salts are carefully dried prior to electrolyte preparation. The procedure to prepare the electrolytic solution is detailed in the following paragraphs:

First, the molecular sieves are washed with deionized water and ethanol. A beaker is filled first with deionized water and the required amount of molecular sieves (approximately 1/3 of the volume of the liquid to be dried) (Molecular sieves, 4Å, beads, 8 – 12 mesh, Sigma Aldrich) (**Figure 2.13** (a)) is added. The content of the beaker is mixed for 10 min using a Branson Sonifier horn (**Figure 2.13** (b)). This procedure is repeated using ethanol instead of deionized water.

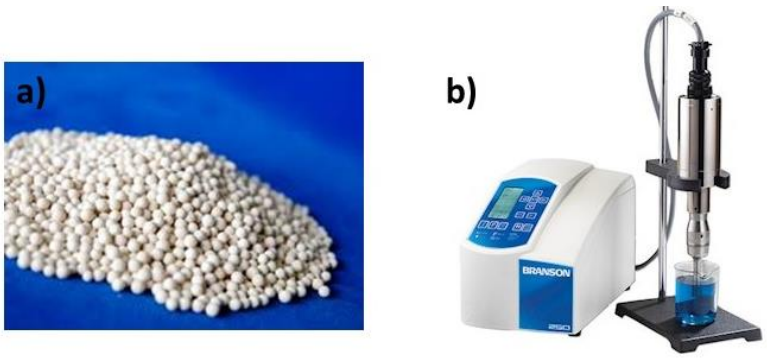

Figure 2.13. (a) Molecular sieves and (b) Branson Sonifier horn.

The molecular sieves are then transferred to an empty vial to be dried overnight in a Büchi oven (**Figure 2.14**) at 80 °C under vacuum and activated at 250 °C under vacuum for 24 h. The activated molecular sieves are transferred to an Ar filled glove box (< 0.5 ppm H_2O and O_2) (mBraun) without exposing them to ambient atmosphere.

Figure 2.14. Büchi oven.

The electrolyte solvent mixture is prepared in a glass bottle and then, the molecular sieves (1/3 of the volume of the liquid) are added. The bottle is covered with Al foil to avoid light sensitivity. After 1 week, the moisture content of the solvent is measured by Karl Fischer titration method. If the water content is below 10 ppm for 4 g of solvent, the required amount of solvent is transferred to a glass bottle and the $NaPF_6$ salt, dried at 60 °C for 24 h under vacuum (50 mbar), is added. The electrolytic solution is prepared using a magnetic stirrer for 24 h, the glass bottle being covered with Al foil while stirring to avoid light sensitivity.

Before validating the electrolytic solution, the H_2O content and the electrical conductivity are measured. The H_2O content is measured by means of Karl Fischer equipment and the conductivity at 23 °C of the electrolytic solution by means of electrochemical impedance spectroscopy in the frequency range from 10^6 Hz to 100 Hz. Once the electrolytic solution is validated (H_2O < 50 ppm and $\sigma = 6 \pm 1$ mS cm^{-1}) it is stored in a dry Al bottle. Al bottle drying procedure consists in drying it at 60 °C for 24 hours under vacuum (50 mbar).

2.4 Cell assembly

2.4.1 Coin cell assembly

In this work, 2032 coin cells are used for basic electrochemical characterization. 12 mm discs are punched from the electrode laminates and dried at 120 °C for 2 hours under vacuum (50 mbar) prior to cell assembly in an Ar filled glove box (< 0.5 ppm H_2O and O_2) (mBraun). A scheme illustrating a coin cell configuration is shown in **Figure 2.15** and the coin cell assembly procedure is described in the following paragraphs. First, the working electrode is disposed in the center of the down part of the coin cell. A ring of polypropylene is used to avoid any short-circuit between the positive and the negative electrodes. Secondly, a 16 mm glass fiber separator (GF/D, Whatman) is placed on top of the working electrode. **Table 2.4** gathers some of the characteristics of the GF/D glass fiber separator.

Table 2.4. Whatman GF/D glass fiber separator characteristics.

Material	Borosilicate glass
Thickness (mm)	0.67
Pore size (µm)	2.7
Max. operating temperature (°C)	500

Then, 80 µl of 1 M $NaFP_6$ EC:DEC electrolyte are added (see electrolyte preparation procedure described in section 2.3, page 61), and the counter/reference electrode is placed on top of the separator. The counter/reference electrode is a 14 mm diameter metallic Na disc in case of half-cell configuration and 12 mm diameter hard carbon anode in case of full-cell configuration. Finally, the spacer, the ring and the upper part of the cell are placed, and the cell is crimped using an automatic coin cell crimper (Hohsen). **Figure 2.16** shows the appearance of un-crimped, badly crimped and well crimped coin cells.

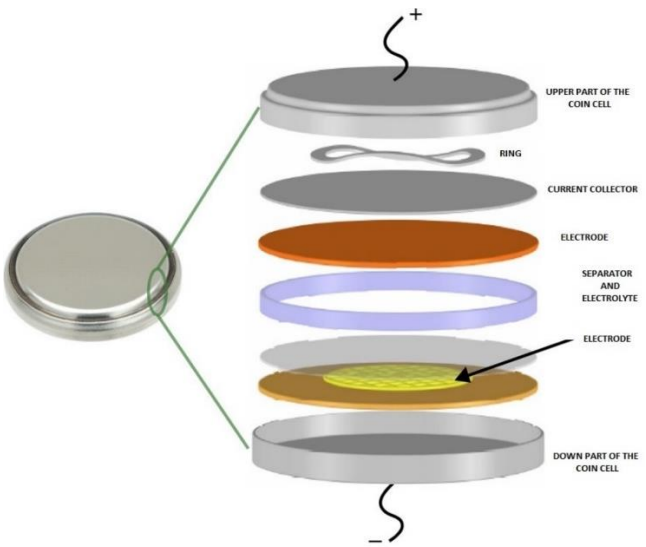

Figure 2.15. Scheme of a coin cell.

Figure 2.16. Comparison of a well crimped coin cell, badly crimped and un-crimped coin cells [198].

2.4.2 Swagelok cell assembly

The Swagelok cell is a 3-electrode configuration cell. This 3-electrode systems consists of a working electrode, a counter electrode and a reference electrode (**Figure 2.17**). A reference electrode refers to an electrode that has an established electrode potential and in an electrochemical cell, it allows to individually monitor the electrochemical behavior of the working and counter electrodes, i.e. the cathode and the anode electrode, vs. the reference electrode.

In this Thesis, 12 mm diameter anode and cathode discs, dried at 120 °C for 2 hours under vacuum (50 mbar), are used for Swagelok cell assembly in an Ar filled glove box (< 0.5 ppm H_2O and O_2) (mBraun). The separator consists of a 13 mm diameter glass fiber (GF/D, Whatman) and a 11 mm diameter metallic Na disc is placed on the top plunger as reference electrode. Excess of electrolyte is added to ensure that the reference electrode is in contact with the electrolyte. Swagelok parts are made of stainless steel (25 µm Kapton foil acts as an insulator) and sealing rings are made of PTFE.

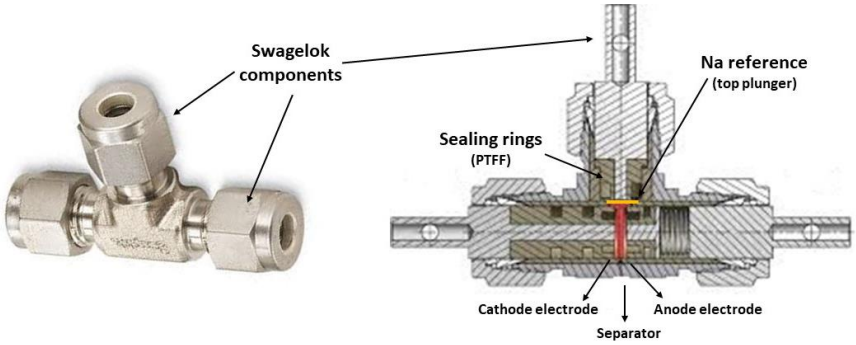

Figure 2.17. Scheme of the Swagelok cell configuration.

2.4.3 Monolayer pouch cell assembly

The pouch cell assembly process is done in dry room environment (dew point of ca. -60 °C and controlled temperature of 21 ± 1 °C). First 20.25 cm^{-2} and 21.84 cm^{-2} cathode and anode electrodes are punched with the notching machine (Solith) (**Figure 2.18**) with independent blades for each electrode. The accuracy of the equipment is ± 0.1 mm.

Figure 2.18. Electrode notching equipment and punched electrodes.

The electrodes and the Celgard 2325 separator are then manually stacked. **Table 2.5** gathers some of the characteristics of the Celgard 2325 separator.

Table 2.5. Celgard 2325 separator characteristics.

Material	Trilayer (PP/PE/PP)
Thickness (µm)	25
Porosity (%)	39
Pore size (µm)	0.028

After the stacking of the different layers of the pouch cell, the Al tab welding to the uncoated area of the electrodes is performed by ultrasonic welding. The ultrasonic welding machine used in this work (**Figure 2.19**) (Sonics) allows modifying the welding frequency, time and energy to adapt the welding conditions to the composition and the number of electrodes to be welded.

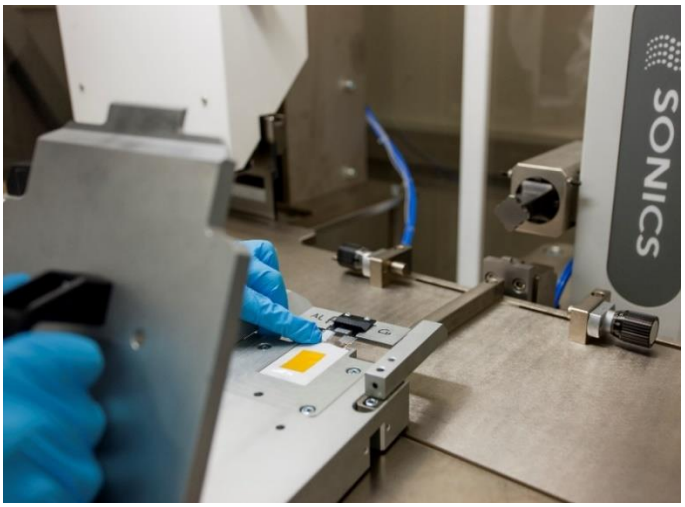

Figure 2.19. Ultrasonic welding equipment.

Then, the cell is placed in the pouch bag that acts as the cell container and 3 of the 4 sides are sealed with the action of heat and pressure. The 3 sealed sides are the one in which the tabs are located, the opposite side and one of the lateral sides. The fourth side remains opened in order to perform the electrolyte filling in the following cell assembly step. The equipment used for the 3-side sealing (Solith) (**Figure 2.20** (a)) can apply a pressure up to 10 kg cm^{-2} and a temperature

of 230 °C ± 1 °C. The pouch bag used in this Thesis is sealed at 6 kg cm^{-2} and a temperature of 170 °C.

Figure 2.20. (a) 3 side sealing equipment and (b) electrolyte filling equipment.

Prior to electrolyte filling, the pouch cell systems are dried at 80 °C for 24 h under vacuum (50 mbar). Then, the pouch cells are filled with 900 µl of 1 M $NaPF_6$ in EC:DEC (50:50 wt%) through the open side of the cell. The electrolyte addition is done using a micropipette and the sealing is done at 400 mbar using a vacuum chamber coupled with sealing bars (Solith) (**Figure 2.20** (b)). Sealing is performed at 6 kg cm^{-2} and 170 °C. Although the electrolyte filling is performed manually, the electrolyte filling machine has the option for automatic electrolyte filling with volume control and pressure can be decreased down to 10 ± 1 mbar. Moreover, the electrolyte filling equipment is compatible with the most common electrolyte components such as PC, EC, DEC, etc. carbonates and $NaPF_6$ and $NaClO_4$ salts.

3 formation cycles are performed at a C-rate of 0.1C in the same voltage range as that selected for cycling stability and rate capability experiments and the degassing and final sealing are done at 700 mbar using a vacuum chamber similar to that used for the electrolyte filling (Solith) (**Figure 2.21** (a)). To ensure the contact between the electrodes the cells are placed in the pressure tool depicted in **Figure 2.21** (b) during the formation cycles.

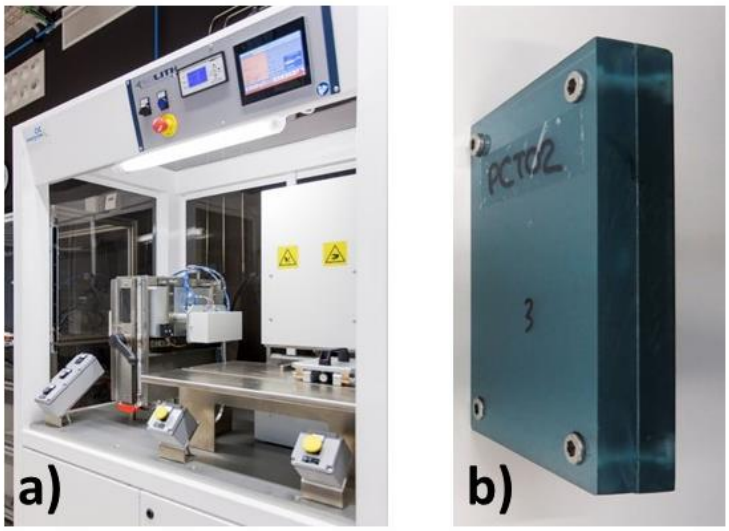

Figure 2.21. (a) Degassing and final sealing equipment and (b) Pressure tool for electrochemical testing.

2.4.4 3-electrode pouch cell assembly

As in the case of Swagelok type cell, 3-electrode cell is also used at pouch cell configuration in order to simultaneously monitor the individual behavior of the cathode, the anode and the full-cell over cycling. **Figure 2.22** shows a scheme of the 3-electrode pouch cell.

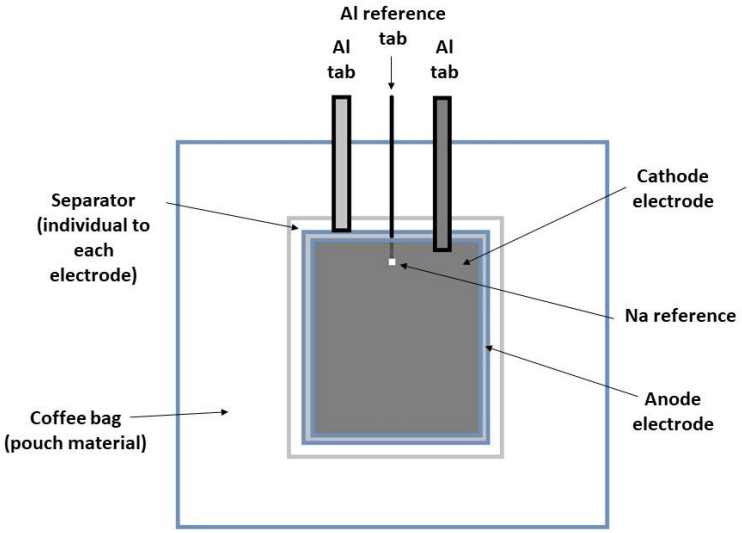

Figure 2.22. Scheme of the 3-electrode pouch cell.

Anode and cathode electrodes are punched with the same dimensions and using the same notching machine than that used for monolayer pouch cell assembly (section 2.4.3, page 66) and Al tabs are welded by ultrasonic welding to each of the electrodes. The two electrodes are wrapped with individual Celgard 2325 pieces and fixed using Kapton tape. Those two tabs together with a third Al tab for the reference electrode are sealed using the 3-side sealing machine (**Figure 2.20** (a)) to the pouch bag. 1.2 mm thick Teflon plates with the same dimensions as the electrodes are placed between the pouch bag and the separator fixed with Kapton tape to improve the contact between the electrodes.

Once the metallic Na piece (reference electrode) is placed in the edge of the 3rd tab, the one which is not in contact neither with the anode nor with the cathode (this process is carried out in an Ar filled glove box with < 0.5 ppm H_2O and O_2), other two of the pouch cell sides are sealed using the same sealing machine than that used for monolayer pouch cell assembly (section 2.4.3, page 66). The position of the reference electrode is represented in **Figure 2.22**. The 1 M $NaPF_6$ in EC:DEC (50:50 wt%) electrolyte addition and 4th side sealing are performed following the same procedure described for monolayer pouch cell assembly (section 2.4.3, page 66) and no degassing is performed in 3-electrode cell assembly.

2.5 Characterization techniques

2.5.1 Electrochemical characterization

2.5.1.1 Galvanostatic charge/discharge cycling

In the galvanostatic cycling techniques, constant-current is applied on the cells while the voltage evolution is being recorded. Those experiments are limited by the upper and lower cut-off voltages defined depending on the tested system. It is commonly stablished that positive currents correspond to the charging process of the cell while negative currents correspond to the cell discharge process. The experiments at different current densities allow determining the cyclability of the cells at different cycling rates. The most common way to represent the current density is the C-rate. As a definition, 1C is the current at which the cell is fully discharged in 1 h. The C-rate is calculated depending on the active material loading of the tested cell.

4 different half-cell systems are tested in this Thesis (3 cathode and 1 anode half-cells). The cycling rate for galvanostatic charge/discharge cycling is determined based on the amount of active material of the tested electrodes. **Table 2.6** displays the current density corresponding to 0.1C and the voltage range used for the electrochemical characterization of these systems.

Table 2.6. Current density corresponding to 0.1C and voltage range used for galvanostatic cycling of half-cells.

$Na//Na_{0.67}Fe_{0.5}Mn_{0.5}O_2$	**$Na//Na_{1-\delta}Ni_{0.32}Ti_{0.32}Mg_{0.16}Mn_{0.20}O_2$**	**$Na//NaFe_{0.4}Mn_{0.3}Ni_{0.3}O_2$**	**Na//Hard carbon**
15 mA g^{-1}_{AM}	15 mA g^{-1}_{AM}	13 mA g^{-1}_{AM}	25 mA g^{-1}_{AM}
1.5-4.3 V	1.5-4.3 V	2.5-4.0 V	0.01-2.0 V

The cycling rate of the full-cells is determined based on the active material loading of the cathode. **Table 2.7** compiles the cycling rate corresponding to 0.1C and the voltage range used for the electrochemical characterization of the different full-cell systems tested in this Thesis.

Table 2.7. Current density corresponding to 0.1C and voltage range used for galvanostatic cycling of full-cells.

Coin cell	Monolayer pouch cell	3-electrode pouch cell
HC//NaN_3/$Na_2C_4O_4$-$Na_{0.67}Fe_{0.5}Mn_{0.5}O_2$: 15 mA g^{-1}_{AMCat} 1.0-4.1 V		
HC//$Na_{1-\delta}Ni_{0.32}Ti_{0.32}Mg_{0.16}Mn_{0.20}O_2$: 15 mA g^{-1}_{AMCat} 1.0-4.2 V		
HC//$NaFe_{0.4}Mn_{0.3}Ni_{0.3}O_2$: 13 mA g^{-1}_{AMCat} 1.0-4.0 V	HC//$NaFe_{0.4}Mn_{0.3}Ni_{0.3}O_2$: 13 mA g^{-1}_{CatAM} 2.0-4.0/2.0-3.9 V	HC//$NaFe_{0.4}Mn_{0.3}Ni_{0.3}O_2$: 13 mA g^{-1}_{CatAM} 2.0-4.0/2.0-3.9 V

If otherwise is not stated, 50 cycles are performed at 0.1C to determine the cycling stability of the cells. For C-rate performance tests, 10 cycles are done at a current density corresponding to 0.1C, 0.2C, 0.5C and 1C, based on the data provided in **Table 2.6** and **Table 2.7**. After the last cycle at 1C, 10 extra cycles are performed at 0.1C to observe the ability of the cell to recover the initial capacity at low C-rates rates. The active material loading used to calculate the cycling current is provided in each section.

From the results obtained by galvanostatic cycling experiments, different graphs can be represented, such as the voltage vs. time (**Figure 2.23** (a)), the voltage vs. specific capacity (**Figure 2.23** (b)) and the voltage vs. cell capacity (**Figure 2.23** (c)) graphs. Other option to display these results is the specific capacity vs. number of cycles (**Figure 2.23** (d)).

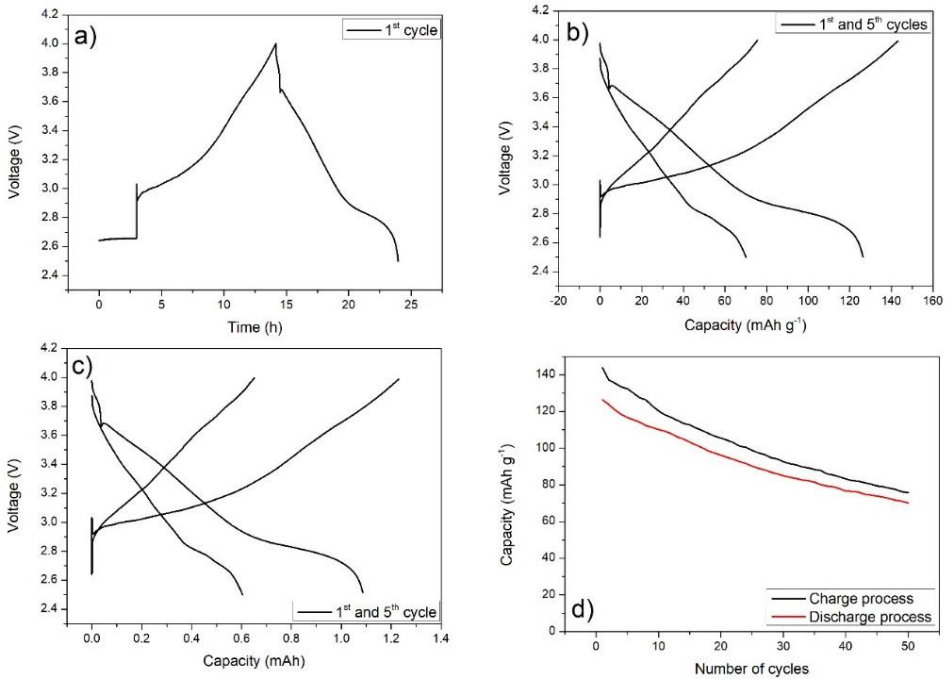

Figure 2.23. a) Voltage vs. time, b) Voltage vs. specific capacity c) Voltage vs. cell capacity and d) Specific capacity vs. number of cycles representations of a galvanostatic cycling of a cathode half-cell.

Coin cells are tested using multichannel Maccor battery tester Series 4000, monolayer pouch cells are tested using BT-Lab BCS-810 (BioLogic) battery tester and 3 electrode cells are tested using multichannel VMP3 potentiostat (BioLogic) at room temperature.

2.5.1.2 Energy density calculation

Based on the galvanostatic cycling data, the energy density of the cells can be calculated. The average voltage and the energy density are calculated using equations (2.1) and (2.2):

$$\text{Average voltage} = \left(\text{Energy (Wh)}/\text{Capacity (Ah)}\right) \quad (2.1)$$

$$\text{Energy density} = \frac{\text{Reversible capacity} \times \text{Average voltage}}{\left(\text{Total mass (cathode AM and/or anode AM)}\right)} \quad (2.2)$$

If otherwise is not stated, for half-cell energy density calculations, the active material mass of the studied electrode is considered, while for the full-cell energy density calculations, the active material mass of the cathode and the anode are considered.

2.5.1.3 Cyclic voltammetry (CV)

In the cyclic voltammetry tests, the current flow is measured while a voltage scan is applied at a constant scan rate. Essentially, a CV is a set of linear-sweep voltammetry (LSV or LV) in which both cathodic and anodic scans are alternatively repeated. The main information obtained from this type of experiments are the number of redox reactions that occur in the cell, including the Faradaic insertion and extraction reaction. By using cyclic voltammetry, the presence of surface reactions and the reversibility of the ion insertion and de-insertion can be determined [199].

Cyclic voltammetry is performed using a BT-Lab BCS-810 (BioLogic) battery tester at room temperature using half-cells. The scan rates for each experiment are calculated based on the active material loading of the working electrode, to perform the scans in 10, 5, 2 and 1 hours. At these cycling scans, the results are comparable with the galvanostatic charge/discharge cycles. The scan rates used for CV tests in this Thesis are provided in **Table 2.8**.

Table 2.8. Scan rates for CV experiments.

Time	Na//$NaFe_{0.4}Mn_{0.3}Ni_{0.3}O_2$ (2.5-4 V)	Na//Hard carbon (0.01-2 V)
10 h	0.042 mV s^{-1}	0.055 mV s^{-1}
5 h	0.083 mV s^{-1}	0.110 mV s^{-1}
2 h	0.208 mV s^{-1}	0.276 mV s^{-1}
1 h	0.417 mV s^{-1}	0.553 mV s^{-1}

As an example, **Figure 2.24** presents the cyclic voltammograms of a sodium layered oxide cathode in a half-cell configuration at different scan rates.

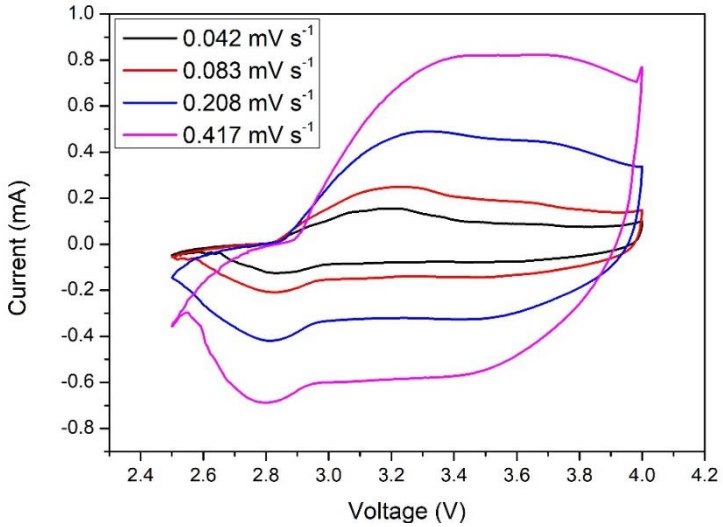

Figure 2.24. Cyclic voltammogram.

The diffusion coefficient of the electroactive species can be determined from cyclic voltammetry curves according to the Randles-Sevcik equation (2.3), which is only valid for reversible reactions [200],

$$I_p = (2.69 \times 10^5) \times n^{\frac{2}{3}} \times A \times D^{\frac{1}{2}} \times V^{\frac{1}{2}} \times C \qquad (2.3)$$

The peak current increases at faster voltage scan rates because the charge transference per unit of time is greater. Reaction kinetics are analyzed by means of the dependency of the peak current on the scan rate. When the reaction kinetic is controlled by diffusion, the oxidation and reduction peak current shows a linear dependence on the square root of the scan rate. It can happen that at lower scan rates, this dependency is linear while at higher scan rates, there is no linear dependence. This phenomenon is observed when the reaction kinetic is controlled by diffusion and adsorption processes. When the relationship is linear, the apparent diffusion coefficient of Na^+ ions can be calculated from the slope of the peak current vs. the square root of the scan rate graph. If an electrode shows a high diffusion coefficient, it means that the diffusion of the Na^+ ions is faster in this host material than in the other electrodes.

As an example, **Figure 2.25** shows the relationship between the peak current and the square root of the scan rate for a layered oxide cathode.

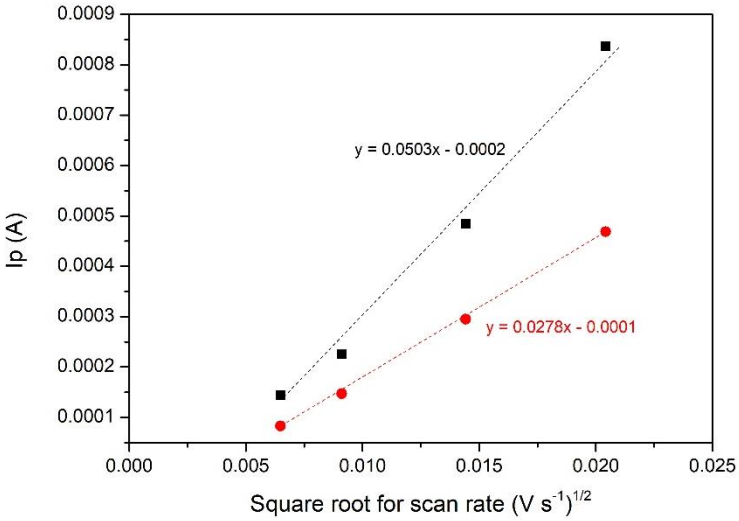

Figure 2.25. Relationship between the peak current and the square root of the scan rate extracted from CV tests.

2.5.2 Rheological analysis

Fluids can be categorized as Newtonian and non-Newtonian. According to the power law of fluids, among the non-Newtonian fluids, there are pseudoplastic or dilatant fluids. The viscosity of pseudoplastic fluids decreases as shear rate is increases (shear thinning behavior), while the viscosity of the dilatant fluids increases as shear rate increases (shear thickening behavior). The pseudoplasticity of the polymers can be explained according to the formation and breaking of interactions between the polymer molecules and the unraveling thereof. In the absence of shear, a molten polymer would be in a random state of "equilibrium", in which the mobility in the chains of the polymer, caused by the temperature, produces the simultaneous disappearance and formation of interactions between the different polymer chains, being the net result null; the presence of these interactions and the possible entanglement between the polymer chains are responsible for the viscosity of the fluid. When a shear stress on the fluid begins to act, greater destruction of the interactions between the polymer chains takes place, but the thermal mobility is able to compensate them, giving rise to barely observable changes in the viscosity of the fluid. However, if the shear stress continues to increase, net interactions are destroyed, resulting in a loss of the present structure. On the other hand, an unraveling and an alignment of the polymer

chains can also occur, which produces a greater separation between them, the net result of both the effects being a decrease in the viscosity of the fluid (pseudoplasticity). In general, the viscosity usually shows a Newtonian zone at low shear rates, with constant viscosity at different shear rates [201].

In general, battery electrode slurries show non-Newtonian shear thinning behavior because when increasing shear rate, the structures created by the aggregates and agglomerates are destroyed [202].

Another important characteristic of the fluids is the yield stress. However, there is not a universal protocol to measure this parameter. The yield stress is the stress that must be applied to a fluid to start to flow. For a gel material, yielding results in a viscoelastic liquid showing shear thinning behavior [203]. Rheological measurements must be done in a wide shear rate range in order to determine if the material has a real yield stress. As can be seen in **Figure 2.26**, yield stress type fluids can be confused with zero shear viscosity type fluids because if the rheological measurements are not performed at low enough shear rates. The yield stress tends to decrease with increasing temperature, that is, lower stress is required for the fluid to start the flow; therefore, yield stress measurements must be performed at controlled temperature [204].

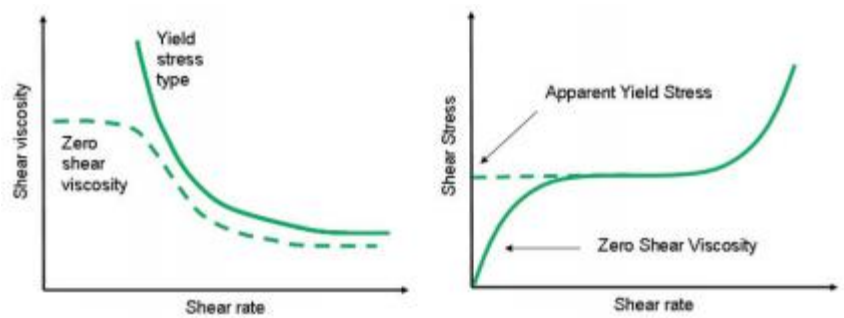

Figure 2.26 Flow curve for a material with a true yield stress and a zero shear viscosity material (left) and a material which appears to have a yield stress but shows viscous behavior at much lower shear rates (right) [204].

There are several models proposed in the literature for the fitting of non-Newtonian fluids (i.e., Power law, Bingham plastic, Herschel-Bulkley, Casson, Sisko, Carreau and Cross) which evaluate and predict the viscosity of a determined viscous fluid [205]. The Herschel-Bulkley and Bingham

models are not accurate enough at low shear rates. The Casson rheological model is an accurate model which allows to characterize the non-Newtonian fluids in a wide shear rate range, including low and high shear rates [206]. In this Thesis, the shear stress curves are fitted to the Casson Model.

The general power law equation for the non-Newtonian curves is represented by Equation 2.4, where K is the power–law liquid factor, n is the flow index, τ is the shear stress and γ is the shear rate.

$$\tau = K\gamma^{n} \qquad (2.4)$$

The equation which describes the Casson model is Equation 2.5, where τ_0 is the yield stress and η_p is the constant plastic viscosity, n is the flow behavior index, and γ is the shear rate.

$$\tau = \sqrt[n]{(\tau_0{}^{n}) + (\eta_p \times \dot{\gamma})^{n}} \qquad (2.5)$$

The simplest model corresponds to the Bingham model (Equation 2.6), where τ_0 is the yield stress and η_B is the Bingham viscosity or plastic viscosity and γ is the shear rate. It should be noted that the Bingham viscosity is not a real viscosity value, it just describes the slope of the Newtonian portion of the curve.

$$\tau = \tau_o + \eta_B\gamma \qquad (2.6)$$

Finally, the Herschel-Bulkey model (Equation 2.7) also describes the yield stress, where K is the consistency, n is the shear thinning index, τ_0 is the yield stress and γ is the shear rate. n describes the degree to which a material shows a shear thinning (n < 1) or shear thickening behavior (n > 1). This model describes the non-Newtonian behavior after yielding.

$$\tau = \tau_o + K\gamma^{n} \qquad (2.7)$$

Figure 2.27 shows a representation of the fluids fitted to the Casson, Bingham and Hershel-Bulkley models.

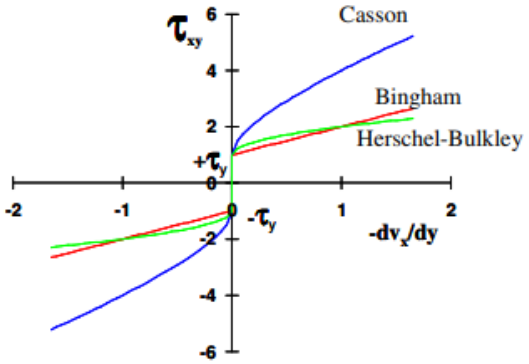

Figure 2.27. Representation of the fluids fitted to Bingham, Hershel-Bulkley and Casson models [207].

The rheological properties of newly made slurries are analyzed using a HAAKE RheoStress 1 rheometer (Thermo Scientific) (**Figure 2.28**) with a 35 mm diameter parallel plate setup connected to a water bath with immersion thermostat for temperature regulation (Digiterm-TFT-200 from Selecta) in this work.

Flow curves were measured in the shear rate range of interest for Doctor Blade casting. The coating speed is maintained constant for electrode casting, while the Doctor Blade gap is varied from 60 to 140 µm for anode slurries and 150 to 300 µm for cathode slurries. Consequently, anode slurries are measured in the shear rate range from 10 s^{-1} to 120 s^{-1} and cathode slurries in the range from 10 s^{-1} to 100 s^{-1}. The configuration is fixed with a gap between the parallel plates of 0.5 mm and 1 mm, for the anode and cathode slurries, respectively. Samples were balanced for 2 min in order to eliminate previous shear rates. All the measurements were performed at a constant temperature of 23 ± 1 ˚C.

Figure 2.28. HAAKE RheoStress 1 rheometer [208].

2.5.3 Peel tests

Adhesion can be defined as the attraction process between different molecular species which have been put into contact. In this Thesis, adhesion corresponds to the attraction between the coated electrode material to the aluminum current collector foil (coated material/binder/current collector interfaces). On the other hand, cohesion is an attraction process between similar molecular species, which in this Thesis corresponds to the attraction between the electrode components themselves (particle/binder/particle interfaces) [209,210].

Several factors have an influence on the adhesion properties of an electrode being some of the most important parameters the contact angle and the surface tension. Slurries must have a small contact angle, which indicates good adhesion due to the interactive forces between the liquid and the solid phase. In addition to this, the presence of pores, surface contamination, conditioning, moisture or roughness of the current collector foil have an effect on the bonding between the slurry and the current collector and can have an effect in the adhesion properties.

The nature of the delamination interface as a consequence of the peel test depends on the combination of the adhesion and cohesion properties of the electrodes. According to Gaikward et al. 3 main situations can happen: (1) if the tape removes all the coated electrode material, its

adhesion strength to the aluminum foil is lower than the cohesion strength. (2) If the tape is able only to remove part of the coated material from the foil, it means that the adhesion is higher than the cohesion strength. (3) If the coated material keeps almost intact in the foil, adhesion and cohesion strength are higher than the adhesion strength of the tape to the coated material [168].

Two types of peel tests are performed to the calendered electrodes in order to determine their adhesion and cohesion properties: 180º peel tests and adhesion strength tests. Peel tests are done using an INSTRON 5967 dynamometer designed for tension, compression, flexibility and peeling tests (**Figure 2.29**).

The experimental setup to perform the 180° peel test is depicted in **Figure 2.29** (a) with the two clamps made of rubber to hold the electrode and 25 mm width single-sided tape (Tesa) is used. The samples to perform these experiments are ca. 25 x 75 mm^2 (width x length) rectangular electrode pieces in which ca. 50 mm long correspond to the coated area and ca. 25 mm long correspond to the uncoated area (bare aluminum foil). A piece of a single-sided tape with the same dimensions is stuck to the coated side of the electrode, taking special care to avoid that the tape gets stuck to the uncoated area of the electrode. These uncoated electrode area and the area of the tape which is not stuck to the electrode are clamped to the upper and lower side clamps of the dynamometer respectively to perform the experiments. All the experiments are performed using a 50 N load cell at a constant speed of 50 mm min^{-1}.

The results of the 180° peel test experiment are usually represented as load vs. length graphs. With the aim of discarding the initial and final part of the experimental results, which are usually less representative of the whole electrode area, the results corresponding to 20 mm in the central area of the electrode are provided. In addition to this, to improve the clarity of the provided data, an average and the standard deviation of the load for 5 mm intervals is provided. The values of the standard deviation can be an estimation of the homogeneity of the electrodes.

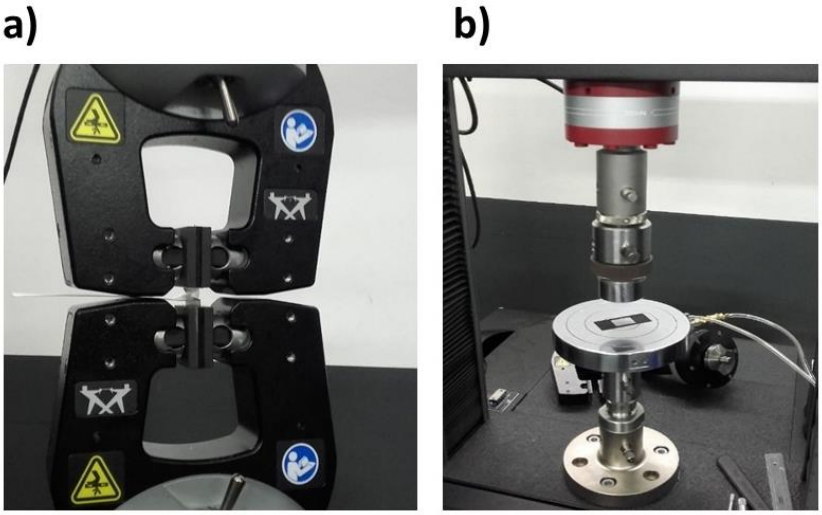

Figure 2.29. INSTRON 5967 equipment configuration for (a) 180° peel and (b) adhesion strength test.

The experimental setup to perform the adhesion strength test is depicted in **Figure 2.29** (b). All the experiments are performed using a 30 kN load cell. A rectangular piece of the electrode of ca. 25 x 50 mm^2 is stuck to the bottom part of the equipment using double-sided tape (Tesa). A 15 x 15 mm^2 of the double side tape is also stuck to the top part of the equipment. Prior to start the adhesion strength test, the samples are compressed to ensure the adhesion of the double-sided tape of the top part of the equipment and the electrode. This compression step is done at 2000 N for 2.5 min and adhesion strength test is performed at a speed of 1000 mm min^{-1}.

Pictures of the samples after the 180° peel tests and the adhesion strength tests are taken for visual inspection after the experiment in order to qualitatively determine the adhesion properties of the electrodes and help with the interpretation of the obtained results.

2.5.4 Scanning Electron Microscopy (SEM)

Historically, electron microscopes were developed because of the limited image resolution of light microscopes, which is imposed by the wavelength of visible light. Since the discovery that electrons can be deflected by the magnetic field in numerous experiments in the 1890s, electron microscopy replaces light source by high energy electron beam [211]. Louis De Broglie proposed

that just as light has both wave-like and particle-like properties, electrons, in this case, also have wave-like properties. Electrons present a characteristic wavelength related with their energy, so in the electron microscope a beam of accelerated electrons is used as a source of light.

The electron gun produces an electron beam by a specific filament which has to be under vacuum in order to avoid corrosion and any deposition on the filament, to avoid any interference of air or gas with the electron path from the sample to the detector, and finally, to maintain chemical and thermal stability. The electron beam is accelerated and focused on the sample by using electrostatic or electromagnetic lenses. The electrons can be adsorbed (transmission electron microscopy) or scattered (scanning electron microscopy) by the sample measured in order to create an image.

SEM images in this Thesis are obtained using a FEI Quanta 200 Field Emission Gun-SEM (**Figure 2.30**). SEM images of a sample are obtained by scanning it with a focused beam of electrons. The electrons interact with the atoms in the sample, producing various signals that can be detected and that contain information about the surface topography and the composition of the sample. The main components of a typical SEM are the electron column, the scanning system, the detectors, the display, the vacuum system and the electronic controls. There are some operating parameters, such as accelerating voltage, depth of field, probe diameter, emission current, objective aperture size and working distance which affect to the image quality and resolution of the image [212].

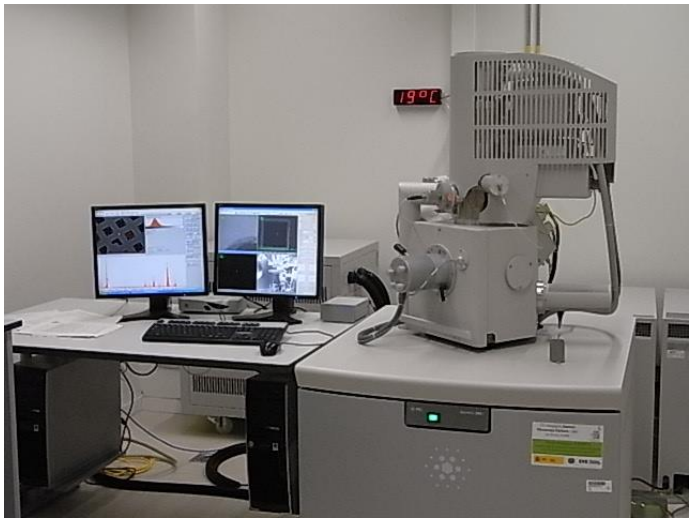

Figure 2.30. FEI Quanta 200 FEG-SEM.

The signals that can be detected include secondary electrons (that produce SEM images), backscattered electrons (BSE), diffracted backscattered electrons (EBSD), photons, visible light and heat. Secondary electrons and backscattered electrons are commonly used for imaging samples: secondary electrons, generated from the collision between the incoming electrons and the loosely bonded outer electrons, are most valuable for showing morphology and topography on samples and backscattered electrons are most valuable for illustrating contrasts in composition in multiphase samples. Backscattered electrodes are the electrons that can escape from the surface when there is a fraction of the incident electrons which are retarded by the electro-magnetic field of the nucleus and the scattering angle is greater than 180°. The electron beam is scanned in a raster scan pattern, and the position of the beam is combined with the detected signal to produce an image. Therefore, by SEM technique it is possible to study topography and morphology (BSED, SED), the chemical composition (EDXSD) and the crystallography and the orientation of grains (EBSD).

The beam current can be higher than 100 nA and it can operate between 3 kV (low vacuum mode) and 30 kV (high vacuum mode) as working voltages. At high working voltages, the SEM can achieve resolution between 3-5 nm. SEM analysis is considered to be "non-destructive"; that is, X-rays generated by electron interactions do not lead to volume loss of the sample, so it is

possible to analyze the same materials, repeatedly. However, some non-conductive samples measured by SEM can get damaged due to contamination and charging [212].

SEM is used for the morphological characterization of several samples. Firstly, powder of raw materials are analyzed by SEM in order to determine the size of the primary particles or the particle agglomerates. The powder is placed directly on the top of double-sided carbon tape which is stuck to the SEM sample holder (**Figure 2.31**).

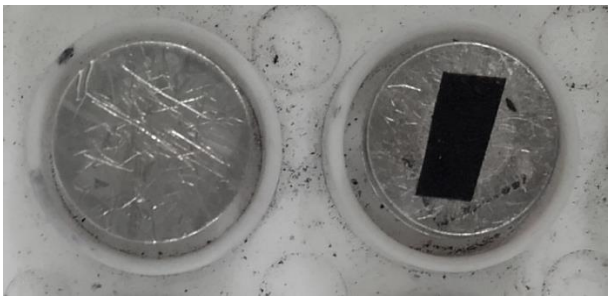

Figure 2.31. SEM sample holders.

Secondly, electrodes before and after cycling are analyzed by means of SEM. The quality of the dispersion and the distribution of the electrode components are analyzed. Possible aging or secondary phase formation in the electrodes after cycling is also evaluated by SEM. For electrode analysis, 12 mm discs are placed on top of the double-sided carbon tape which is stuck to the SEM sample holder. In case of electrochemically tested electrodes, the samples are washed in a DEC bath to remove the electrolyte salt traces inside an Ar filled glove box. The electrodes evaluated after cyclability tests are disassembled in the fully discharged state.

2.5.5 X-Ray Diffraction (XRD)

X-ray diffraction (XRD) is a rapid analytical and non-destructive technique primarily used for phase identification of a crystalline material and it can provide information on unit cell dimensions and other detailed structural information. As X-ray diffraction technique is used in order to characterize crystal structures. A crystal consists of a periodic arrangement of the unit cell into a lattice. The unit cell can contain a single atom or atoms in a fixed arrangement. Crystals

consist of planes of atoms that are spaced in a determined distance. The lengths and the angles between planes are called lattice parameters and they can be determined by X-ray diffraction [213].

The Bragg's Law relates the wavelength (λ) of the X-rays to the diffraction angle (θ, known as Bragg angle) and the spacing between the lattice planes (d) in a crystalline sample. The value of n is the diffraction order and can always be taken as unity. The phenomenon on which is based the X-ray diffraction (**Figure 2.32**) is the dispersion in particular directions of scattered X-rays which are generated by the interaction of an incident X-ray waves with the electrons of the sample measured [213]. When conditions satisfy Bragg's Law (2.8), the interaction of the incident rays with the sample produces a diffracted ray. These diffracted X-rays are then detected, processed and analyzed.

$$n\lambda = 2d \times \sin\theta \qquad (2.8)$$

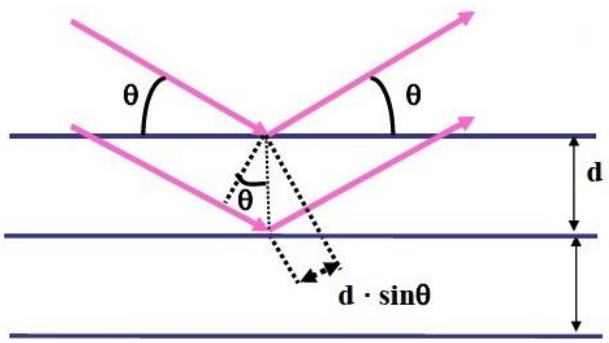

Figure 2.32. Schematic description of the diffraction of lattice planes, following Bragg´s law.

By scanning the sample through a range of 2θ angles, all possible diffraction directions of the lattice should be attained due to the random orientation of the powdered or electrode material. Conversion of the diffraction peaks to d-spacings allows the identification of the mineral because each mineral has a set of unique d-spacings. Typically, this is achieved by comparison of d-spacings with standard crystallographic structures reported in inorganic crystal structure database (ICSD).

XRD patterns are obtained by using CuKα radiation of λ = 1.5418 Å within 2θ range of 10-80º for 2 hours on a Brüker D8 Advance X-ray diffractometer equipped with a LYNXEYE detector mounted with Ni filter to attenuate the diffraction of K_β radiation (**Figure 2.33**).

Figure 2.33. Brüker D8 Advance X-ray diffractometer.

X-ray diffraction has been used in this work to determine the structural properties of the cathode components synthesized for this Thesis and cycled electrodes.

Finely grinded powders are directly placed in the XRD sample holder, while for the measurement of the electrodes, a glass piece is used to ensure that the height of the electrode is adequate for the XRD measurement. As most of the Na layered oxides are moisture sensitive, all the samples are prepared in an Ar filled glove box (< 0.5 ppm H_2O and O_2) (mBraun) and measurements are performed using air sensitive sample holders (**Figure 2.34**). In the case of cycled electrodes, prior to the measurement, they are washed in a DEC bath to remove the electrolyte salt traces.

The refinement of the XRD patterns performed to obtain the cell parameters are performed by Lebail method using FullProf software.

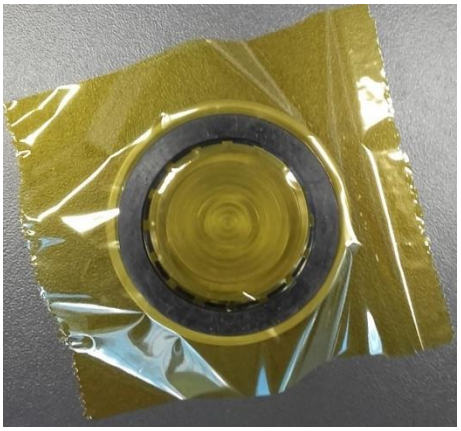

Figure 2.34. Air sensitive X-ray sample holder.

2.5.6 Solid State Nuclear Magnetic Resonance (NMR)

Nuclear Magnetic Resonance is an analytical chemistry technique which allows analyzing the molecular structure of a material by studying the interaction of the nuclear spins in a powerful magnetic field. It is based on the fact that many nuclei have spin and all nuclei are electrically charged. When the powerful magnetic field is applied, there is the possibility of producing an energy transfer between the base energy to a higher energy level (generally, a single energy gap) at a determined frequency, and when the spin returns to its base level, energy is emitted at the same frequency. The signal that matches this transfer is measured and processed in order to yield an NMR spectrum for the nucleus concerned.

This technique is only applied in the Chapter 3 of this Thesis (section 2.5.6) to analyze the Na^+ population in the cycled cathodes. ^{23}Na Magic Angle Spinning Nuclear Magnetic Resonance (MAS NMR) experiments were performed at 52.9 MHz, on a Bruker-300 spectrometer (**Figure 2.35**) charged to a field of 4.7 T using a 1.3 mm MAS probe. The rotor spinning speeds were set to 50 kHz for 0-NaN_3, 58 kHz for 10-NaN_3, 60 kHz for 15-NaN_3 and 60 kHz for 20-NaN_3. These spinning rates were selected in order to avoid the superposition of the signals with MAS sidebands.

For the NMR experiments, cycled coin cells are disassembled, and the cathodes are scratched out of the aluminum current collector. The powders are fitted into the rotors inside an Ar-filled glovebox, in order to avoid any moisture contamination.

Figure 2.35. Bruker-300 NMR equipment.

2.6 Experimental determination of thermal parameters

In the following sections the equipment and the methodology developed to calculate the heat capacity, the thermal conductivity, the internal resistance and the entropic heat coefficient are described.

2.6.1 Selected Na-ion battery description

A monolayer Na-ion pouch cell with the properties summarized in **Table 2.9** is selected for the calculation of the heat generation model.

Table 2.9. Properties of the Na-ion cell used for the heat generation model.

Cathode	$NaFe_{0.4}Mn_{0.3}Ni_{0.3}O_2$:C65:PVDF (87:5.7:7.3)
Anode	Hard carbon:PVDF (95:5)
Electrolyte	1 M $NaPF_6$ in EC:DEC (50:50 wt.)
$R_{N/P}$ (Q)	1.6
Cell dimensions	80 mm x 60 mm x 0.5 mm
Cell mass	5 g
Nominal capacity	10.5 mAh
Nominal voltage	2.9 V

The mixing device with the dissolver type impeller (see slurry preparation procedure in Chapter 5, section 5.1.1, page 161) is used for the preparation of the cathode slurry, while the planetary mixer is used for the anode slurry preparation (see slurry preparation procedure in Chapter 6, section 6.1.1, page 217). The cell assembly procedure is described in (Chapter 2, section 2.4.3, page 66).

2.6.2 Heat Capacity

Na-ion batteries are composed of different elements, which have specific heat characteristics. The sum of the specific heat capacity of each of the materials is called average heat capacity (Cp). This parameter is calculated by an adiabatic calorimeter, which is the most standard method to quantify it.

2.6.2.1 Experimental equipment

An accelerating rate calorimeter (ARC) (EV Standard Calorimeter, THT) is used to measure the heat capacity of the cells. The heating source is a variable voltage GPR-3510HD Power Supply and temperature is measured with Agilent 34970A voltmeter with thermocouples (**Figure 2.36**).

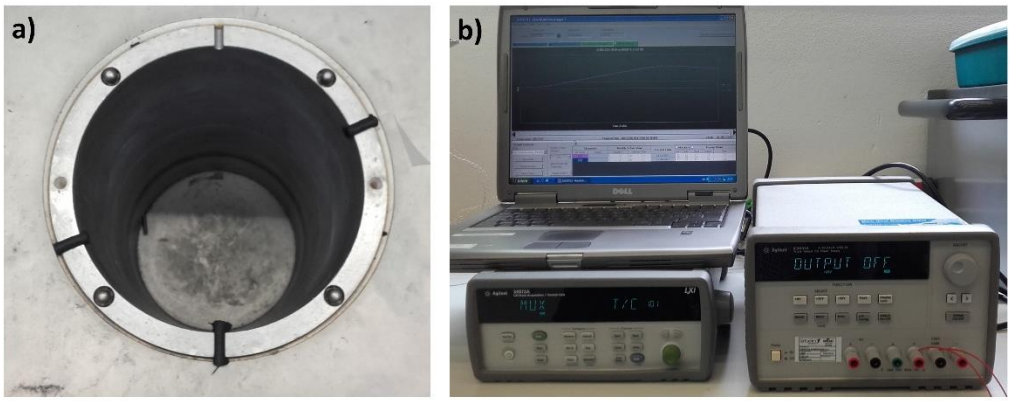

Figure 2.36. (a) Accelerating Rate Calorimeter (b) GPR-3510HD Power Supply coupled to Agilent 34970A voltmeter with thermocouples.

2.6.2.2 Methodology for experimental tests

The method used to carry out the measurement of the heat capacity is the adiabatic calorimetry. In order to develop this experiment, two similar Na-ion cells are required. These two cells are disposed together with a polyamide Kapton resistance between them which supplies the required power to heat the cells (**Figure 2.37**). The aluminum tabs of both pouch cells are protected with tape in order to avoid a short-circuit. It is important that the resistance is placed centered between both pouch cells in order to ensure that all the emitted heat is transferred to the batteries [214]. The polyamide Kapton resistance is connected to a variable voltage power supply.

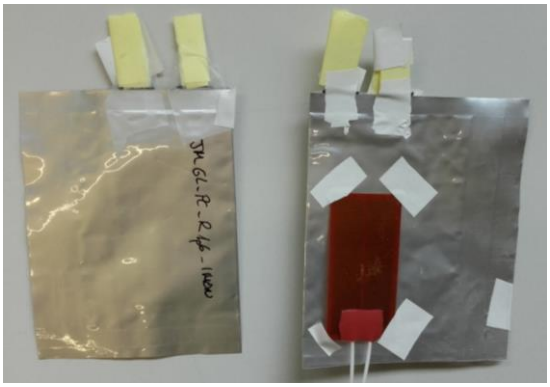

Figure 2.37. Polyamide Kapton Resistance placed between two Na-ion cells.

According to the equation 2.9, the power provided to the cell is:

$$q = Cp \times M \times \frac{dT}{dt} \qquad (2.9)$$

where Cp (J g^{-1} K^{-1}) is the heat capacity, M (g) is the total mass of the two cells and dT/dt (K s^{-1}) is the heating rate. The experiments are carried out in a temperature range from 20 °C to 35 °C, with a heating rate of 1 °C min^{-1}, which is a safe range. The mass of the Na-ion cells is 5 g. As a first approach, the Cp value is set as 1 J g^{-1} K^{-1}, which is a value close to commercial Li-ion batteries as it was reported by Maleki et al., reporting standard Cp data values from Li-ion cells [215], or M.S. Rad et al. [216]. Based on this first assumption, a power of 2.44 W is obtained. A resistance of 124.4 Ω given by the polyamide Kapton resistance is calculated using a voltmeter. By applying the Ohm's Law (Equation 2.10), where I is the current density applied, P is the power required and R is the resistance supplied by the planar resistance, the current density which needs to be applied to heat the battery is calculated:

$$P = I^2 \times R \qquad (2.10)$$

Current was provided by using Agilent E3631A equipment. The voltage and current are limited to 17.43 V and 0.14 A, respectively. However, it is observed that if this power is applied, temperature increases too fast and the results are not reliable enough. Hence, power supply is decreased down to 0.1 W and 0.3 W in order to ensure the obtention of optimal experimental

data and perform a comparison between both power voltage supplies. In this case, the voltage and current are limited to 6.0 V and 0.05 A.

The set-up shown in **Figure 2.38** is developed to perform the experiment. Temperature scanning is done in the outer part of each cell, in order to ensure reproducible measurement independently of the device used to measure the temperature. The adiabatic calorimeter ensures that there is no heat loss involved in the experiment. When the power supply is activated, the temperature starts to increase, and the heat capacity can be evaluated.

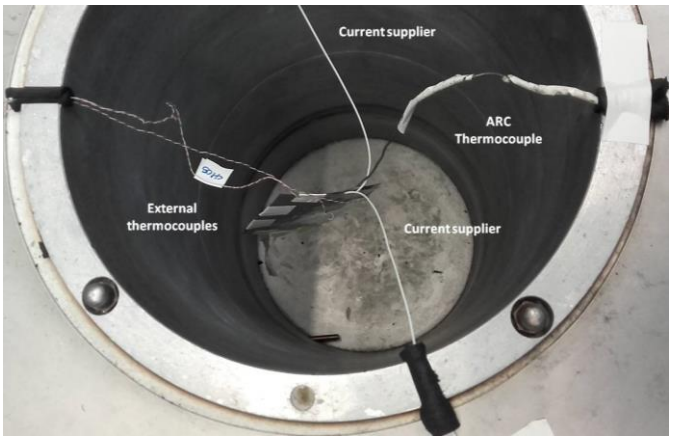

Figure 2.38. Experimental set-up for heat capacity calculation.

2.6.3 Thermal Conductivity

The thermal conductivity (λ) is a thermophysical property of a material. Thermal conductivity is a key factor when designing engineering systems in which temperature and thermal stress are main concerns. Several methods exist to measure the thermal conductivity, even for thin film solid-state materials, as is the case of the Na-ion pouch cells of this study which has a thickness < 1 mm. For thin film measurement, i.e. the 3ω method and the transient thermo reflectance technique can be mentioned [217]. Among the different techniques to measure the thermal conductivity, there are steady-state and transient techniques. While the steady-state techniques are used when the temperature does not change with the time, the transient techniques are used when there is a heating process [218].

Thermal conductivity has an orthotropic property which is based on the differences on the thermal conductivity value depending on the considered directions to perform the measurement, on plane or transversal.

2.6.3.1 Experimental equipment

The same equipment to that used for heat capacity measurements is used to measure the thermal conductivity of the cells. Heating is provided by a variable voltage GPR-3510HD Power Supply, which is coupled to a voltmeter Agilent 34970A with 4 thermocouples attached to the pouch cell. Moreover, in order to develop the experimental measurements under stationary conditions, cells are located inside a tube (**Figure 2.39**). Two Na-ion pouch cells are placed in the center of the tube while an air flow is passing through the tube, from the fan to the outer part. Therefore, constant temperature on the surfaces of both cells can be expected after the application of the voltage to the resistance.

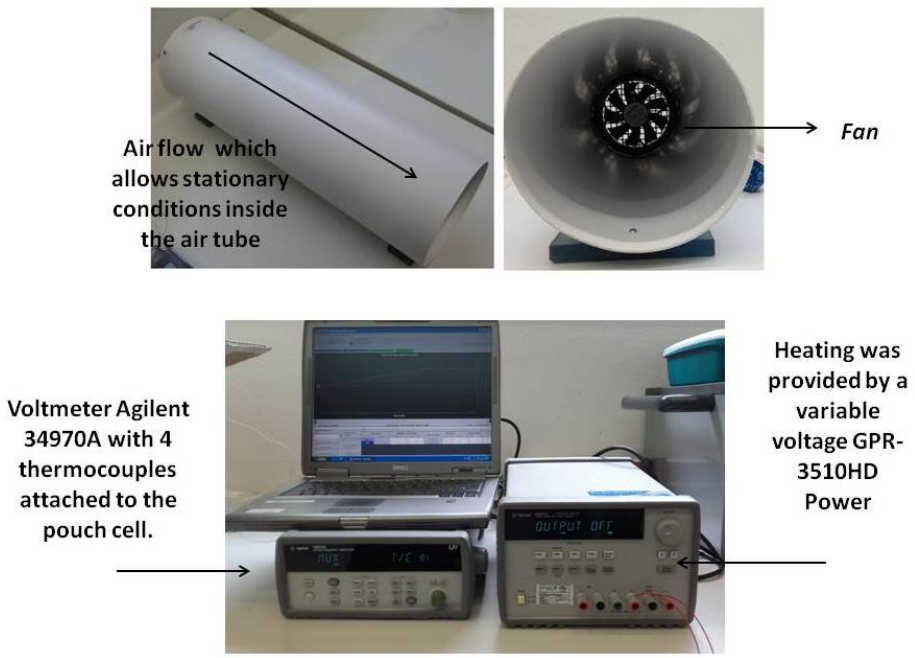

Figure 2.39. Air tube used to simulate stationary conditions. GPR-3510HD Power Supply coupled to a voltmeter Agilent 34970A with 4 thermocouples.

2.6.3.2 Methodology for experimental tests

The steady-state technique is applied in cross-plane type measurement. As in the case of heat capacity measurement, a polyamide Kapton resistance is placed between two Na-ion cells (called PCI and PCII hereinafter) in order to provide the power (**Figure 2.37**), located in a centered position. In this case, four thermocouples are attached to the cells. Two thermocouples to the outer part of the two cells (T01 and T033) and the other two thermocouples to the inner part of the two cells (T02 and T04).

The thermal conductivity is calculated using Equation 2.11, where Q is the power (or heat flux when it is expressed per area), A is the area of the resistance placed between the two cells, L is the length or thickness of the sample measured (depending if the cells are located in horizontal or vertical position) and ΔT is the gradient between T01 and T02 (PCI) and T03 and T04 (PCII).

$$Q = \lambda \times \frac{A}{L} \times \Delta T \qquad (2.11)$$

When the power supply is activated, the temperature starts to increase until it is stabilized. The experiments are done over a range of power (0.1 W, 0.3 W, 0.61 W, 1.22 W and 2.44 W) in order to determine at which power a stable temperature on the outer surfaces of the pouch cells can be maintained. It is assumed that Q is equally divided between both the cells. The experiments are performed with the cells in the horizontal and vertical setup, taking into account that both cells have to be equally exposed to the air flow.

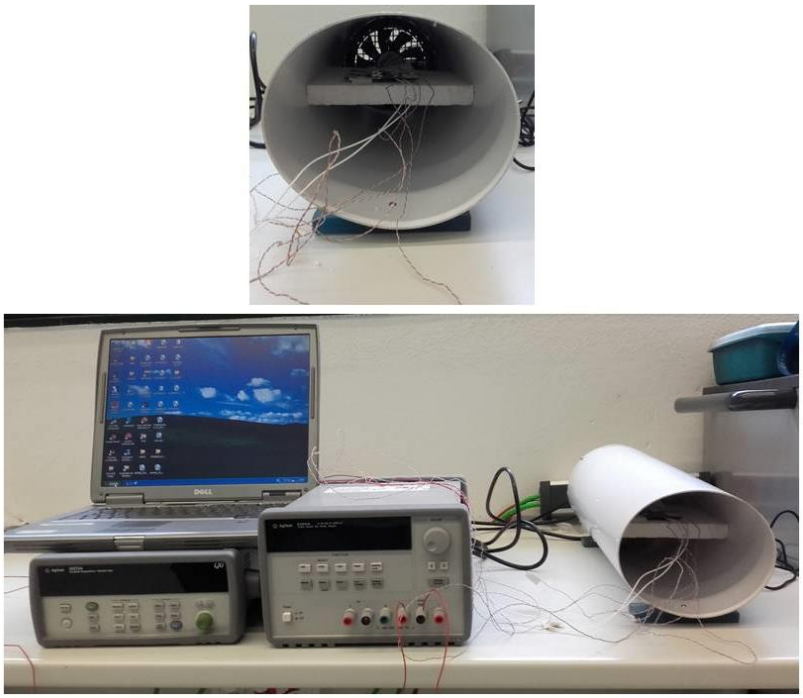

Figure 2.40. Experimental setup for thermal conductivity measurements.

2.6.4 Internal Resistance

The cells with low internal resistance are more efficient as the heat generation is lower. This value can be calculated using different methods, which can lead to different results. In this work, the internal resistance (R_{in}) of the Na-ion cells, which depends on the temperature and the SOC, is determined by means of constant current discharge pulses. Unfortunately, those values could not be validated using an ARC, because the irreversible heat generation in the studied cells is lower than the sensitivity of the ARC (0.05 °C min^{-1}).

2.6.4.1 Experimental equipment

The internal resistance measurements are performed in a climatic chamber (CTS, Clima Temperature System) which is able to maintain the target temperature within ± 0.75 K (**Figure 2.41** (a)). For the realization of the constant current pulses, the cell is connected to a BT-Lab BCS-

810 (BioLogic) battery tester. The temperature in the outer part of the pouch cells, as well as the real temperature inside the climatic chamber, is measured by using a voltmeter, Agilent 34970A, connected to a rack of thermocouples (**Figure 2.41** (b)). The equipment is scanning different temperatures every minute. The voltmeter accuracy specifications is ± 1 °C.

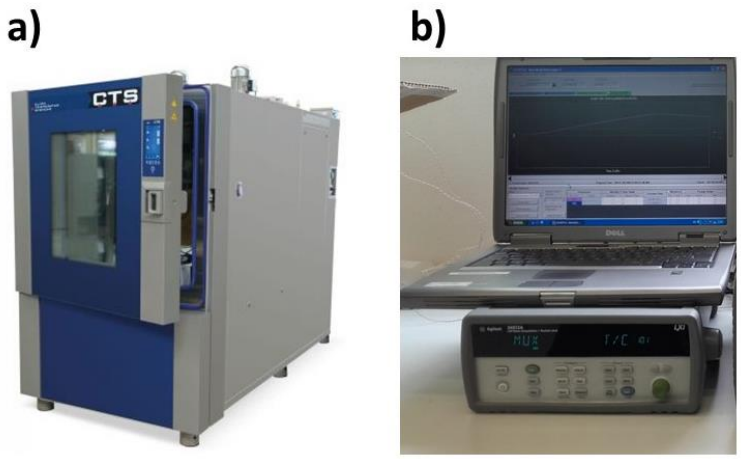

Figure 2.41. Experimental equipment used for internal resistance measurements by means of constant current discharge pulses: (a) climatic chamber and (b) Agilent 34970A voltmeter.

2.6.4.2 Methodology for experimental tests

The voltage drop due to a current pulse is related to the ohmic resistance of the cell, which is a very fast process, and partially to the concentration polarization. The relaxation period corresponds to the concentration polarization in the liquid electrolyte and solid electrode materials, which is a very slow process [219]. The internal resistance of the cell was determined from the final equilibrium voltage of the battery after the pulse, at different SOC and temperature, and the OCV. Equation 2.12 is used to calculate the internal resistance:

$$\mathrm{Rin} = \frac{\mathrm{OCV-Vterminal}}{\mathrm{I}} = \frac{V_3 - V_2}{\mathrm{I}} \qquad (2.12)$$

V_3 and V_2 are illustrated in **Figure 2.42** in which feature of a constant current discharge pulse is depicted.

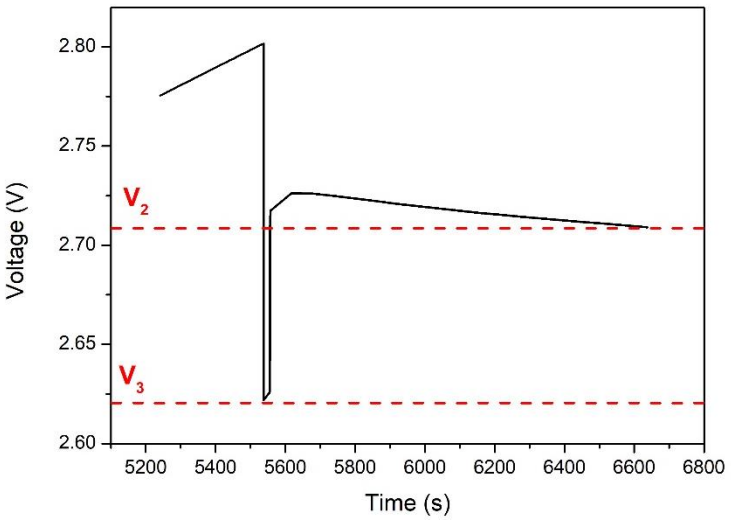

Figure 2.42. Representation of the voltage response to a discharge pulse. V_3 and V_2 are represented.

The internal resistance of the cells was calculated at different SOC and temperatures (15 °C, 25 °C and 35 °C). Higher and lower temperatures were discarded to avoid significant cell degradation. The charge and discharge processes were performed at a cycling rate of 0.1C, and the constant current discharge pulses with a duration of 18 seconds and a current rate of 1C were performed at selected SOC while the voltage response was recorded over time. The time and the current rate of the pulses were selected after a batch of experiments with different pulse conditions (1C and 18s; 1C and 10s; 2C and 18s; 2C and 10s). The difference between the internal resistances measured at different conditions are lower than 1 Ω for each SOC at 25 °C. According to Forgez et. al., who also made measurements using current pulses, spite of having different magnitudes of the current pulses, the temperature dynamics can be similar [220].

The pulses were done at a SOC of 20%, 40%, 60% and 80% in the charge and the discharge processes. Two methodologies were used for internal resistance measurements depending on the resting periods of the cycling protocol. The first protocol has a relaxation period of 5 hours after SOC changes (**Figure 2.43** (a)), and the second protocol includes a resting period of 10 hours after SOC changes (**Figure 2.43** (b)). In both the protocols a resting period of 5 hours was done after the pulses.

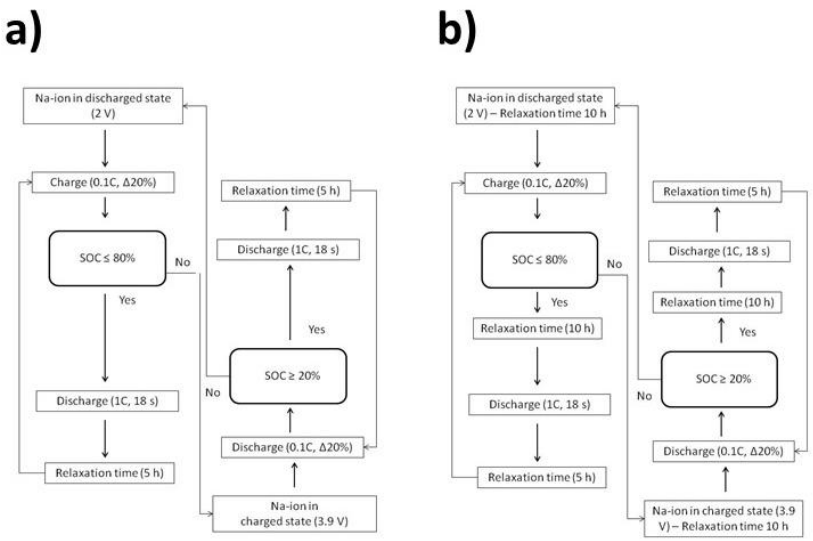

Figure 2.43. Schematic of the (a) first methodology for internal resistances measurements as a function of SOC without relaxation time before constant pulse current and (b) second methodology for internal resistances measurements as a function of SOC with relaxation time of 10 hours before constant pulse current.

2.6.5 Entropic Heat Coefficient

Potentiostat methodology is selected to calculate the entropic heat coefficient in this work, which is almost direct, easy and the most versatile technique. This parameter is usually measured as a function of the SOC.

2.6.5.1 Experimental equipment

The same equipment than that used for the internal resistance calculation was used for the entropic heat coefficient. Experiments were performed at controlled temperature with a climatic chamber (CTS, Clima Temperature System) and a BT-Lab BCS-810 (BioLogic) battery tester for the monitorization of the voltage. An accurate measurement of the voltage is extremely important since small voltage variations result in high increments on the entropic heat coefficient [221]. As in the case of the internal resistance measurements, the temperature was controlled by means of a voltmeter, Agilent 34970A, connected to a rack of thermocouples.

2.6.5.2 Methodology for experimental tests

The protocol defined for the entropic heat coefficient calculation is displayed in **Figure 2.44** (a). The cell was charged and discharged in Δ20% SOC intervals in the voltage range between 2-3.9 V. At each SOC the cell temperature was varied in the climatic chamber following the sequence displayed in **Figure 2.44** (b) (10 h at 25 °C, 5 h at 35 °C, 5h at 15 °C and 5h at 25 °C). As it was reported by Nieto et al. [222] similar entropic heat coefficient results are expected to be obtained at every temperature. The time needed for electrochemical equilibrium is usually longer than the time needed for thermal equilibrium, because the thermal inertia is shorter than that of diffusion of sodium ions through the solid electrode phase. That is why a resting time of 10 hours was established after every modification of the SOC. The OCV was monitored along the whole thermal cycle and the entropic coefficient was determined as a function of the SOC with the gradient of the dV/dT curve [223].

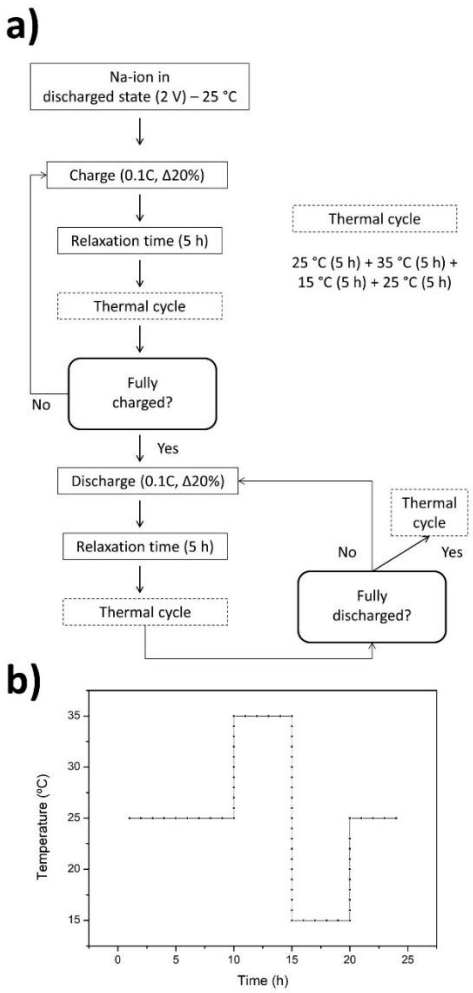

Figure 2.44. (a) Protocol for Entropic Heat Coefficient determination. (b) Thermal cycle profile used to determine entropic heat coefficient.

Figure 2.45 shows an example of the variation of the voltage during the thermal cycle at a SOC 60%. The experimental data are fitted to the fitting function (2.13) to extract the entropic heat coefficient parameter. A, B and C are constant values which were determined by means of fminsearch function of Matlab. This fminsearch, minimizes the deviation from the experimental OCV values and the fitting function. B corresponds to the entropic heat coefficient dV/dT in the fitting function (2.13).

$$V(t,T) = A + B \times T + C \times t \qquad (2.13)$$

B coefficient of the fitting bilinear function corresponds to the slope of the line presented by the relation of the voltage trace and the temperature at a determined SOC.

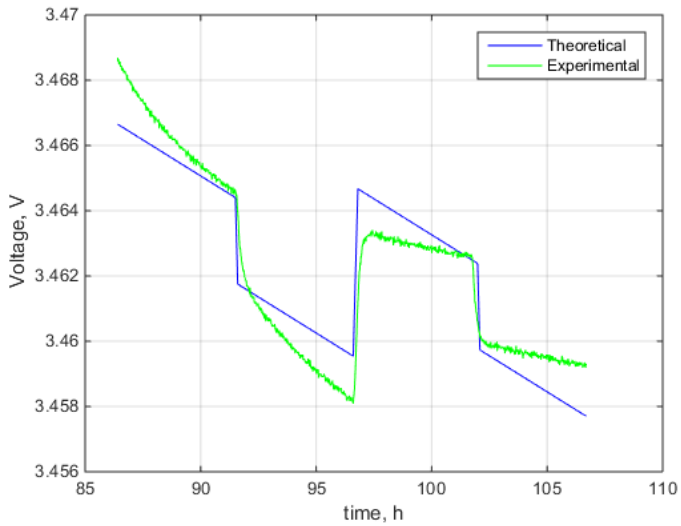

Figure 2.45. Variation of the voltage during the thermal cycle for the entropic heat coefficient calculation at a SOC of 60% in the charge process.

Chapter 3. NaN_3 and $Na_2C_4O_4$ as sacrificial salts in P2-type Na_xMO_2 cathodes

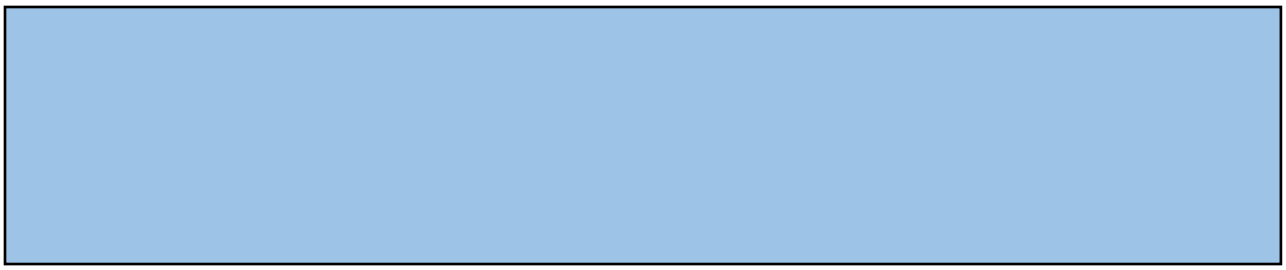

In this chapter, the use of two sacrificial salts is proposed in order to compensate the sodium deficiency issue of P2-type layered oxides. Concretely, $Na_{0.67}Fe_{0.5}Mn_{0.5}O_2$ has been selected as the cathode active material and NaN_3 and $Na_2C_4O_4$ as the sacrificial salts. Full-cells with hard carbon and $NaN_3/Na_2C_4O_4$ – $Na_{0.67}Fe_{0.5}Mn_{0.5}O_2$ composites have been assembled in coin cell configuration and cycled to assess the cycling stability of the cells. Moreover, *ex-situ* SEM, XRD and NMR analyses have been performed on the composite cathodes to study the morphological and structural changes that happen over cycling. Finally, a comparative study between the two systems in terms of cyclability and energy density is provided.

3.1 Introduction

Typical sodium layered oxide cathodes can be categorized in the P2- and O3-type structures according to Delmas' notation, being P2-type structures usually sodium deficient ($x < 0.74$) [78]. Approximately, one third of the Na^+ cations are missing in the P2-type structures, therefore maximum of 0.67 Na^+ ions per cathode formula unit can only be exchanged in the electrochemical charge/discharge reaction in full-cell configuration, when using non-sodium containing anode materials such as hard carbons. Consequently, this sodium deficiency gives a significant reduction in the delivered capacity of hard carbon//P2-type layered oxide full-cells.

To increase the reversible capacity of these types of P2-type materials is a significant challenge that has been addressed by other researchers. Chemically increasing the sodium content from 0.74 to 1 has an impact on the crystal structure of the material, which changes from P2- to O3-type, the later showing inferior electrochemical performance in certain cases such as $NaFe_{0.5}Mn_{0.5}O_2$ [84]. Opposite to this, when the sodium content is increased by electrochemical means, it leads to the formation of a distorted orthorhombic P2-type structure, named as P2' [126,224], which maintains the good electrochemical properties of the P2-type phases [225,84,126]. Based on this fact, some researchers have performed a pre-sodiation on P2-type cathodes using half-cell configuration. The cathode of the dismantled cell is used then against a pre-sodiated hard carbon anode for basic lab-scale tests [225]. Other researchers have also electrochemically pre-sodiated the anode using a third Na metal electrode and assembled the full-cell with a fully sodiated cathode in order to overcome the 1st cycle irreversibility of the anode [226]. However, these two approaches cannot be considered viable at industrial level.

The most common strategy reported in the literature to increase the reversible capacity of sodium deficient materials in full-cells is the use of sacrificial salts which decompose at the voltage range of interest. The use of NaN_3 was presented by Singh et al. for the first time as an approach to overcome the sodium deficiency issue in $Na//Na_{0.67}Fe_{0.5}Mn_{0.5}O_2$ [193]. They were successful in obtaining a reduction from 59 mAh g^{-1} to 27 mAh g^{-1} of the 1st cycle irreversible capacity in half-cell configuration when adding 5% of NaN_3 to the cathode. Unfortunately, NaN_3

is a toxic compound, with an unstable arrangement of molecule that tends to react to form a more stable N_2 gas. Therefore, risk of explosion under the effect of heat, shock or friction cannot be avoided. Other option is the use of Na_3P [227], however Na_3P cannot be handled in air, even in a dry room environment and the fate of leftover P is unknown. Sathiya et al. also studied the use of Na_2CO_3 as a sacrificial salt for P2-Na_xMO_2 by introducing this precursor in the synthesis to create a P2-Na_xMO_2-Na_2CO_3 composite. Sodium carbonate oxidation is likely to release O_2 as part of the gaseous products, which needs to be removed as it recombines at the negative electrode. Thus, the formation cycles and the synthesis of this composite have to be still optimized. More recently, $NaNO_2$ has been used coupled with an orthorhombic P'2-type $Na_{2/3}Co_{0.05}Mn_{0.95}O_2$ cathode material. $NaNO_2$ produces Na^+ ions and nitrogen gas in its activation and it has shown to increase the initial charge capacity from 154 to 210 mAh g^{-1} [228].

$Li_2C_4O_4$, together with other Li salts were proposed as a sacrificial salt with the aim to compensate the 1st cycle irreversibility of Li-ion battery anodes by Shanmukaraj et al. [229]. This work concluded that $Li_2C_4O_4$ could be among the best candidates based on the ease of synthesis and decomposition voltage. Focusing in this type of compounds in Na-ion technology, $Na_2C_4O_4$ was in a list reported by Chihara et al. [230] as possible anode materials for sodium-ion cells. However, due to the irreversibility of the electrochemical reaction, this composition was discarded. The same group also reported the use of $Na_2C_xO_x$ and $K_2C_6O_6$ salts as possible cathode materials for sodium ion batteries [231,232]. Recently, new research on $Na_2C_4O_4$ has been published. Shanmukaraj et al. [233] used the oxosalt in order solve the 1st cycle irreversibility issue of the hard carbon anode in the full-cell configuration when using $Na_3(VO)_2(PO_4)_2F$ cathode material and achieved a 100% capacity increase. This oxocarbon salt is a white crystalline powder, synthesized through potentially low-cost processes, free of toxic solvents. Therefore, it has the potential to be of low cost and is environmentally friendly. Finally, not having hydrogen could be considered as an advantage because it minimizes side reactions with the electrolyte.

3.2 Experimental procedure

The preparation of the electrodes and half/full-cells as well as the electrochemical characterization of the cells was carried out following the general procedures described in Chapter 2. In the following paragraphs, specific details of the experimental procedures used in this chapter will be provided.

Anodes with hard carbon:PVDF = 95:5 (wt. %) were selected for this study. In the case of the cathode, the P2-$Na_{0.67}Fe_{0.5}Mn_{0.5}O_2$ cathode active material was synthesized as described in Chapter 2 (section 2.1.1.1, page 48) and cast on an aluminum foil after being mixed in a mortar with the sacrificial salt (NaN_3 or $Na_2C_4O_4$), C65 conductive additive, PVDF binder and NMP solvent. NaN_3 (Sigma Aldrich) was used as received and $Na_2C_4O_4$ was synthesized as described by Martínez de Ilarduya et al. [234]. The AM:CB:PVDF ratio was maintained at 75:15:10 (wt%) with different amounts of sacrificial salt corresponding to 10%, 15%, 20% and 16%, 23%, 31% (wt%) for NaN_3 and $Na_2C_4O_4$ respectively. These percentages correspond to the ratio between the sacrificial salt and the dry powder mass including the active material, the conductive additive and the binder. In order to make a straightforward comparison between the two salts, variations in the percentages of sacrificial salt were made taking into consideration the experimental capacity that was achieved in the voltage range below 4.1 V (315 mAh g^{-1} for NaN_3 [193] and 186 mAh g^{-1} for $Na_2C_4O_4$ [234]). The full-cells comprising these cathode composites will be referred according to the percentage of the sacrificial salt hereinafter: 10-NaN_3, 15-NaN_3, 20-NaN_3 and 16-$Na_2C_4O_4$, 23-$Na_2C_4O_4$, 31-$Na_2C_4O_4$.

Cathode and anode active material loadings were selected so as the cells are not anode limited and the risk for Na plating is mitigated. The average active material loading for the cathodes is 5.3 mg cm^{-2}, irrespective of the composition of the sacrificial salt.

3.3 Electrochemical performance of individual cell components

3.3.1 $Na_{0.67}Fe_{0.5}Mn_{0.5}O_2$ as cathode active material

Half-cells of Na//$Na_{0.67}Fe_{0.5}Mn_{0.5}O_2$ were cycled between 1.5 and 4.3 V at 15 mA g^{-1}_{AM} to evaluate the electrochemical performance of the selected cathode active material composition with no sacrificial salt. **Figure 3.1** (a) shows that 117 mAh g^{-1} is obtained in the first charge, corresponding to the extraction of ~ 0.45 Na^+. During the subsequent discharge, more sodium ions, ~ 0.70 Na^+, corresponding to additional capacity of 66 mAh g^{-1}, are inserted back in the structure leading to a discharge capacity of 183 mAh g^{-1}. These values are in agreement with those previously reported by Yabuuchi et al. (~ 190 mAh g^{-1}) [84]. It is important to mention that the insertion of more sodium ions than those extracted in the first charge is possible due to the presence of sodium metal in the half-cell, which is acting as a source of Na^+ ions.

The reaction mechanism during the charge/discharge process has widely been studied on the same composition [192]. During the first charge, Na^+ ion intercalation is associated to Mn^{+3} to Mn^{+4} oxidation followed by Fe^{+3} to Fe^{+4} oxidation (**Figure 3.1** (b)). It has also been reported that at the end of the charge, P2 and OP4 coexist in the biphasic region [192]. The plateau near 2.0 V at the end of the discharge (**Figure 3.1** (a)) indicates the presence of a biphasic region that corresponds to a P2-type distorted orthorhombic phase [192, 126]. The capacity fade from 183 mAh g^{-1} to 166 mAh g^{-1} observed in 10 cycles (**Figure 3.1** (c) and (d)) can be attributed to the wide voltage window chosen for the cycling test and the consequent structural changes over this wide voltage region.

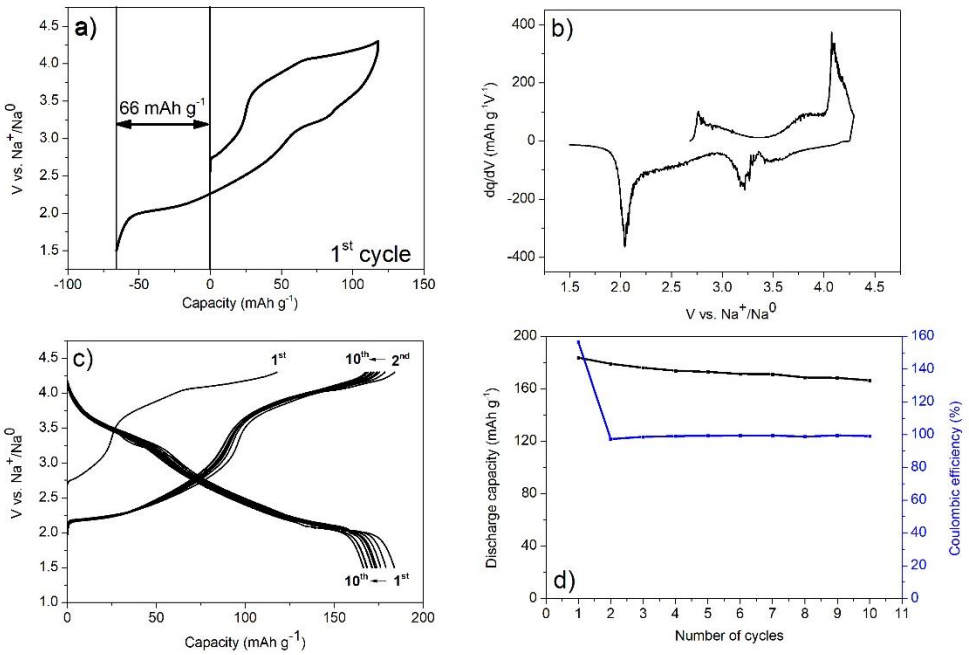

Figure 3.1. Cycling performance of $Na_{0.67}Fe_{0.5}Mn_{0.5}O_2$ vs. Na^+/Na^0 at 15 mA g^{-1}_{AM} between 1.5 – 4.3 V. a) First charge/discharge cyclic voltage profile, b) First charge/discharge differential capacity vs. voltage plot, c) Voltage profile evolution for the first 10 cycles and d) Evolution of the discharge capacity and the coulombic efficiency for the first 10 cycles.

3.3.2 Hard carbon as anode active material

The cycling behavior of the hard carbon electrodes used in this chapter (active material loading of 5 mg cm^{-2}) is shown in **Figure 3.2** (a) and (b). The initial discharge and charge capacities are 288 mAh g^{-1} and 257 mAh g^{-1} respectively, with a first cycle irreversible capacity of ~ 31 mAh g^{-1} that could be attributed to the SEI formation. As shown in **Figure 3.2** (b), the capacity and coulombic efficiency of this hard carbon remains stable at ca. 220 mAh g^{-1} and ca. 100% for the first 10 cycles.

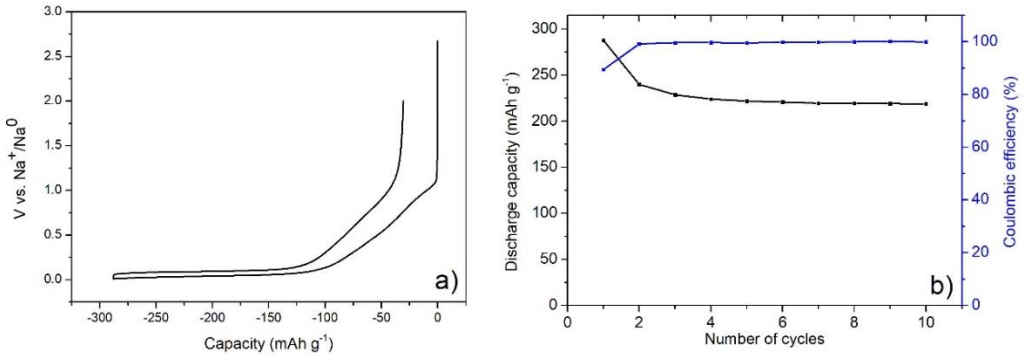

Figure 3.2. (a) Voltage profile of the first galvanostatic charge/discharge and (b) cycling performance and coulombic efficiency for the first 10 cycles of the hard carbon anode vs. Na^+/Na^0 at 25 mA g^{-1} within 0.01-2 V.

3.3.3 NaN_3 and $Na_2C_4O_4$ as sacrificial salts

In order to determine the electrochemical activity of NaN_3 and $Na_2C_4O_4$, NaN_3:C65 and $Na_2C_4O_4$:C65 mixtures (70:30 wt. %) were prepared and electrochemically tested in half-cell configuration using metallic Na as the counter and reference electrode. The voltage profiles of the electrochemical reactions are shown in **Figure 3.3** (a) and (b) and the proposed electrochemical reactions (3.1 and 3.2) are written below [193,233]:

$$2NaN_3 \rightarrow 3N_2 + 2Na^+ + 2e^- \quad (3.1)$$

$$Na_2C_4O_4 \rightarrow 2\,CO_2 + 2\,C + 2Na^+ + 2e^- \quad (3.2)$$

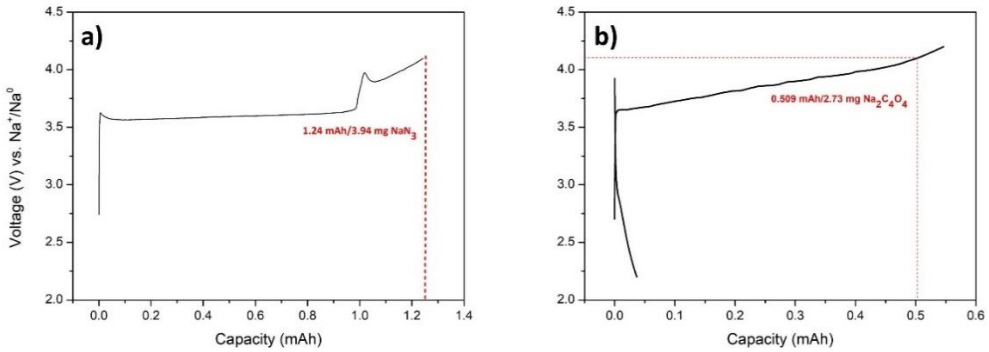

Figure 3.3. Voltage profiles of the electrochemical decomposition of (a) NaN_3 and (b) $Na_2C_4O_4$.

According to the voltage profiles in **Figure 3.3**, NaN_3 and $Na_2C_4O_4$ start to decompose above 3.5-3.6 V almost irreversibly delivering a capacity of 315 and 186 mAh g^{-1}, respectively below 4.1 V at 15 mA g^{-1}_{AM}. This decomposition reaction is expected to happen together with the Na^+ ion extraction from the $Na_{0.67}Fe_{0.5}Mn_{0.5}O_2$ cathode active material. The Na^+ ions coming from the active material and from the decomposition of the sacrificial salts react with the anode, being some of the Na^+ ions irreversibly consumed in this reaction. During the following discharge, the Na^+ ions that did not irreversibly react with the anode are reinserted back in the cathode structure, compensating for the sodium deficiency if enough sacrificial salt is incorporated. Based on this principle, the sacrificial salt acts as both, a source for the compensation of the sodium deficiency of the cathode and the irreversible sodium consumption of the hard carbon anode.

According to the reactions 3.1 and 3.2, both the salts electrochemically decompose releasing Na^+ ions to the electrolyte and forming N_2, CO_2 and C as reaction products. N_2 and CO_2 gases can be released during the degassing step of cell fabrication and C can be an added advantage that could contribute towards enhanced electronic conductivity.

3.4 Use of NaN_3 as sacrificial salt

3.4.1 Electrochemical performance

Full-cells were assembled with the three different composite cathodes named as 10-NaN_3, 15-NaN_3 and 20-NaN_3 together with a cell with no sacrificial salt as a reference (0-NaN_3) and the effect of the amount of sacrificial salt in the cycling performance was analyzed. As shown in

Figure 3.4, in the absence of any sacrificial salt, the HC//$Na_{0.67}Fe_{0.5}Mn_{0.5}O_2$ full-cell exhibits a first charge capacity of 101 mAh g^{-1}. This value is lower than that corresponding to the half-cell, which is 117 mAh g^{-1} (**Figure 3.1**). This has been attributed to the lower upper voltage cut-off used in the full-cell configuration. Noteworthy, although the capacity is less, more stable performance is observed owing to the limited voltage cut-offs, which are more suitable from the point of view of the structural stability of the material [235]. Reversible capacity of 50 mAh g^{-1} for the first cycle, a stable cyclability with reversible capacity of 45 mAh g^{-1} and coulombic efficiency as high as 99.88% after 40 charge/discharge cycles are observed for the cell without sacrificial salt.

For 10-NaN_3, there is an increase of more than 100% of the reversible capacity and the cell maintains good cycling stability for 40 cycles. A maximum reversible capacity of 114 mAh g^{-1} is obtained in the 15th cycle and 101 mAh g^{-1} at the end of the experiment. For 15-NaN_3, an increment of 58 mAh g^{-1} of the reversible capacity with respect to 0-NaN_3 is obtained, showing the best capacity retention (92%) of all the NaN_3 containing cells. Finally, for 20-NaN_3, a maximum reversible capacity of 163 mAh g^{-1} is observed with capacity fade starting from the 10th cycle. The fact that the capacity increases during the initial cycles in all the NaN_3 containing cells indicates that the accessibility of the active material or the salt to the electrolyte is improved due to the activation of NaN_3, which is further confirmed by the SEM images explained later.

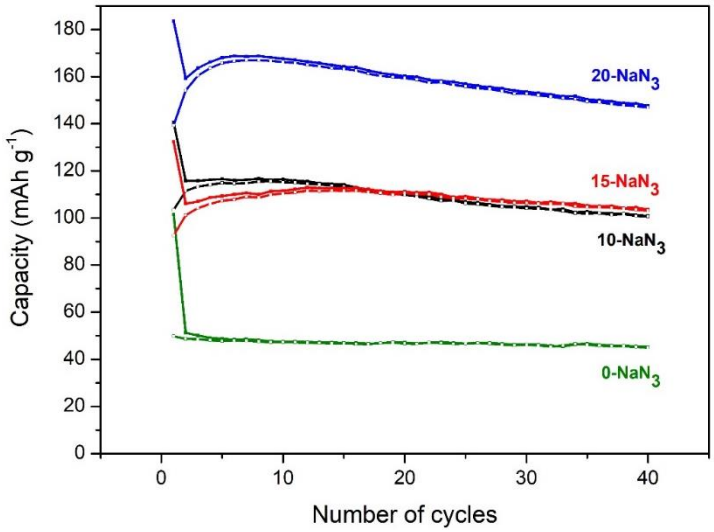

Figure 3.4. Cycling stability of 0-NaN_3, 10-NaN_3, 15-NaN_3 and 20-NaN_3 full-cells (15 mA g^{-1}_{AMcat}; 1-4.1 V).

Different from what expected, capacity values did not increase progressively when increasing the amount of sacrificial salt and very similar electrochemical performances were observed in the case of 10-NaN_3 and 15-NaN_3, e.g. 100 and 103 mAh g^{-1} reversible capacities after 40th cycles, respectively. As it will be explained later, SEM images of the cathodes after 40 cycles showed different microstructures which will support the unexpected behavior of the 15-NaN_3 cell.

The amount of Na^+ ions remaining in the cathode for different NaN_3 contents are also estimated based on the following assumptions: (1) the amount of Na^+ per formula unit in the pristine $Na_{0.67}Fe_{0.5}Mn_{0.5}O_2$ at the beginning of the experiment is 0.67, (2) the amount of Na^+ per formula unit extracted from the cathode during the first charge is constant for all cells and is calculated as the amount of Na^+ ions extracted from the cathode in the cell with no sacrificial salt in its composition (101 mAh g^{-1}, Figure 3.4), which corresponds to 0.39 Na^+ per formula unit; therefore, the Na^+ ions per formula unit remaining in the cathode after the first charge are 0.28, and (3) the sodium content in the subsequent cycles is calculated based on the discharge/charge capacity delivered by the cell, assuming that no secondary reactions happen upon cycling. Based on these calculations, the amount of Na^+ per formula unit remaining in the cathode active material after 40 cycles increased from x = 0.41 for 0-NaN_3, to x = 0.55 for 10-NaN_3 and x = 0.60 for 20-NaN_3.

The amount of reacted NaN_3 was also estimated assuming that the theoretical capacity for NaN_3 is 412.3 mAh g^{-1} and that the charge capacity delivered by the active material, independent of the NaN_3 content, is the same as that corresponding to the full-cell with no sacrificial salt; therefore, the extra capacity delivered in the first charge is attributed to the electrochemical decomposition of the salt. According to these calculations, while for 10-NaN_3 and 20-NaN_3, ~ 46% of the salt reacted, the percentage of reacted salt is lower for 15-NaN_3.

As it is shown in the voltage profile in **Figure 3.5** (a), for 10-NaN_3, 15-NaN_3 and 20-NaN_3, the addition of NaN_3 has a great influence in the 1st irreversible capacity which decreases from 47 mAh g^{-1} to 37.5 mAh g^{-1}, 39.8 mAh g^{-1} and 44.07 mAh g^{-1} for 10-NaN_3, 15-NaN_3 and 20-NaN_3 respectively. The charge profiles of the full-cells with NaN_3 are similar to the full-cell without NaN_3, except from an additional kink observed at ~ 3.5 V, which can be attributed to the activation of the salt (**Figure 3.5** (a) and (b)). This kink is more evident as the amount of NaN_3 in the composite increases, which leads to an additional 1st charge capacity of 46 mAh g^{-1}, 37 mAh g^{-1} and 88 mAh g^{-1} for 10-NaN_3, 15-NaN_3 and 20-NaN_3, respectively. During the discharge, higher capacity is observed compared to the sample without NaN_3, showing that more sodium ions are inserted in the cathode crystal structure while discharging.

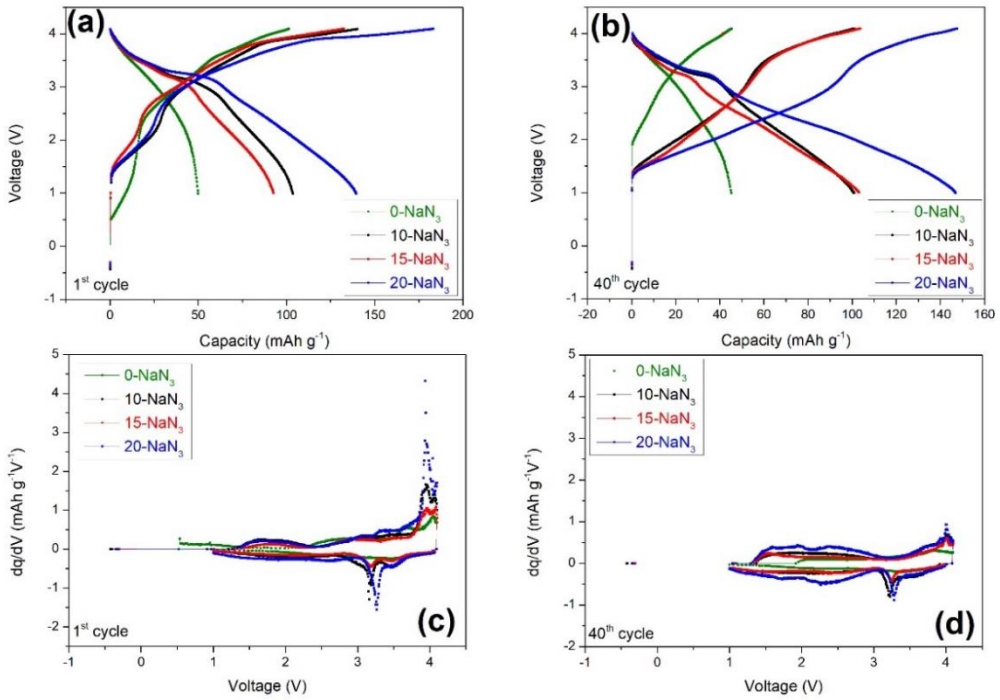

Figure 3.5. (a) 1st and (b) 40th galvanostatic cycles and differential capacity curves of the (c) 1st and (d) 40th cycles for 0-NaN_3, 10-NaN_3, 15-NaN_3 and 20-NaN_3 full-cells (15 mA g^{-1}_{AMcat}; 1-4.1 V).

The differential capacity curves of the 1st and 40th cycles are represented in **Figure 3.5** (c) and (d). In the cathode without NaN_3, during the 1st charge, a broad oxidation peak is observed between 2.5-3.5 V along with a sharp peak at ~ 4.0 V (**Figure 3.5** (c)). In the following discharge process only a broad peak is observed at ~ 3.55 V. This redox peak at high voltage i.e., 4.0/3.55 V is associated to the $Fe^{+3/+4}$ redox process [84]. With the addition of 10, 15 and 20% of NaN_3, additional peaks during the first charge are observed at ~ 3.5 V, larger for higher amounts of salt, which are assigned to the decomposition reaction of NaN_3. In the following discharge processes (**Figure 3.5** (c) and (d)), the reduction peak which corresponds to the reduction of $Fe^{+3/+4}$ (at ~ 3.55 V in case of the sample without NaN_3) is shifted to lower voltages with higher intensities. On the other hand, new peaks appear below 3.0 V, which are assigned to the reduction of Mn^{+4} and which are bigger for higher amounts of salt. These changes in the peak position and intensity can be associated to the reduction of Mn^{+4} to a larger extent due to the insertion of more Na^+ ions

in the cathode structure. This has been further confirmed by the *ex-situ* XRD and NMR studies as explained in the following sections.

3.4.2 Post-test morphological and structural analysis

The microstructural analysis of the cathodes after 40 cycles has been carried out by means of SEM. SEM images in **Figure 3.6** (a), (b), (c) and (d) show the surface of discharged $Na_{0.67}Fe_{0.5}Mn_{0.5}O_2$ cathode electrodes corresponding to 0-NaN_3, 10-NaN_3, 15-NaN_3 and 20-NaN_3 full-cells respectively. The creation of some voids in the cathode structure is observed in the NaN_3 containing electrodes. The size of the pores increases while increasing the amount of NaN_3 from 10 to 20% wt. Therefore, these holes are attributed to NaN_3 which is electrochemically decomposed.

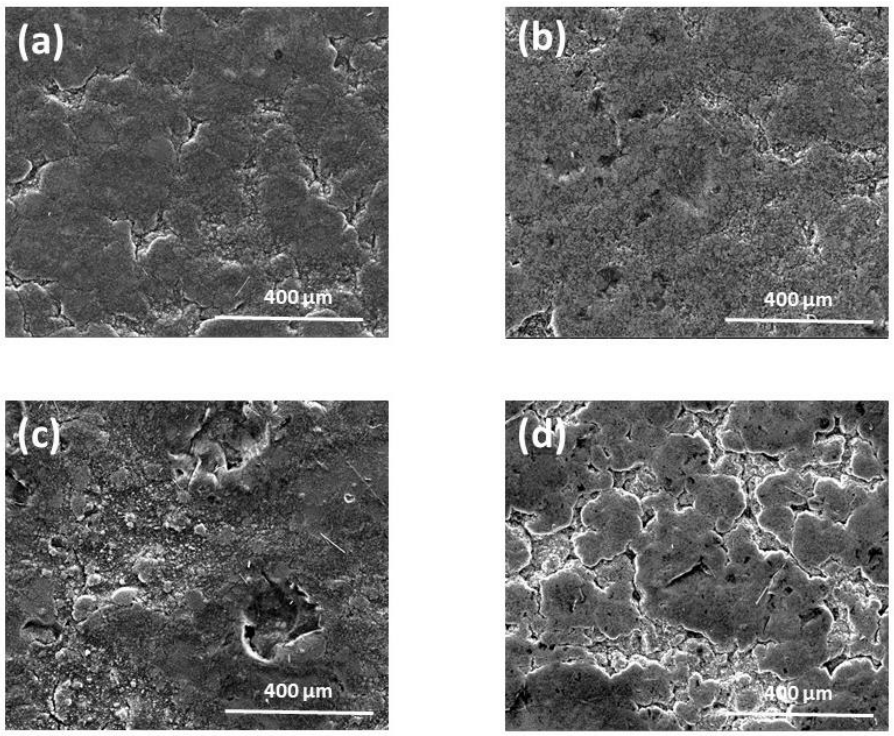

Figure 3.6. SEM pictures of the fully discharged cathodes of (a) 0-NaN_3, (b) 10-NaN_3, (c) 15-NaN_3 and (d) 20-NaN_3 after 40 cycles.

Focusing on the sample corresponding to 15-NaN_3, larger voids than those observed in the samples corresponding to 10-NaN_3 and 20-NaN_3, indicate that the salt and the active material were not homogeneously mixed. As a consequence, lower capacity values than expected are obtained, as it is shown in **Figure 3.4**. In order to focus the structural analysis in the cells that did not showed an abnormal behavior, 15-NaN_3 was excluded from further post-test analysis.

In addition to SEM, cycled cathodes were further analyzed by XRD. As it has been reported by Singh et al. [192] and Mortemard de Boisse et al. [126], there is a change of the position and intensity of the diffracted peaks over the charge/discharge processes, related to the crystallographic changes of the $Na_{0.67}Fe_{0.5}Mn_{0.5}O_2$ cathode over cycling. As the oxide losses Na^+ ions during the charging process, the crystal structure of the material evolves from its initial P2-type structure towards a biphasic P2 + OP4 structure. When the Na^+ content is minimum, the oxide shows an OP4 structure. In the discharge process, a reversible phase transformation is observed from the OP4 to the OP4 + P2 and the P2-type structures. At the end of the discharge process, the cathode structure undergoes a biphasic mechanism and the P2-phase and a distorted orthorhombic P2-type structure coexist.

Ex-situ X-ray diffraction patterns of the pristine and fully discharged (1 V) positive electrodes of the full-cells with and without NaN_3 after the 40th cycle are shown in **Figure 3.7** (a - b). The pristine sample presents a P2-type structure and the cycled cathodes show different structures depending on the amount of sacrificial salt. 0-NaN_3 shows a structure close to a biphasic domain of OP4 and P2-type structures while 10-NaN_3 and 20-NaN_3 present a P2-type hexagonal and orthorhombic *Cmcm* phase already identified in earlier reports [224,126]. This affirmation is supported by the lower intensity and the shift of the (002) peak (**Figure 3.7** (b)) towards lower 2θ angles in the case of 0-NaN_3, indicating lower sodiation level than the pristine P2-type structure, and the shift towards higher 2θ angles in the case of 10-NaN_3 and 20-NaN_3, indicating higher sodiation level than the pristine P2-type structure.

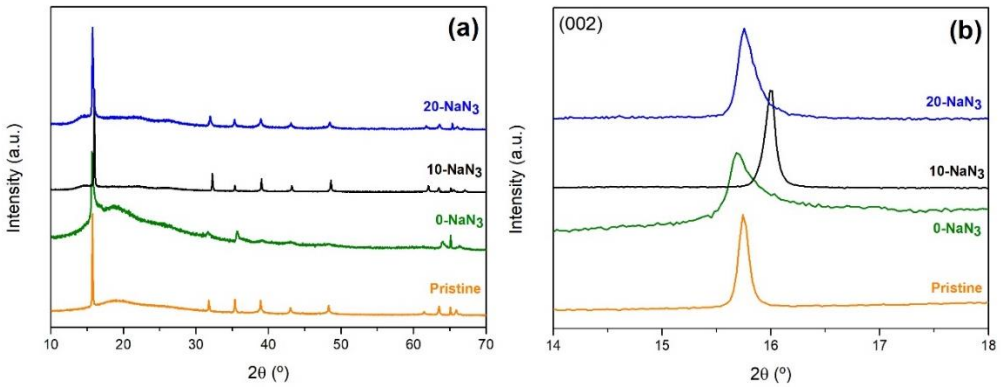

Figure 3.7. (a) *Ex-situ* X-ray diffractograms of pristine $Na_{0.67}Fe_{0.5}Mn_{0.5}O_2$ and fully discharged full-cells of 0-NaN_3, 10-NaN_3 and 20-NaN_3 cathodes. Detail of the diffraction patterns (b) between 14-18°.

The ^{23}Na solid state NMR spectra of the three samples with different amounts of NaN_3 are shown in **Figure 3.8**. Several signals are evident in the spectra with intensity maxima extending from ~ 0 to 2000 ppm. The typical NMR chemical shift range of ^{23}Na nuclei in a diamagnetic environment is observed between 30 to -30 ppm. Strong shifts out of this range are induced when paramagnetic interactions are present between transition metal centers and the nuclei under observation. The shifts induced by such interactions can result in NMR signals resonating at up to several thousands of ppm. This is especially the case when strong paramagnetic ions are involved like Fe^{3+} or Mn^{3+}. Therefore, the resonances marked by "+" at around 0 ppm, are ascribed to Na-containing diamagnetic species like Na_2CO_3 commonly observed in Na-based cathode samples or/and to Na^+ ions related to the electrolyte decomposition reactions. The Gaussian-shaped signals de-convoluted in the spectra on the other hand, are assigned to the Na^+ population inside the bi-dimensional layers of the cathode material. The paramagnetic shifts governing these signals are a through-bond effect sensitive to the unpaired electron density that is effectively delocalized from the transition metal centers to an "s" orbital of sodium. They are therefore highly dependent to changes in bond distances and angles and to the number of unpaired electrons at the metallic cations. Finally, the signals marked with "*" in the spectra are MAS rotational side-bands.

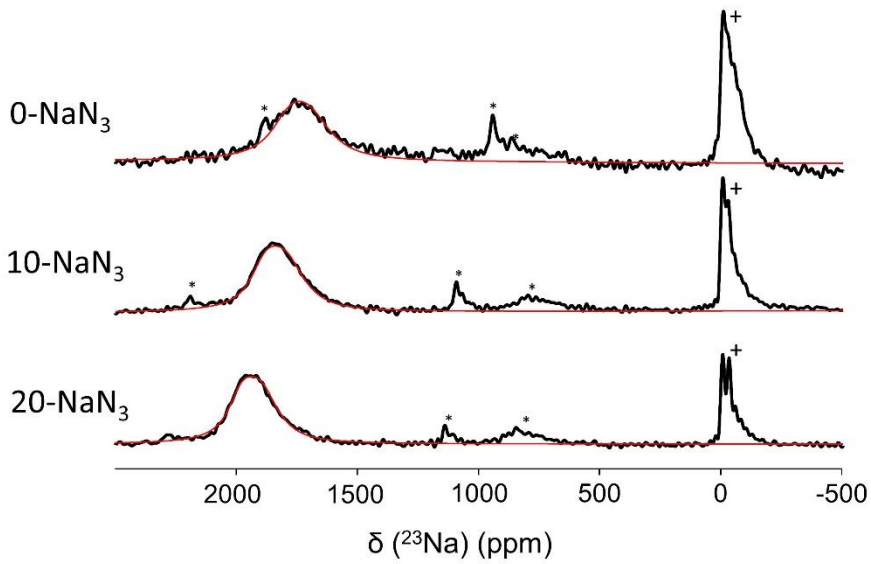

Figure 3.8. *Ex-situ* ^{23}Na NMR pattern of the fully discharged full-cells of 0-NaN_3, 10-NaN_3 and 20-NaN_3 cathodes after 40 cycles using full-cell configuration.

It is interesting to notice that in all the spectra represented in **Figure 3.8,** only a single paramagnetic Gaussian-shaped signal is observed. Due to the heterogeneous composition of the transition metal layers, different sodium environments are expected in the structure and different signals are consequently predicted. This is in agreement with the results obtained previously by solid state NMR in similar layered oxides and is explained by fast ionic mobility of Na^+ ions in the 2D layers of the cathode effectively averaging the distinct paramagnetic shifts, leading to an averaged signal [192, 236, 237]. The shift of this signal is therefore determined by the averaged unpaired electron density of the compound and can be used to indirectly determine the oxidation state of the transition metal cations. The introduction of extra Na^+ population in the material in the samples of 10-NaN_3 and 20-NaN_3, is coupled to a partial reduction of Mn^{4+} to Mn^{3+} and consequently to an increase in the averaged unpaired electron density in the compound. This is in agreement with the shift evolution observed in **Figure 3.8** and plotted in **Figure 3.9**. The increment in Na^+ population in the treated cathode samples is therefore demonstrated by the increments in the paramagnetic shifts similarly as observed previously in *ex-situ* NMR measurements [192]. The linear behavior observed in **Figure 3.9** suggests a regular

increment in Na^+ population, although the interrelation of NMR shifts and populations is not necessary linear due to the increments in the interlayered spaces coupled to the inclusion of Na^+ population.

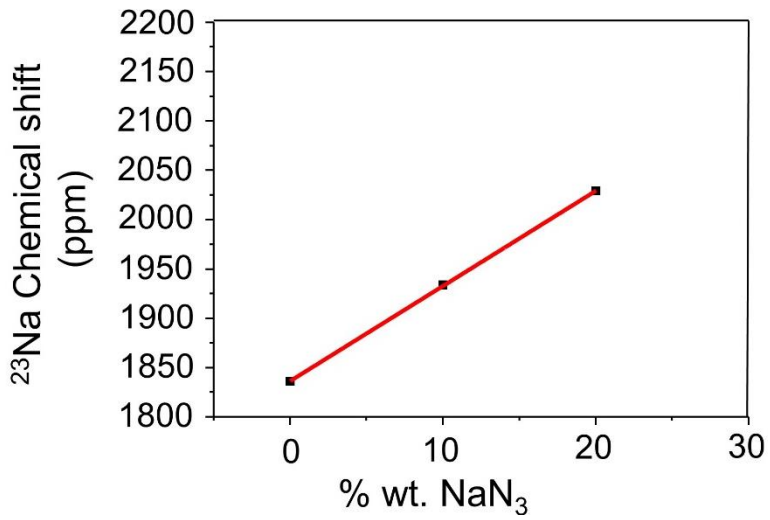

Figure 3.9. ^{23}Na chemical shift as a function of the cathode NaN_3 content.

3.5 Effect of the use of $Na_2C_4O_4$ as sacrificial salt

3.5.1 Electrochemical performance

As an alternative to NaN_3, $Na_2C_4O_4$ was also studied as a candidate to be used as a sacrificial salt. P2-$Na_{0.67}Fe_{0.5}Mn_{0.5}O_2$ cathode with different amounts of sacrificial salt (0, 16, 23 and 31%) was assembled in full-cell configuration using hard carbon as the anode material. Cells were electrochemically tested at a constant current of 15 mA g^{-1}_{AMcat} in the voltage range between 1 and 4.1 V. **Figure 3.10** (a) shows the 1st galvanostatic charge and discharge curve for each cathode composition. The graph clearly shows that the capacity increases when increasing the amount of sacrificial salt in the cathode, being the first charge capacities 101 mAh g^{-1}, 131 mAh g^{-1}, 162 mAh g^{-1} and 185 mAh g^{-1} for 0-$Na_2C_4O_4$, 16-$Na_2C_4O_4$, 23-$Na_2C_4O_4$ and 31-$Na_2C_4O_4$, respectively.

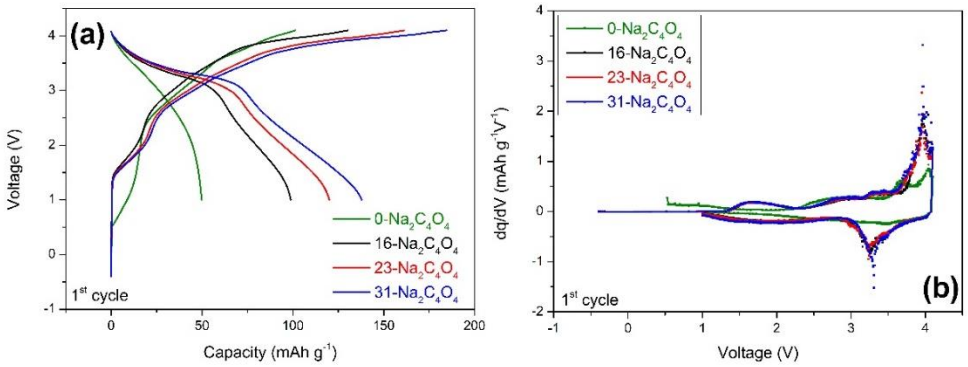

Figure 3.10. (a) 1st galvanostatic cycling profiles and (b) differential capacity curves of 0-$Na_2C_4O_4$, 16-$Na_2C_4O_4$, 23-$Na_2C_4O_4$ and 31-$Na_2C_4O_4$ full-cells (1-4.1 V).

Differential capacity curves of the 1st cycle (**Figure 3.10** (b)) have also been analyzed in order to explain the different activity of the transition metals of the active material as a function of the $Na_2C_4O_4$ content. A broad oxidation peak is observed between 2.5-3.5 V for 0-$Na_2C_4O_4$, which corresponds to the Mn^{+3} oxidation. The redox peak at higher voltages, 3.5 - 4.0 V, is associated to the $Fe^{+3/+4}$ redox process. When adding 16%, 23% and 31% of $Na_2C_4O_4$, the broad oxidation peak, observed for 0-$Na_2C_4O_4$ between 2.5-3.5 V, shifts to lower voltages. Moreover, a clear broad reduction peak attributed to Mn^{+4} appears between 1-2 V. This happens due to the fact that more sodium ions are inserted back during the discharge due to the presence of the sacrificial salt. In addition to this, a redox peak attributed to $Fe^{+3/+4}$ can clearly be observed as a consequence of the activity of the iron.

The cycling stability of the full-cells without any sacrificial salt (0-$Na_2C_4O_4$) and those with different amounts of $Na_2C_4O_4$ (16-$Na_2C_4O_4$, 23-$Na_2C_4O_4$, 31-$Na_2C_4O_4$) were evaluated at 15 mA $g^{-1}{}_{AMcat.}$ (**Figure 3.11**). Stable capacity values are obtained for all the cells after few conditioning cycles in which a progressive capacity increase is observed. The capacity values obtained after 40 cycles are 45, 100, 132 and 155 mAh g^{-1}, respectively for 0-$Na_2C_4O_4$, 16-$Na_2C_4O_4$, 23-$Na_2C_4O_4$ and 31-$Na_2C_4O_4$. Thus, the capacity values obtained with the cells having the sacrificial salt in their composition represent an improvement of more than 100% with respect to the cells without $Na_2C_4O_4$.

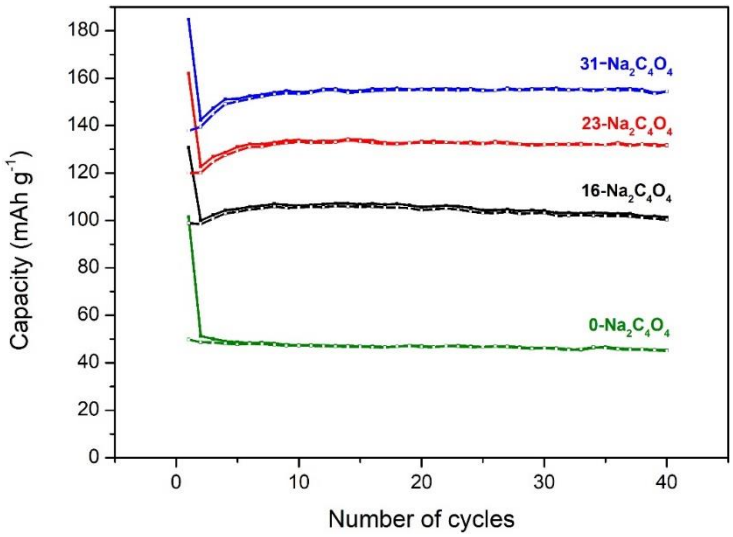

Figure 3.11. Cycling performance of 0-$Na_2C_4O_4$, 16-$Na_2C_4O_4$, 23-$Na_2C_4O_4$ and 31-$Na_2C_4O_4$ full-cells (1-4.1 V).

The amount of Na^+ ions remaining in the cathode structure were estimated to be x = 0.41, 0.44, 0.64 and 0.71 Na^+ respectively for 0-$Na_2C_4O_4$, 16-$Na_2C_4O_4$, 23-$Na_2C_4O_4$ and 31-$Na_2C_4O_4$ after 40 cycles, which agrees with the progressive increase in the delivered capacity shown in **Figure 3.11**. The cycling stability of all the cells is remarkable with capacity retention values after 40 cycles of 92.2%, 97.65% and 99.5% for 16-$Na_2C_4O_4$, 23-$Na_2C_4O_4$ and 31-$Na_2C_4O_4$, respectively (capacity retention calculated with respect to the maximum capacity, delivered in the 10th cycle).

Based on the fact that the capacity increase in the first cycles is higher for the cells with higher amount of $Na_2C_4O_4$, initial conditioning cycles are attributed to the activation of the sacrificial salt over cycling. Lower coulombic efficiencies of the initial cycles in **Figure 3.11** are also consistent with progressive sacrificial salt decomposition together with SEI formation during these initial cycles. This fact can be observed in the X-ray diffraction patterns collected after 1 and 40 cycles for 31-$Na_2C_4O_4$ (**Figure 3.12**). The $(002)_{P2}$, $(012)_{Na2C4O4}$ and $(020)_{Na2C4O4}$ peaks were fitted to Lorentz function and their full width at half maximum (FWHM) were analyzed. The ratio of FWHM between $(002)_{P2}/(012)_{Na2C4O4}$ and $(002)_{P2}/(020)_{Na2C4O4}$ are shown in **Table 3.1**. These ratios are higher in the 40th cycle than in the 1st one, which indicates a decrease in the height of the reflection peaks corresponding to $Na_2C_4O_4$ with respect to that of the active material and

consequently, a lower amount of sacrificial salt remaining in the electrode after 40 cycles than after the first cycle.

Table 3.1. Ratios of FWHM of the reflection peaks corresponding to the 31-$Na_2C_4O_4$ full cell assigned to the cathode active material and $Na_2C_4O_4$ after 1 and 40 cycles.

	FWHM (°)	
Cycle	**$(002)_{P2}/(012)_{Na2C4O4}$**	**$(002)_{P2}/(020)_{Na2C4O4}$**
1st	0.099	0.059
40th	0.420	0.426

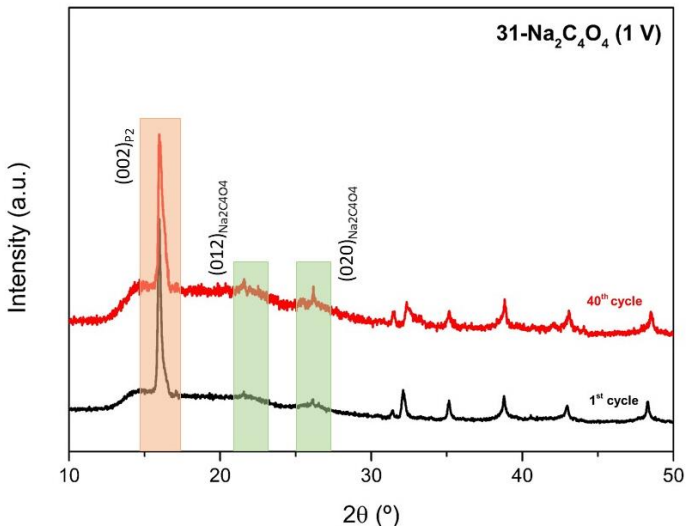

Figure 3.12. *Ex-situ* X-ray diffractograms of 31-$Na_2C_4O_4$ cathodes at 1st and 40th cycle at fully discharged state (1 V). The $(002)_{P2}$, $(012)_{Na2C4O4}$ and $(020)_{Na2C4O4}$ peaks are highlighted in orange and green.

3.5.2 Post-test morphological and structural analysis

Microstructural analysis of the cycled cathodes was performed by SEM. Images corresponding to the cathodes from 0-$Na_2C_4O_4$, 16-$Na_2C_4O_4$, 23-$Na_2C_4O_4$ and 31-$Na_2C_4O_4$ taken after 40 cycles were analyzed to evaluate the influence of the sacrificial salt in the electrode microstructure. It is expected that due to the decomposition reaction of $Na_2C_4O_4$, which forms CO_2 (gas) in addition to C, an increase in porosity will be observed as the amount of $Na_2C_4O_4$ increases. This hypothesis was confirmed by the SEM images in **Figure 3.13** which reveals that porosity is higher for the

cathodes with higher $Na_2C_4O_4$ content. Different from **Figure 3.13** (a), in which the microstructure of the cathode with no sacrificial salt is shown, (**Figure 3.13** (b – d)) show that well dispersed pores are formed in the cathode microstructure as a consequence of the decomposition of the sacrificial salt during the electrochemical reaction.

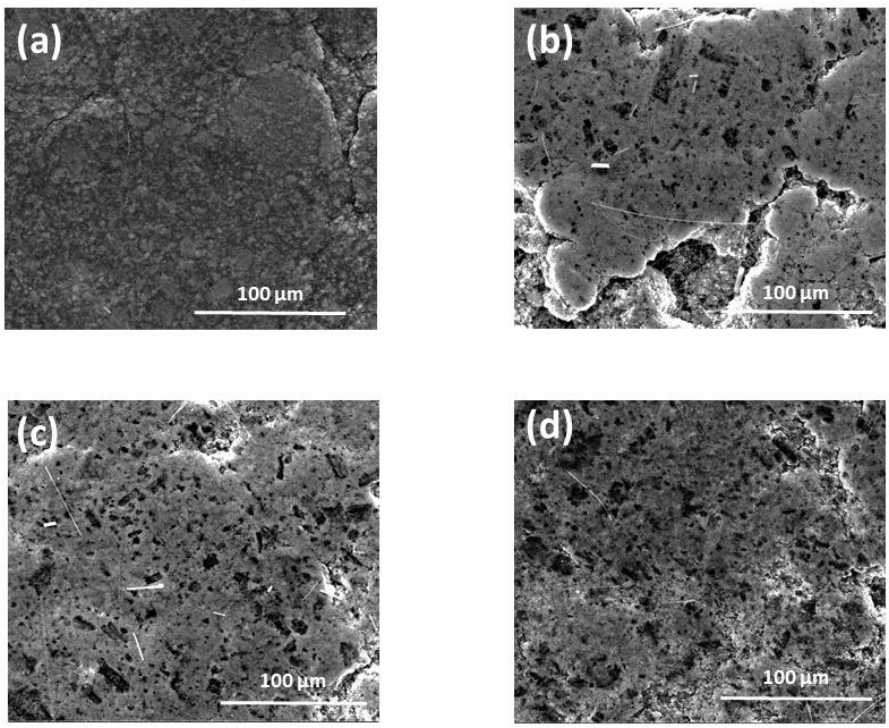

Figure 3.13. SEM pictures of the fully discharged cathodes from (a) 0-$Na_2C_4O_4$ (b) 16-$Na_2C_4O_4$ (c) 23-$Na_2C_4O_4$ and (d) 31-$Na_2C_4O_4$ of $Na_2C_4O_4$ after 40 cycles using full-cell configuration.

Figure 3.14 shows the X-ray diffraction patterns of the fully discharged cathodes together with the diffraction pattern of the pristine powder. Focusing in the 2θ range between 14-18° (**Figure 3.14** (b)), it can be observed that the increase of the amount of $Na_2C_2O_4$ in the cathodes leads to a shift of the (002) peak towards higher 2θ angles, which is consequent with the higher level of sodiation expected for the cathodes with higher salt content [192,126].

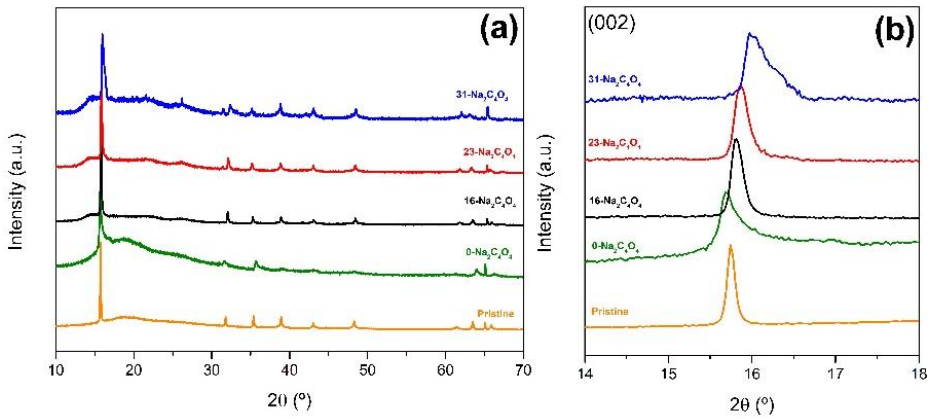

Figure 3.14. (a) *Ex-situ* X-ray diffractograms of pristine $Na_{0.67}Fe_{0.5}Mn_{0.5}O_2$ and fully discharged cathodes of 0-$Na_2C_4O_4$, 16-$Na_2C_4O_4$, 23-$Na_2C_4O_4$ and 31-$Na_2C_4O_4$full-cells. (b) Detail of the diffraction pattern between 14-18˚.

3.5.3 *Ex-situ* morphological and structural analysis of 31-$Na_2C_4O_4$

The electrodes with 31% of $Na_2C_4O_4$ were selected to perform a more detailed *ex-situ* morphological and structural analysis as more evident changes are expected due to their higher amount of the oxosalt. Since the morphological changes that may happen during the 1st charge and discharge process are expected to be similar at half-cell and full-cell level, *ex-situ* SEM study was performed using half-cells (**Figure 3.15**).

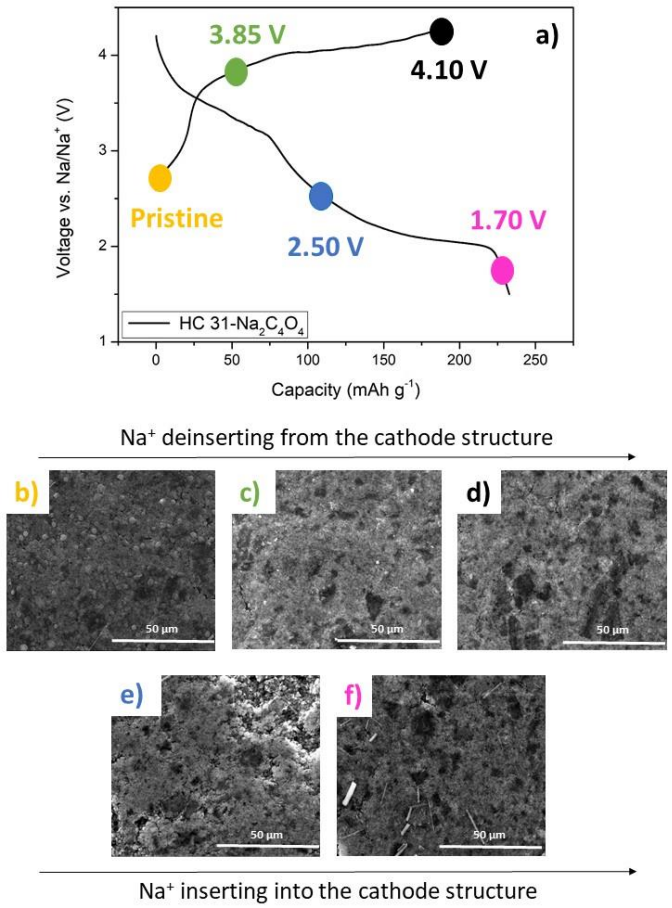

Figure 3.15. (a) 1st galvanostatic charge and discharge curves of Na/31-$Na_2C_4O_4$ halfcell. The voltages at which the charge/discharge experiments were stopped for ex-situ SEM analysis are marked. SEM pictures of the (b) pristine and (c-f) cycled 31-$Na_2C_4O_4$ cathode using half-cell configuration. Images during the 1st charge process at (c) 3.85 V and (d) 4.1 V and during the 1st discharge process at (e) 2.5 V and (f) 1.7 V.

SEM images were collected from pristine (**Figure 3.15** (b)) and cycled (**Figure 3.15** (c - f)) 31-$Na_2C_4O_4$ cathodes at different stages of the first charge/discharge process according to the voltage profile in **Figure 3.15** (a). In **Figure 3.15** (b) the microstructure of the pristine cathode composite, before being cycled, can be observed. The image shows the presence of the $Na_2C_4O_4$ salt as lighter color spheres of approximately 2 µm, well spread all over the surface of the electrode. Once the electrochemical reaction starts, the voids created due to the decomposition of $Na_2C_4O_4$ are visible (**Figure 3.15** (c - f)). During the charge process, as the voltage increases the amount of pores increases too and the desodiated cathode at the end of charge presents larger

voids in its surface (**Figure 3.15** (d)). During the discharge process, no remarkable differences related to the formation of voids are observed (**Figure 3.15** (e - f)).

Ex-situ XRD measurements of the 31-$Na_2C_4O_4$ cathode at selected voltages (i.e. different state of charge) of the 1st discharge at full-cell configuration were recorded in order to study the effect of the addition of the sacrificial salt to the sodium deinsertion/insertion mechanisms. **Figure 3.16** (a) shows the first discharge curve where the selected voltages (1) 4.1 V (fully charged cell), (2) 3.5 V, (3) 2.3 V and (4) 1.0 V (fully discharged cell) are highlighted. The capacity values at each selected voltage are (1) 236 (1st charge capacity), (2) 23, (3) 83 and (4) 175 mAh g^{-1} (1st discharge capacity). Based on the capacity values at each selected voltage, the amount of Na^+ ions in the cathode per formula unit (x) were estimated doing the same assumptions as those described before in section 3.4.1 for NaN_3 cyclability tests. According to this, the amount of Na^+ per formula unit is 0.28, 0.36, 0.60 and 0.95 Na^+ at 4.1 V, 3.5 V, 2.3 V and 1 V, respectively.

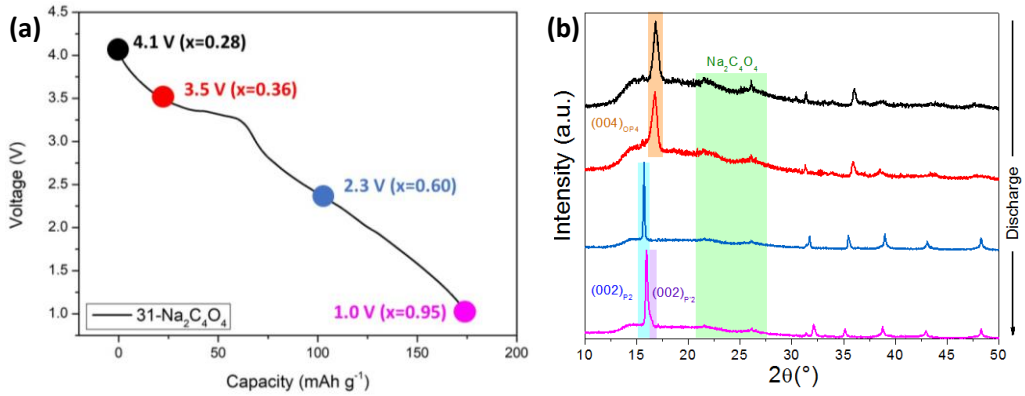

Figure 3.16. (a) 1st galvanostatic discharge curve of the 31-$Na_2C_4O_4$ full-cell and (b) ex-situ XRD patterns at selected voltages.

Figure 3.17 shows the Le Bail refinement for the 31-$Na_2C_4O_4$ cathode at OCV, which clearly shows that the phase can be indexed to the P2-$Na_xFe_{0.5}Mn_{0.5}O_2$. The extra peaks observed are attributed to the oxosalt and the aluminum foil. The XRD recorded at 4.1 V (**Figure 3.16** (b)), can be indexed to a well-known OP4-type structure (characteristic $(004)_{OP4}$ peak highlighted in orange in **Figure 3.16** (b)). This phase transition from P2 to OP4, is due to the gliding of the MO_2 layers, as it has been previously reported [84,192]. During the discharge, at 3.5 V, the OP4 phase

is still observed, as it was expected (characteristic $(004)_{OP4}$ peak highlighted in orange in **Figure 3.16** (b)). The P2-OP4 transition is highly reversible; this fact is well observed at 2.3 V, where the *ex-situ* XRD recorded corresponds to a P2 phase (characteristic $(002)_{P2}$ peak highlighted in orange in **Figure 3.16** (b)). Once the cathode is fully discharged at 1 V, the expected coexistence between P2-type hexagonal and orthorhombic *Cmcm* phase [224,126] is observed (characteristic $(002)_{P2}$ and $(002)_{P'2}$ peaks highlighted in blue and pink in **Figure 3.16** (b)). *Ex-situ* XRD measurements corroborated that the sodium insertion mechanism during the discharge is not affected by the addition of $Na_2C_2O_4$.

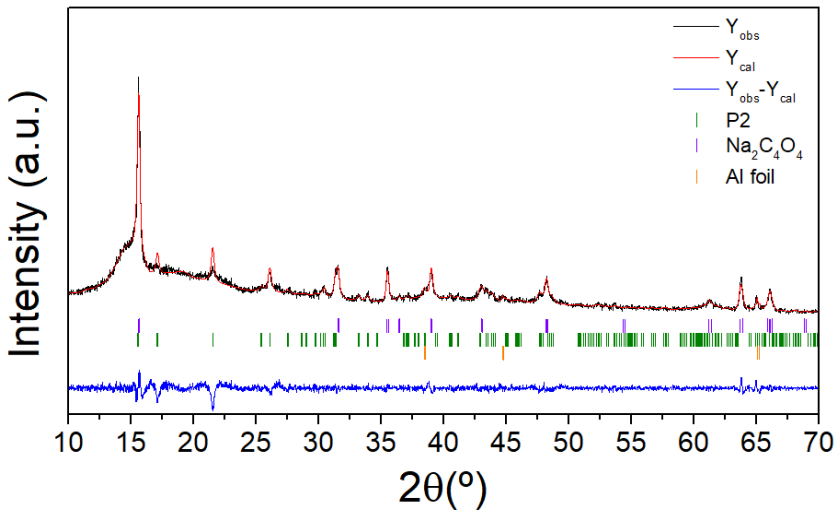

Figure 3.17. Le Bail refinement of the XRD pattern of the 31-$Na_2C_4O_4$ cathode at OCV.

3.6 Comparative of NaN_3 and $Na_2C_4O_4$ as sacrificial salts

Further insight is provided as a comparison between the use of $Na_2C_4O_4$ and NaN_3 as sacrificial salts in a Na-ion full-cell with $Na_{0.67}Fe_{0.5}Mn_{0.5}O_2$ as a sodium deficient layered oxide cathode. Cycling performance graph indicates that $Na_2C_4O_4$-containing full-cells show in general terms, better capacity values after 40 cycles than those containing NaN_3. Reversible capacities after 40 cycles delivered by the NaN_3 containing full-cells are 101, 103 and 147 mAh g^{-1} for 10-NaN_3, 15-NaN_3 and 20-NaN_3, respectively as mentioned in the section 3.4.1 of this document. While the

capacity delivered by the full-cell containing 16-$Na_2C_4O_4$ is similar to that containing 10-NaN_3, an increment of 22% and 5% of is observed for the cells with 23-$Na_2C_4O_4$ and 31-$Na_2C_4O_4$ compared to 15-NaN_3 and 20-NaN_3, respectively.

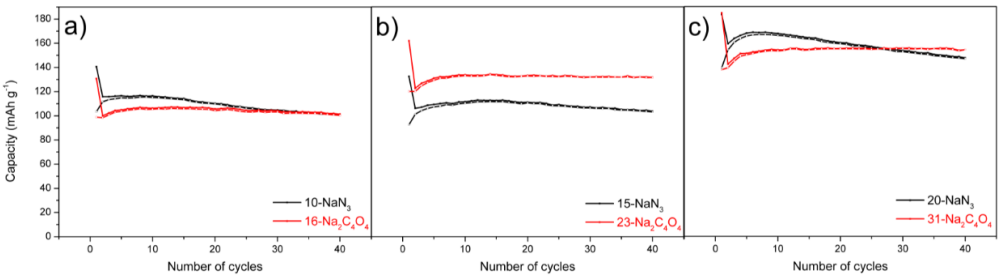

Figure 3.18. Cycling performance of (a) 10-NaN_3 and 16-$Na_2C_4O_4$, (b) 15-NaN_3 and 23-$Na_2C_4O_4$ and (c) 20-NaN_3 and 31-$Na_2C_4O_4$ full-cells.

Another advantage associated to the use of $Na_2C_4O_4$ instead of NaN_3 is the cycling stability. While all the $Na_2C_4O_4$ containing full-cells show a highly stable cycling performance after initial conditioning cycles, capacity fade is observed in NaN_3 containing full-cells. The reason for such a difference in the cycling behavior can be related to the electrode microstructure obtained depending on the selected sacrificial salt. SEM images in **Figure 3.19**, **Figure 3.20** and **Figure 3.21** show that there is an evident difference in the type of voids created when both the sacrificial salts are electrochemically decomposed. The amount of pores increases with the salt content independent of using NaN_3 or $Na_2C_4O_4$. However, smaller and better distributed holes can be observed in the microstructure of the cathode when $Na_2C_4O_4$ is used as the sacrificial salt. The approximate size of the voids formed when NaN_3 is used is 30 µm, while the size decreases to below 10 µm when $Na_2C_4O_4$ is used. This could explain the improvement in the cycling stability.

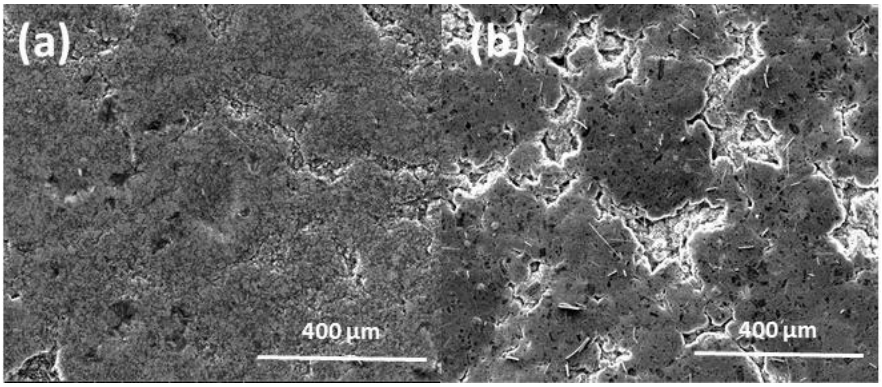

Figure 3.19. SEM pictures of the fully discharged cathodes from (a) 10-NaN_3 and (b) 16-$Na_2C_4O_4$ after 40 cycles using full-cell configuration.

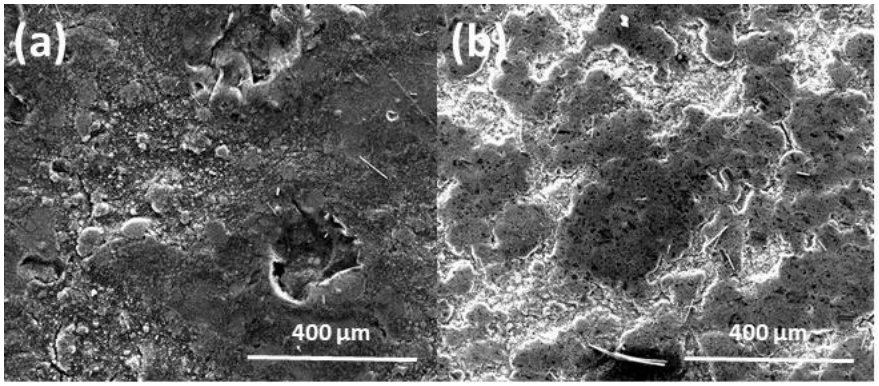

Figure 3.20. SEM pictures of the fully discharged cathodes from (a) 15-NaN_3 and (b) 23-$Na_2C_4O_4$ after 40 cycles using full-cell configuration.

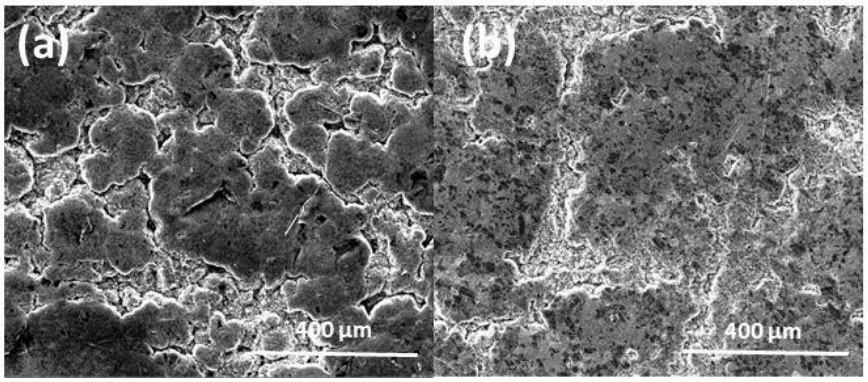

Figure 3.21. SEM pictures of the fully discharged cathodes from (a) 20-NaN_3 and (b) 31-$Na_2C_4O_4$ after 40 cycles using full-cell configuration.

The energy density of the full-cells was calculated taking into account the mass of the active materials (anode and cathode) and the sacrificial salt remaining in the cells after the electrochemical decomposition of the corresponding salt. The mass of the N_2 and CO_2 which are formed in the decomposition reaction were not considered to make the calculation since it is expected that in a pouch cell they will be extracted during the degassing step of the cell fabrication. However, the contribution of the carbon formed as the decomposition product of $Na_2C_4O_4$, was taken into account. Apart from that, as the less favorable scenario, it was considered that the salt decomposition reaction only happened during the first charge process in order to simplify calculations. The amount of salt that remained unreacted was calculated taking into account that independently of the amount and composition of the sacrificial salt, the capacity delivered by the active material in the first charge is the same as that delivered by the cell with no sacrificial salt (101 mAh g^{-1}); therefore, the additional capacity delivered by the cells is due to the decomposition of the sacrificial salt. The capacity and cell voltage in the 40th cycle were used for the calculations. **Table 3.2** summarizes the energy density values obtained for the cells with NaN_3 and $Na_2C_4O_4$, which range from ca. 126 to 165 Wh kg^{-1} as a function of the amount of sacrificial salt. Moreover, similar energy density values are obtained for the 10-NaN_3/16-$Na_2C_4O_4$ and 20-NaN_3/31-$Na_2C_4O_4$ cell pairs.

Table 3.2. Energy density calculated for 16-$Na_2C_4O_4$, 23-$Na_2C_4O_4$, 31-$Na_2C_4O_4$, 10-NaN_3, 15-NaN_3 and 20-NaN_3

Full-cell	Energy density (Wh kg^{-1})	Full-cell	Energy density (Wh kg^{-1})
10-NaN_3	128	**16- $Na_2C_4O_4$**	126
15-NaN_3	124	**23- $Na_2C_4O_4$**	144
20-NaN_3	162	**31- $Na_2C_4O_4$**	165

3.7 Conclusions

It has been demonstrated that NaN_3 and $Na_2C_4O_4$ can be used as sacrificial salts in order to compensate the Na deficiency of P2-type sodium layered oxides. By means of *ex-situ* SEM, XRD and NMR analysis, it has been proved that NaN_3 and $Na_2C_4O_4$ electrochemically decompose in the voltage range of interest (ca. 3.5-4.1 V) and that generated Na^+ ions are able to insert back in the cathode structure during the cell discharge process. A progressive increment of the reversible capacity is observed with the addition of the two sacrificial salts. However, more stable cycling behavior is observed when $Na_2C_4O_4$ is used. This fact was attributed to the better microstructure that is generated in the $Na_2C_4O_4$ containing cells once the salt is electrochemically decomposed. In conclusion, although similar energy density values are obtained after 40 cycles for the two sacrificial salt options, $Na_2C_4O_4$ represents a safer and more cost-effective solution than NaN_3 to compensate the Na deficiency of P2-type layered oxides.

Chapter 4. $Na_{1-\delta}Ni_{0.32}Ti_{0.32}Mg_{0.16}Mn_{0.20}O_2$ as cathode active material for SIBs

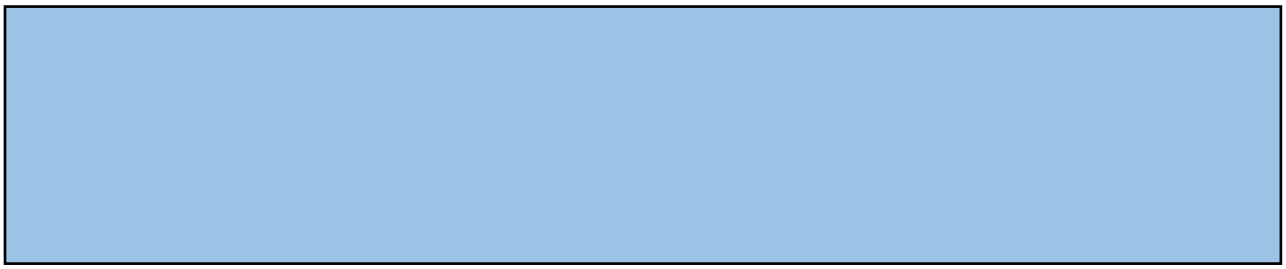

In this chapter, $Na_{1-\delta}Ni_{0.32}Ti_{0.32}Mg_{0.16}Mn_{0.20}O_2$ is evaluated as the cathode active material for Na-ion battery. First of all, synthesis parameters such as calcination time and temperature and precursors mixing/grinding media are optimized with the aim of minimizing the amount of $Mg_{1-x}Ni_xO$ impurities. Once the pure material is obtained, basic formulation studies are performed at half-cell level to assess the viability of the compound using electrodes which are more similar in terms of active material and conductive additive/binder contents to those suitable for high energy density cells. Finally, full-cells are assembled and mass balance studies are performed to evaluate the feasibility of the hard carbon // $Na_{1-\delta}Ni_{0.32}Ti_{0.32}Mg_{0.16}Mn_{0.20}O_2$ Na-ion battery system, which could be used as the bases for further studies towards pouch cell fabrication.

4.1 Optimization of $Na_{1-\delta}Ni_{0.32}Ti_{0.32}Mg_{0.16}Mn_{0.20}O_2$ synthesis conditions

$Na_{1-\delta}Ni_{0.32}Ti_{0.32}Mg_{0.16}Mn_{0.20}O_2$ was synthesized by conventional solid state synthesis route using the stoichiometric amounts of the following precursors, Na_2CO_3 (99.5%, Sigma Aldrich), NiO (Ni 78.5%, Alfa Aesar), TiO_2 (99.9%, Alfa Aesar), MgO (99%, Alfa Aesar) and MnO_2 (98%, Alfa Aesar). Based on what reported by Barker et al., as a strategy to minimize the formation of NiO of impurities, the amount of Na_2CO_3 was fixed to synthesize $Na_{1-\delta}Ni_{0.32}Ti_{0.32}Mg_{0.16}Mn_{0.20}O_2$, being 1-$\delta$ = 0.95 [93]. Several calcination conditions were tested in this work and precursors were mixed by dry and wet ball-milling (Pulverisette 5) in ethanol. 5 mm diameter ZrO_2 balls were used in the mixing/milling process and balls to powder mass ratio was fixed at 30:1. Ball-milling parameters such as speed and time were set at 300 rpm and 45 minutes, respectively.

The powder mixtures were compressed in the form of pellets using a uniaxial press (Specac) under a load of 4 ton in^{-2} and the pellets were calcined in a box furnace at 900, 1000, 1050 °C. Lower calcination temperatures were discarded in order to ensure the formation of the crystalline grains. On the other hand, calcination temperature was limited to 1050 °C to avoid undesired reactivity of the precursors with the alumina crucibles. After the calcination in air, the reaction products were quenched in air and stored in an Ar filled glove box (< 0.5 ppm H_2O and O_2) in order to avoid any moisture contamination. **Table 4.1** summarizes the synthesis conditions used in this work.

Table 4.1. $Na_{1-\delta}Ni_{0.32}Ti_{0.32}Mg_{0.16}Mn_{0.20}O_2$ synthesis conditions.

Calcination temperature (°C)	Calcination time (h)	Ball-milling media
1050	12	Dry
1000	12	Dry
1000	12	Ethanol
900	8	Ethanol

Figure 4.1 shows the Le Bail refinement of the material calcined at 1050 °C for 12 h. The well-defined peak at 2θ = 16 ° indicates the formation of crystalline grains under these synthesis conditions. As Xie et al. explained, at high calcination temperatures, cathode materials are expected to exhibit sharp diffraction peaks associated to the high crystallinity of the compounds [[238]]. Most of the peaks can be indexed to a rhombohedral *R*3*m* space group symmetry corresponding to the α-$NaFeO_2$ O3-type structure.

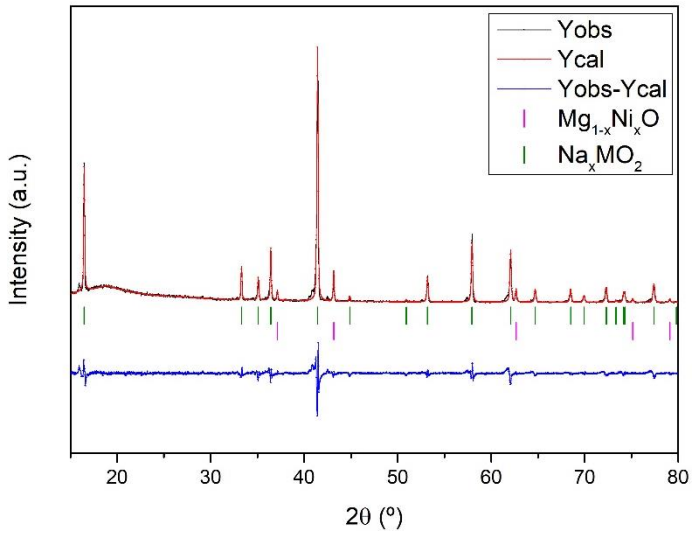

Figure 4.1. Le Bail refinement of the diffraction pattern of $Na_{1-\delta}Ni_{0.32}Ti_{0.32}Mg_{0.16}Mn_{0.20}O_2$ calcined at 1050 °C for 12 hours.

The diffraction pattern in **Figure 4.1** also shows the presence of some impurities with a cubic space group of *Fm*3*m*. Similar impurities were identified as a mixture of NiO and MgO in an earlier publication by Keller et al. [[80]]. Both compounds were used as precursors for the synthesis of this layered oxide, therefore the same impurity could have been formed. NiO and MgO have cubic space group of *Fm*3*m*; however, they differ in their lattice parameters, being *a* = 4.177 Å [[239]] in the case of NiO and 4.212 Å in the case of MgO [[240]]. The lattice parameter of the impurity detected in this synthesis is 4.187 Å. Therefore, according to Vegard's law, the composition of the impurity was identified as $Mg_{1-x}Ni_xO$, being x = 0.285.

It is important to obtain a pure phase of the active material in order to ensure an optimal electrochemical performance [93]. In order to reduce the $Mg_{1-x}Ni_xO$ impurity, calcination temperature was reduced to 1000 °C. The XRD pattern of the material refined by Le Bail method in **Figure 4.2** clearly shows that the intensities of the peaks attributed to the impurity are significantly reduced when decreasing the calcination temperature from 1050 to 1000 °C.

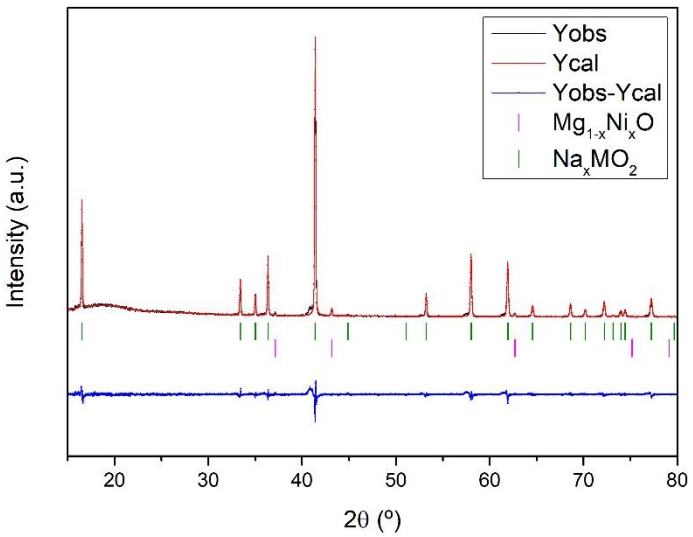

Figure 4.2. Le Bail refinement of the diffraction pattern of $Na_{1-\delta}Ni_{0.32}Ti_{0.32}Mg_{0.16}Mn_{0.20}O_2$ calcined at 1000 °C for 12 hours.

As an alternative to the dry ball-milling mixing procedure, the effect of performing this ball milling step in ethanol was also analyzed. According to the XRD pattern shown in **Figure 4.3** the intensity of the $Mg_{1-x}Ni_xO$ peaks comparatively decreased with respect to the peaks shown in **Figure 4.2**, indicating that the amount of impurities is further reduced when performing the precursor mixing by wet ball-milling in ethanol.

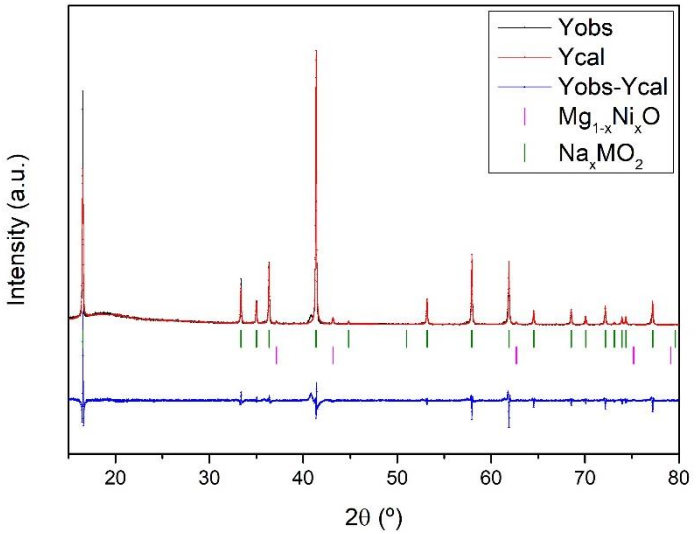

Figure 4.3. Le Bail refinement of the diffraction pattern of $Na_{1-\delta}Ni_{0.32}Ti_{0.32}Mg_{0.16}Mn_{0.20}O_2$ calcined at 1000 °C for 12 hours. Precursors mixing performed by wet ball milling in ethanol.

As it has been observed that ethanol helps to remove in further extent the $Mg_{1-x}Ni_xO$ impurities, with the aim of reducing the calcination time and temperature a new synthesis was carried out at 900 °C for 8 h. **Figure 4.4** shows the Le Bail refinement of the diffraction pattern of the resulting material. The amount of Impurities of the cubic phase was calculated by means of Rietveld refinement which was 1.64% compared to 6.23% when the synthesis was performed at 1050 °C for 12 hours and the mixing of the precursors was performed by dry ball milling. The material synthesized using the last synthesis conditions was selected for further analysis in this Thesis.

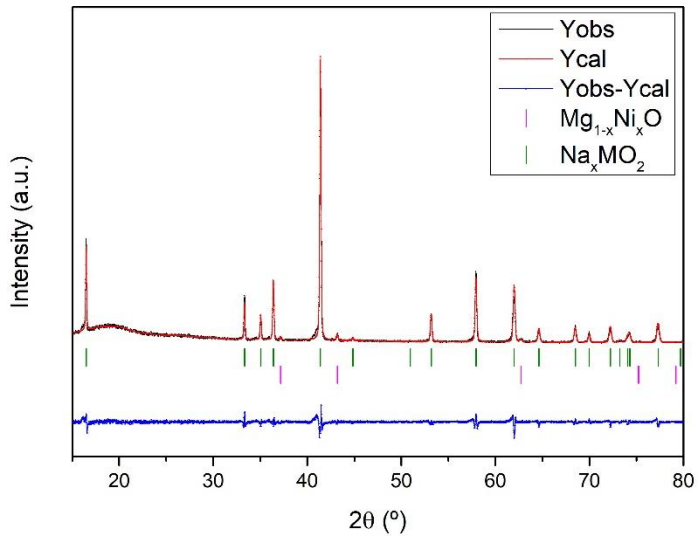

Figure 4.4. Le Bail refinement of the diffraction pattern of $Na_{1-\delta}Ni_{0.32}Ti_{0.32}Mg_{0.16}Mn_{0.20}O_2$ calcined at 900 °C for 8 hours. Precursors mixed by wet ball milling in ethanol.

The lattice parameters calculated by Le Bail refinement are gathered in **Table 4.2**. These data were analyzed in order to observe any variation that could happen in the crystal structure of the samples due to the variations of the synthesis conditions. The diffraction patterns of the four compounds synthesized at different conditions are indexed as O3-type structures with a space group of *R*3*m*.

Table 4.2. Summary of the lattice parameters calculated for the different synthesis conditions.

Calcination temperature (°C)	**Calcination time (h)**	**Ball-milling media**	**Active material lattice parameters (*a*=*b*; Å)**	**Active material lattice parameters (*c*; Å)**	**$Mg_{1-x}Ni_xO$, lattice parameters (*a*=*b*=*c*; Å)**
1050	12	Dry	2.98759(7)	16.1281(6)	4.1893(2)
1000	12	Dry	2.99453(4)	16.0771(3)	4.1884(2)
1000	12	Ethanol	2.99571(4)	16.1002(4)	4.1884(3)
900	8	Ethanol	2.99135(5)	16.1198(4)	4.1866(3)

As reported by Nguyen et al. [83], as the calcination temperature increases (i.e. from 800 to 1000 °C), the peak widths of sodium active materials become narrower and the relative intensities of the characteristic peaks gradually increase, indicating that a crystalline structure of the material is formed more perfectly. When they increased the calcination temperature in P2-type samples, the lattice parameter *a* decreased while the lattice parameter *c* slightly increased. A similar behavior is observed in our samples when the lattice parameters of the samples synthesized at 1050 °C and 1000 °C, are compared. This implies that sodium ions should be easier intercalated in the cathode structure due to the wider c-axis gap as the calcination temperature increases [83]. As expected, when the mixing of the precursors was performed by wet ball-milling, higher *c* parameter values were obtained due to the improvement of the mixing/milling process. However, the reduction of the calcination time and temperature from 1000 to 900 °C and 12 to 8 hours, respectively, surprisingly resulted in higher *c* parameter values. These differences could be caused by small differences in the Na^+ content and consequent differences in the repulsion forces between the oxide layers. The *a* parameter shows only slight changes when comparing the different synthesized materials as it is less dependent on the Na content [83].

The microstructural analysis of the active material selected for further studies was done by means of Scanning Electron Microscopy. SEM images in **Figure 4.5** show the well-defined platelet-shaped morphology typical of layered structures, characterized by a series of planes forming single particles. The average particle size of the synthesized material is close to 3 µm.

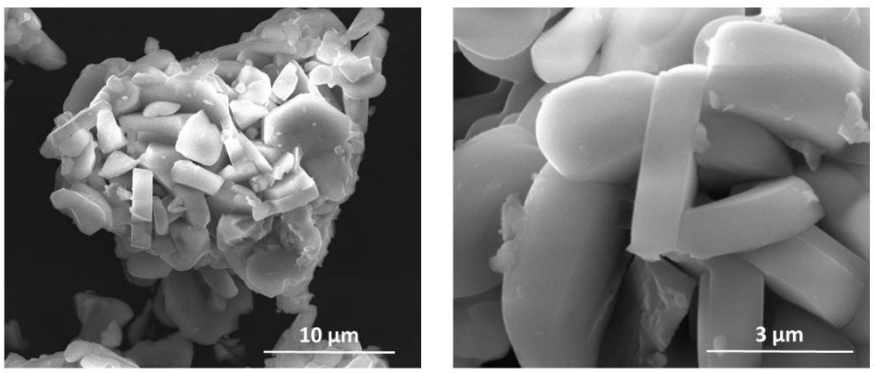

Figure 4.5. SEM images of $Na_{1-\delta}Ni_{0.32}Ti_{0.32}Mg_{0.16}Mn_{0.20}O_2$ powder calcined at 900 °C for 8 hours. Precursors mixed by wet ball-milling in ethanol.

The electrochemical performance of the compound was evaluated at room temperature using electrodes with 3 mg cm^{-2} active material loading. The details on the electrode and cell preparation procedure are provided in Chapter 2. Charge/discharge voltage profile and cycling stability for the first forty cycles are shown in **Figure 4.6** (a) and (b). Average discharge voltage of approximately 3 V has been obtained. **Figure 4.6** (a) shows an initial charge capacity of approximately 184 mAh g^{-1}, corresponding to the extraction of 0.7 Na^+ ions during initial charge to 4.3 V. During the discharge 0.53 Na^+ ions are reinserted back in the structure leading to 138 mAh g^{-1} of capacity. Therefore, first cycle irreversible capacity corresponds to 46 mAh g^{-1}.

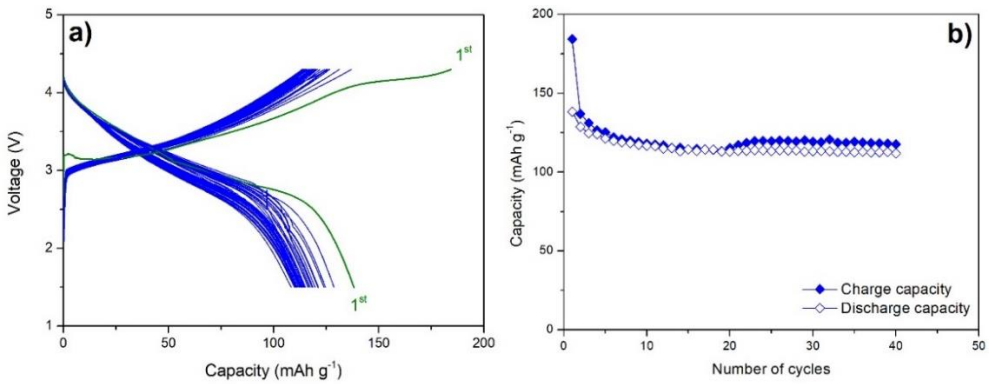

Figure 4.6. (a) Voltage profile (1st cycle is highlighted in green) and (b) cycling stability of $Na_{1-\delta}Ni_{0.32}Ti_{0.32}Mg_{0.16}Mn_{0.20}O_2$ in half-cell configuration at 15 mA g^{-1}_{AM} between 1.5-4.3 V.

The smooth voltage profile shown in **Figure 4.6** (a), without multiple plateaus, indicates that apparently no complicated structural transitions happen during sodium insertion and extraction. Also, a voltage plateau is observed at the end of the first charge which it is not observed in the further charging curves. This may be due to some irreversible structural change that occurs in the crystal structure and hence leads to some irreversible capacity in the first cycle. In the studied voltage range, between 1.5 and 4.3 V, Ni is the only redox active specie which reversibly oxidizes and reduces between Ni^{2+} and Ni^{4+} oxidation states. In this composition, Ni and Mg are included as M^{2+} while Mn and Ti are present as M^{4+} [241]. This material shows reversible capacity of approximately 110 mAh g^{-1} for 40 cycles (**Figure 4.6** (b)).

4.2 Half-cell studies on cathode formulation

Cathode half-cell studies were developed in order to optimize the cathode formulation with the aim of increasing the energy density. This initial approach consisted on increasing the active material content with respect to those electrode formulations usually prepared for initial material characterization tests, being the active material content in the range of 75-80% wt. In addition to this, the C65:PVDF ratio was also optimized. The motivation to optimize the cathode formulation is to maximize the active material content and loading to maximize the cell capacity and to balance the ratio between C65 and PVDF to have enough conductivity, optimal particle-to-particle contact and good mechanical integrity of the electrodes.

Layered oxides are poor electronic conducting compounds and they do not actively contribute to the electronic conductivity of the composite. Hence, by increasing the active material content of the electrodes, the electronic conductivity can decrease. However, as concluded by Trask et al. [242], in high-voltage positive electrodes, the amount of C65 has to be minimized, because it tends to deteriorate over cycling and it contributes to the impedance rise.

Different cathode formulations were prepared for this study. AM:C65:PVDF = 75:15:10 (wt. %) was selected as the reference formulation and these electrodes were compared to electrodes with higher active material contents, i.e. 88 and 94%w, and different C65: PVDF ratios, i.e. 0.2:1, 0.4:1, 0.6:1 and 0.8:1. Active material loadings in the range between 7 to 13 mg cm^{-2} were prepared based on these formulations. All the tested formulations are summarized in **Table 4.3**.

Table 4.3. Summary of the cathode formulations tested in this chapter.

C65:PVDF	AM content (wt. %)	AM loading (mg cm^{-2})
1.5:1	75	7
0.2:1	88	11
0.4:1		
0.6:1		
0.8:1		
0.4:1	94	13
0.6:1		

When the amount of active material is increased from 75% to 88%, significant changes are observed in the voltage profile (**Figure 4.7**) and cycling stability (**Figure 4.9** and **Figure 4.10**) of the material which evidences the importance of the optimization of the C65: PVDF ratio.

As the binder has an insulator character, an excess of this component should be avoided [167,243]. When the amount of binder in the electrode composition is too high, active material and conductive additive particles can be encased by the excess of binder, limiting the electron and ion transport and increasing the internal cell resistance. On the other hand, the particles of the conductive agent should be in contact at every spot on the surface of active particle to allowing the insertion/deinsertion of the Na^+ ions. Moreover, a minimum amount of conductive additive is needed in order to generate a percolation network [244].

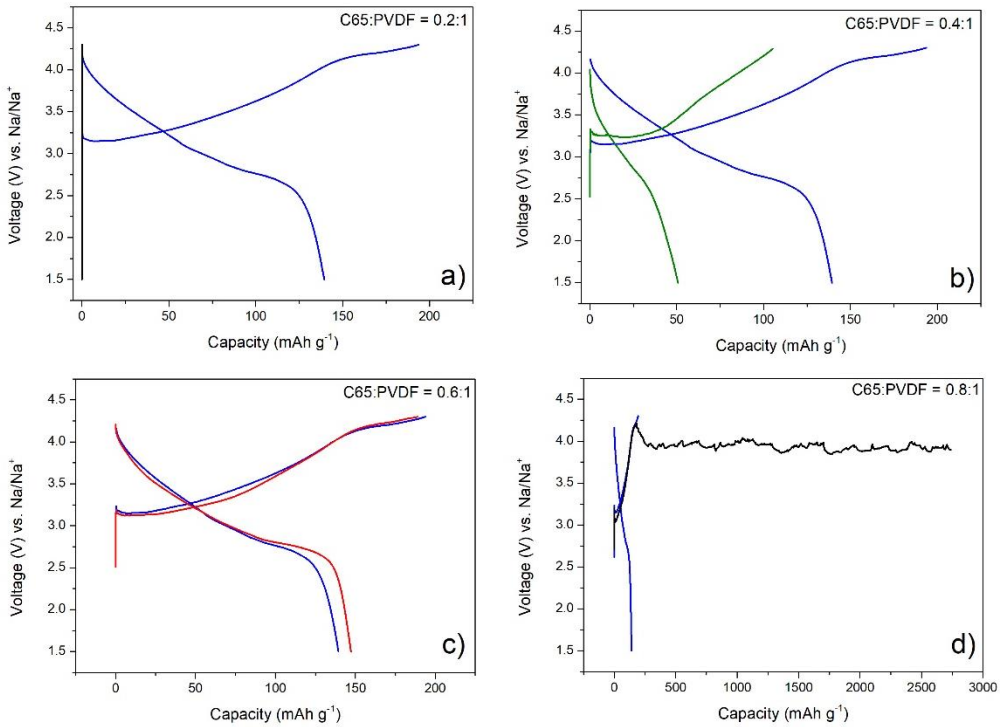

Figure 4.7. 1st galvanostatic cycle voltage profile of electrodes with 88% of active material and different C65:PVDF ratios, (a) 0.2:1, (b) 0.4:1, (c) 0.6:1 and (d) 0.8:1. The blue curves correspond to the AM:C65:PVDF = 75:15:10 reference electrodes.

The binder rich electrode with 88% AM (i.e. C65:PVDF = 0.2:1, **Figure 4.7** (a)) shows a highly resistive electrochemical performance and does not deliver any capacity in the studied voltage range. On the contrary, the electrode with high conductive additive and low binder content (i.e. C65:PVDF = 0.8:1, **Figure 4.7** (d)) shows an endless charge profile which indicates the presence of a secondary reaction that happens before reaching the cut-off voltage.

In the **Figure 4.8** (a), un-calendered SEM images of the cathode with 88% of AM and C65:PVDF = 0.2:1 can be observed. The SEM image clearly shows the lack of C65 which resulted in the poor electrochemical performance of this electrode composition.

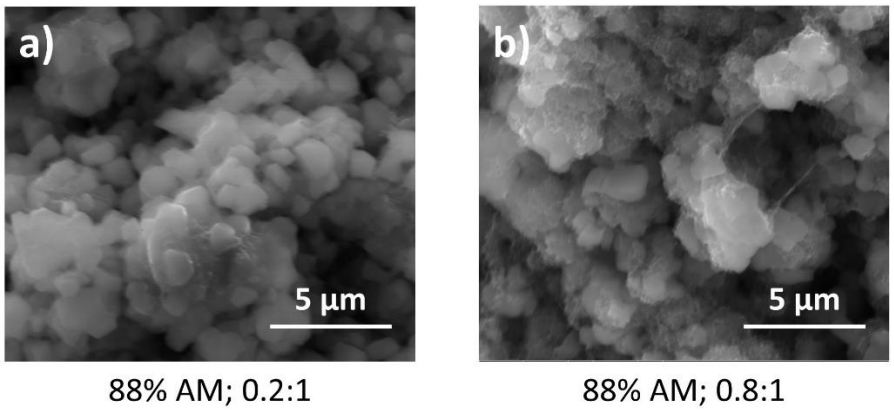

Figure 4.8. SEM images of two cathodes with 88% AM and different C65:PVDF a) 0.2:1 and b) 0.8:1.

The cause of the low electrochemical performance of the electrode with the highest conductive additive content (**Figure 4.7** (d)), i.e. C65:PVDF = 0.8:1, can be the presence of a secondary reaction that is promoted when used this particular electrode composition as it is observed in the first cycle charge curve. In addition to this, **Figure 4.8** (b) shows the presence of C65 aggregates. One would expect a maximum electronic conductivity for this electrode composition due to the high conductive additive content. However, if the amount of CB is too high, this could lead to a decrease in the conductivity due to the agglomeration of conductive additive particles, their non-homogeneous distribution in the electrode and the lack of binder that promotes that the particles are not effectively held together as reported by Zheng et al. [245].

The cell with C65:PVDF = 0.4:1 (**Figure 4.7** (b)), leads to poor first charge/discharge specific capacities (105 and 51 mAh g^{-1}, respectively) corresponding to the extraction of 0.4 Na^+ and the insertion of 0.20 Na^+ which suppose large 1st cycle irreversible capacity and low cycling stability. This poor electrochemical performance could be caused by the lack of carbon black which is still insufficient to guarantee enough electronic conductivity of the electrode. When the C65:PVDF = 0.6:1, the half-cell presents lower 1st cycle irreversible capacity (42 mAh g^{-1}) than the reference cell (54 mAh g^{-1}) (**Figure 4.7** (c)), which could be caused by the lower C65 content of the former electrode composition. The half-cell exhibits a first cycle charge capacity of 189 mAh g^{-1} corresponding to extraction of 0.72 Na^+ and during the discharge 0.56 Na^+ are reinserted back in the structure leading to 147 mAh g^{-1} discharge capacity.

Figure 4.9 represents the cycling stability of the half-cells with 88% of active material and a C65:PVDF of 0.4:1 and 0.6:1. As a reference, the cycling performance of a cell with 75% of active material and C65:PVDF = 1.5:1 is also included in the graph. Compared to the cell with C65:PVDF = 0.4:1, the increase in the C65:PVDF ratio leads to an enhancement in the cycling stability of the cell. Moreover, these electrodes show similar cycling stability than the reference cell with ~ 100 mAh g^{-1} after 40 cycles and a capacity retention close to 70%. However, the composition with 88% of AM allows to maximize the energy density due to the higher active material content of the electrode.

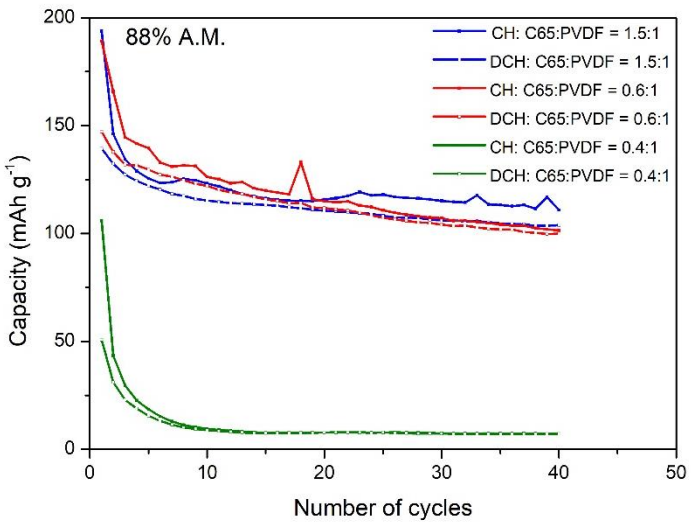

Figure 4.9. Cycling stability of the cathodes with 88% AM and C65:PVDF of 0.4:1 and 0.6:1 compared to the reference cell with 75% AM at 15 mA g^{-1}_{AMcat} between 1.5-4.3 V.

The cycling performance of the cells with 94% of AM (**Figure 4.10**) shows that the amount of inactive electrode components are clearly insufficient to ensure the correct cycling of the electrode. The half-cell with C65:PVDF = 0.4:1 does not deliver any capacity after the first cycle and even the half-cell with CB:PVDF = 0.6:1, which showed to be the best combination for an active material content of 88%, shows a capacity fade of 60% at the 15th cycle when the active material content is increased to 94%. This could have happened due to the non-homogeneous distribution of C65 and PVDF all over the electrode volume as a consequence of the low amount of these components in the electrode composition. As reported by Zheng et al. [245] mechanical

integrity failure can also be a reason for fast capacity fade because the amount of binder is not enough to create a percolation network that accommodates the volume changes that happen as a consequence of the continuous de-insertion/insertion of Na^+ ions in the active material structure and some of the particles become inactive.

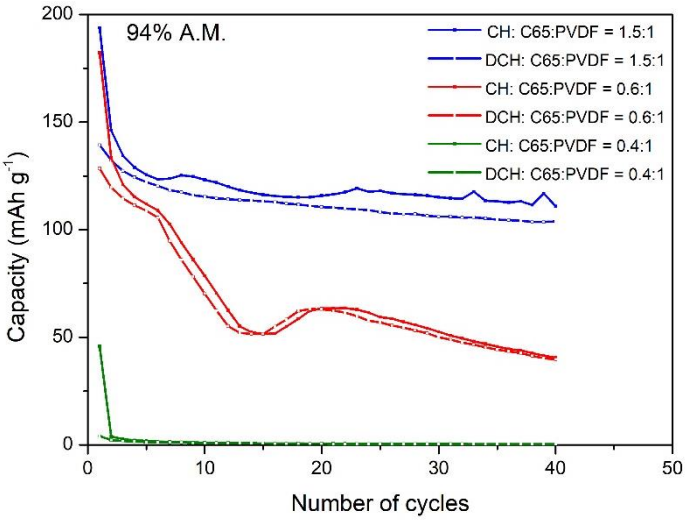

Figure 4.10. Cycling stability of the cathodes with 94% AM and C65:PVDF of 0.4:1 and 0.6:1 compared to the reference cell with 75% AM at 15 mA g^{-1}_{AM} between 1.5-4.3 V.

Figure 4.11 includes the SEM images of un-calendered electrodes to provide visual evidence of the electrode's components distribution. The difference in the microstructure of the electrodes which were analyzed is evident and it agrees with the electrochemical responses of the corresponding half-cells. Since in the images corresponding to the electrodes that exhibited good electrochemical performance (**Figure 4.11** (a) and (c)) the presence well distributed C65 particles that allowed to have sufficient conductivity and thus low internal resistance is clear, in those images corresponding to the electrodes that did not cycled properly (**Figure 4.11** (b), (d) and (e)) the active material particles are not surrounded by the conductive additive particles and consequently the internal resistance of the half-cells was too high.

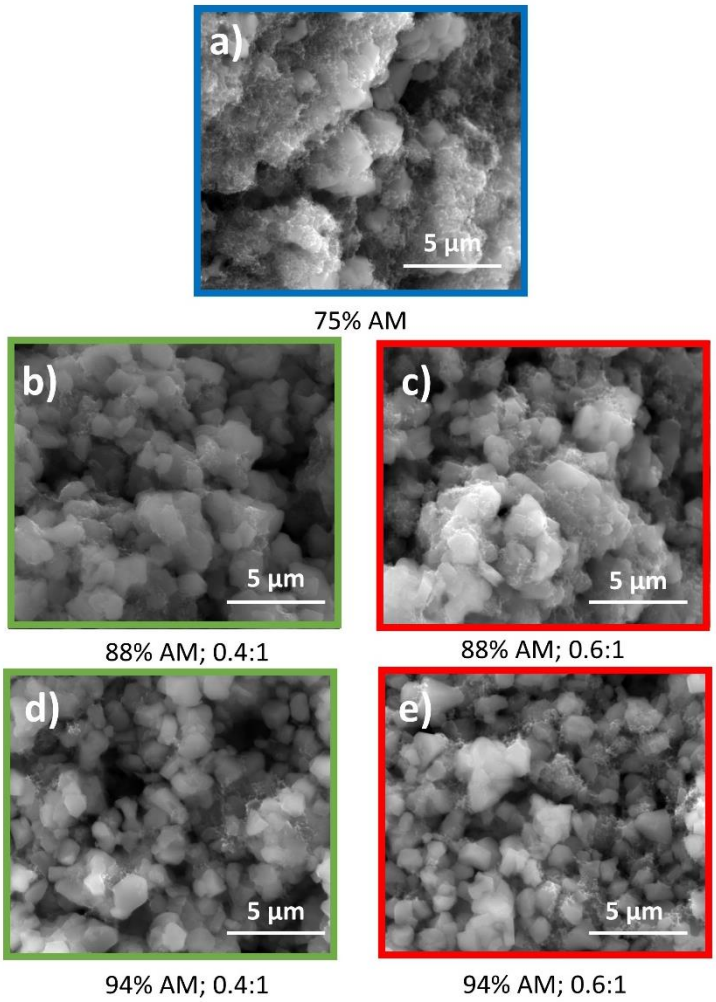

Figure 4.11. SEM images of different cathode compositions. (a) 75% of AM and C65:PVDF = 1.5:1, (b) and (c) 88% of AM and C65:PVDF = 0.4:1 and 0.6:1 and (d) and (e) 94% of AM and C65:PVDF = 0.4:1 and 0.6:1.

4.3 Full-cell studies

4.3.1 General overview

As a result of the study performed in the previous section, electrodes with 88% of active material and C65:PVDF = 0.6:1 (cathode composition of AM:C65:PVDF = 88:4.5:7.5 wt%) were selected to perform additional experiments with the aim of going one step further towards optimized full-

cell assembly. The anode selected for this study is a hard carbon, supplied by Kuraray (more details on the characteristics of this hard carbon are provided in Chapter 2. The charge/discharge reactions (4.1 and 4.2) of this cell are described below,

$$\text{Charge: } Na_xMO_2 + C \rightarrow Na_{x-y}MO_2 + Na_yC \qquad (4.1)$$

$$\text{Discharge: } Na_{x-y}MO_2 + Na_yC \rightarrow Na_{x-z}MO_2 + Na_zC \qquad (4.2)$$

where x=0.95 is the amount of Na^+ ions per formula unit when the cell is fully discharged and z is the amount of Na^+ ions consumed in the SEI formation.

The half-cell reactions on the cathode side are described below (4.3 and 4.4), and the electrochemical performance of a representative cell has already been presented in **Figure 4.6**, being the reversible capacity ca. 110 mAh g^{-1}.

$$\text{Charge: } Na_xMO_2 \rightarrow Na_{x-y}MO_2 + yNa^+ + ye^- \qquad (4.3)$$

$$\text{Discharge: } Na_{x-y}MO_2 + (y-z)Na^+ + (y-z)e^- \rightarrow Na_{x-z}MO_2 \qquad (4.4)$$

The half-cell reactions on the anode side are described below (4.5 and 4.6), and the electrochemical performance of a representative cell is shown in **Figure 4.12**, being the reversible capacity ca. 245 mAh g^{-1}.

$$\text{Charge: } C + ye^- + yNa^+ \rightarrow Na_yC \qquad (4.5)$$

$$\text{Discharge: } Na_yC \rightarrow Na_zC + (y-z)Na^+ + (y-z)e^- \qquad (4.6)$$

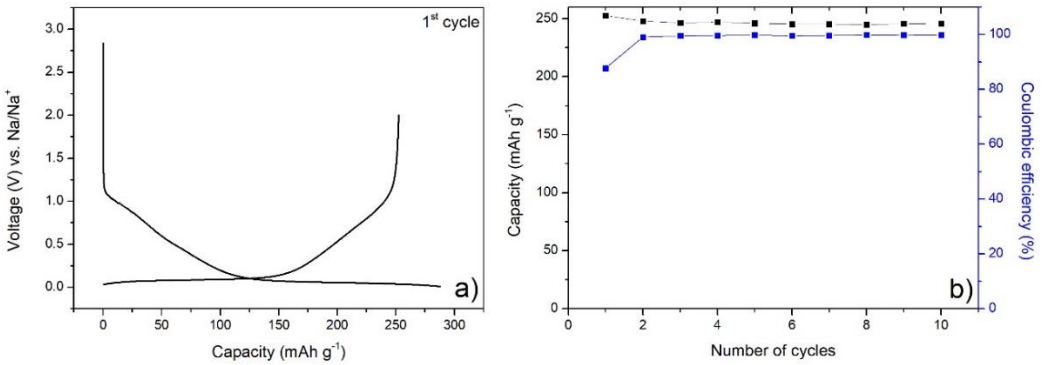

Figure 4.12. (a) 1st galvanostatic charge/discharge curve and (b) cycling stability for 10 cycles of hard carbon half-cell at 15 mA g^{-1}_{AM} in the voltage range of 0.01-2.00 V.

Since the specific capacity of the selected cathode and anode components are not the same when cycled as half-cell *versus* metallic Na, the amount of active material of the two electrodes needs to be balanced to obtain the same capacity when combined in full-cell configuration. Moreover, Na^+ ions are consumed in the SEI formation and need to be somehow compensated. Finally, to avoid the risk of Na plating, the capacity of the anode is usually oversized compared to the cathode capacity. One would expect that when the capacity of the anode is oversized the energy density would decrease, therefore, the main objectives that are pursued from electrode balancing are, on the one hand, to maximize the energy density of the cell and on the other hand, to minimize safety hazards (i.e. sodium plating in the anode). Other key points such as the voltage limits need also to be taken into account when assembling full-cells because if the upper cut-off voltage is too high, the cathode will operate above its optimum voltage range and aging of the cell will be accelerated. In addition to this, the risk of Na plating in the anode will exist.

The anode to cathode ratio of a full-cell can be defined in terms of active material mass or capacity, named as $R_{N/P}$ (AM) and $R_{N/P}$ (Q), respectively hereinafter. According to Kasnatscheew et al., [246] the $R_{N/P}$ (AM) data is more suitable compared to more usually provided $R_{N/P}$ (Q) from the perspective of better reproducibility as it contains the whole information for cell assembly. However, as it will be explained in the following sections, the active material loading also has an influence on the electrochemical performance of the electrodes. On the other hand, $R_{N/P}$ (Q) provides direct information on the capacity excess/deficiency of the electrode pairs, but the capacity of the electrodes as half-cells depends on the cycling conditions and once the mass

balance is defined for a determined current density, it should also work for different cycling rates. Consequently, $R_{N/P}$ (AM) and $R_{N/P}$ (Q) will be provided in this work in order to have a complete description of the selected mass balance.

4.3.2 Electrochemical performance of selected half-cell electrodes

In order to characterize the individual performance of selected anode/cathode components, corresponding half-cells were electrochemically tested at a cycling rate of 15 mA g^{-1}_{AM} using different active material loadings. Cathode electrodes with a composition AM:C65:PVDF = 88:4.5:7.5 and an active material loadings of ca. 6, 8 and 11 mg cm^{-2} and anode electrodes with a composition of AM:PVDF = 95:5 wt% and an active material loadings of ca. 4, 6 and 8 mg cm^{-2} were prepared as described in Chapter 2. Cathode half-cells were cycled in coin cell configuration in a voltage range between 1.5 and 4.3 V while the anode half-cells were cycled between 0.01 and 2 V. **Table 4.4** gathers the first cycle charge and discharge capacity values for cathode and anode half-cells, respectively and the reversible capacities measured at the 10^{th} cycle for different active material loading anode and cathode half-cells. Reversible capacities in the range from 230 to 248 and from 97 to 122 are obtained for the anode and the cathode, respectively.

Surprisingly, the reversible capacity of the cathode decreases with the low active material loading, most likely due to the higher first cycle irreversibility of the low loading cathodes. First charge capacity values are similar for the three different active material loadings tested, so the 1^{st} cycle irreversibility is reduced, from 62 mAh g^{-1} to 42 mAh g^{-1}, respectively from low to high active material loading cathodes. This 1^{st} irreversible capacity could be related to the SEI formation, which is larger in the case of lower active material loadings.

Table 4.4. Summary of the electrochemical performances of cathode and anode half-cells with different active material loadings at 15 mA g^{-1}_{AM}.

Cathode half-cells			Anode half-cells		
AM loading (mg cm^{-2})	**1st charge capacity (mAh g^{-1})**	**Reversible capacity* (mAh g^{-1})**	**AM loading (mg cm^{-2})**	**1st discharge capacity (mAh g^{-1})**	**Reversible capacity* (mAh g^{-1})**
6.25	180	97	3.78	288	248
8.32	185	102	6.22	274	230
10.88	188	122	7.90	275	240

*Reversible capacity measured in the 10th cycle.

As it was mentioned before, leaving aside the Na^+ ion consumption for the SEI formation and the usual anode capacity excess to avoid Na plating, the capacity of the anode and the cathode are expected to be the same for the full-cell to be balanced, that is, the amount of Na^+ ions inserted in the cathode to be the same as those de-inserted from the anode during the discharge process. In order to stablish the anode and cathode active material masses that deliver the same discharge capacity, the reversible capacity data collected in **Table 4.4** are represented in **Figure 4.13**. In the studied active material loading range, the reversible capacity increases proportionally with the loading and the equations that represent the relationship between the two parameters are displayed in **Figure 4.13**. Based on these equations, the active material loading of the cathode and anode which deliver the same capacity can be calculated by the equation 4.7.

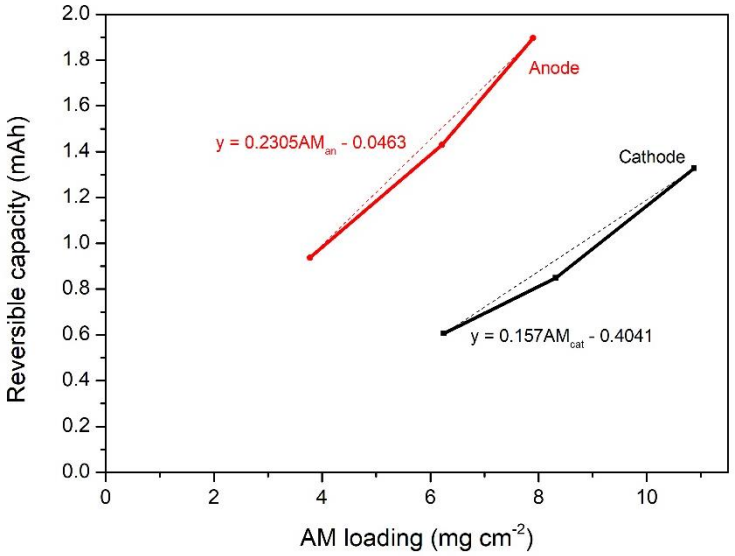

Figure 4.13. Relationship between the anode/cathode active material loading and the reversible capacity measured in the 10th cycle.

$$AM_{an} = 0.681AM_{cat} - 1.95 \qquad (4.7)$$

4.3.3 Cycling stability of full-cells

Since the electrochemical performance of the half-cell electrodes depends on the active material loading, full-cells with two different cathode active material loadings (ca. 6 and 10 mg cm^{-2}) and several anode active material loadings, i.e. several mass balances, were assembled and electrochemically tested at a cycling rate of 15 mA g^{-1}_{AMCat} in the voltage range between 1-4.2 V. The corresponding $R_{N/P}$ (Q) values for each $R_{N/P}$ (AM) are calculated on the basis of the reversible half-cell capacity values displayed in **Table 4.4**.

The cycling stability of the full-cells with a cathode active material loading of ca. 6 mg cm^{-2} and $R_{N/P}$ (Q) in the range from 1.2 to 2.6 is represented in **Figure 4.14**. The highest reversible capacity after 25 cycles (90 mAh g^{-1}_{AMCat}) is obtained when using $R_{N/P}$ (Q) = 2.1 or $R_{N/P}$ (AM) = 0.9 and $R_{N/P}$ (Q) = 2.6 or $R_{N/P}$ (AM) = 1.1 with a capacity retention of 82% and 74%, respectively. Significantly lower performances are obtained for $R_{N/P}$ (Q) = 1.7 and 1.2 with reversible capacity values of 51 and 30 mAh g^{-1}_{AMCat}, respectively, after 25 cycles. Unexpectedly high $R_{N/P}$ values show the best

cycling performances. As it has been mentioned earlier, the 1st cycle irreversible capacity is higher for low active material loading cathodes. This high 1st charge capacity needs higher amount of anode active material available to accommodate the high amount of deinserted Na^+ ions and avoiding the sodium plating in the electrode surface [247]. Consequently, the cells with low cathode active material loadings show optimum cycling performances with higher $R_{N/P}$ than usual negative to positive ratios used in the literature for Li-ion batteries, in the range between ca. 1.1-1.2 [246]. Based on this hypothesis, the low cycling performance of the cells with $R_{N/P}$ (Q) = 1.7 and 1.2 can be attributed to the sodium plating that happens when the anode operates at voltages below 0 V vs. Na/Na^+. Among the cells with $R_{N/P}$ (Q) = 2.1 and 2.6, the worse cycling performance of the later can be explained by the over-desodiation of the cathode due to excessive anode excess. As it was explained by Kasnatscheew et al., this could lead to further structural changes in the cathode active material creating a detrimental effect in the electrochemical performance, i.e. reducing cycle life of the battery. In addition to this, if there is an increase of the cathode voltage, there is a risk of further decomposition of the electrolyte [246].

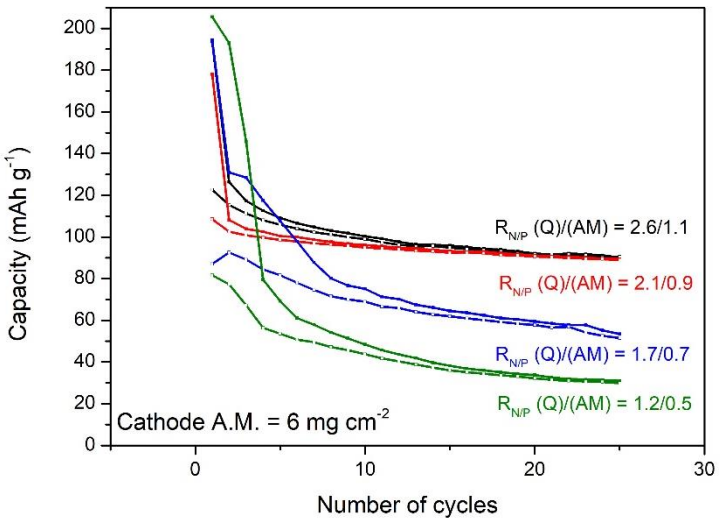

Figure 4.14. Cycling stability of full-cells with a cathode active material loading of 6 mg cm^{-2} and different mass balances (cells cycled at 15 mA g^{-1}_{AMCat}, between 1-4.2 V).

For the full-cells with a cathode active material loading of ca. 10 mg cm^{-2} (**Figure 4.15**), the highest reversible capacity after 25 cycles is obtained using $R_{N/P}$ (Q) = 1.6 (114 mAh g^{-1}_{AMCat} with a capacity retention of 82%). Similar cycling performance is obtained when $R_{N/P}$ (Q) = 1.8, while the performance is worse for $R_{N/P}$ (Q) = 1.2, being the reversible capacity and the capacity retention 100 mAh g^{-1}_{AMCat} and 78%, respectively, after 25 cycles. In this case, lower $R_{N/P}$ (Q) values compared to those that are the optimum for lower cathode active material loadings, show the best electrochemical performances since the 1st cycle irreversible capacity of the cathode is lower, and consequently, the required oversizing of the anode is not that high.

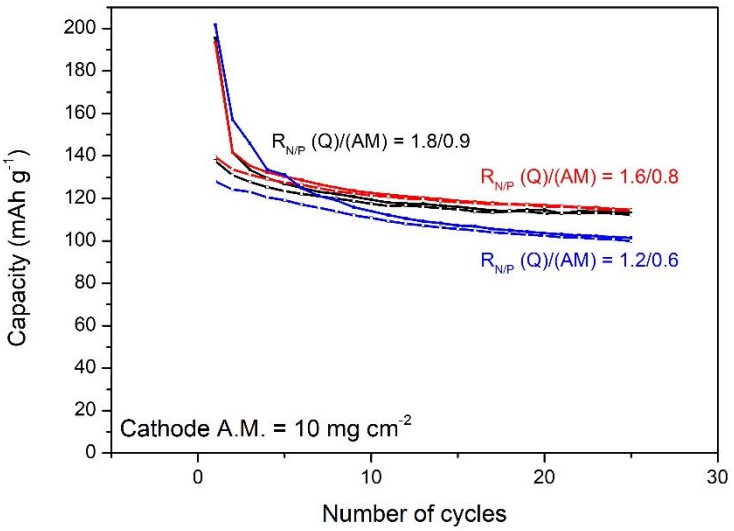

Figure 4.15. Cycling stability of full-cells with a cathode active material loading of 10 mg cm^{-2} and different mass balances (cells cycled at 15 mA g^{-1}_{AMCat}, between 1-4.2 V).

The specific energy density is proportional to the cell voltage and capacity and inversely proportional to the mass of the components of the cell (Equation 4.8). Therefore, the strategies to maximize the energy density are to minimize the mass of the inactive components and to increase the cell voltage and/or the capacity. The energy density at materials level of the cells which showed the best electrochemical performance after 25 cycles is calculated in **Table 4.5** (the mass of the inactive components is considered for these calculations). The average voltage is in the range from 2.85-2.75 V for both full-cells and the cell with a cathode active material loading of 10 mg cm^{-2} delivers an energy density of 111 Wh kg^{-1}. An energy density of 73 Wh kg^{-}

[1] is estimated using the AM:C65:PVDF = 75:15:10 reference cathode composition, a cathode active material loading of 10 mg cm^{-2} and a $R_{N/P}$ (Q) = 1.6, assuming that the same voltage and capacity are delivered by this full-cell. Therefore, the increase from 75 to 88% of the active material content in the cathode composition would result in an energy density increment of 38 Wh kg^{-1}.

$$\text{Energy density} = \frac{\text{Reversible capacity} \times \text{Average voltage}}{(\text{Mass cathode} + \text{Mass anode})} \quad (4.8)$$

Table 4.5. Energy density of hard carbon//$Na_{1-\delta}Ni_{0.32}Ti_{0.32}Mg_{0.16}Mn_{0.20}O_2$ cells.

Cathode AM loading (mg cm^{-2})	$R_{N/P}$ (Q)	$R_{N/P}$ (AM)	Energy density (Wh kg^{-1})
10	1.6	0.8	111
6	2.1	0.9	60

4.4 Conclusions

O3-$Na_{1-\delta}Ni_{0.32}Ti_{0.32}Mg_{0.16}Mn_{0.20}O_2$ is synthesized by means of solid-state route with minimum amount of $Mg_{1-x}Ni_xO$ impurities. It is concluded that calcination time and temperature promote the formation of the impurity phase and that the mixing of the precursors by wet ball-milling allows to reduce the temperature and time of calcination; thus, reducing the amount of impurities present in the final product. The optimum $Na_{1-\delta}Ni_{0.32}Ti_{0.32}Mg_{0.16}Mn_{0.20}O_2$ synthesis procedure consists in the mixing of the precursors by wet ball milling and subsequent calcination in air at 900 °C during 8 hours. Furthermore, it is observed that by reducing the calcination temperature the lattice parameter *c* increases, which could be an indicator of higher sodium content of the compound.

The effect of cathode formulation in the electrochemical performance is also studied. The amount of active material in the electrode composition is increased from 75% to 88% with comparable results (100 mAh g^{-1} after 40 cycles and capacity retention close to 70%). It is concluded that for an active material content of 88%, the optimum C65:PVDF ratio is 0.6:1. However, when the amount of active material is increased to 94%, the amounts of inactive components are not sufficient to provide good electrochemical response.

Optimized cathodes with 88 wt. % of active material content are used for full-cell fabrication with balanced anode electrodes. It is necessary to oversize the capacity of the anodes in order to avoid the risk of sodium plating which causes severe aging and it is considered as a safety hazard. Moreover, the required anode excess is higher for the low active material loading cathode (ca. 6 mg cm^{-2}) full-cells compared to high active material loading cathode (ca. 10 mg cm^{-2}) full-cells due to the high 1st cycle irreversibility of the formers. Maximum reversible capacity of 114 mAh g^{-1}_{AMCat} and energy density of 111 Wh kg^{-1} at materials level is obtained with a capacity retention of 82% when using a cathode active material loading of 10 mg cm^{-2} and $R_{N/P}$ (Q) = 1.6. These features make the hard carbon//$Na_{1-\delta}Ni_{0.32}Ti_{0.32}Mg_{0.16}Mn_{0.20}O_2$ cell an attractive choice of components which can evolve to further scal

Chapter 5. Analysis of the $NaFe_{0.4}Mn_{0.3}Ni_{0.3}O_2$ processing parameters for SIBs cathode applications

In this chapter, O3-$NaFe_{0.4}Mn_{0.3}Ni_{0.3}O_2$ layered oxide is evaluated as the cathode active material for Na-ion battery. This composition has already been studied by other researchers from the synthesis and structural point of view; therefore, this work will be focused in the engineering aspects of electrode preparation. As the electrode slurry preparation is the first step of the cell manufacturing sequential process and it determines its final properties, formulation studies in terms of conductive agent/binder contents and active material content/loading are performed. The effect of the mixing procedure is also evaluated and different strategies to improve the obtained electrode microstructure, such as the use of dispersing additives and variation of the active material morphology are also analyzed. The last part of this chapter is focused on the electrode drying process. Morphological, rheological, mechanical and electrochemical characterizations are included in this chapter.

5.1 Influence of the C65: PVDF ratio

Binder and conductive additives are essential components of metal-ion battery electrodes. Binder provides mechanical strength to the system, cohesion between particles and adhesion of the coated material to the current collector and the conductive additive allows reducing the electrode resistance. According to Bauer et al., PVDF presents affinity to the carbon black nanoparticles in the slurry and these two components tend to form an interconnecting film which contributes to improve the electronic conductive network [165]. Therefore, the ratio between them is one of the parameters that needs to be optimized.

5.1.1 Slurry preparation

In this section, slurries were prepared with 5 different C65:PVDF ratios, i.e. 0.2:1, 0.4:1, 0.6:1, 0.8:1 and 1.0:1. All the slurries were prepared using the mixing device with an overhead stirrer with the paddle type impeller. The C65 was dispersed in a 8% binder solution at 600 rpm for 1 hour and 15 min and then, the active material was incorporated (mixing speed and time of 700 rpm 2 h, respectively) (see Chapter 2, section 2.2.1.1, page 54 for additional information on this mixing device). **Table 5.1** summarizes the studied slurry formulations.

The solid content of the slurries (**Table 5.1**) progressively increases when increasing C65:PVDF. This happened because the total amount of dry powders (AM + C65 + PVDF) was maintained constant (11.5 g) for all the slurries and the amount of solvent was determined by the amount of PVDF in each slurry, being PVDF:NMP = 8:92 w%. Therefore, as the C65:PVDF increases, the amount of PVDF (and consequently NMP) decreases and higher solid content slurries are obtained. The reason why similar solid content slurries are obtained for C65:PVDF = 0.6:1, 0.8:0.1 and 1.0:1 is that extra NMP had to be added in order to make the high C65 containing slurry less viscous and suitable to work with.

Table 5.1. Composition of the studied cathode slurries (weight and volume percentages correspond to the dry powders and the solid content is calculated as the total dry powder mass/volume divided by the total slurry mass/volume).

C65:PVDF	AM content	C65 content	PVDF content	NMP	Solid content
0.2:1.0	87.0% w/w 74.4% v/v 10 g	2.2% w/w 3.9% v/v 0.25 g	10.8% w/w 21.7% v/v 1.25 g	14.3 g	44.5% w/w 18.8% v/v
0.4:1.0	87.0% w/w 74.6% v/v 10 g	3.7% w/w 6.7% v/v 0.43 g	9.3% w/w 18.7% v/v 1.07 g	12.3 g	48.4% w/w 21.2% v/v
0.6:1.0	87.0% w/w 74.8% v/v 10 g	4.9% w/w 8.8% v/v 0.56 g	8.1% w/w 16.4% v/v 0.93 g	11.2 g	50.7% w/w 22.7% v/v
0.8:1.0	87.0% w/w 75.0% v/v 10 g	5.8% w/w 10.4% v/v 0.66 g	7.2% w/w 14.6% v/v 0.83 g	11.2 g	50.7% w/w 22.7% v/v
1.0:1.0	87.0% w/w 75.1% v/v 10 g	6.5% w/w 11.7% v/v 0.75 g	6.5% w/w 13.2% v/v 0.75 g	10.9 g	51.2w% 23% v/v

5.1.2 Slurry characterization

The viscosity of these systems is influenced by the concentration (i.e. the solid content) and the composition of the dispersed phase. Ligneel et al. [164] studied the effect of the solid content on the morphology and the electrochemical performance of the composite electrode. According to them, on the one hand, for lower solid contents than the optimal one, the electrochemical performance shows a decay because of the poor electronic wiring of the active material. On the

other hand, if too high solid contents are reached, there is a risk of sedimentation of some of the components of the mixture.

The rheological properties of the slurries were analyzed by means of flow curves in the shear rate range from 10 to 100 s^{-1} (**Figure 5.1**). All the slurries show a non-Newtonian shear thinning behavior, typical from inks and coatings, as the viscosity decreases when the shear rate increases. It is expected that when increasing the solid content and the amount of C65, viscosity will also increase [202,248]. This behavior is evident in the slurries with C65:PVDF = 0.6:1, 0.8:1 and 1.0:1 (**Table 5.1**), in which the combined effect of higher solid content and C65 concentration results in higher viscosity values in the studied shear rate range. 0.8:1 slurry presents slightly lower viscosity than 0.6:1 and 1.0:1 which could be derived from the better dispersion of the mixture.

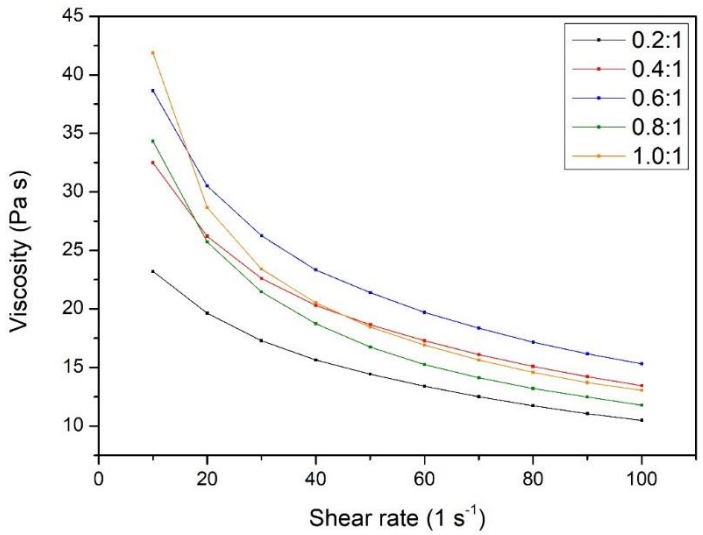

Figure 5.1. Flow curves of the of the studied cathode formulations.

According to Bauer et al. [165] the shear thinning behavior increases by increasing the carbon black amount in the slurry formulation. The results shown in **Figure 5.1** agree with this behavior since the difference of the viscosity measured at low and high shear rates increases progressively from C65:PVDF = 0.2:1 to 1.0:1 showing the latter more pseudo plastic behavior.

The shear stress curves were fitted to the Casson model (5.1) where τ_0 is the yield stress, η_p is the constant plastic viscosity, $\dot{\gamma}$ is the shear stress and n is the flow behavior index. The fitted curves and the obtained fitting parameters are displayed in **Figure 5.2** and **Table 5.2,** respectively.

$$\tau = \sqrt[n]{(\tau_0{}^n) + \left(\eta_p \times \dot{\gamma}\right)^n} \qquad (5.1)$$

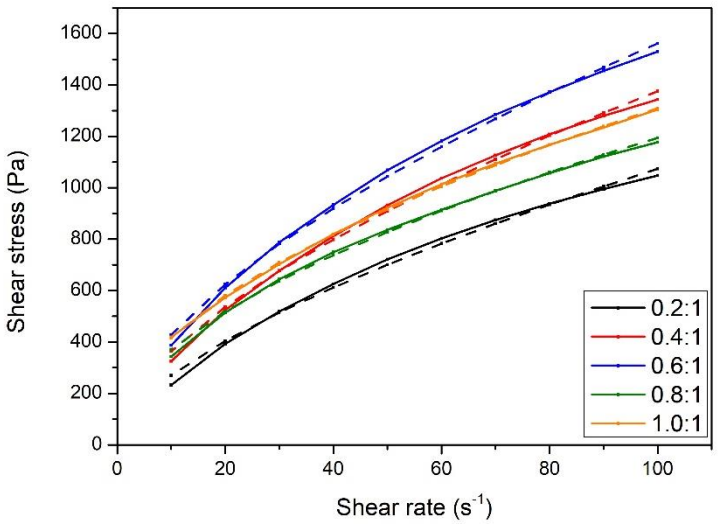

Figure 5.2. Measured shear stress curves (solid lines) and fitting to the Casson model (dashed lines).

Table 5.2. Casson model fitting parameters.

C65:PVDF	τ_0 (Pa)	n	η_p (Pa·s)
0.2:1	0.015	0.088	0.049
0.4:1	0.059	0.092	0.057
0.6:1	0.120	0.094	0.054
0.8:1	0.604	0.102	0.026
1.0:1	0.393	0.091	0.011

The fitting parameters show that when the C65:PVDF ratio increases from 0.2:1 to 0.8:1, there is an increment of the yield stress from 0.015 to 0.604 Pa. The yield stress, or critical shear stress, corresponds to the minimum stress necessary for the fluid to start to flow and is a manifestation of the network structure present in the dispersion. As the solid content increases, the

connectivity throughout the system grows and the yield stress increases [202]. This is consistent with the increment observed in the yield stress from 0.2:1 to 0.8:1. However, this tendency is not followed by the slurry with C65:PVDF = 1.0:1 due to the weaker interactions between the slurry components, as there is an extra difficulty to homogenize the 1.0:1 slurry.

The viscosity and solid content of the slurries have a direct effect on the active material loading of the casted electrodes. **Figure 5.3** shows the active material loading for the 5 different slurries as a function of the Doctor Blade gap (casting speed was maintained constant at 70 cm min^{-1}). The active material loading of the electrodes increases almost linearly with the gap of the doctor blade, which indicates that the viscosity of the slurries is in the range suitable for Doctor Blade casting. Moreover, although the active material content is maintained constant at 87% for all the formulations, the active material loading increases by increasing the C65:PVDF ratio as a consequence of the higher viscosity and solid content of the slurries. In spite of having lower viscosity, the active material loadings of the electrodes with C65:PVDF = 0.8:1 are slightly higher than those with C65:PVDF = 1.0:1. This unexpected behavior can be related to the higher yield stress of the former, which is related to higher solid contents, likewise related to the evaporation of the solvent.

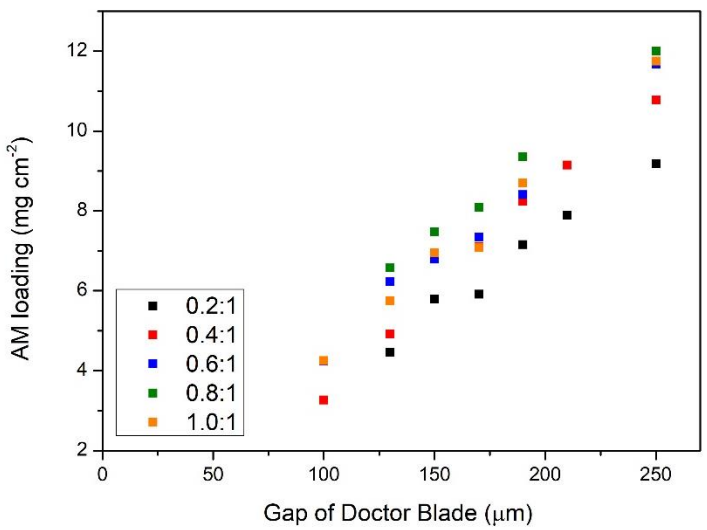

Figure 5.3. Active material loading of casted electrodes as a function of the doctor blade gap for different C65:PVDF ratios.

5.1.3 Electrode characterization

5.1.3.1 Morphological characterization

Surface SEM images were taken in order to analyze the microstructural differences between the electrodes with different C65:PVDF ratios. **Figure 5.4** clearly shows that when increasing C65:PVDF from 0.2:1 to 1.0:1, the amount of C65 is higher and that there is a variation of the carbon black network formed around the active material particles. It is important that the carbon black particles are well distributed all over the electrode volume to improve the electronic conductivity of the composite. By increasing the C65:PVDF ratio, continuous electronic paths are enhanced from side to side of the electrode, decreasing interfacial resistance, as it was explained in their study by Lee [249].

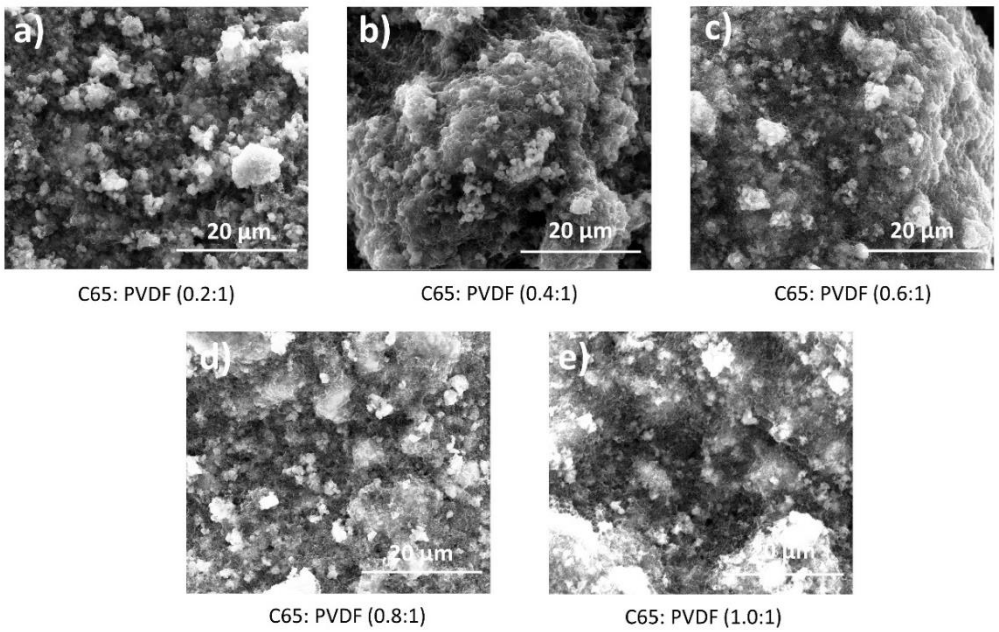

Figure 5.4. Surface SEM images of the electrodes with different C65:PVDF ratios. (a) 0.2:1, (b) 0.4:1, (c) 0.6:1, (d) 0.8:1 and (e) 1.0:1.

5.1.3.2 Adhesion/cohesion properties

The mechanical properties of the laminates with different C65:PVDF ratios were evaluated by adhesion strength tests. Electrodes with 8.7 ± 0.8 mg cm^{-2} active material loading were used for these tests (further details on the sample preparation and experimental procedure are provided in Chapter 2, section 2.5.3, page 80). **Figure 5.5** shows the maximum tensile strength to delaminate the coated foils. As expected, the maximum tensile strength values are higher for the laminates with C65:PVDF = 0.2:1 and 0.4:1 than for those with C65:PVDF = 0.6:1, 0.8:1 and 1.0:1 due to the high amount of binder.

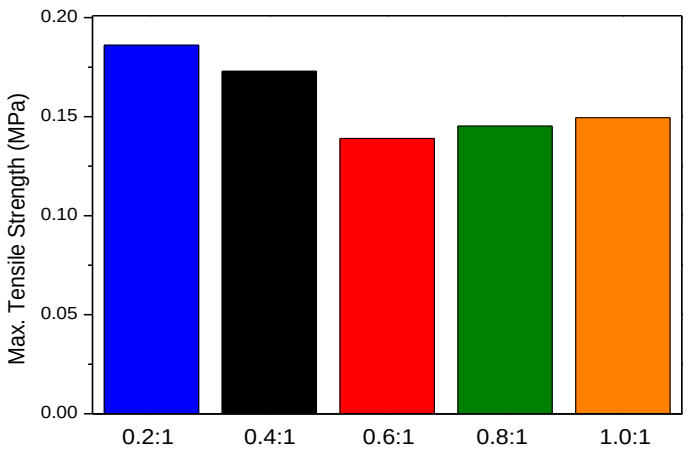

Figure 5.5. Maximum tensile strength obtained by adhesion strength test.

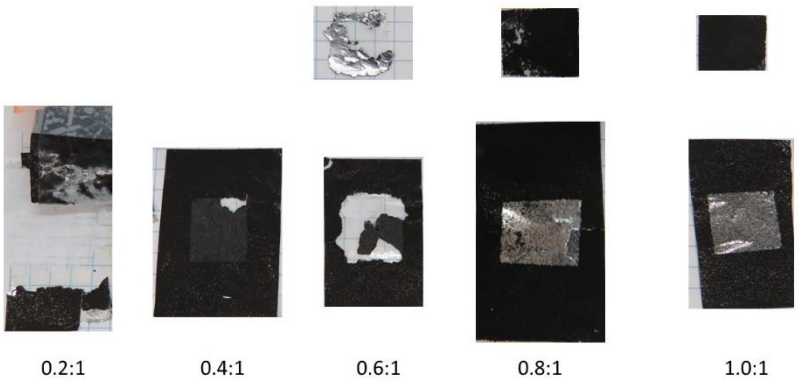

Figure 5.6. Electrode appearance after the adhesion strength tests.

The images in **Figure 5.6** correspond to the laminates after the adhesion strength test. The fact that the samples with C65:PVDF = 0.2:1, 0.4:1 and 0.6:1 are either completely destroyed (i.e. the aluminum foil is broken for C65:PVDF = 0.2:1 and 0.6:1) or hardly affected (i.e. most of the electrode remains adhered to the current collector for C65:PVDF = 0.4:1), evidence the excellent adhesion and cohesion properties of these electrodes. Contrarily, almost complete delamination is shown for the electrodes with C65:PVDF = 0.8:1 and 1.0:1 which indicates that the cohesion among particles is better than the adhesion between the coating and the current collector. Good adhesion and cohesion properties will have a positive influence on the electrochemical performance of the electrodes.

5.1.3.3 Electrochemical performance

The electrochemical performance of the electrodes with different C65:PVDF ratios was evaluated using half-cell configuration in CR2032 coin cells. Electrodes with 8.7 ± 0.8 mg cm^{-2} AM loading, 1 M $NaPF_6$ in EC:DEC and metallic Na were selected as the working electrode, the electrolyte and the counter/reference electrodes, respectively. Additional details on the cell preparation and experimental setup are provided in Chapter 2, section 2.4.1, page 63.

Figure 5.7 shows the first galvanostatic charge and discharge curves of the half-cells with C65:PVDF = 0.2:1, 0.4:1, 0.6:1, 0.8:1 and 1.0:1 in the voltage range between 2.5-4 V. At 13 mA g^{-1}_{AM}, the obtained 1st discharge capacities are 71, 83, 116, 110 and 126 mAh g^{-1}, respectively. The half-cells with C65:PVDF = 0.6:1, 0.8:1 and 1.0:1 show first cycle capacity values in the expected

range for this layered oxide. Contrarily, the half-cells with C65:PVDF = 0.2:1 and 0.4:1 show lower discharge capacity values. According to Liu et al. [167], there are 2 conductivity regions depending on the AB:PVDF (AB = Acetylene Black) ratio of the electrodes. Below AB:PVDF = 0.2:1, the AB network is not formed and the conductivity is too low. In this region, small variations of the AB content result in a significant variation of the electrode conductivity. The second region is the conductivity plateau region in which the conductivity changes are less pronounced if the AB content is varied. This region corresponds to the fully formed AB network. Above AB:PVDF = 0.8:1, there is a decrease in the conductivity due to insufficient binder to maintain the AB network structure. According to the experimental results shown in **Figure 5.7**, the conductive network in these electrodes is not formed when C65:PVDF ≤ 0.4:1 and the electrodes with C65:PVDF ≥ 0.6:1 are in the conductivity plateau region. The differences among the study of Liu et al. and our experimental results in the limit between the two regions can be attributed to the different conductive additives that were used to make the experiments (AB vs. C65).

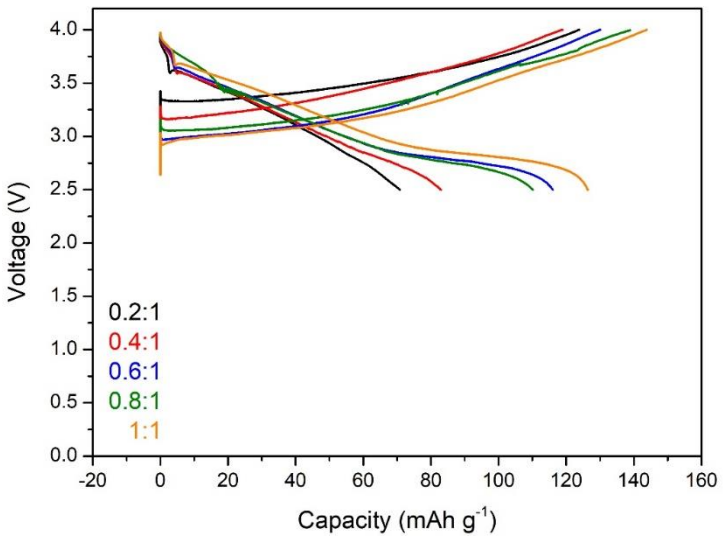

Figure 5.7. 1st galvanostatic charge/discharge curves at 13 mA g^{-1}_{AM} of the half-cells with C65:PVDF = 0.2:1, 0.4:1, 0.6:1, 0.8:1 and 1.0:1 (4.0-2.5 V).

Figure 5.8 shows the cycling stability of the half-cells at 13 mA g^{-1}_{AM} over 50 cycles. Discharge capacities of 41, 47, 58, 91 and 70 mAh g^{-1} are obtained for C65:PVDF = 0.2:1, 0.4:1, 0.6:1, 0.8:1 and 1.0:1, respectively at the end of the experiment. As it could be expected, low reversible

capacities are obtained for the half-cells with C65:PVDF = 0.2:1 and 0.4:1 due to the low carbon black and high binder content of these electrodes which result in insufficient electrode conductivities. When the C65 content is increased to C65:PVDF = 0.6:1 and 0.8:1, the conductive network is formed and the cycling stability is improved. When the C65 content is further increased up to C65:PVDF = 1.0:1, the cycling stability of the half-cell is worse due to the formation of C65 agglomerates and the lack of binder which is insufficient to maintain the conductive particles together as a network resulting in a polarization increment.

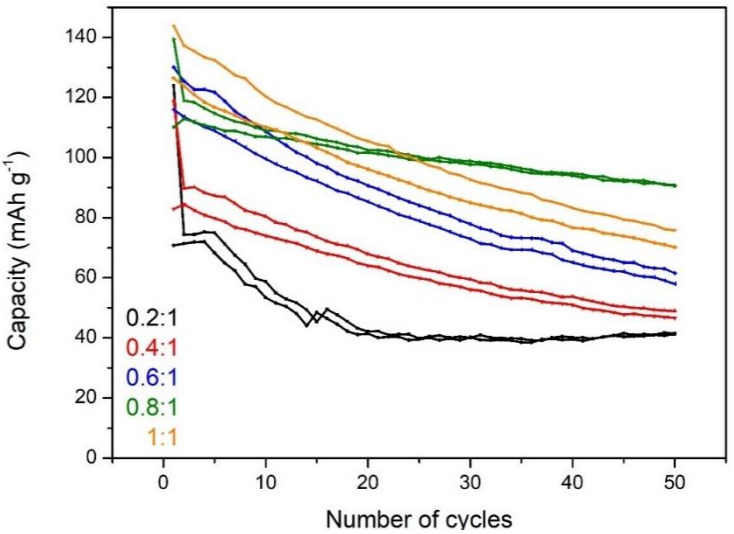

Figure 5.8. Cycling performance at 13 mA g^{-1}_{AM} over 50 cycles of the half-cells with C65:PVDF = 0.2:1, 0.4:1, 0.6:1, 0.8:1 and 1.0:1 (4.0-2.5 V).

The rate performance is also influenced by the C65:PVDF ratio of the electrodes. **Figure 5.9** shows that lower capacities are obtained at higher rates as a consequence of the polarization increase. At 65 mA g^{-1}_{AM} and 130 mA g^{-1}_{AM}, no capacity is delivered by the cells with C65:PVDF = 0.2:1 and 0.4:1. Moreover, the rate capability of the cell with C65:PVDF = 0.6:1 is also significantly lower than that of the cells with higher C65 contents, which indicates that the amount of conductive additive is not enough for fast cycling. C65:PVDF = 0.8:1 and 1.0:1 show similar C-rate capability being the capacity at 130 mA g^{-1}_{AM} higher for the cell with C65:PVDF = 0.8:1. Similar of what happened in the cycling stability tests, the lower rate performance is attributed to the agglomeration of the conductive additive particles that results in lower electrode conductivities.

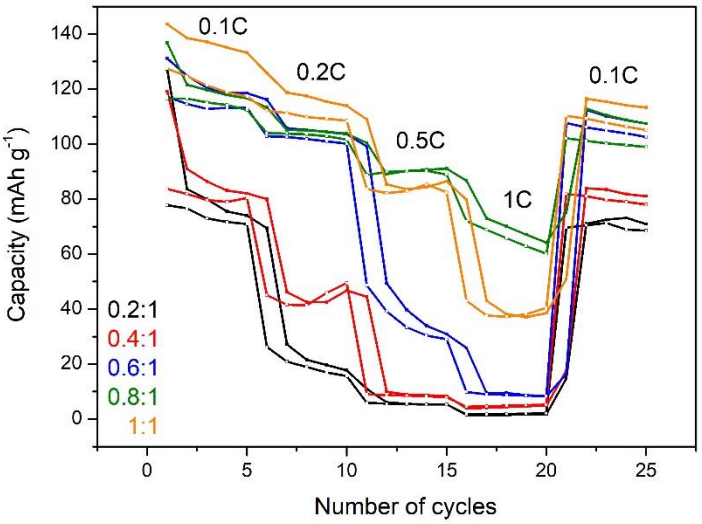

Figure 5.9. C-rate performance of the half-cells with C65:PVDF = 0.2:1, 0.4:1, 0.6:1, 0.8:1 and 1.0:1 (4-2.5 V).

The diffusion coefficient values of the electrodes with different C65:PVDF ratios were calculated using the Randles–Sevcik equation (5.2) in which I_p is the peak current (A), n is the number of electrons transferred during the charge and discharge processes, A is the surface area of the electrode (cm^2), V is the potential scan rate ($V\ s^{-1}$), and C is the concentration of Na^+ ($mol\ cm^{-3}$). The values of the Na^+ diffusion coefficients were calculated by the linear relationship between the peak current and the square root of the scan rate, which is typical for the equilibrium behavior of an intercalation-type electrode [200].

$$I_p = (2.69 \cdot 10^5) \cdot n^{\frac{2}{3}} \cdot A \cdot D^{\frac{1}{2}} \cdot V^{\frac{1}{2}} \cdot C \qquad (5.2)$$

The diffusion coefficient values of all the tested electrodes shown in **Figure 5.10** are in the range between $3.70 \cdot 10^{-12}$ to $2.57 \cdot 10^{-11}$; showing a maximum for the electrode with C65:PVDF = 0.8:1. The best rate capabilities observed in **Figure 5.9** for this electrode composition are consistent with the highest diffusion coefficient values, indicative of fast sodium ion movement.

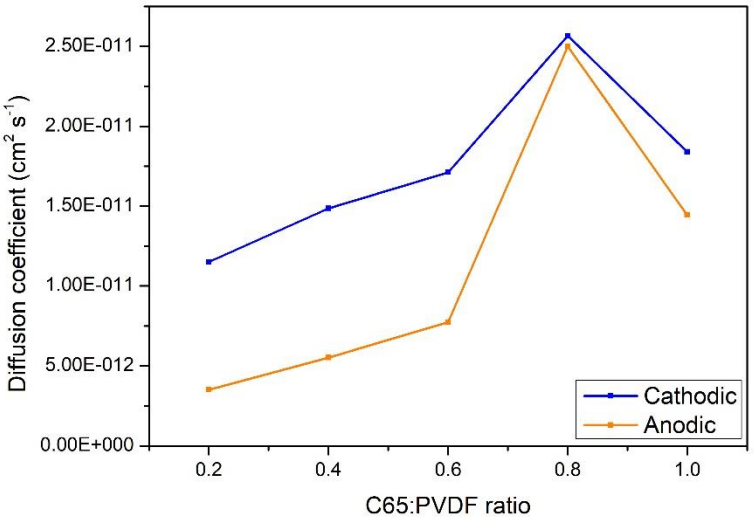

Figure 5.10. Diffusion coefficient of the electrodes with C65:PVDF = 0.2:1, 0.4:1, 0.6:1, 0.8:1 and 1.0:1 taking into consideration the cathodic/anodic processes of the cyclic voltammograms.

5.2 Influence of the AM content and loading

Using low AM contents (ca. 75-80%) and loadings (2-3 mg cm^{-2}), which allows to minimize resistance and diffusion limitations, is a strategy commonly used at lab-scale to perform basic electrochemical studies of new electrode materials. However, if high energy densities want to be achieved at full-cell level, active material content/loadings need to be maximized without compromising the electrochemical properties and the mechanical integrity of the electrodes. As an example, commercial Li-ion battery cathodes have active material contents of ca. 90% and active material loadings corresponding to ca. 2 mAh cm^{-2}, approximately [250]. In this section, the effect of increasing the active material content from 75% to ca. 90% is analyzed in terms of rheological properties of the slurries and mechanical and electrochemical properties of the resulting electrodes. The effect of the active material loading is also evaluated for each electrode formulation.

5.2.1 Slurry preparation

Three different formulations were prepared with 75% (reference cell), 87% and 90% of active material, named as 75%AM, 87%AM and 90%AM hereinafter. Based on the results obtained in section 5.1, C65:PVDF was maintained at 0.8:1 for the 87%AM and 90%AM formulations, while C65:PVDF = 1.5:1 was used for the 75%AM formulation. All the slurries were prepared using the mixer with the dissolver type impeller by dispersing first the C65 at 1700 rpm for 2 hours in 8% binder solution and the active material later at 1700 rpm for 2 hours (see Chapter 2 for the details of the mixing device) and **Table 5.3** summarizes the studied formulations. The solid content of the 75%AM formulation is significantly lower compared to the other two formulations due to the high C65 content and the consequent need of extra NMP to obtain a slurry suitable to be casted using the Doctor Blade.

Table 5.3. Composition of the studied cathode slurries (weight and volume percentages correspond to the dry powders and the solid content is calculated as the total dry powder mass/volume divided by the total slurry mass/volume).

Slurry	AM content	C65 content	PVDF content	NMP	Solid content
75%AM	75.0% w/w 57.8% v/v 25 g	15% w/w 24.1% v/v 5 g	10% w/w 18.1% v/v 3.3 g	52.8 g	38.7% w/w 16.8% v/v
87%AM	87.0% w/w 75.0% v/v 30 g	5.8% w/w 10.4% v/v 2 g	7.2% w/w 14.6% v/v 2.5 g	28.6 g	54.6% w/w 25.6% v/v
90%AM	90% w/w 80.0% v/v 30 g	4.4% w/w 8.1% v/v 1.46 g	5.7% w/w 11.9% v/v 1.9 g	25.3 g	56.9% w/w 26.8% v/v

5.2.2 Slurry characterization

Figure 5.11 shows the flow curves of the three slurries in the shear rate range between 10 and 100 s^{-1}. The measured viscosity of all the samples decreases with the shear rate; therefore, all of them have a non-Newtonian shear thinning behavior. However, the difference between the viscosity at low and high shear rates is lower for high active material content slurries, i.e, the non-Newtonian character is less pronounced.

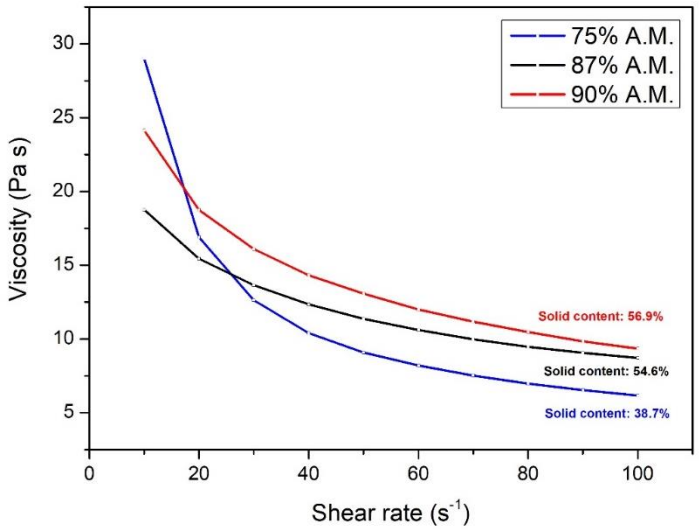

Figure 5.11. Flow curves of the cathode formulations with different AM content.

According to Bauer et al., [165] based on the Stokes Law, high viscosities allow to decrease the rate of sedimentation of the particles, reducing the kinetic energy of the particles. However, there must be a balance between the low sedimentation rate and the feasibility to coat the slurry onto the aluminum foil. The 87%AM and 90%AM slurries present quite high slurry viscosity from medium shear rates, and therefore, good particle kinetic energy.

The active material, carbon black and binder are expected to form a uniform network structure having a determined yield stress. The shear stress curves of the three slurries were fitted to the Casson model (equation 5.1 in p. 135) (**Figure 5.12**) in order to calculate this critical yield stress

value. **Table 5.4** displays the fitting parameters; the value of the yield stress ranging from 210 Pa to 0.1 Pa and showing a minimum value of 0.03 Pa for the 87%AM slurry.

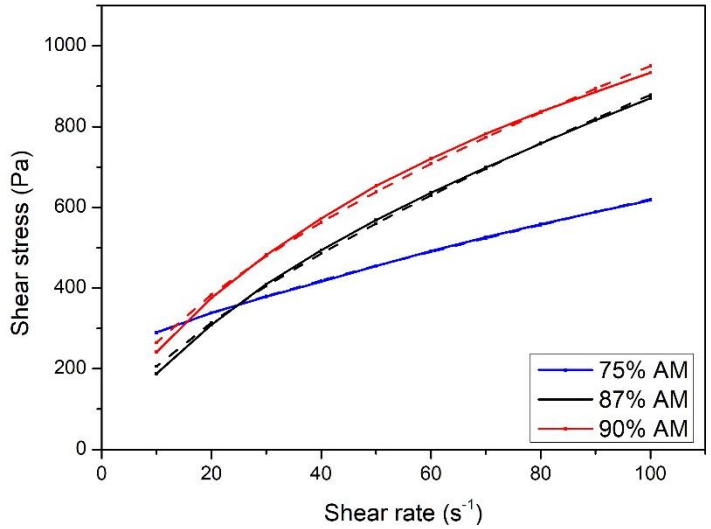

Figure 5.12. Measured shear stress curves (solid lines) and fitting to the Casson model (dashed lines) for the slurries with different active material contents.

Table 5.4. Casson model fitting parameters.

%AM	τ_0 (Pa)	n	η_p (Pa·s)
75%AM	210.2	0.644	2.121
87%AM	0.031	0.105	0.162
90%AM	0.100	0.095	0.033

Once the slurry is prepared, the coating process is performed. **Figure 5.13** represents the relationship between the gap of the Doctor Blade and the active material loading as a function on the active material content. This relationship varies depending on the AM and solid content and the viscosity of the slurries. It is important to mention that the AM loading of the electrodes increases almost linearly with the gap of the Doctor Blade for the three slurries being this increment more pronounced as the AM and solid content and the viscosity increases.

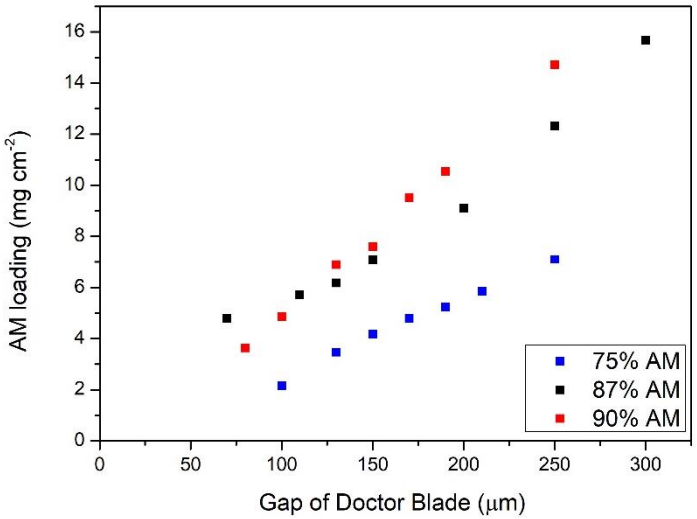

Figure 5.13. Active material loading of casted electrodes as a function of the Doctor Blade gap for the 3 slurries with different AM content.

5.2.3 Electrode characterization

5.2.3.1 Morphological characterization

Figure 5.14 shows the SEM images of 75%AM, 87%AM and 90%AM electrodes. The electrode with the highest PVDF and C65, i.e.75%AM, evidences a binder and C65 network surrounding the active material particles. On the other hand, when the other two electrodes with the high active material content are compared, slightly lower size agglomerates are observed in the 87%AM electrode, which can help to improve the conductive paths.

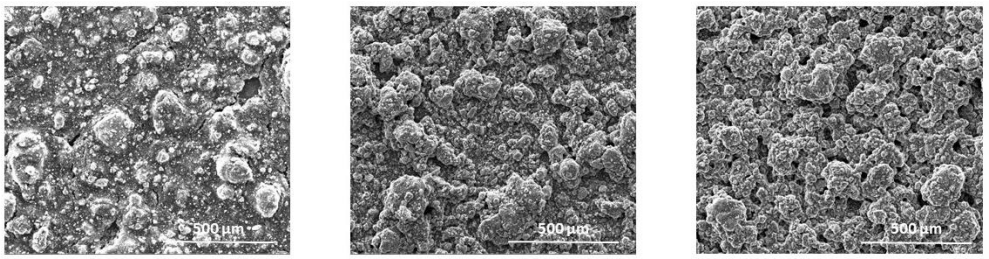

Figure 5.14. Surface SEM images of the un-calendered electrodes with different AM contents.

5.2.3.2 Adhesion/cohesion properties

Adhesion strength test and 180˚ peel test techniques are used in order to elucidate the differences between different formulations (further details on the sample preparation and experimental procedure are included in Chapter 2, section 2.5.3, page 80).

In order to evaluate de influence of the electrode thickness on the mechanical properties, adhesion strength tests were performed in electrodes with different active material loadings. According to the results displayed in **Figure 5.15** the maximum tensile strength values are in the range from ca. 0.1 to 0.13 MPa and do not show clear tendencies depending on the active material content and loadings. However, by observing the photographs of the electrodes after the adhesion strength test (**Figure 5.16**), there are clear differences as a consequence of the different electrode formulations. While 87%AM and 90%AM electrodes present complete delamination, 75%AM electrode presents high adhesion strength to the aluminum foil and the cohesion properties are worse. This can be explained because of the higher binder content of the 75%AM formulation that adheres to the current collector but the less homogeneous distribution of the components due to the difficulty to disperse that high amount of C65 that hiders the cohesion between particles.

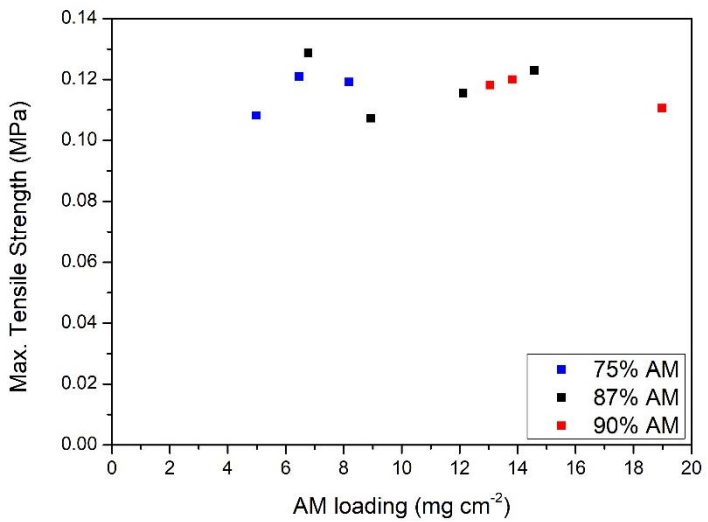

Figure 5.15. Maximum tensile strength obtained by adhesion strength test.

Figure 5.16. Electrode appearance after the adhesion strength tests.

In addition to the adhesion strength tests, 180˚ peel tests were also performed on 75%AM, 87%AM and 90%AM electrodes with different active material loadings in order to clarify the role of this parameter on the adhesion/cohesion properties for each formulation.

In **Figure 5.17, Figure 5.19 and Figure 5.21,** the average load measured in the 180° test is represented for 75%AM, 87%AM and 90%AM, respectively. The 75%AM laminates present similar adhesion strength for the range of loadings analyzed (**Figure 5.17**) with slightly higher adhesion strength as the active material loading increases. Moreover, the appearance of the electrodes taken after the peel test (**Figure 5.18**) show that the adhesion property is better than the particle-to-particle cohesion for these electrodes. This could be due to the difficulty of mixing the high amount of carbon black of this formulation which tends to form agglomerates.

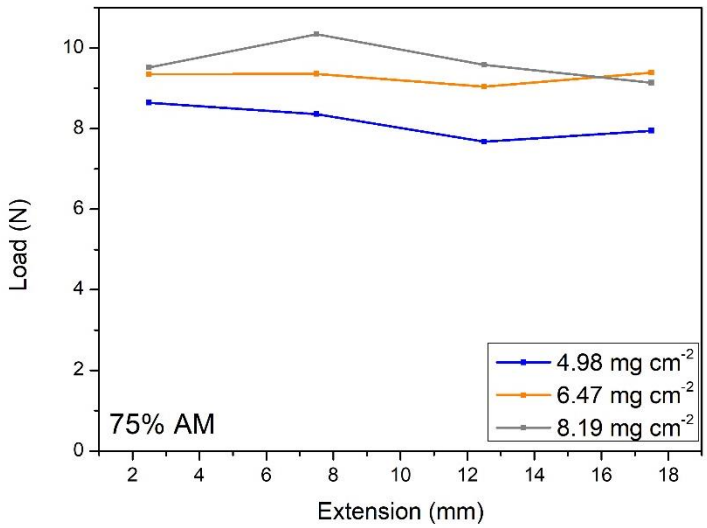

Figure 5.17. Average load measured in the 180˚ peel test on 75%AM electrodes with different AM loadings.

75% A.M.
4.98 mg cm^{-2} A.M.

75% A.M.
6.47 mg cm^{-2} A.M.

75% A.M.
8.19 mg cm^{-2} A.M.

Figure 5.18. Aspect of the 75%AM electrodes with different AM loadings after the 180˚ peel test experiments.

In the case of the 87%AM electrodes, there is an evident loss of the adhesion properties when increasing active material loading, as can be seen in **Figure 5.19** and **Figure 5.20**. A progressive loss of the adhesion properties is evident being the electrodes with 14.58 mg cm^{-2} completely delaminated from the current collector substrate. As a consequence of the lower PVDF content of these electrodes, they present lower load values than those measured for the 75%AM electrodes (**Figure 5.17**).

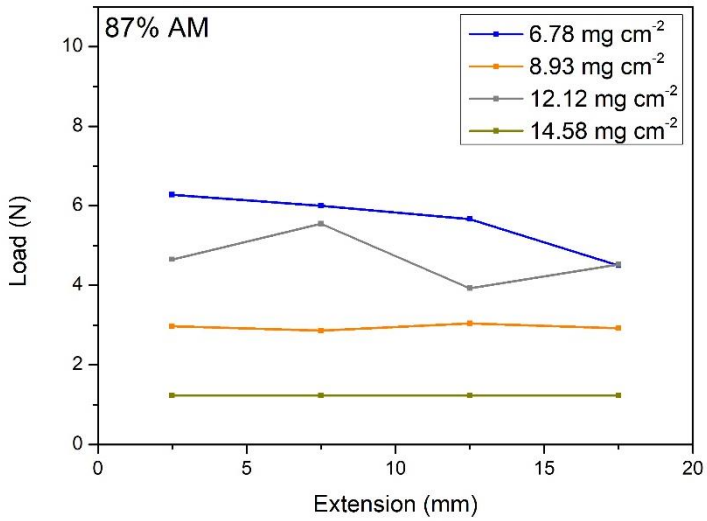

Figure 5.19. Average load measured in the 180˚ peel test on 87%AM electrodes with different AM loadings.

Figure 5.20. Aspect of the 87%AM electrodes with different AM loadings after the 180˚ peel test experiments.

The adhesion/cohesion properties of the electrodes with 90%AM and ca. 11-13 mg cm^{-2} (**Figure 5.21** and **Figure 5.22**) are in the range of those obtained for 87%AM for equivalent active material loadings (**Figure 5.19** and **Figure 5.20**) and the adhesion properties of the 90%AM with 19 mg cm^{-2} are totally lost. In spite of the lower binder content of these electrodes, the load measured in the peel test is higher than that for the electrodes with 87%AM and 14.58 mg cm^{-2} due to the higher amount of material that needs to be removed from the current collector.

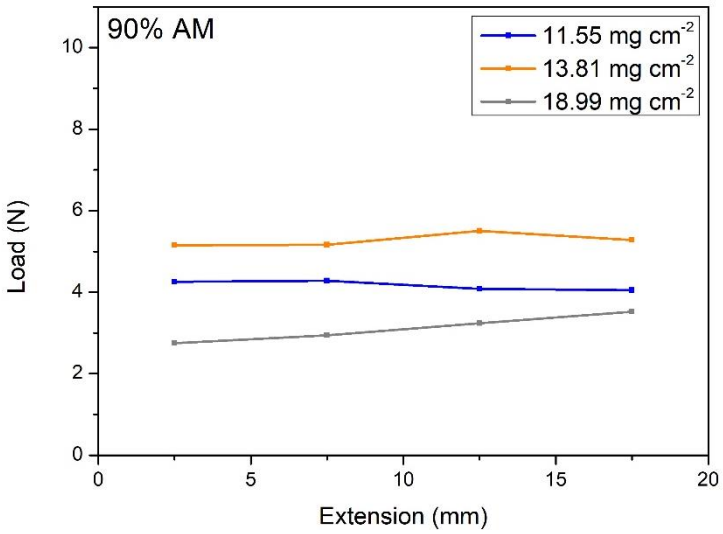

Figure 5.21. Average load measured in the 180˚ peel test on 90%AM electrodes with different active material loadings.

Figure 5.22. Aspect of the 90%AM electrodes with different AM loadings after the 180˚ peel test experiments.

5.2.3.3 Electrochemical performance

The effect of the active material loading for the electrodes with different active material contents was evaluated at different C-rates, 13 mA g^{-1}, 26 mA g^{-1}, 63 mA g^{-1} and 130 mA g^{-1}. **Table 5.5** collects all the active material loadings with their corresponding active material contents used to perform the experiments.

Table 5.5. Active material loadings (mg cm^{-2}) of the electrodes used to perform C-rate capability tests.

75%AM	87%AM	90%AM
3.65	4.32	4.06
4.78	5.08	5.65
8.83	9.47	8.60
10.69	11.70	11.31

Similar reversible capacities are obtained at 13 mA g^{-1} and 26 mA g^{-1} for the 75%AM electrodes in the whole active material loading range studied (**Figure 5.23**). The reduction on the C-rate capability is not that important for the active material loadings lower than 9 mg cm^{-2}. However, for the electrodes with 10.68 mg cm^{-2}, there is a high impact of the C-rate. A fast capacity fade from 80 mAh g^{-1} to 30 mAh g^{-1} is observed in 10 cycles at 65 mA g^{-1} and the reversible capacity decreases to 15 mAh g^{-1} at 130 mA g^{-1}. This is related to the increment of the cell resistance by increasing the electrode thickness.

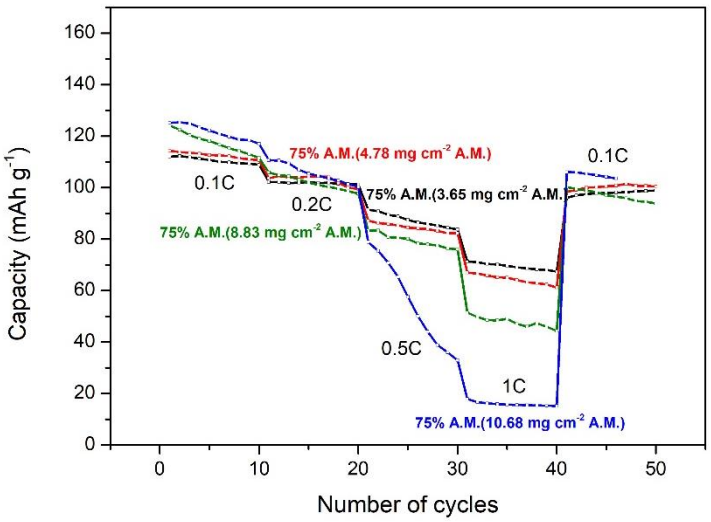

Figure 5.23. C-rate performance of the half-cells with 75%AM and different active material loadings (4-2.5 V).

While the C-rate performance of the electrodes with 75%AM presents a progressive decay depending on the active material lading (**Figure 5.23**), when the active material content is

increased to 87%AM, the effect of the active material loading is not that clear (**Figure 5.24**). Surprisingly, the electrode with 9.47 mg cm^{-2} shows slightly better C-rate capability than the electrodes with ca. 4-5 mg cm^{-2}. It is considered that the electrochemical performance of these three electrodes is in the range of variability for this type of cells. Contrarily, a clear limitation is observed when the active material loading is increased to 11.70 mg cm^{-2}. The reversible capacity starts to decay at 26 mA g^{-1} and at 65 mA g^{-1} the reversible capacity drops to 15 mAh g^{-1}. It is important to highlight that all the cells recovered the capacity obtained before the C-rate capability tests.

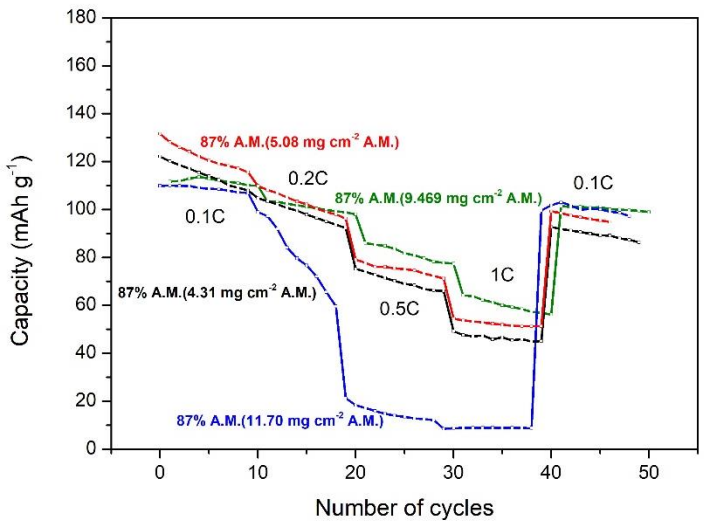

Figure 5.24. C-rate performance of the half-cells with 87%AM and different active material loadings (4-2.5 V).

The C-rate capability limitation for the 90%AM electrodes is higher than for the electrodes with 87%AM as it can be observed in **Figure 5.25**. A significant capacity fade happens above 65 mA g^{-1} for the electrodes with active material loadings above 5 mg cm^{-2}. Moreover, the reversible capacities at 130 mA g^{-1} are lower than 20 mAh g^{-1} for the active material loadings above ca. 8 mg cm^{-2}. According to the data presented in **Figure 5.25**, the amount of carbon black needed for the electrodes with 90%AM to show good C-rate capability properties should be higher or the mixing procedure should be improved to create the microstructure that will allow fast

charge/discharge cycling. Again, it is remarkable to mention that even with the high active material content of 90%, the capacity is recovered after the C-rate capability tests.

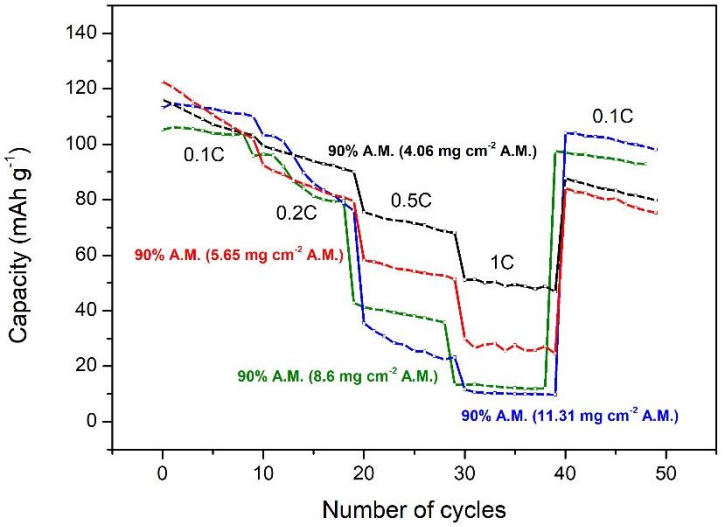

Figure 5.25. C-rate performance of the half-cells with 90%AM and different active material loadings (4-2.5 V).

Taking into account the previous experimental data and trying to maximize the active material loading on each formulation without compromising neither the mechanical integrity nor the electrochemical performance, electrodes with active material loadings of 8 ± 0.6 mg cm^{-2} were used to compare the electrochemical performance of the three different formulations. The electrochemical performance of these cells with different active material contents at 13 mA g^{-1}_{AM} (**Figure 5.26**) do not present significant differences. The reversible capacity after 50 cycles is close to 90 mAh g^{-1} for 75%AM, 87%AM and 90%AM, being the capacity retention 83.4%, 82.6% and 77.3%, respectively.

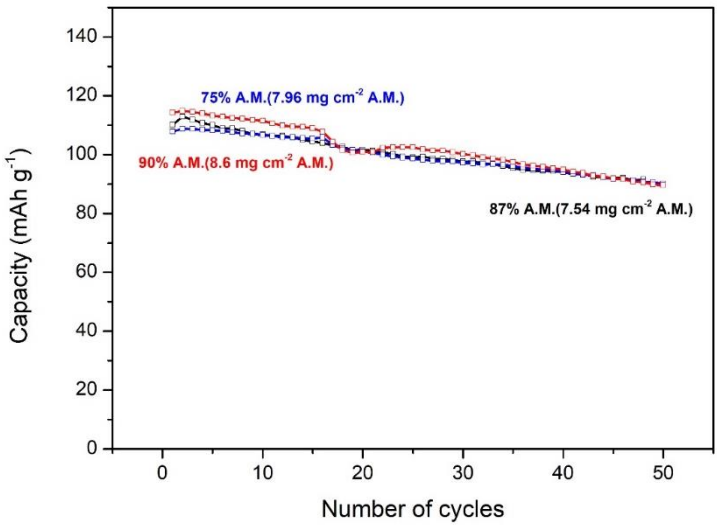

Figure 5.26. Cycling performance at 13 mA g^{-1}_{AMCat} over 50 cycles of the half-cells with 75%AM, 87%AM and 90%AM (4.0-2.5 V).

The C-rate performance is similar for the cells with 75%AM and 87%AM (**Figure 5.27**). However, at high C-rates, the cells with 90%AM show a capacity fade, especially at 65 mA g^{-1} and 130 mA g^{-1}, which could be caused by the low quantity of the conductive carbon black and poor adhesion properties of these electrodes.

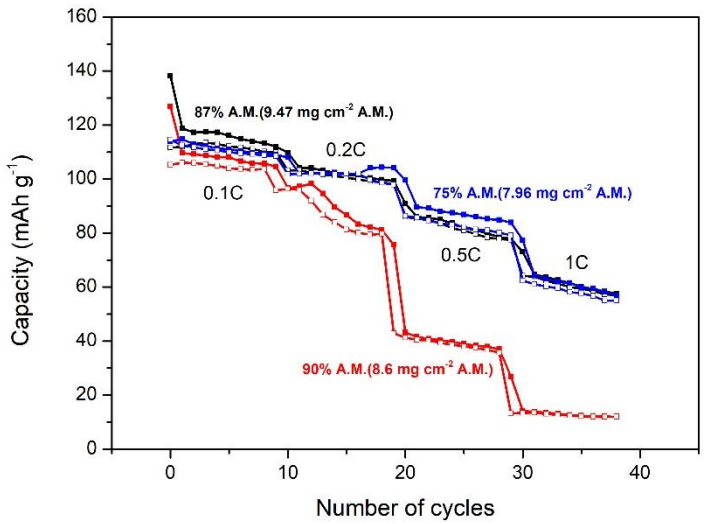

Figure 5.27. C-rate performance of the half cells with 75%AM, 87%AM and 90%AM (4-2.5 V).

As it has been said at the beginning of the section, the main goal of this chapter is to analyze the processing parameters of $NaFe_{0.4}Mn_{0.3}Ni_{0.3}O_2$ with the aim to maximize the energy density of the cells. **Table 5.6** shows the energy density calculated for the cathode half-cell and a full-cell for the cathodes with different active material contents to visualize the effect of this parameter. The mass of the C65 conductive additive and the PVDF binder was considered for this calculation. A hard carbon with a formulation of HC:PVDF = 95:5 and a $R_{N/P}(Q)$ = 1.3 was selected as the anode for the calculation corresponding to the full-cells. The average voltage and the capacity values (3.14, 3.18 and 3.19 V and 0.81, 0.77 and 0.86 mAh, respectively for 75%AM, 87%AM and 90%AM) correspond to the 50th cycle in **Figure 5.26**.

In spite of the similar cathode active material loading, the energy density increases from 123 to 165 Wh kg^{-1} at half-cell level (the mass of the inactive components is considered for these calculations) from 97 to 108 Wh kg^{-1} at full-cell level (the mass of the inactive components is considered for these calculations) when increasing the active material content from 75% to 90% due to the reduction of the electrochemically inactive components of the electrodes. In addition to this, despite the capacity of the cells with 87%AM and 90%AM being slightly lower than the capacity of the cell with 75%AM, the higher active material content compensates the penalty in the capacity. However, it needs to be in consideration for the design of full-cells using this active material that the rate capability of the half-cells with 90%AM is not as good as that shown by the half-cells with 87%AM.

Table 5.6. Energy density estimations at half-cell and full-cell level for the cathode electrodes with different active material contents.

	75%AM (Wh kg^{-1})	**87%AM (Wh kg^{-1})**	**90%AM (Wh kg^{-1})**
Half-cell	123	155	165
Full-cell	97	106	108

5.3 Effect of mixing equipment in slurry and electrode properties

5.3.1 Slurry preparation

In this section, the effect of the mixing device on the rheological properties of the slurries and the morphology and electrochemical performance of the resulting electrodes is analyzed. Taking into account the results obtained in the section 5.1 and section 5.2 of this chapter, the slurry formulation is maintained constant at AM:C65:PVDF = 87:5.8:7.2 (C65:PVDF = 0.8:1). The mixing devices used for this analysis are: (1) an overhead stirrer with the paddle type impeller (PTI), (2) a planetary centrifugal vacuum mixer (PM), (3) a combination of the overhead stirrer with the paddle type impeller and a planetary mixer (PTI+PM), (4) a mixer with a dissolver type impeller (DTI), (5) a planetary ball-milling equipment (BM) and (5) a combination of the ball-milling equipment with the dissolver type impeller (BM+DTI). Further details on these mixing equipment are included in Chapter 2, section 2.2.1.1.

A binder solution with 8% of PVDF in NMP was used for the slurry preparation but in some of the procedures, extra NMP solvent had to be added to properly disperse the C65 and the active material. In spite of this, the solid content was maintained in the range from 50 to 55 % w/w. **Table 5.7** summarizes the main characteristics of each slurry.

Table 5.7. Composition of the studied cathode slurries (weight and volume percentages correspond to the dry powders and the solid content is calculated as the total dry powder mass/volume divided by the total slurry mass/volume).

Type of mixing equipment	AM content	C65 content	PVDF content	NMP	Solid content
PTI	87.0% w/w 74.9% v/v 10 g	5.8% w/w 10.4% v/v 0.66 g	7.2% w/w 14.6% v/v 0.83 g	11.17 g	50.7% w/w 22.7% v/v
PM	87.0% w/w 74.9% v/v 10 g	5.8% w/w 10.4% v/v 0.66 g	7.2% w/w 14.6% v/v 0.83 g	11.32 g	50.4% w/w 22.5% v/v

PTI+PM	87.0% w/w 74.9% v/v 10 g	5.8% w/w 10.4% v/v 0.66 g	7.2% w/w 14.6% v/v 0.83 g	10.24 g	52.9% w/w 24.2% v/v
DTI	87.0% w/w 74.9% v/v 10 g	5.8% w/w 10.4% v/v 0.66 g	7.2% w/w 14.6% v/v 0.83 g	9.54 g	54.6% w/w 25.6% v/v
BM	87.0% w/w 74.9% v/v 4.84 g	5.8% w/w 10.4% v/v 0.32 g	7.2% w/w 14.6% v/v 0.4 g	4.62 g	54.6% w/w 25.6% v/v
BM+DTI	87.0% w/w 74.9% v/v 10 g	5.8% w/w 10.4% v/v 0.66 g	7.2% w/w 14.6% v/v 0.83 g	10.55 g	54.6% w/w 25.6% v/v

Below, the slurry mixing procedure followed for each mixing device is described. Some of the difficulties observed during the slurry preparation process are commented:

1) *PTI* (**Figure 5.28**): Bigger containers than those used for other mixing equipment are needed due to the big size of the paddle type impeller. Heating of the slurry and consequent NMP condensation was detected.

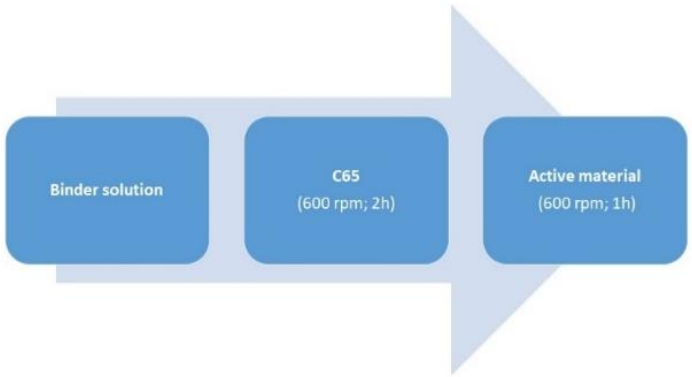

Figure 5.28. Slurry mixing procedure using the overhead stirrer with the paddle type impeller.

2) *PM* (**Figure 5.29**): It shows as one of the main advantages that the same procedure could be used for different size containers.

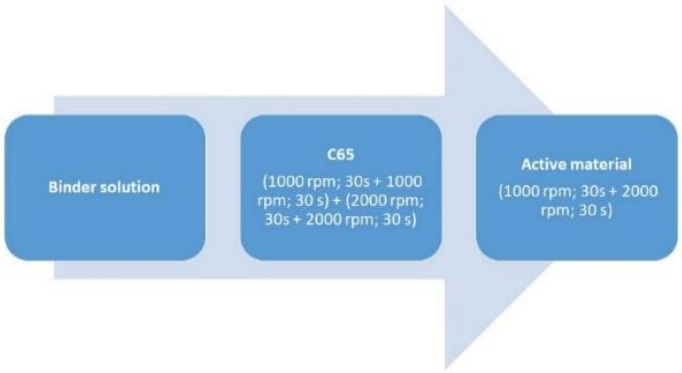

Figure 5.29. Slurry mixing procedure using the planetary centrifugal vacuum mixer.

3) *PTI+PM* (**Figure 5.30**): The use of the planetary mixer allow minimizing the amount of material that remains unmixed in the dead zones of the mixing equipment with the paddle type impeller. Moreover, it allows increasing the shear (mixing speed) from 600 rpm to 2000 rpm.

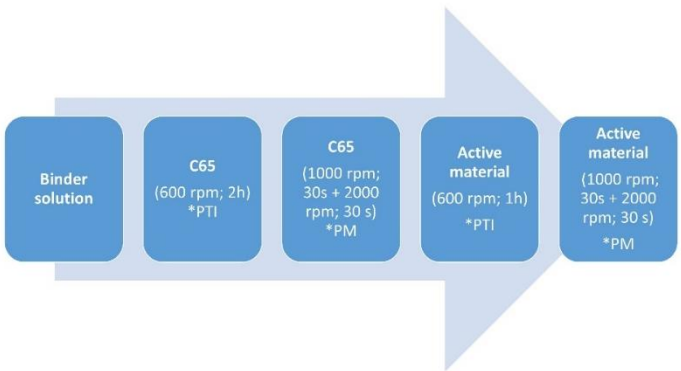

Figure 5.30. Slurry mixing procedure using the mixer with the paddle type impeller combined with the planetary centrifugal vacuum mixer.

4) *DTI* (**Figure 5.31**): It is a versatile device that allows using high speed and mixing times. The mixing tank has a cooling jacket which avoids the heating of the slurry.

Figure 5.31. Slurry mixing procedure using the mixer with a dissolver type impeller.

5) *BM* (**Figure 5.32**): There is a risk of significant overheating that promotes the polymerization of the PVDF binder. The maximum amount of processed material is limited to ca. 5 g in the equipment used in this Thesis. One of the main drawbacks is the limited scalability of this equipment.

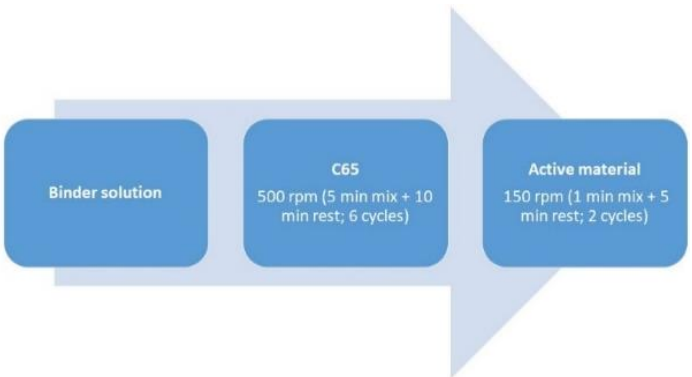

Figure 5.32. Slurry mixing procedure using a planetary ball milling.

6) *BM+DTI* (**Figure 5.33**): Dry mixing of the active material and the conductive additive was performed using the ball milling and the wet mixing with the binder solution was done using the disperser with the dissolver type impeller.

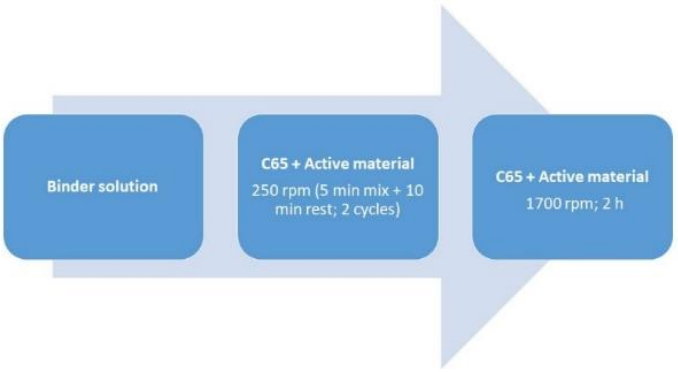

Figure 5.33. Slurry mixing procedure using a planetary ball milling and the mixer with a dissolver type impeller.

5.3.2 Slurry characterization

Similar rheological analysis as that performed in Section 5.1.2 and Section 5.2.2 was done with the slurries prepared using the different equipment. However, the flow curve of the slurry prepared using the ball-milling procedure was not measured due to material limitation to perform the measurements.

The flow curves in **Figure 5.34** show that the lowest viscosity values are obtained for the slurries prepared using de dissolver type impeller. In this case, the high mixing intensity apparently resulted in high carbon black de-agglomeration and therefore, in lower starting viscosity, as it was concluded by Kwade et al. [251]. The slurry prepared with the overhead stirrer with the paddle type impeller shows slightly higher viscosity, indicative that the dispersion of the components is worse. The highest viscosity value corresponds to the slurries prepared using the planetary mixer, and the combination of the mixer with the paddle type impeller and the planetary mixer results in an intermediate viscosity value of that obtained for the slurries prepared using the individual equipment.

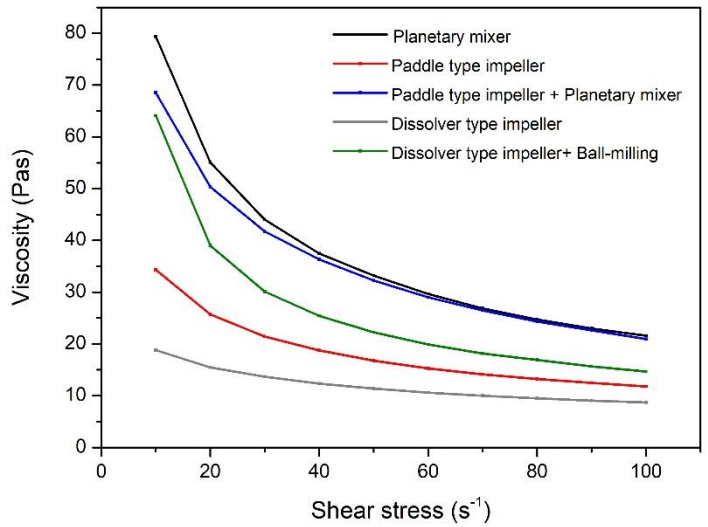

Figure 5.34. Flow curves of the slurries prepared with different mixing equipment/procedure.

The model used to fit the shear stress data of these slurries is the Casson model (**Figure 5.35**). According to the fitting (**Table 5.8**), the highest value of the yield stress, 159.4 Pa, is obtained for the combination ball-milling and dissolver type impeller. It is expected that this high critical yield stress will allow maintaining a better slurry character over time.

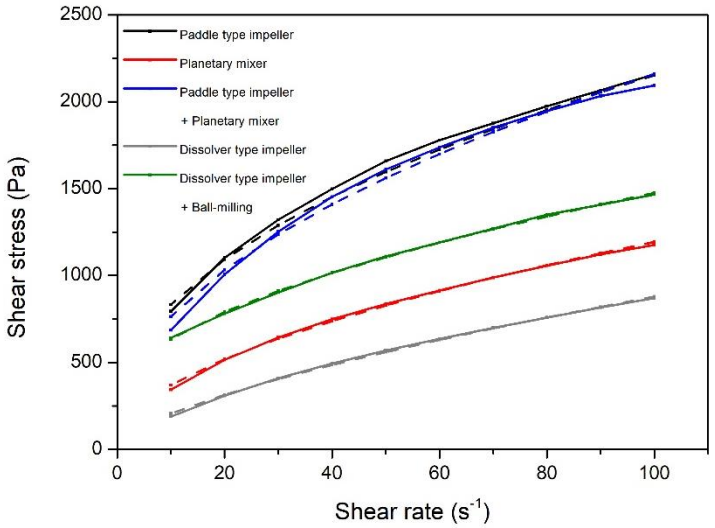

Figure 5.35. Measured shear stress curves (solid lines) and fitting to the Casson model (dashed lines).

Table 5.8. Casson model fitting parameters.

Type of mixing device	τ_0 (Pa)	n	η_p (Pa·s)
PTI	0.604	0.102	0.026
PM	5.238	0.096	0.004
PTI+PM	0.989	0.084	0.003
DTI	0.031	0.105	0.162
BM+DTI	159.4	0.259	0.608

5.3.3 Electrode characterization

5.3.3.1 Morphological characterization

The microstructural analysis of the electrodes prepared using the different mixing devices/procedures was carried out by SEM of un-calendered samples. The level of dispersion of the components and the size of the particle agglomerates have been studied.

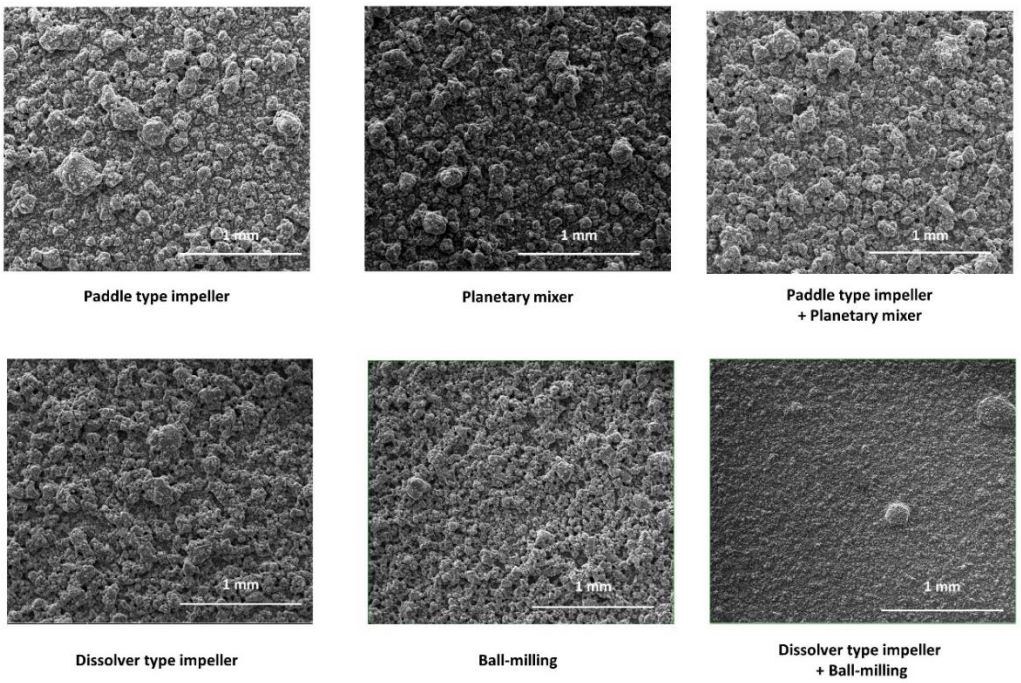

Figure 5.36. Surface SEM images of the electrodes prepared using different equipment/procedure.

Figure 5.36 evidences that the size of the agglomerates varies depending on the electrode preparation equipment/procedure. The two electrodes prepared using ball milling equipment are the ones which show the smallest agglomerates due to the highly energetic milling process involved in this slurry preparation procedure that promotes the breakage of the agglomerates. Contrarily, the mixing procedures using the paddle type impeller and the planetary mixer are less energetic and the size of the agglomerates is significantly higher. Finally, the electrodes prepared using with the dissolver type impeller, show agglomerate size in between.

Agglomeration of the submicron particles is sometimes beneficial as higher tap densities can be achieved and the secondary particles allow radial paths for the sodium ions intercalation [252]. In principle, the big agglomerates present in **Figure 5.36** corresponding to the electrodes prepared using the overhead mixer with the paddle type impeller, the planetary mixer and the disperser with the dissolver type impeller are not considered to be the most appropriate neither from the processing nor the electrochemical performance point of view. As stated by Yazami et. al., in the case of particle agglomeration, electrolyte wetting problems can arise which will limit the electrochemical performance of the cells. The cause for limited wettability is the size of the agglomerates, rather than the size of individual primary particles [253]. Moreover, difficulties were found for homogeneous casting of these slurries using continuous casting methods such as comma bar coating, since the agglomerates promote the appearance of defects as lines on the electrodes. Additional work was performed with the aim of improving the microstructure of the electrodes in the section 5.4, page 197 of this chapter.

5.3.3.2 Electrochemical performance

Similar active material loading electrodes of 8 ± 0.2 mg cm^{-2} were used for the electrochemical performance analysis in order to avoid further variabilities due to cathode loading differences.

Figure 5.37 shows the 1st charge/discharge cycles of the half-cells. The highest 1st charge capacity is obtained for the procedure that involves a dry ball-milling process combined with the dispersion of components using the disperser with the dissolver type impeller, 157.4 mAh g^{-1}, same value as that obtained by Kuze et al. [76]. However, it is remarkable that the capacity

retention and the reversible capacity are independent from the 1st cycle capacity values as it will be shown in the following paragraphs.

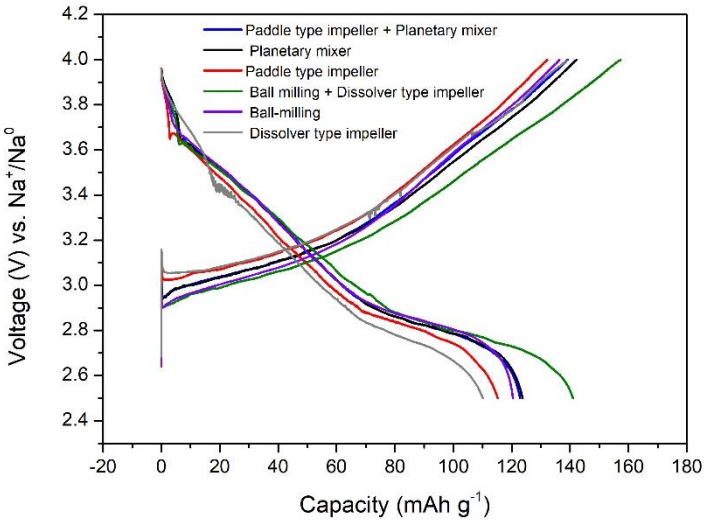

Figure 5.37. 1st galvanostatic charge and discharge curves at 13 mA g^{-1} (4.0-2.5 V).

Figure 5.38 shows the cycling performance for 50 cycles at 13 mA g^{-1} and **Table 5.9** gathers the capacity data corresponding to the 1st and 50th cycles. The capacity retention after 50 cycles is in the range between 50% and 60% for most of the mixing equipment/procedures used, such as the paddle type impeller, the planetary mixer, the combination of both of them and the ball milling. On the other hand, although the 1st discharge capacity of the electrodes prepared using the disperser with the dissolver type impeller is the lowest, 110 mAh g^{-1}, capacity retention increases up to 83.2%, indicating that despite of the large agglomerates, the microstructure of the electrodes is the best for cycling stability. Surprisingly, the electrodes which show the smallest agglomerates, prepared by dry ball milling and subsequent dispersion, are the ones with the lowest capacity retention, 42.5%.

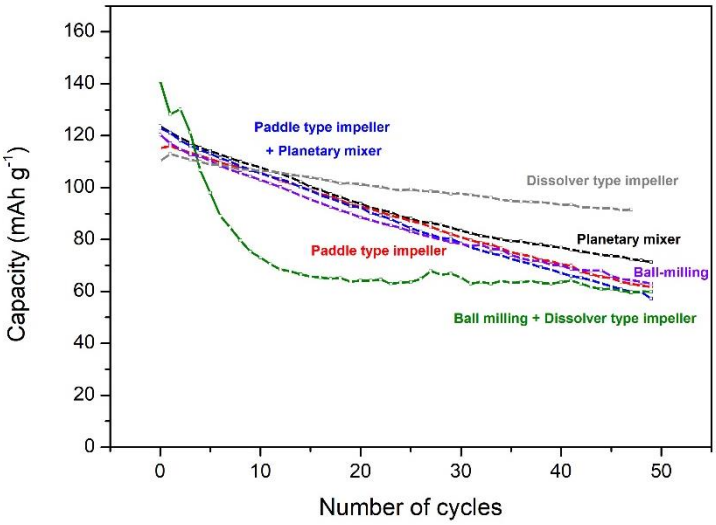

Figure 5.38. Cycling performance at 13 mA g^{-1} over 50 cycles of the half-cells prepared using different mixing procedures/equipment (4.0-2.5 V).

Table 5.9. Discharge capacity in the 1st and 50th cycles and capacity retention for different mixing procedures/equipment.

Type of mixing equipment	1st discharge capacity (mAh g^{-1})	Reversible capacity after 50 cycles (mAh g^{-1})	Capacity retention after 50 cycles (%)
PTI	115	62	53.6
PM	124	71	57.6
PTI+PM	123	62	50.5
DTI	110	92	83.2
BM	120	63	52.4
BM+DTI	141	60	42.5

The C-rate performance of these electrodes is shown in **Figure 5.39**. Similar to what observed in the cyclability test, the procedure combining the ball-milling and the dissolver type impeller shows poor C-rate capability, despite the pre-mixing step of the active material and carbon black allows to des-agglomerate the active material particles, being the capacity close to 10 mAh g^{-1} at C-rates above 26 mA g^{-1}. However, a limitation for active material deagglomeration can exist, above which an extreme decrease of the paths among active material particles happen. According to Bauer et al. [165], when the slurry mixing process includes a dry mixing step a not

percolated structure can be created. On the other hand, the higher surface area exposed to the electrolyte can promote the presence of secondary reactions that irreversibly consume Na^+ ions.

The electrodes prepared using the planetary mixer, show non-stable capacity at high rates, which can be an indicative of the poor mixing ability of the planetary mixer due to the short mixing times and consequent heterogeneous electrode microstructures.

More stable electrochemical performances are obtained in the C-rate capability tests for dissolver type impeller, the paddle type impeller, the combination of the paddle type impeller with the planetary mixer and the ball-milling procedures. The best electrochemical performance at high C-rates are obtained for the electrodes prepared with the dissolver type impeller. At 65 and 130 mA g^{-1}, reversible capacities of 82 and 65 mAh g^{-1}, respectively, are obtained.

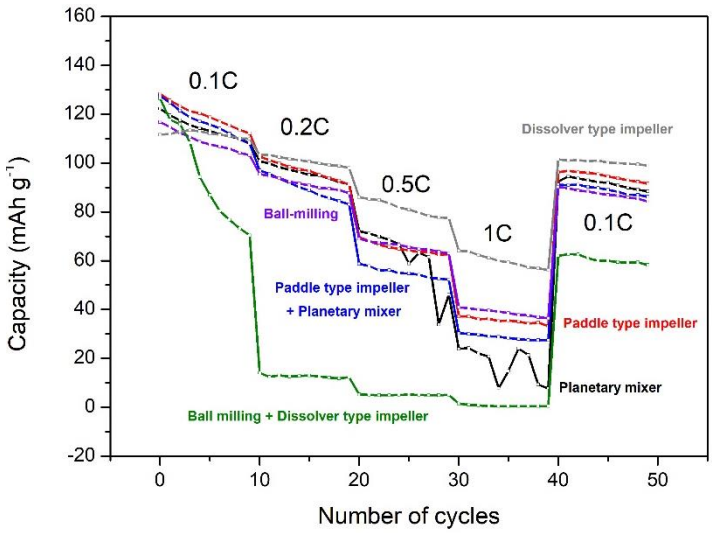

Figure 5.39. C-rate performance of the half-cells prepared using different mixing procedures/equipment (4-2.5 V).

5.4 Strategies to improve electrode microstructure

After the analysis of different mixing equipment performed in the previous section, reasonably good electrochemical performances were obtained using the disperser equipment with the dissolver type impeller. However, the presence large primary particle agglomerates is still an

issue, both from the process ability point or view in the casting step and from the electrochemical performance point of view.

Different approaches can be followed to avoid the formation of these agglomerates. On the one hand, efforts can be dedicated to modifying the morphology of the particles by tuning the synthesis procedure (the synthesis route, temperature, pressure, pH-value… can be modified). On the other hand, the use of dispersing additives during the slurry preparation can also be an option to improve the microstructure of the electrodes. Finally, the morphology of the particles can be tuned by post-processing of the synthesized raw material. In this section, the last two approaches have been evaluated to enhance the microstructure of the electrodes and hence, improve the casting ability and electrochemical performance of the electrodes.

5.4.1 Use of dispersing additives

PVP and SDS were tested as dispersing additives. PVP was used as an alternative of the PVDF binder following the same slurry preparation procedure as that described in **Figure 5.31**. On the other hand, SDS was used as a compound that lowers the surface tension. Small amounts of surfactants are usually enough to observe a significant effect, therefore 1% of SDS was incorporated to the 8% PVDF binder solution during the slurry preparation procedure described in **Figure 5.31**. The equipment selected to prepare the slurries is the disperser with the dissolver type impeller and the formulation is the same as that used in the analysis of the mixing equipment/procedure (AM:C65:PVDF/PVP = 87:5.8:7.2; C65:PVDF = 0.8:1).

The flow curves of the three slurries prepared with the different dispersing agents are plotted in **Figure 5.40**. It is observed that the addition of SDS slightly increases the viscosity in the studied shear rate range which represents a good balance between process ability and the feasibility to coat the slurry (it has previously been shown in sections 5.1.2 and 5.2.2 that a good control of the active material loading can be achieved with slurries with similar rheological properties). Both the slurries show non-Newtonian shear thinning behavior.

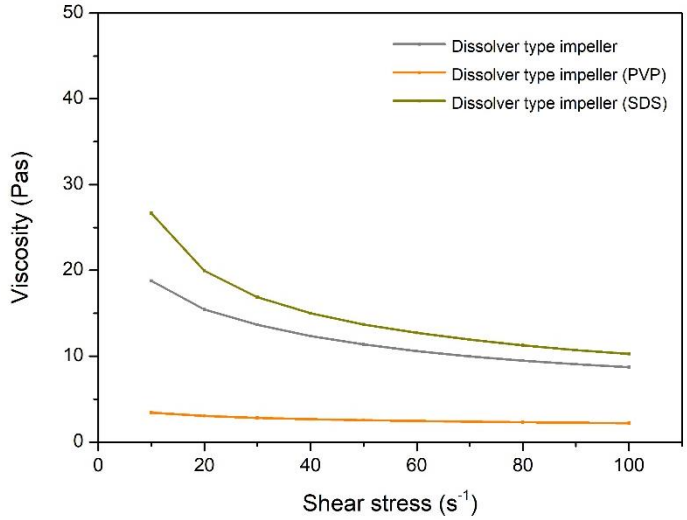

Figure 5.40. Flow curves of the slurries prepared using dispersing agents.

Contrarily, the slurry with PVP shows almost constant viscosity values over the studied shear rate range, that is, the slurry shows almost Newtonian character. According to Jacob et. al., particle agglomeration is responsible for the shear-thinning effects of slurries, and de-agglomeration of the particles can change a non-Newtonian system into a Newtonian one [254]. This could be happening in the PVP containing slurry.

The model used to fit the shear data of these slurries is the Casson model (**Figure 5.41**). According to the fitting values (**Table 5.10**), the use of PVP significantly reduces the yield stress as its resistance to flow is very small. Therefore, stability problems over time and difficult control of the active material loading of the electrodes are expected for this slurry.

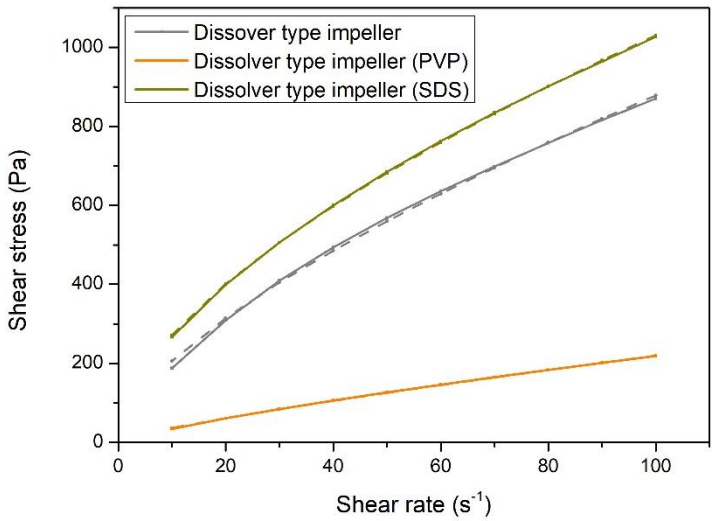

Figure 5.41. Measured shear stress curves (solid lines) and fitting to the Casson model (dashed lines).

Table 5.10. Casson model fitting parameters.

Dispersant	τ_0 (Pa)	n	η_p (Pa·s)
None	0.031	0.105	0.162
PVP	0.001	0.133	0.449
SDS	0.014	0.082	0.022

The SEM images obtained from the surface of un-calendered electrodes (**Figure 5.42**) evidence that the size of the $NaFe_{0.4}Mn_{0.3}Ni_{0.3}O_2$ primary particle agglomerates is similar and that the problem of the presence of large agglomerates still exists.

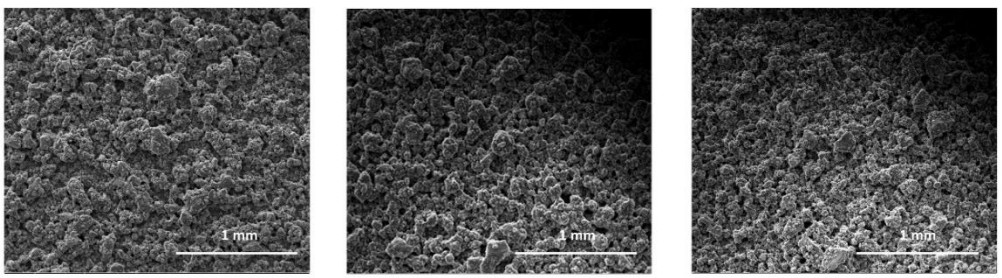

Figure 5.42. Surface SEM images of the electrodes with different dispersing agents.

According to the electrochemical performance data at 13 mA g^{-1} (**Figure 5.43**), the use of PVP instead of PVDF has a detrimental effect. The reversible capacity and capacity retention of the half-cell after 50 cycles are 31 mAh g^{-1} and 26.15%, respectively (**Table 5.11**). As it was stated by Bresser et al., the PVP has a highly hygroscopic character, due to the tertiary amide group, which can result in water adsorption of the highly hygroscopic cathode active material and combination of the electrolyte salt. This fact can limit the reversible electrochemical reaction of the sodium ions [255]. The capacity retention of the SDS containing slurry also decays in comparison to the slurry without any additive, 83.2% vs. 53.5%.

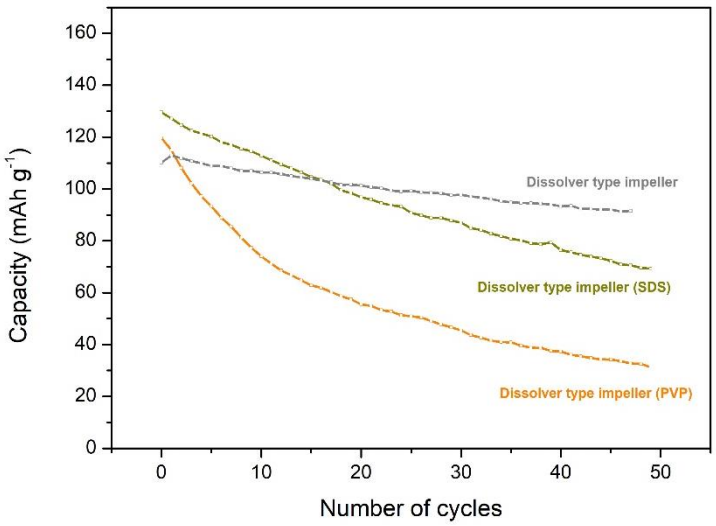

Figure 5.43. Cycling performance at 13 mA g^{-1} over 50 cycles of the half-cells with different dispersing agents (4.0-2.5 V).

Table 5.11. Discharge capacity in the 1st and 50th cycles and capacity retention for different dispersing agents.

Dispersant	1st discharge capacity (mAh g^{-1})	Reversible capacity after 50 cycles (mAh g^{-1})	Capacity retention after 50 cycles (%)
None	110	92	83.2
PVP	120	31	26.2
SDS	130	69	53.5

Similar C-rate performances are obtained for the electrodes without any dispersing additive and with SDS (**Figure 5.44**). Slightly lower capacity fade is observed for the electrodes with no dispersing agent, especially at low C-rates. Similar to what observed at low C-rates, the electrodes with PVP as binder/dispersing agent show poor electrochemical performance due to reactivity with the electrolyte.

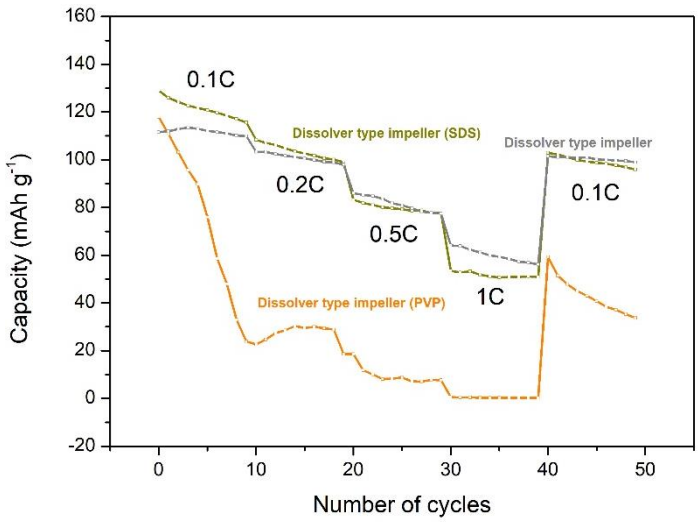

Figure 5.44. C-rate performance of the half-cells with different dispersing agents (4-2.5 V).

No improvement in the morphological, rheological and/or electrochemical properties of the electrodes was observed by adding dispersant agents. Therefore, this approach was discarded.

5.4.2 Effect of the active material morphology

As a second approach to improve the electrode microstructure, the effect of active material morphology is modified in this section. The raw material named as original morphology hereinafter was subjected to two different post-synthesis treatments: 1) a ball milling treatment to promote the de-agglomeration of the particles (named as de-agglomerated morphology hereinafter) and 2) a spray drying treatment to promote the formation of spherical particles which do not tend to further agglomerate [256] (named as spherical morphology hereinafter). All

the treatments were performed by an external company and no information was provided on the treatment conditions based on confidentiality issues.

All of the slurries done in this section are prepared by means of the disperser with the dissolver type impeller following the procedure already described in **Figure 5.31** (page 151) and the formulation is the same as that used in the analysis of the mixing equipment/procedure (AM:C65:PVDF/PVP = 87:5.8:7.2; C65:PVDF = 0.8:1).

The SEM images of the electrodes (**Figure 5.45**) show that the agglomerates remain there when using the de-agglomerated material. However, the shape of the agglomerates significantly changed and spherical agglomerates with a similar agglomerate size than the original morphology are obtained. In the case of spherical particles formed by means of spray drying, the size of the agglomerates is significantly lower and the dispersion is enhanced. The decrease of the size of the agglomerates allows the preparation of electrodes using the continuous coating machine without the presence of defects created by the large agglomerates present in the slurries prepared with the original and the de-agglomerated materials.

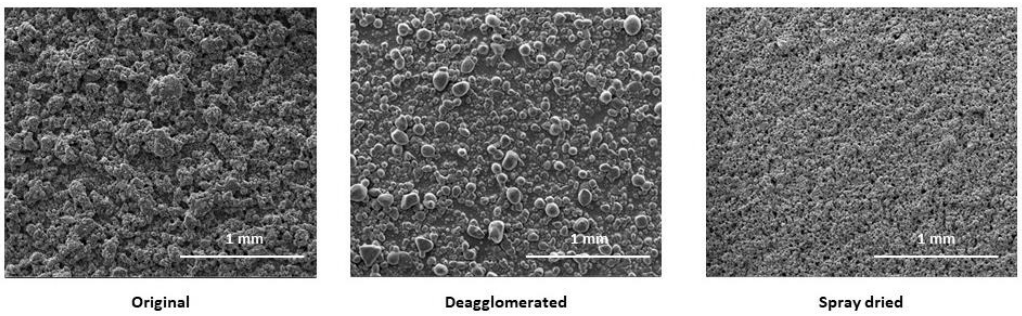

Figure 5.45. Surface SEM images of the electrodes with different active material morphology.

The microstructure of the electrodes has strong consequences in the electrochemical performance. It determines the specific surface area in contact with the electrolyte, which determines the transportation paths for the sodium ions. An optimal microstructure also enables the fast transport of the electrons which improves the cycling performance [256].

For the electrochemical performance analysis, electrodes with active material loading between 8.5 ± 0.5 mg cm^{-2} at coin cell level are selected. The electrochemical performance at 13 mA g^{-1} of

the de-agglomerated material is significantly lower than the original and spherical morphology materials, as there is an evident reduction of the initial and the reversible capacity after 50 cycles (**Figure 5.46**). In the case of spray dried material, similar discharge capacities as the original material are obtained after 50 cycles, 78 and 91 mAh g^{-1}, respectively. It is remarkable that there is a decrease in the coulombic efficiency when the active material is subjected to post-synthesis treatment compared to the original material. This could be related to the increase of the secondary reactions over cycling which are consuming Na ions in a larger extent.

The better electrochemical performance at the initial cycles of the electrodes with spherical morphology can be related to the ability to absorb possible volume changes related to the insertion and de-insertion of the sodium ions in the host structure. Another positive characteristic of this type of morphology is related to the mixing with the conductive additive. The well-defined boundaries of the material can ensure an enhancement of the contact between the active material and the conductive carbon over cycling. Due to this fact, the electrolyte soaking could be better, and the sodium ion transportation paths are improved [257].

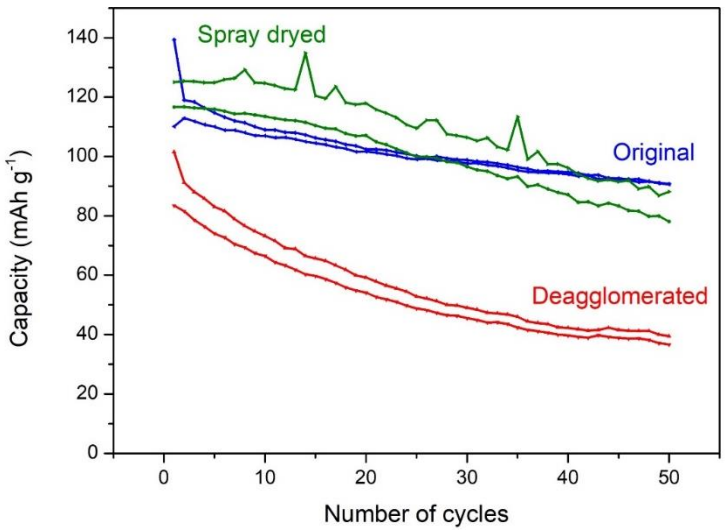

Figure 5.46. Cycling performance at 13 mA g^{-1} over 50 cycles of the half-cells with different active material morphology (4.0-2.5 V).

The C-rate performance of these cells (**Figure 5.47**) present a similar behavior than that presented at 13 mA g^{-1}. The de-agglomerated material is discarded due to the poor C-rate

capability. In the case of the cathodes with spherical morphology, the discharge capacity at 13 and 26 mA g^{-1} is comparable to the original cathode, while the discharge capacity is slightly lower at higher C-rates.

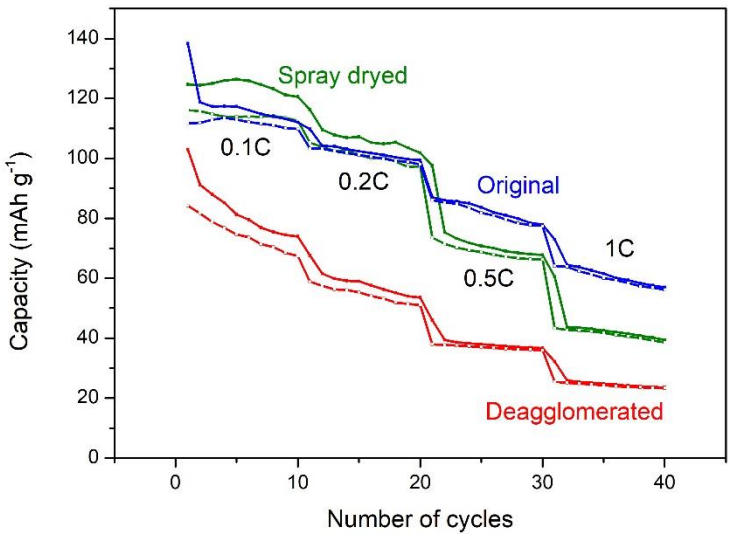

Figure 5.47. C-rate performance of the half-cells with different active material morphology (4-2.5 V).

In conclusion, despite the slightly lower electrochemical performance of the spray dried material compared to the original, both of them are selected to prepare the electrodes for full-cell assembly and subsequent electrochemical characterization in Chapter 7. The reason is that the cathode with spherical morphology allows preparing the electrodes without defects using the continuous coating machine.

5.5 Drying process influence

No experimental studies dealing with $NaFe_{0.4}Mn_{0.3}Ni_{0.3}O_2$ material and its optimal drying temperature were found in the literature. In fact, most of the research in Na-ion layered oxides cathodes is developed at different drying conditions (time, temperature, equipment, etc.). Therefore, in this section the effect of $NaFe_{0.4}Mn_{0.3}Ni_{0.3}O_2$ electrode drying conditions in the electrochemical performance of the cells is evaluated to determine the optimal temperature at which the electrodes should be dried.

5.5.1 Electrode preparation

The electrodes were prepared following the general procedure described in Chapter 2, section 2.2, using the formulation in **Table 5.12** and the mixing procedure described in **Figure 5.31** (page 190). The active material loading of the resulting electrodes was 8.47 ± 0.98 mg cm^{-2}. For this study, the electrodes were dried at room temperature under dry room conditions (dew point of ca. 60 °C and controlled temperature of 21 ± 1 °C) and at 60 °C, 80 °C, 100 °C, 120 °C and 130 °C for 10 minutes under vacuum (50 mBar).

Table 5.12. Composition of the studied cathode slurry (weight and volume percentages correspond to the dry powders and the solid content is calculated as the total dry powder mass/volume divided by the total slurry mass/volume).

Type of mixing equipment	AM content	C65 content	PVDF content	NMP	Solid content
Disperser type impeller	87.0% w/w 74.9% v/v 10 g	5.8% w/w 10.4% v/v 0.66 g	7.2% w/w 14.6% v/v 0.83 g	9.54 g	54.6% w/w 25.6% v/v

5.5.2 Electrode characterization

5.5.2.1 Morphological properties

According to Goren et al. [200] the drying temperature affects to the polymer chain mobility and the final distribution and morphology of the binder. When increasing the temperature, the polymer chains have enough mobility to occupy the free space left by the solvent, which leads to a more compact structure. The interrelation of the binder with the active material in the electrode leads to changes in the electrochemical performance. However, in the SEM images in **Figure 5.48** that show the distribution of $NaFe_{0.4}Mn_{0.3}Ni_{0.3}O_2$, the conductive additive and the binder in the electrodes dried at different temperatures, no significant differences can be observed.

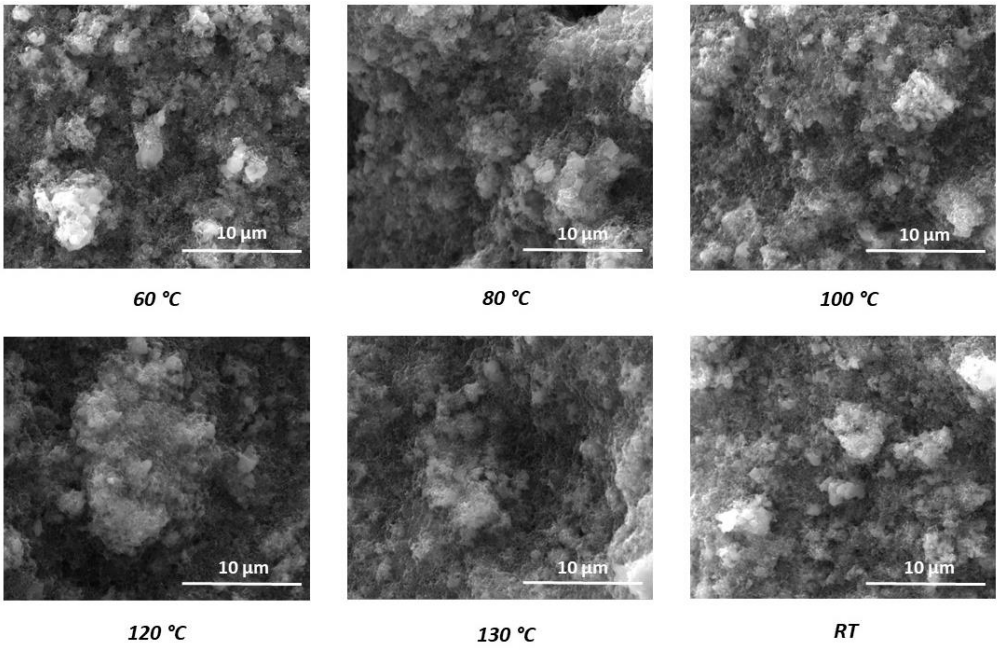

Figure 5.48. Surface SEM images of the electrodes dried at different temperatures.

The porosity of the electrodes is calculated by measuring their mass and thickness and assuming the densities of the active material, the C65 and the PVDF of 4.18 g cm^{-3}, 2 g cm^{-3} and 1.78 g cm^{-3}, respectively (**Table 5.13**). The porosity of all the electrodes is in the range of 70%. The porosity is higher in the temperature range from 80 °C to 130 °C (ca. 74%), while at room temperature and at 60 °C, it is close to 66%.

Table 5.13. Electrode porosity calculated for different drying temperatures.

Drying temperature (°C)	Porosity (%)
25	67.25
60	65.74
80	76.38
100	74.21
120	72.99
130	73.35

5.5.2.2 Adhesion/cohesion properties

The effect of the drying temperature on the mechanical properties of the electrodes have been studied by 180˚ peel tests. The load measured for the peeling process is plotted in **Figure 5.49**. The highest peeling strength is obtained for the electrodes dried at 100 °C, while the lowest peeling strength is obtained for the electrodes dried at 80 °C. But overall, all the electrodes show good adhesion and cohesion properties based on the appearance of the electrodes after the peeling test (**Figure 5.50**) in which most of the electrode remains adhered to the current collector. According to Jaiser et al., one of the reasons which might cause the adhesion to deteriorate is high drying rates [258]. However, based on these results, the drying rate is good enough in these electrodes. Moreover, as it will be discussed later, contrary to what it is expected, the electrochemical performance of the electrodes which show the best adhesion properties do not present the best cycling stability after 50 cycles. This fact suggests that a critical adhesion value is reached for all the drying conditions and minor variations in the peeling strength value do not significantly influence in the electrochemical performance of the electrodes.

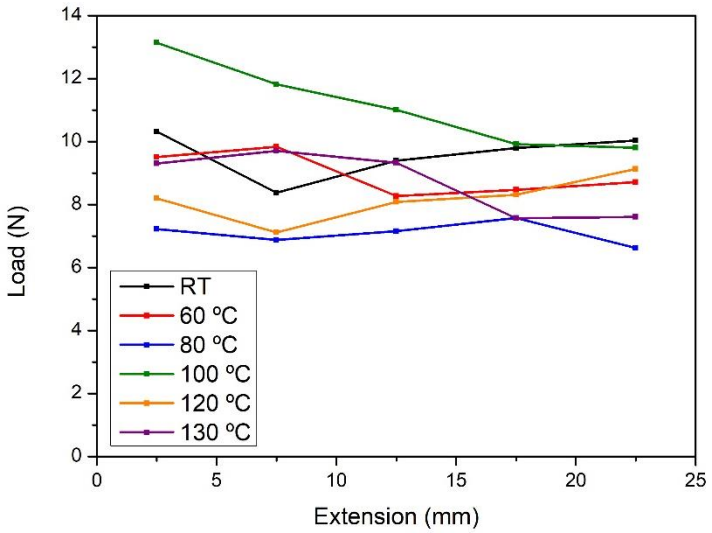

Figure 5.49. Average load measured in the 180˚ peel test on electrodes dried at different temperatures.

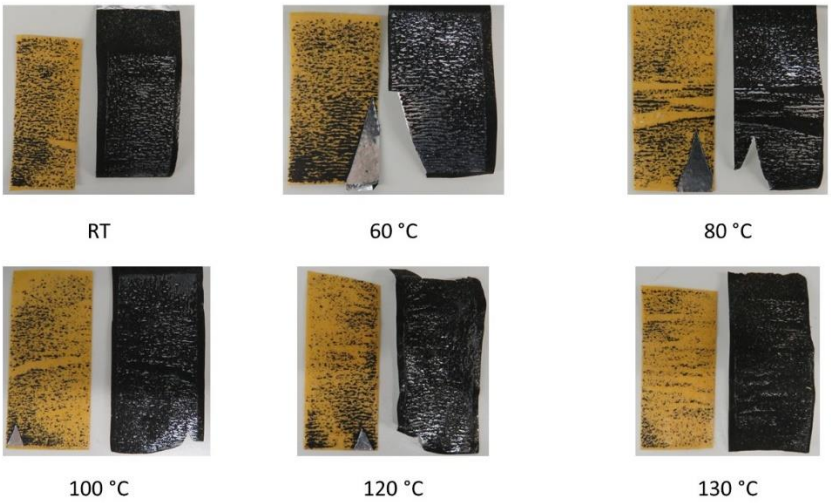

Figure 5.50. Electrode appearance after 180˚ peel test experiments.

5.5.2.3 Electrochemical performance

Figure 5.51 shows the diffusion coefficient in the charge/discharge processes depending on the drying temperature of the electrodes following the procedure described in Chapter 2, section 2.5.1.3, page 74. High diffusion coefficients allow fast Na^+ ions transport. The diffusion coefficient values measured In this study are in the range between $3.67 \cdot 10^{-12}$ to $1.94 \cdot 10^{-11}$ cm^2 s^{-1}. The highest diffusion coefficients are obtained at 60 °C in the cathodic process and at 80 °C in the anodic process. Overall, the electrodes dried at room temperature, 60 °C, 80 °C and 100 °C presents higher charge and discharge diffusion coefficients. This is consistent with the analysis of the electrochemical performance results presented in the following pages (**Figure 5.52** and **Figure 5.53**).

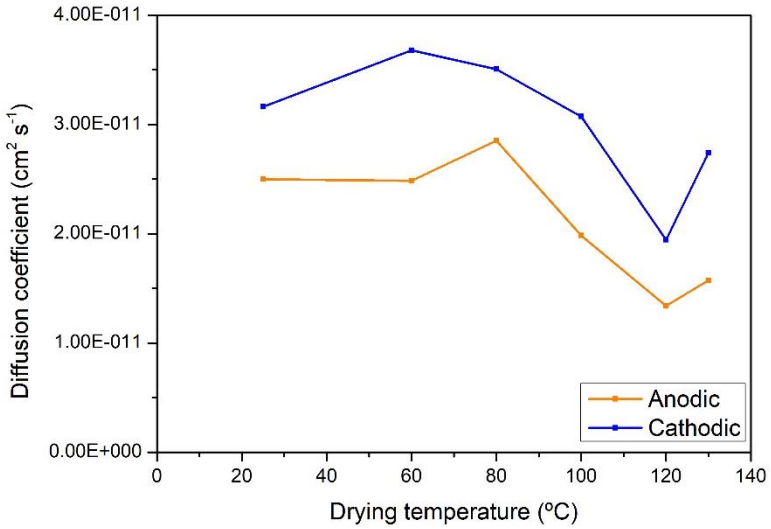

Figure 5.51. Diffusion coefficient of the electrodes dried at different temperatures taking into consideration the cathodic/anodic processes of the cyclic voltammograms.

The galvanostatic cycling stability at 13 mA g^{-1} in the voltage range between 2.5-4.0 V is represented in **Figure 5.52**. All the electrodes show similar cycling stability over 50 cycles which indicates the drying temperature does not significantly affect to this electrodes at a cycling rate of 13 mA g^{-1}. This fact is in agreement with the higher symmetry of the CV profiles at 13 mA g^{-1} which could be derived from the better de-insertion/insertion of Na^+ ions at slow C-rates.

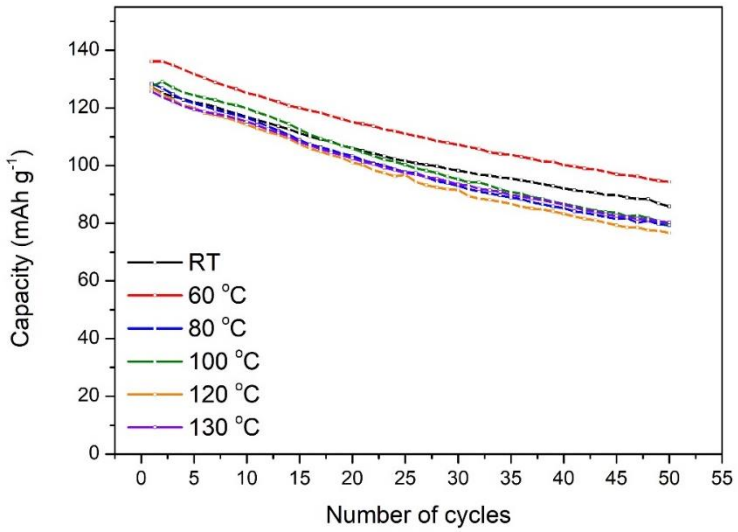

Figure 5.52. Cycling performance at 13 mA g^{-1} over 50 cycles of the half-cells with electrodes dried at different temperatures.

Galvanostatic cycles at different C-rates have been also done in the voltage range from 2.5 to 4.0 V for all the cathodes dried at different temperatures (**Figure 5.53**). It is noticeable that better C-rate capability is obtained for those electrodes dried at RT, 60 °C and 80 °C, while the electrodes dried at 130 °C and 120 °C show the worst results at higher C-rates. The electrodes dried at 60 °C and 80 °C have a discharge capacity of ca. 60 mAh g^{-1} at 130 mA g^{-1}, while for the electrodes dried at 130 °C the discharge capacity is lower than 40 mAh g^{-1}. These results are in agreement with the highest charge/discharge diffusion coefficient of the electrodes dried at 60 °C and 80 °C which are showing faster Na^+ ion diffusion that allows cycling at high C-rates.

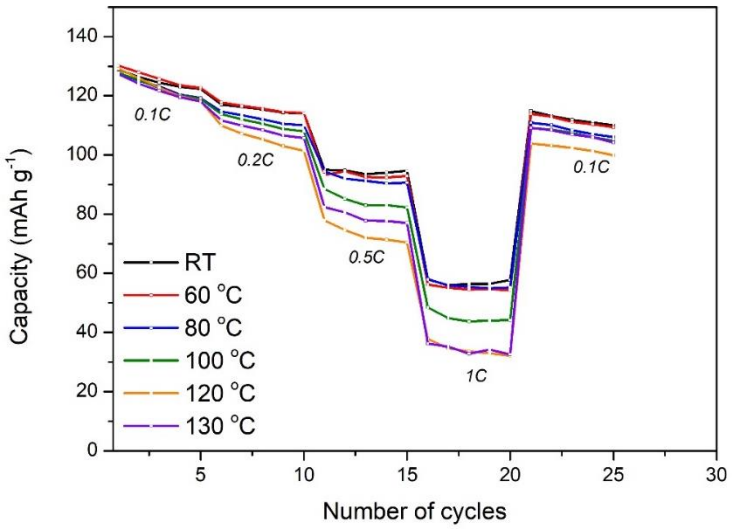

Figure 5.53. C-rate performance of the half-cells with electrodes dried at different temperatures.

The experimental results obtained in this section indicate that low drying temperatures in the range between 60-80 °C are the optimum from the perspective of the electrochemical performance of the half-cells. However, from the process ability point of view higher temperatures can be required in order to guarantee that the electrodes are completely dried in a continuous process. This represents a trade-off between the optimal temperature and the time required to dry the electrodes since higher temperatures than 60-80 °C might be needed to complete the drying process in short times.

5.6 Conclusions

The effect of different cathode processing parameters in the rheological, morphological, mechanical and electrochemical characteristics of the electrodes has been analyzed in this chapter.

First, the interaction of the C65 conductive additive and the PVDF binder was studied. The rheological properties of the slurries with different C65:PVDF ratios show that all the formulations show a shear thinning behavior and this effect is more pronounced for high C65 containing slurries. On the other hand, the electrodes with low C65:PVDF ratios (i.e. 0.2:1 and

0.4:1) show the best adhesion/cohesion properties due to the high binder content of these electrodes.

Focusing on the electrochemical performance of the electrodes with different C65:PVDF ratios, the cooperation between both inactive materials of the cathode slurry formulation results in different cell performances. In spite of having the best adhesion/cohesion properties, the electrodes with low C65:PVDF ratios, i.e. 0.2:1 and 0.4:1, present low reversible capacity and cycling stability at low C-rates and poor C-rate performance due to the ion-blocking effect of the binder and insufficient amount of conductive additive which lead to poor connectivity between the inactive particles. Although C65:PVDF ratios of 0.6:1 are suitable for low C-rate cyclability, at high C-rates, the cell performance is significantly reduced. When increasing the ratio between the carbon black and the binder to above 0.8:1, the amount of agglutinant is not enough to keep the conductive particles together and therefore, mechanical integrity of the electrode can be affected over cycling with an increment in the cell polarization. Moreover, conductive agent aggregation can also cause growth of cell resistance which can cause a failure in the electrochemical performance. The highest diffusion coefficient values calculated for C65:PVDF = 0.8:1 also agree with the best cycling and C-rate performances observed for this formulation. After 50 cycles at ca. 0.1C, this formulation presents a reversible capacity of 91 mAh g^{-1} with a capacity retention of 82.3%.

With the aim to move towards higher active material loadings and hence, higher capacities/energy densities, the active material content was increased with respect to formulations with 75-80% of active material usually employed in the development of new electrode active materials. It is important to highlight that in addition to increasing the active material loading, the slurry preparation procedure with lower C65 contents (i.e. 87%AM and 90%AM) is easier, higher solid contents can be used and the viscosity is lower. Moreover, the resulting electrodes show more homogeneous microstructure than those with high C65 contents (i.e. 75%AM). Similar cycling performances (90 mAh g^{-1} after 50 cycles) were obtained at slow C-rates for the electrodes with 75%AM, 87%AM and 90%AM and active material loading of ca. 8 mg cm^{-2}. However, the C-rate capability is significantly lower for the 90%AM electrodes due to the low conductive carbon black content and the loss of mechanical integrity. Therefore, an

active material content of 87% was selected as the optimum electrode composition which delivers 106 Wh kg^{-1} at materials level.

The disperser type impeller is considered as the best option for the mixture of the cathode components. It presents the best compromise between the components dispersion, electrode microstructure and electrochemical performance. It presents a reversible capacity after 50 cycles of 92 mAh g^{-1} with a acceptable capacity retention of 83%. However, the size of the agglomerates hinders the use of a continuous comma bar coating machine for electrode preparation. Therefore, two different approaches, the use of dispersive agents and the modification of the active material morphology, were followed with the aim to reduce the size of the agglomerates and enhance the microstructure of the electrodes. No improvement was observed with the use of dispersive agents and the spherical active material morphology (formed by spray drying treatment) resulted in electrodes with smaller agglomerates that enabled the preparation of electrodes using the continuous comma bar coating machine.

Finally, it is important to highlight the importance of the drying temperature in the electrode processing for sodium-ion batteries. Maximum diffusion coefficients are calculated for the electrodes corresponding to a drying temperature of 60 °C and 80 °C, which is consistent with the analysis of the electrochemical performance. Maximum reversible capacities of 94 mAh g^{-1} after 50 cycles were obtained for the electrodes dried at 60 °C with. Moreover, the best C-rate capabilities are also achieved for the electrodes dried at room temperature, 60 °C and 80 °C, while those dried at 130 °C and 120 °C show the worst results with higher polarization values.

Chapter 6. ANALYSIS OF THE HARD CARBON ANODE PROCESSING PARAMETERS FOR SIBs

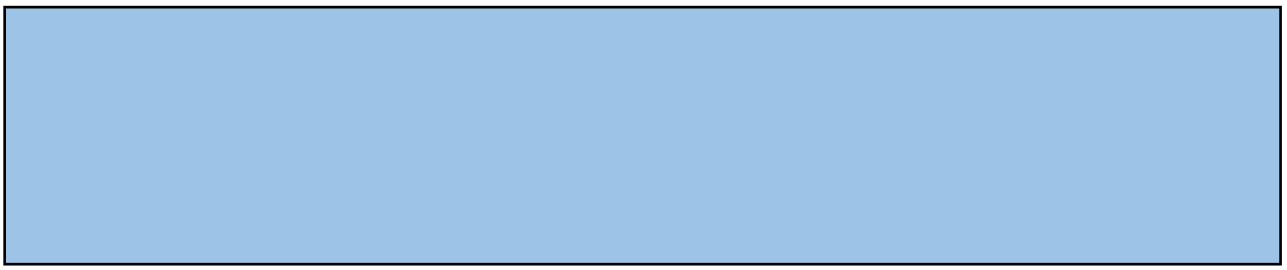

In this chapter, a hard carbon is analyzed as anodic material for Na-ion battery. Different active material contents and loadings are studied, as these parameters are important to balance in an optimal way the positive and negative electrodes in a full-cell. The effect of calendering conditions on the electrode porosity and consequent electrochemical performance are also studied. Morphological, rheological, mechanical and electrochemical characterizations are included in this chapter.

6.1 Influence of the AM content and loading

6.1.1 Slurry preparation

3 different slurries with variation in the active material and conductive additive content are evaluated in order to determine the optimal anode formulation. All the slurries were prepared using the planetary centrifugal vacuum mixer following the procedure described in **Figure 6.1**. In these experiments, the binder content and the solid content were maintained constant at 5% and ca. 54% respectively. **Table 6.1** summarizes the studied anode slurry formulations.

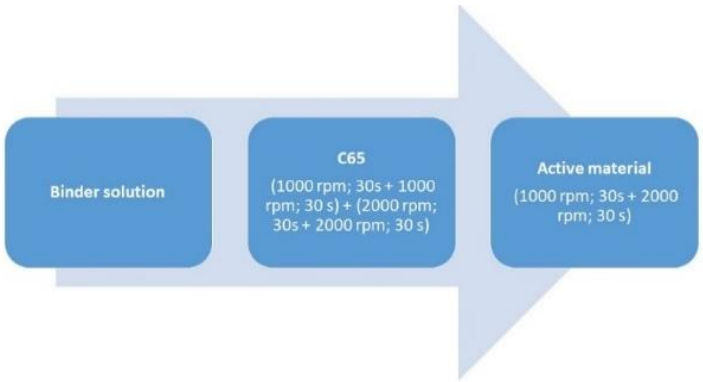

Figure 6.1. Anode slurry mixing procedure using the planetary centrifugal vacuum mixer.

Table 6.1. Composition of the studied anode slurries (weight and volume percentages correspond to the dry powders and the solid content is calculated as the total dry powder mass/volume divided by the total slurry mass/volume).

AM content	C65 content	PVDF content	NMP	Solid content
95.0% w/w	0% w/w	5% w/w	9 g	53.8% w/w 37.6% v/v
94.4% v/v	0% v/v	5.6% v/v		
10 g	0 g	0.53 g		
92.5% w/w	2.5% w/w	5% w/w	9.3 g	53.8% w/w 37.6% v/v
91.9% v/v	2.5% v/v	5.6% v/v		
10 g	0.27 g	0.54 g		
90% w/w	5% w/w	5% w/w	9.6 g	53.8% w/w 37.6% v/v
89.4% v/v	4.9% v/v	5.6% v/v		
10 g	0.56 g	0.56 g		

6.1.2 Slurry characterization

The composition of the slurries directly impacts in their rheological properties. Due to the fact that the solid content and the mixing procedure were kept constant for the three different formulations, the addition of the carbon black is expected to be the main parameter affecting the rheological properties of the formulations. **Figure 6.2** shows a pseudo-plastic behavior, also called shear thinning, for the three slurries [259]. Shear thinning materials present a decrease in the viscosity when increasing the deformation speed or shear rate. Although the fully Newtonian behavior was never observed in the studied shear rate range, at high shear rates, viscosity values tend to stabilize because of the destruction of the created structures [202,260]. The slope of the curve at high shear rates is 0.04, 0.07 and 0.1 for 0%, 2.5% and 5% of C65 respectively. The lower slope of the slurry without C65 is an indicative of the behavior of this slurry closer to that of a Newtonian fluid.

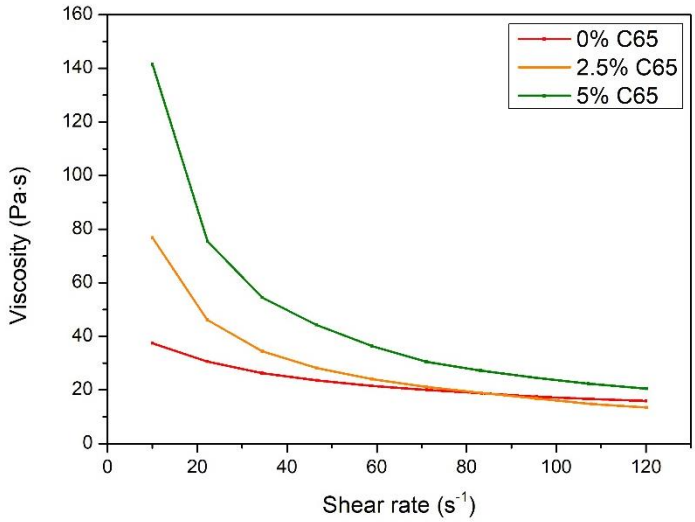

Figure 6.2. Flow curves of the anode formulations with different composition.

Figure 6.2 also shows that the slurry with no carbon black presents lower viscosity values, especially at low shear rates, which can be related to the improvement of the powder dispersion in the slurry. According to Bockholt et al., when comparing slurries with and without carbon black, those without carbon black can show a different behavior, as the Newtonian behavior starts at lower shear rates, which is related to the liquid-like behavior of this kind of dispersions. In this case, the viscosity is mainly dependent on the properties of the binder and the solvent [261]. When increasing the carbon black content to 2.5% and 5%, slurries present an important increase in the viscosity at low shear rates. This can be beneficial for electrode processing since it means a more stable structure due to the carbon agglomeration. More resistance to present sedimentation than in the case of 0% of carbon black is expected for these slurries [261].

Figure 6.3 shows the evolution of the shear stress with the shear rate. These data are fitted using the Casson model, with non-lineal profile for any formulation. Details on the Casson model characteristics and experimental procedure for rheological measurements are provided in Chapter 2, section 2.5.2, page 76. **Table 6.2** summarizes the fitting data.

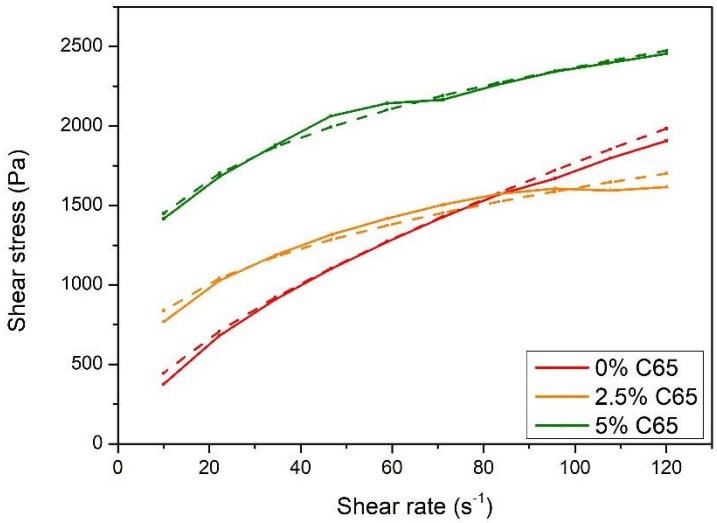

Figure 6.3. Measured shear stress curves (solid lines) and fitting to the Casson model (dashed lines).

Table 6.2 Casson model fitting parameters.

%C65	τ_0 (Pa)	n	η_p (Pa·s)
0	0.03323	0.09032	0.09506
2.5	11.62	0.07259	$1.047 \cdot 10^{-6}$
5	159.6	0.09815	$8.361 \cdot 10^{-6}$

From the fitting parameters, the yield stress (τ_0) parameter, indicator of the strength of the internal network formed by the different components of the slurry, is calculated (**Table 6.2**). The particles connected in this network are able to transmit a force and support a shear stress. Therefore, the stronger the network, the greater the stress which is required for the slurry to start to flow [164]. The critical yield stress exponentially increases from 0.03 to 159 Pa by increasing the carbon black content in the formulation (**Table 6.2**). The high yield stress is expected to be beneficial to maintain the dispersed powder particles in suspension over storage time and avoid possible sedimentation.

The rheological properties of the slurries are important to determine the coating parameters either by Doctor Blade as in this section, or by other continuous coating equipment. **Figure 6.4** shows the active material loading of the casted electrodes as a function of the Doctor Blade gap. It is observed that in the studied range, the loading of the active material progressively increases between ca. 2 and 11 mg cm^{-2}, which indicates that the rheological properties of the anode slurries are suitable for Doctor Blade casting. Spite of the fact that the slurry with 0% of C65 has the maximum active material content, lower active material loadings were obtained for the same Doctor Blade gap compared to the slurries with a C65 content of 2.5% and 5% due to the lower viscosity and yield stress of the former.

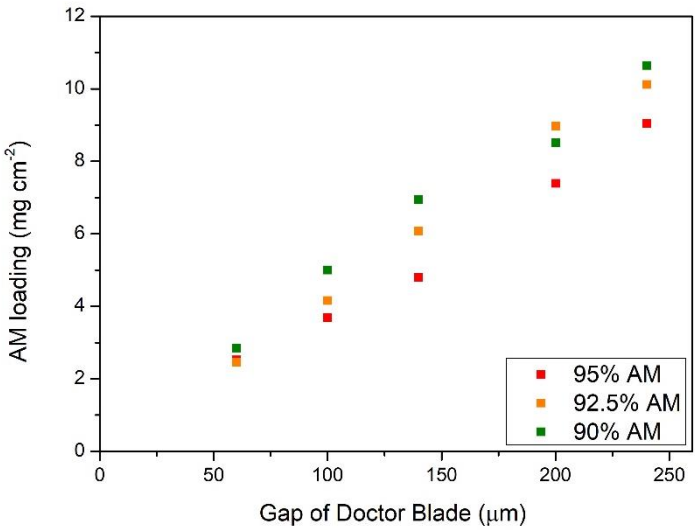

Figure 6.4. Active material loading of casted electrodes as a function of the Doctor Blade gap for different anode slurries.

6.1.3 Electrode characterization

The active material content in the anode formulation is analyzed in combination with the active material loading by means of morphological, mechanical and electrochemical properties. The active material loading is a parameter which has a large influence when assembling a full-cell prototype. As it has been shown before (**Figure 6.4**), electrodes with a wide range of active

material loadings were obtained for each formulation by setting the gap of the Doctor Blade at 60 µm, 100 µm, 140 µm, 200 µm and 240 µm. Different cell performances are expected for the electrodes with different active material loadings. By increasing this parameter, the areal capacity as well as the energy density of the cells which are some of the main objectives in the development of a new Na-ion battery should ideally increase.

6.1.3.1 Morphological properties

SEM images of different formulations for anode side shows primary particles of hard carbon with a flake shape morphology in the few micron range (**Figure 6.5**). Independently of the formulation used to develop anode coated foils, primary particles remain without forming further agglomerates. By increasing percentage of carbon black, from 0% wt. to 5% wt., the increment of the net of conductive agent around hard carbon particles is evidently shown. The main difference between 92.5%AM and 90%AM electrodes is the more disperse carbon black of the latter all around the active material and binder which could help to improve the conductive pathways between particles.

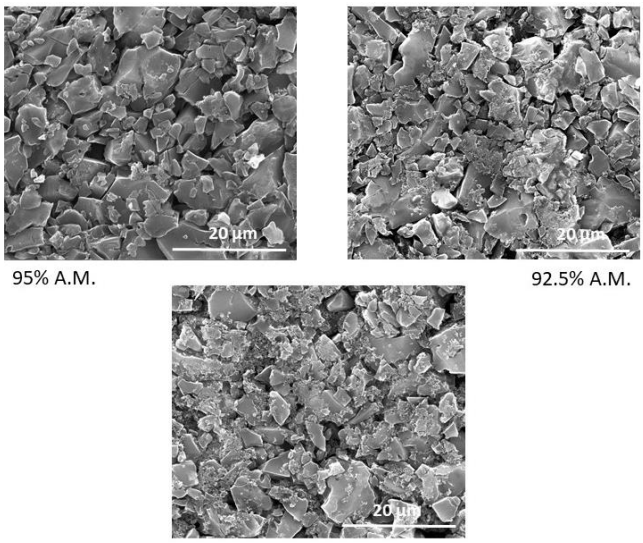

Figure 6.5. Surface SEM images of the un-calendered electrodes with different active material contents. 95%AM, 92.5%AM and 90%AM.

6.1.3.2 Adhesion/cohesion properties

As it was reported by Haselrieder et al., the adhesion properties of the coated electrodes with different loadings are important parameters that need to be considered in order to maximize the energy density of a battery as they affect to the electrochemical performance of the cells [262]. On the other hand, according to Son et al., to optimize the energy and power delivered by the cells optimal adhesion properties should be achieved, by improving the electrode composition or its interface with the current collector [263]. In this study, 180° peel tests were conducted on 95%AM, 92.5%AM and 90%AM electrodes with 2 different active material loadings. 2 ± 0.5 mg cm^{-2} and 10 ± 0.3 mg cm^{-2} were considered respectively as low and high loading electrodes. The experimental procedure is described in Chapter 2, section 2.5.3, page 80.

As it was expected, by increasing the loading of the electrodes, a decrease on the adhesion properties is produced in all the studied formulations (**Figure 6.6**). The load values measured for high loading electrodes are in the range of 1.5 N while the low loading electrodes are in the range of 3.5 N. This could happen because in the case of high loading electrodes, a homogeneous distribution of the binder in the whole electrode is more difficult due to the migration effects of the binder molecules during drying that result in lower volume concentrations at the interface of the coating and the substrate [264].

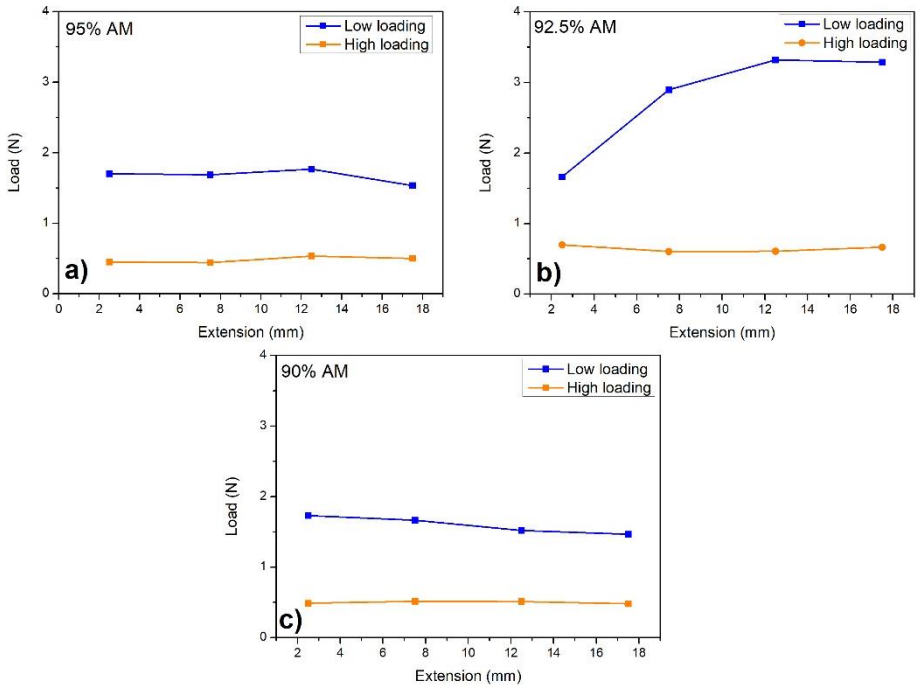

Figure 6.6. Average load measured in the 180˚ peel test on (a) 95%AM, (b) 92.5%AM and (c) 90%AM electrodes with low and high loadings.

According to the pictures of the peeled anodes (**Figure 6.7**), both low and high loading electrodes present better cohesion than adhesion properties, as all of them are completely delaminated after the peeling test.

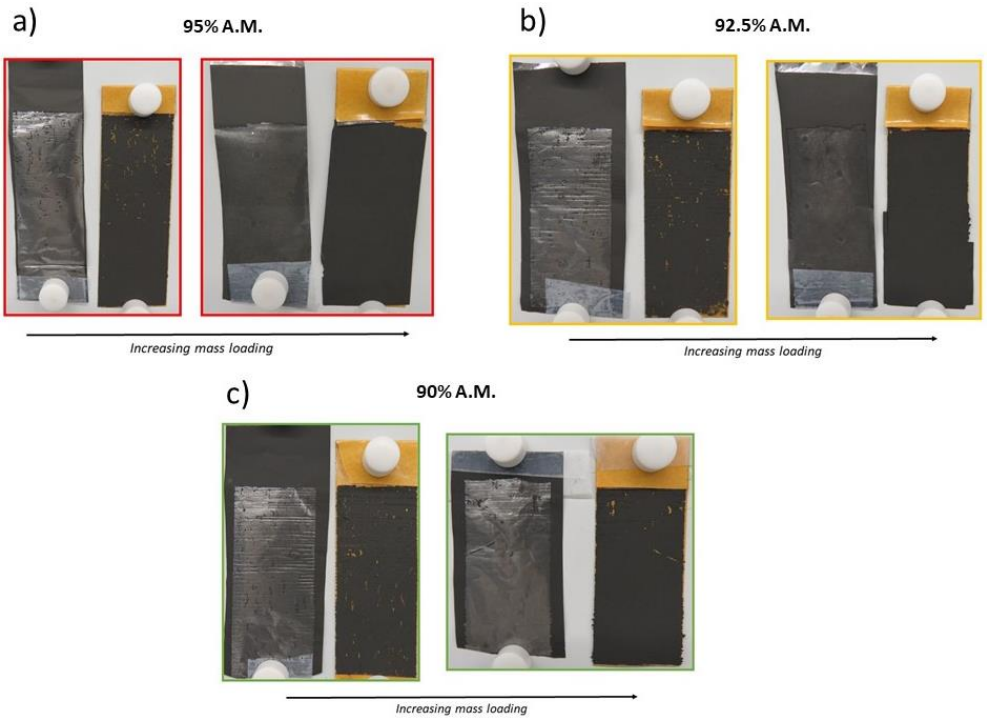

Figure 6.7. Aspect of the (a) 95%AM, (b) 92.5%AM and (c) 90%AM electrodes with low and high loadings after the 180˚ peel test experiments.

Figure 6.8 shows the standard deviation of the load measured in the 180° peel test in order to provide an indicator of the homogeneity of the electrodes. **Figure 6.8** (b) clearly shows that the 92.5%AM electrode presents more irregular profile.

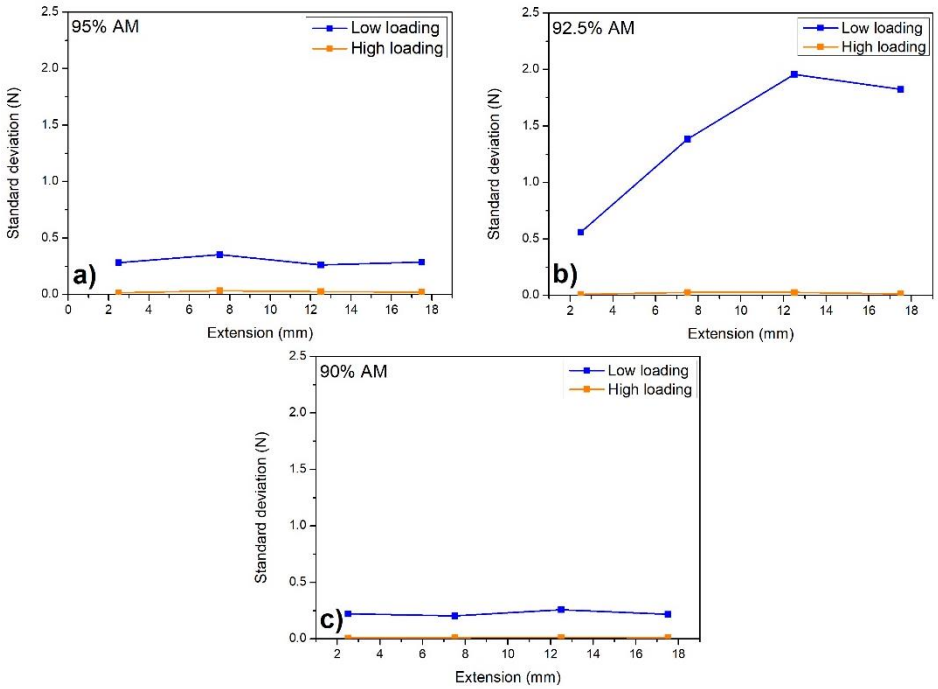

Figure 6.8. Standard deviation of the load measured in the 180° peel test on (a) 95%AM, (b) 92.5%AM and (c) 90%AM electrodes with low and high loadings.

Focusing on the effect of the formulation in the adhesion and cohesion properties (**Figure 6.6**), no significant differences are observed for high loading electrodes, while the maximum load of ca 3.2 N is measured for the 92.5%AM electrode with low loading. In the case of low loading 95%AM and 90%AM electrodes, similar load values of ca. 1.5 N are measured in the peeling test.

The 92.5%AM electrodes present the most irregular profile, probably due to the difficulties to homogenize lower quantities than 5% of carbon black in the anode formulation using the planetary centrifugal vacuum mixer. Due to this irregular behavior, electrochemical studies were focused on the 95%AM and 90%AM electrode formulations.

6.1.3.3 Electrochemical performance

For the electrochemical performance analysis of the different formulations, a wide range of active material loadings in the range between ca. 2 - 7 mg cm^{-2} were tested. In this section,

95%AM and 90%AM formulations are analyzed. As it has been mentioned in the previous section, the formulation with 2.5% of carbon black does not have enough carbon additive material to be homogeneously spread, so its influence is not as effective as in the case of 5% of carbon black electrodes. Therefore, the electrochemical performance of the 92.5%AM electrodes is not included in this section.

6.1.3.3.1 1st cycle irreversibility

As a consequence of the addition of the carbon black, there is a variation in the 1st cycle irreversible capacity as it is shown in **Figure 6.9**. The irreversible capacity decreases as the active material loading increases for both the formulations especially below ca. 4 mg cm^{-2}. Above 4 mg cm^{-2}, the 1st cycle irreversibility is more stable. This 1st cycle irreversible capacity is related to the SEI formation, which is larger in the case of low active material loadings and allows to avoid secondary reactions in a further extent [265].

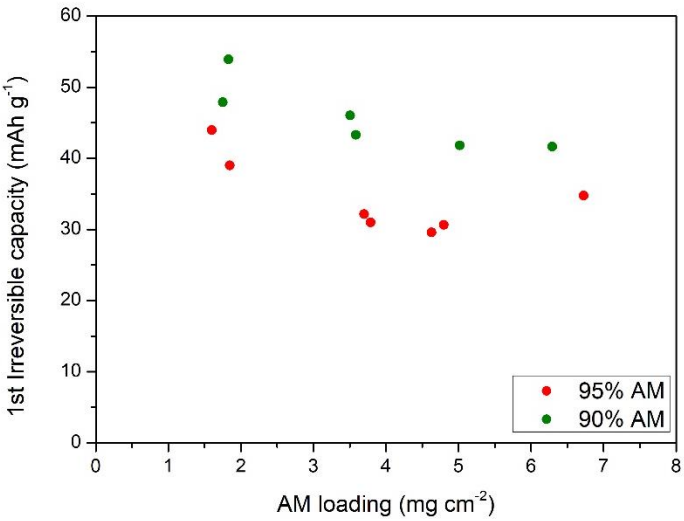

Figure 6.9. 1st cycle irreversible capacity as a function of the active material loading for 2 different formulations: 95%AM and 90%AM.

Independent of the active material loading, the 1st cycle irreversible capacity is higher for the carbon black containing electrodes. In the case of 95%AM, the irreversible capacity ranges from 30 mAh g^{-1} to 44 mAh g^{-1}, while in the case of 90%AM, it ranges from 42 mAh g^{-1} to 54 mAh g^{-1}.

As Fransson et al. reported, carbon black shows a large 1st cycle irreversible capacity when cycled in the low-potential region [266]; therefore, the increase of the 1st cycle irreversible capacity when adding the carbon black is consistent with these findings.

According to Alcántara et al. the principal factor that causes high 1st cycle irreversible capacity is related to the external carbon surface area of the disordered structure with bent layers and the low density of the carbon black [265]. **Figure 6.10** (a) and (b) show the voltage profile and the differential capacity curve of the carbon black used in this work during the 1st cycle. A mixture of carbon black and PVDF (70:30) was coated on top of aluminum foil and resulting electrodes were cycled versus metallic Na for this experiment. An irreversible capacity of 203 mAh g^{-1} is observed in **Figure 6.10** (a) and the differential capacity curve (**Figure 6.10** (b)) shows a big peak at ca. 0.5 V, which corresponds to the SEI layer formation. During the following cycles, reversible insertion/extraction of Na^+ ions takes place and only one peak at < 0.1 V is visible in the differential capacity curve in **Figure 6.10** (b). Although the 1st cycle irreversibility of the carbon black used in this work is lower than those reported by Alcántara et al., the higher irreversibility of the electrodes with the conductive additive was attributed to the presence of this component [265]. In spite of this, it is expected that it can have a positive influence in the reversible capacity values of the hard carbon.

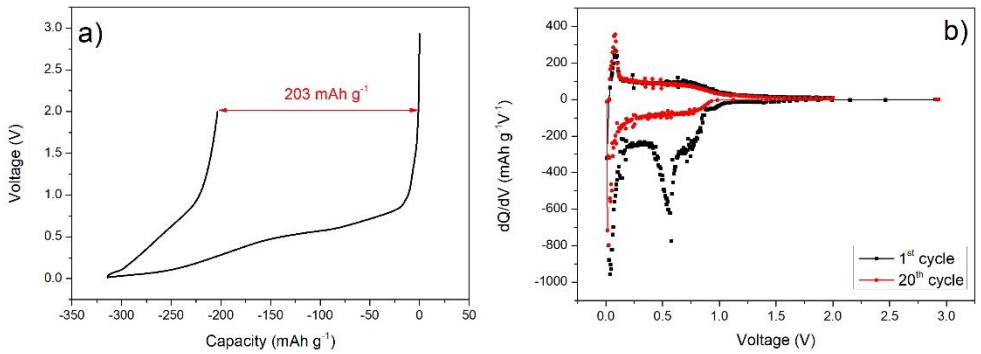

Figure 6.10. (a) 1st cycle galvanostatic curve of carbon black and (b) differential capacity curve of carbon black in the 1st and 20th cycles.

6.1.3.3.2 Diffusion coefficient calculation

Cyclic voltammetry tests were conducted at a scanning rate of 0.1 mV s^{-1} for 95%AM and 90%AM electrodes and the 1st, 2nd and 5th cycle were plotted in order to elucidate some differences in the SEI formation depending on the anode formulation and the active material loading. Electrodes with 2.4 mg cm^{-2} and 5.8 mg cm^{-2} were used for these tests.

According to Pan et al., during the first reduction step, sodium ions are intercalated into the graphene layers of the hard carbon. The pair of redox peaks close to 0 V, 0.20/0.0 V, are related to the cathodic and anodic insertion and de-insertion of the Na ions into the graphitic layers and the deposition of the Na metal clusters into micro voids [267]. The peak at, approximately, 0.1 V is characteristic of pore filling and on the reverse oxidation curve, there is a peak at 0.2 V which is related to the de-insertion of sodium ions from the pores [268]. In the 1st cathodic process, there is an additional broad peak, at approximately 0.75 V, which is related to the SEI formation, proportional to the surface area of the carbon material used, according to Bommier et al. [125].

In the case of 95%AM electrodes with no carbon black (**Figure 6.11** (a)), the peaks attributed to the sodium ions insertion and de-insertion into the pores of the hard carbon [125] at 0.01 V and 0.25 V, are in the same voltage position although they are more intense in the case of higher active material loadings. The same happens in the following cycles. So, the main difference in the cyclic voltammetry profiles observed when increasing the active material loading is the increment of the polarization and the peak intensity. The 2nd and 5th cyclic voltammetry curves are almost overlapped independently of the active material loading which indicates a good capacity retention over cycling of the hard carbon anode [269] in the studied active material loading range.

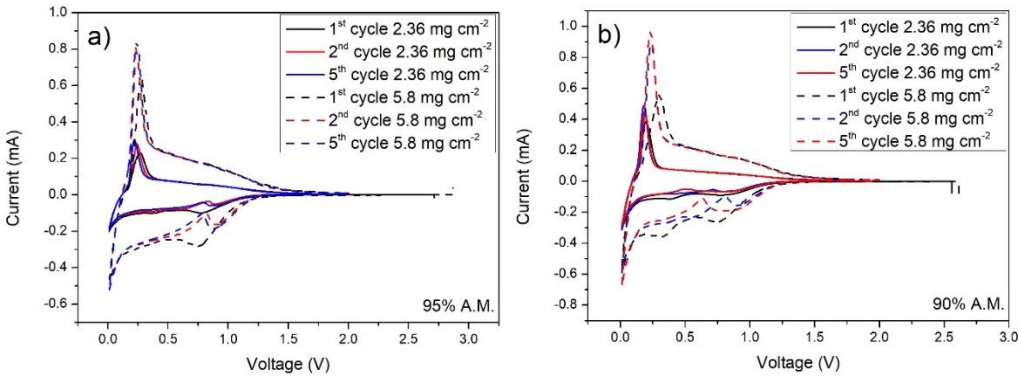

Figure 6.11. 1st, 2nd and 5th cyclic voltammetry curves of the (a) 95%AM and (b) 90%AM electrodes with different active material loadings.

In the case of the 90%AM electrodes with 5% of carbon black (**Figure 6.11** (b)), it can be observed that the curves are not totally overlapped, which is related to the irreversible character of the electrochemical reaction [270]. An additional reduction peak, at ca. 0.3 V can be observed in the first cycle independent of the active material loading. This peak is attributed to the presence of the carbon black [266].

Diffusion coefficients (**Figure 6.12**) are calculated from the relationship between peak current and square root of the scan rate for the anode formulations and active material loadings based on the Randles-Sevcik equation (see additional information in Chapter 2, section 2.5.1.3, page 74). Samples showing higher values of diffusion coefficient have higher sodium ion kinetics.

For the low active material loading electrodes, the diffusion coefficient values are in the range between $8.8 \cdot 10^{-11}$ and $1.34 \cdot 10^{-10}$ cm^2 s^{-1}, with slightly higher diffusion coefficient values for the 90%AM electrodes measured in the cathodic process. In the case of 90%AM electrodes, the presence of carbon black in the electrode composition could help to the sodium ions to diffuse in a further extent. For high active material loadings, the diffusion coefficients are in the range between $3.66 \cdot 10^{-11}$ and $6.67 \cdot 10^{-11}$ cm^2 s^{-1}, one order of magnitude lower than those values measured for low active material loading electrodes for both formulations, supporting the negative effect of this increment on the electrochemical performance.

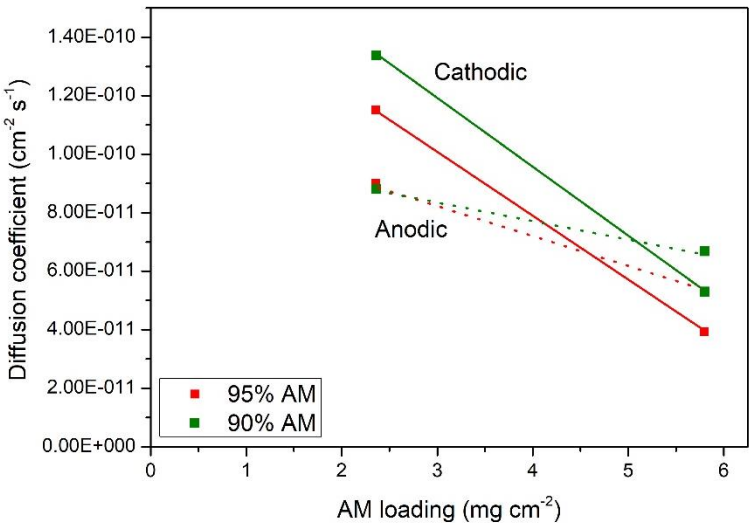

Figure 6.12. Diffusion coefficient measured for the cathodic/anodic processes for different anode formulations and active material loadings.

6.1.3.3.3 Rate capability

The hard carbon electrodes were cycled at different C-rates in half-cell configuration. The rate capability tests were done at 25 mA g^{-1}, 50 mA g^{-1}, 125 mA g^{-1} and 250 mA g^{-1} (10 cycles at each current) to observe how the material behaves at different cycling rates using different formulations and active material loadings (**Figure 6.13** and **Figure 6.14**).

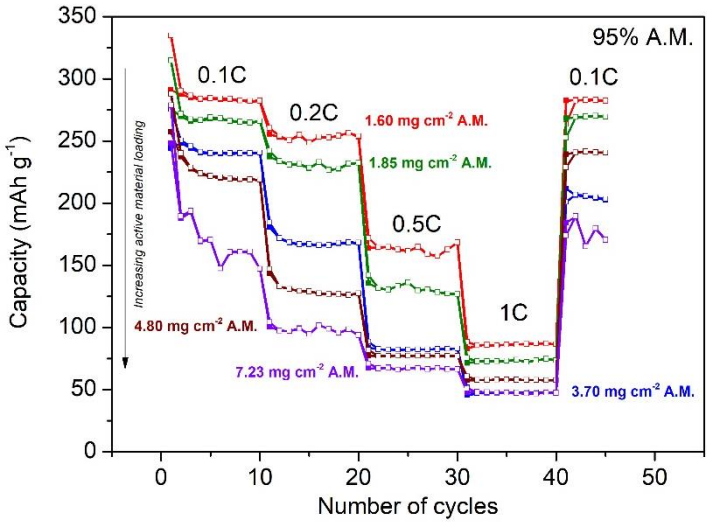

Figure 6.13. C-rate performance of the 95%AM half-cells with different active material loadings.

Figure 6.13 shows the C-rate capability of the 95%AM electrodes with different active material loadings. A decrease of the reversible capacity is clearly visible when increasing the active material loading. Concretely, the maximum value of the 1st discharge capacity of 334 mAh g^{-1} is obtained for the electrode with 1.60 mg cm^{-2} at 25 mA g^{-1} while for intermediate active material loadings of 3.70 mg cm^{-2}, the 1st discharge capacity is 275 mAh g^{-1} at the same cycling rate. For higher active material loadings of 7.23 mg cm^{-2}, the 1st discharge capacity value reaches 325 mAh g^{-1}; however, there is a significant capacity fade and the 2nd discharge capacity decreases to 290 mAh g^{-1}. The capacity fade in the initial 10 cycles at low C-rates as well as the capacity fade after the C-rate capability test is also higher for high active material loading electrodes. The reversible capacity at high C-rates of 250 mA g^{-1} ranges from ca. 80 to 50 mAh g^{-1} respectively for low and high active material loading electrodes.

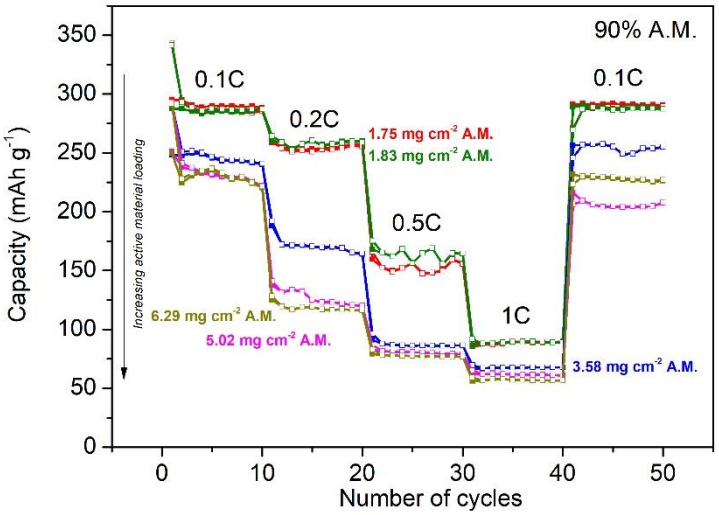

Figure 6.14. C-rate performance of the 90%AM half-cells with different active material loadings.

A similar trend as that observed for the electrodes with 0% of C65 is observed for the 90%AM electrodes with 5% of C65 (**Figure 6.14**). Overall, there is a general decrease of the reversible capacity at each C-rate, as well as a decrease in the capacity recovery at 25 mA g^{-1} after the cycles at high C-rates when increasing the active material loading. However, the capacity is more stable at each C-rate for these electrodes. Again, the reversible capacity at high C-rates of 250 mA g^{-1} ranges from ca. 80 to 50 mAh g^{-1} respectively for low and high active material loading electrodes.

The decrease in the reversible capacity observed in **Figure 6.13** and **Figure 6.14** as the active material loading increases is related to the increment of the cell resistance because of the increment of the electrode thickness consequence of the increment of the active material loading. Moreover, as it was analyzed in the previous section (see section 6.1.3.2 page 223), the adhesion strength of the coated foil to the current collector is deteriorated by increasing the loading of the electrodes. This issue can also contribute to the poor reversible capacities obtained for high active material loadings.

Aside from that, another effect associated to the low active material loadings is that there is a higher variability at 25 mA g^{-1} and 50 mA g^{-1}. As Long et al. stated, as the electrode active mass decreases, in their case, the inherent error in capacity increases. They concreted that the

capacity of any two cells in a given test set can differ by ~5 mAh g^{-1} and still be considered comparable. [271].

Figure 6.15 shows the 1st cycle voltage profiles at different C-rates for the 95%AM and 90%AM electrodes with an active material loading of ca. 3.5 mg cm^{-2}. Two main regions can be differentiated in the voltage profile apart from the first voltage drop from OCV to ca. 1 V: the sloping region and a plateau. The sloping region is related to the intercalation of sodium ions into the graphene layers and the plateau is related to the filling of the pores [122]. Most of the capacity delivered by hard carbons usually corresponds to the plateau region. However, at high C-rates, this plateau region is smaller or almost disappears; therefore, the capacity of the cells is lower. Zhu et al. also reported that at high C-rates, the capacity corresponding to the plateau region decays rapidly [270].

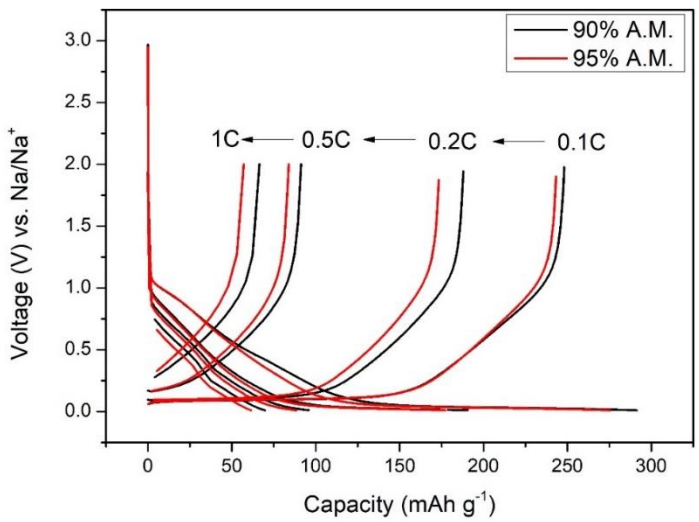

Figure 6.15. Voltage profiles of the 95%AM and 90%AM electrodes measured at different current densities, 25, 50, 125 and 250 mA g^{-1}.

The reversible capacity measured at the 10th cycle of the 95%AM and 90%AM anode half-cells is represented as a function of the active material loading and the C-rate in **Figure 6.16**. The graphs show that the addition of carbon black to the slurry does not play a significant role in the

reversible capacity and that it decreases with the active material loading; however, the capacity fade is more or less pronounced depending on the C-rate.

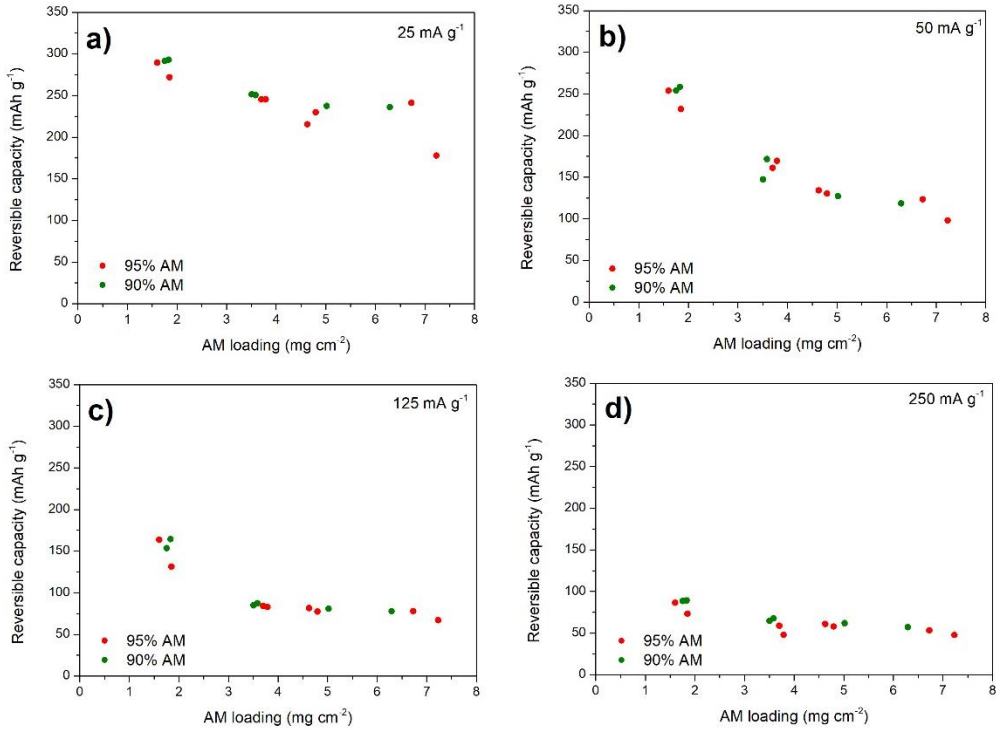

Figure 6.16. Reversible capacity measured as a function of the active material loading for the 95%AM and 90%AM electrode half-cells at a) 25 mA g^{-1}, b) 50 mA g^{-1}, c) 125 mA g^{-1} and d) 250 mA g^{-1}.

At low C-rates of 25 mA g^{-1} there is a contribution of the sloping region and the plateau in the whole range of active material loadings. However, as the C-rate increases, the contribution of the plateau region in the total capacity is lower, and this decrease is more pronounced for high active material loading electrodes. That is the reason why at 50 mA g^{-1} the capacity fade as a function of the active material loading is higher. At 125 mA g^{-1} the contribution of the plateau is only visible for ca. 2 mg cm^{-2} active material loading electrodes, while at 250 mA g^{-1} only the sloping region contributes to the total capacity of the cell and it is barely affected with the active material loading.

In spite of the decrease of the specific reversible capacity when increasing active material loading, it is important to highlight that the areal capacity, which is a key parameter for high

energy density full-cell assembly increases as can be seen in **Figure 6.17**. In this work, the highest areal capacities obtained with good cycling stability are in the range of 1.2 mAh cm^{-2} with an active material loading of ca. 5 mg cm^{-2}.

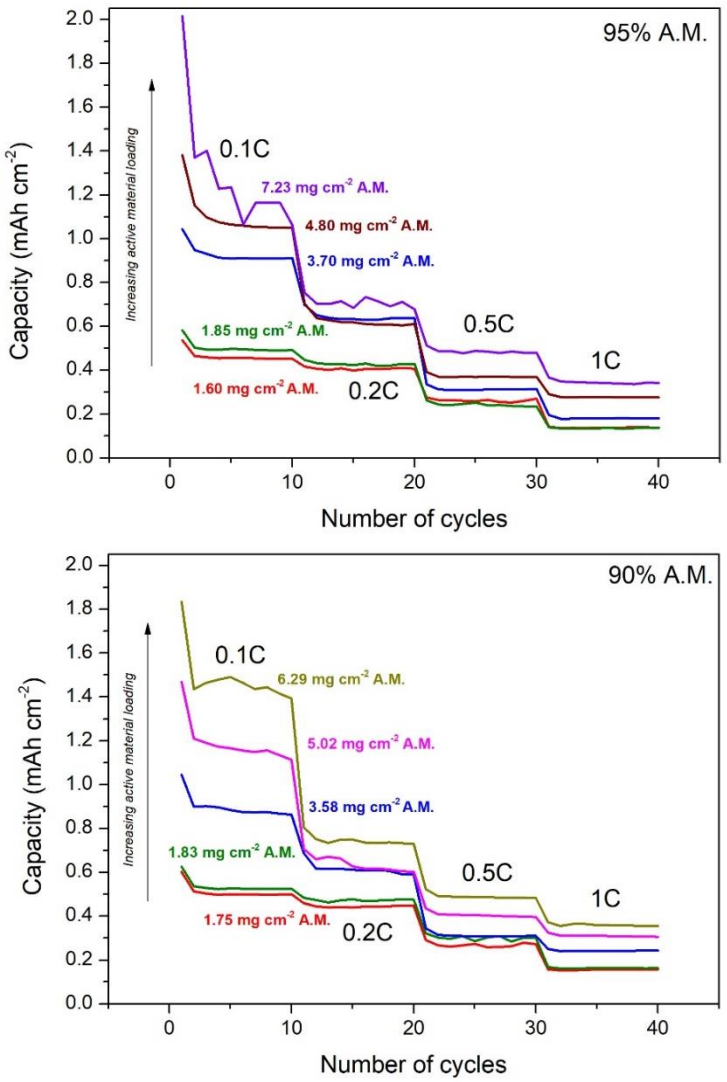

Figure 6.17. C-rate performance of the 95%AM and 90%AM half-cells with different active material loadings expressed as a real capacity in mAh cm^{-2}.

6.2 Effect of calendering in electrode properties

Once anode coated foils are casted and dried, the calendering process is necessary to improve the adhesion to the current collector, to adjust the porosity and to increase the volumetric energy density. Calendering is expected to affect to different electrode properties such as the conductivity, the electrode surface homogeneity, the total porosity, the pore size, etc. [272]. Shim et al. for example, found that the electrochemical performance of highly pressed graphite electrodes decreases compared to moderate-pressed electrodes. This fact can be caused by the trade-off between the ohmic and polarization resistances in the porous electrodes [273]. Damages caused in the structure can also be the reason for poor performance of highly pressed electrodes according to Gnanaraj et al [274]. Therefore, the optimum porosity should balance the decrease of the ohmic resistance promoted by highly porous electrodes and the increase of the polarization (resistance of Na^+ ions transport in the electrolyte through the electrode) which is expected as the porosity and thickness of the electrodes decrease [273].

Figure 6.18 shows the C-rate performance of pressed and non-pressed 95%AM hard carbon electrodes corresponding to a porosity of 37.5% and 45% respectively with 6.7 mg cm^{-2} active material loading. The cycling stability decreases in a larger extent in the case of the non-pressed electrode, especially at 25 mA g^{-1}, from 268 mAh g^{-1} in the 1st cycle to 104 mAh g^{-1} in the 10th cycle (capacity retention of 40%). On the contrary, in the case of the pressed electrode, the reversible capacities in the 1st and 10th cycles are 269 and 216 mAh g^{-1} respectively, and the capacity retention is close to 80%. In addition to this, in the case of the un-pressed electrode, there is a capacity fade of 79.5% from 25 mA g^{-1} to 50 mA g^{-1} and no capacity is delivered at 125 mAh g^{-1} and 250 mAh g^{-1}. In the case of the pressed electrode, the cell delivers a capacity of 30 mAh g^{-1} at 250 mAh g^{-1}.

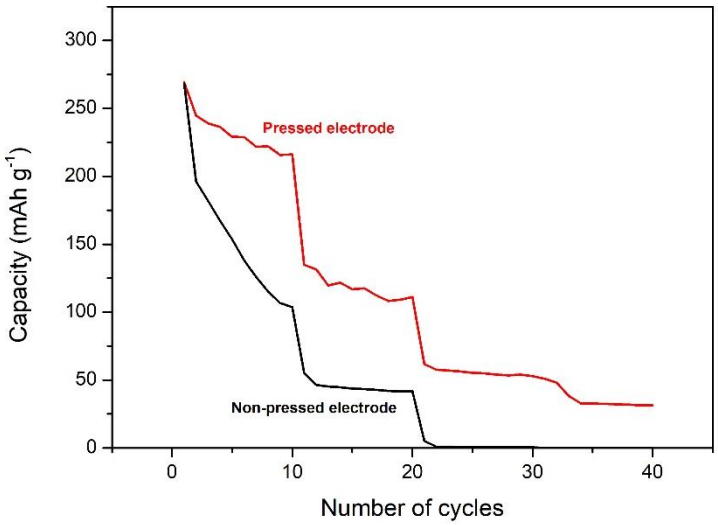

Figure 6.18. C-rate performance of the pressed and non-pressed anode half-cells.

Several reasons can explain the different cycling behavior of the two cells. In the un-pressed electrode, the porosity and therefore the surface area available for the side reactions with the electrolyte is higher, forming an insulating layer in a further extent. The insulating layer hinders the Na^+ ions intercalation in the anode and hence, there is a more pronounced deterioration of the capacity values. On the contrary, the structure of the pressed electrode is less porous and the side reactions take place in a lesser extent. The formation of a thinner insulating layer allows an easier intercalation of the Na^+ ions in the anode improving the cell performance. In addition to this, lower thickness and the improved contact between particles in the case of the pressed electrode is expected to increase the electronic conductivity and enhance the cell performance [275]. Finally, the adhesion in the pressed electrode to the current collector is expected to be better than that in the non-pressed electrode, which reduces the contact resistance and enhances the cycling stability and C-rate performance of the half-cells.

Based on these results, the effect of the calendering conditions in the anode properties was analyzed. For this study 95%AM electrodes with an active material loading of 6.7 mg cm^{-2} and an average thickness of 102 µm, including the 16 µm thick current collector, were selected. The slurry was prepared following the procedure described in section 6.1.1 (**Figure 6.1**) and with the aim of reducing the variability of the electrode thickness, the continuous comma bar coating

machine was used for electrode preparation (see Chapter 2, section 2.2.2, page 59 for more details). The density of these non-calendered electrodes is 0.82 g cm^{-3}, which corresponds to a porosity of 45% assuming hard carbon material density of 1.48 g cm^{-3}.

With the aim of using a systematic approach to select the experimental conditions and to perform the results analysis, Design of Experiments (DOE) methodology was implemented in this study. In this case, a Complete Factorial Design of Experiments (CFD) was used. 4 factors (calendering parameters) were studied at 2 levels. The studied factors, (A) gap between rollers (µm), (B) temperature (°C), (C) rollers speed (cm s^{-1}) and (D) number of repetitions and the 2 levels at which the experiments are performed are displayed in **Table 6.3**.

Table 6.3. Factors and levels selected to perform the CFD.

Adjustable parameter	Renamed parameter	Minimum level	Maximum level
Gap between rollers	A	40 µm	70 µm
Temperature	B	60 °C	100 °C
Roller speed	C	1.1 cm s^{-1}	1.4 cm s^{-1}
Number of repetitions	D	4	8

The CFD consists of all possible combinations of levels for all factors and allows analyzing the effect of the individual factors and their interactions in the calculated response. In this study, the 1^{st} order interactions will only be taken into consideration. The total number of experiments in a CFD is determined by the number of factors, 4 in this case and the levels at which each factor is tested (possible values associated to each parameter), in this case 2. Therefore, this CFD consists in a total of 2^4 = 16 experiments.

Table 6.4. Summary of the CFD experiment conditions.

EXP	Gap between rollers (μm)	Temperature (°C)	Rollers speed (cm s^{-1})	Number of repetitions
1	40	60	1.1	4
2	40	60	1.1	8
3	40	60	1.4	4
4	40	60	1.4	8
5	40	100	1.1	4
6	40	100	1.1	8
7	40	100	1.4	4
8	40	100	1.4	8
9	70	60	1.1	4
10	70	60	1.1	8
11	70	60	1.4	4
12	70	60	1.4	8
13	70	100	1.1	4
14	70	100	1.1	8
15	70	100	1.4	4
16	70	100	1.4	8

Table 6.4 summarizes the calendering conditions of the 16 experiments performed for this analysis. The effect of the calendering parameters on the electrode thickness and porosity, on the electrode microstructure and the electrochemical performance was analyzed with the aim to optimizing the calendering process conditions. The results of the experiments are displayed in **Table 6.5**.

Table 6.5 Summary of the CFD experiment results.

EXP	A	B	C	D	Thickness (µm)	Porosity (%)	1st cycle irreversibility (mAh g^{-1})	Reversible capacity (mAh g^{-1})
1	40	60	1.1	4	92.9	37.42	32.21	176.60
2	40	60	1.1	8	90.2	35.17	32.64	207.81
3	40	60	1.4	4	86.7	32.01	34.23	221.69
4	40	60	1.4	8	89.9	34.91	32.29	220.15
5	40	100	1.1	4	90.89	35.76	31.22	182.72
6	40	100	1.1	8	88.33	33.52	30.75	159.43
7	40	100	1.4	4	90.45	35.39	31.00	138.08
8	40	100	1.4	8	91	35.86	28.44	141.10
9	70	60	1.1	4	94.89	38.98	32.13	130.39
10	70	60	1.1	8	94	38.29	32.42	211.55
11	70	60	1.4	4	94.75	38.87	31.93	130.38
12	70	60	1.4	8	93.3	37.74	32.17	171.32
13	70	100	1.1	4	93	37.50	31.42	229.60
14	70	100	1.1	8	92.22	36.87	32.06	217.28
15	70	100	1.4	4	92	36.69	31.45	136.66
16	70	100	1.4	8	91.36	36.16	31.75	188.69

In the following sections, the effect of the calendering conditions on different electrode properties is analyzed.

6.2.1 Thickness and porosity

As the porosity of the electrodes is calculated based on the electrode mass and thickness measured after the calendering process, the same conclusions can be extracted from the analysis of the electrode thickness and porosity. The effect of the individual factors and the 1st order interactions on these two responses are represented in equations (6.1) and (6.2).

$$\partial = 91.62 + 3.14A - 0.92B - 0.87C - 0.66D - 1.17AB + 0.20AC - 0.28AD + 0.96BC - 0.20BD + 1.07CD \quad (6.1)$$

$$\Phi = 36.32 + 2.63A - 0.71B - 0.74C - 0.51D - 0.96AB + 0.19AC - 0.23AD + 0.85BC - 0.22BD + 0.9CD \quad (6.2)$$

The highest the absolute value which multiplies the individual factors (A, B, C, D) and the 1st level interactions (AB, AC, AD, BC, BD and CD) in equations (6.1) and (6.2), the highest is the effect of this factor/interaction in the analyzed response. Therefore, based on these two equations, factor 'A' (gap between the rollers) is clearly the parameter which has the most significant effect in the electrode thickness and porosity. Moreover, since the sign corresponding to this factor is positive, it means that the higher the gap between the rollers, the higher the thickness and porosity of the resulting electrodes will be. Likewise, the lower the gap between the rollers, the lower the thickness and porosity of the resulting electrodes will be. Consequently, in order to decrease the thickness and the porosity of the electrodes, it will be necessary to decrease the gap between the rollers.

Figure 6.19, **Figure 6.20**, **Figure 6.21** and **Figure 6.22** represent the thickness of the electrodes after calendering. The numbers beside the points correspond to the experiment number according to **Table 6.4** and **Table 6.5** and the lines are visual guides that indicate that only one factor was modified in the two experiment pairs that are joined by them.

The conclusion extracted from equation (6.1) agrees with the experimental data represented in **Figure 6.19**. The average thickness/porosity of the electrodes calendered with a gap between the rollers of 40 µm (90.04 µm/35.00%) is lower than that obtained for those calendered with a gap of 70 µm (93.19 µm/37.64%). It is remarkable that although one could expect a final thickness of 40.8% and 71.4% with respect to the initial thickness respectively for 40 and 70 µm, the electrodes were not compressed at that extent and minimum thickness/porosity of 86.7 µm/32.01% is obtained, corresponding to 88.4% of the initial thickness.

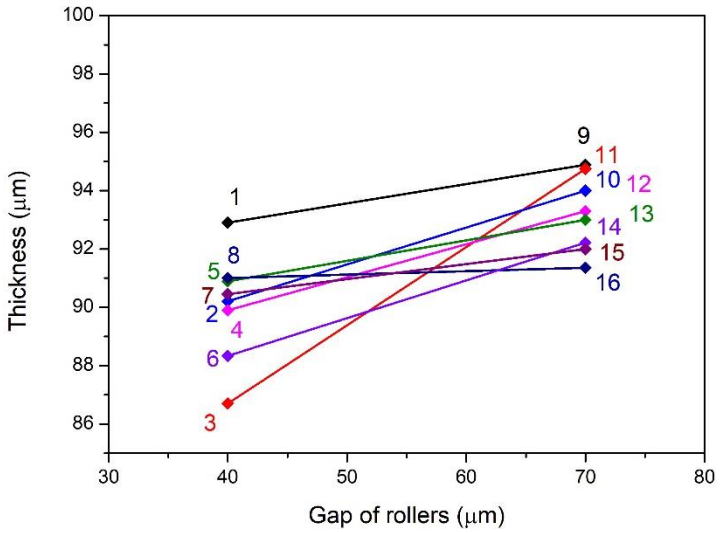

Figure 6.19. Effect of the gap between rollers in the electrode thickness.

The influence of the temperature of the rollers, parameter B, in the electrode thickness is analyzed in **Figure 6.20**. For most of the calendering conditions, when increasing the temperature from 60 to 100 °C, the electrode thickness and porosity decrease; hence, it is another key parameter to obtain the desired electrode density. While at 60 °C, the electrode thickness/porosity is in the range from 86.7 μm/32.01% to 94.89 μm/38.98%, with an average of 92.08 μm/36.67%, at 100 °C, the thickness range is narrower (from 88.3 μm/33.52% to 93 μm/37.5%) and the average value slightly lower (91.16 μm/35.97%).

When the gap between the rollers is 70 μm, when increasing the calendering temperature from 60 to 100 °C, the thickness and porosity of the electrodes systematically decreases. Moreover, the effect of the rollers speed and number of repetitions corresponds to what expected, i.e. thickness and porosity decrease at low speeds and high number of repetitions. Contrarily, when the gap between the rollers is 40 μm, when increasing the calendering temperature from 60 to 100 °C, the thickness of the electrodes decreases at low speeds and increases at high speeds.

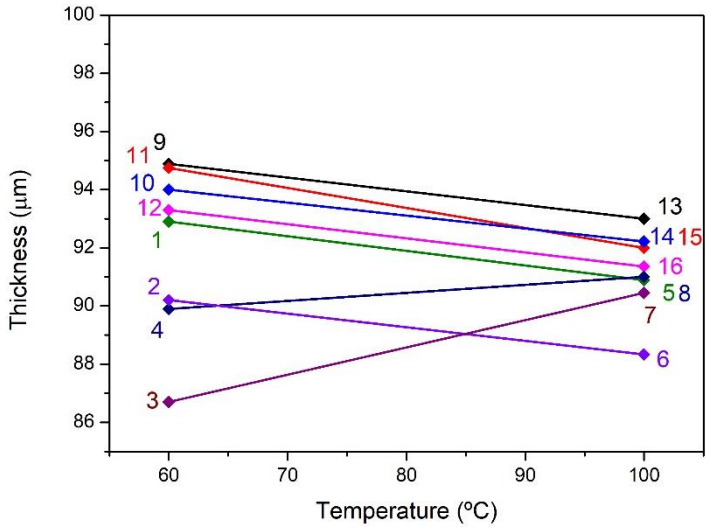

Figure 6.20. Effect of the calendering temperature on the electrode thickness.

The effect of the rollers speed and the number of repetitions (C and D) in the electrode thickness/porosity is less clear. **Figure 6.21** shows that except from the 1-3 and 6-8 experiment pairs, when increasing the rollers speed the electrode thickness hardly varies. The effect of the number of repetitions is slightly higher. **Figure 6.22** shows that except from the 3-4 and 7-8 experiment pairs, when increasing the number of repetitions, the electrode thickness slightly decreases.

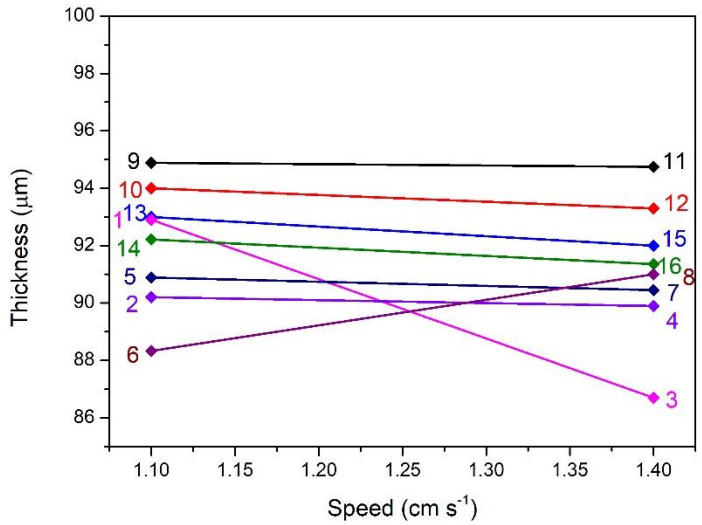

Figure 6.21. Effect of the calendering speed in the electrode thickness.

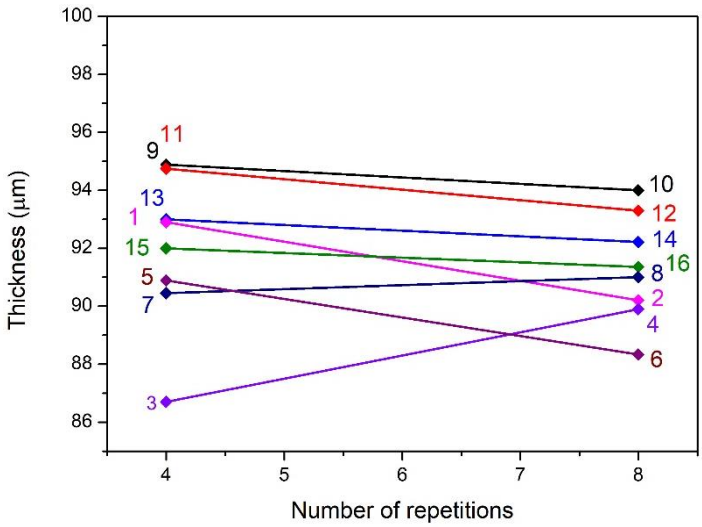

Figure 6.22. Effect of the number of repetitions in the electrode thickness.

These experiments show that the gap between rollers and the temperature, especially the first one, are the main parameters that affect to the electrode thickness and porosity.

6.2.2 1st cycle irreversibility

Focusing on the effect of the 4 calendering parameters in the 1st cycle irreversibility, the effect of the temperature (B) and the interaction with the gap between the rollers (AB) are the most significant effects according to equation (6.3).

$$IR = 31.76 + 0.32A - 1.49B - 0.20C - 0.38D + 1.00AB + 0.01AC + 0.75AD - 0.51BC - 0.14BD - 0.61CD \quad (6.3)$$

As it can be observed in **Figure 6.23**, the 1st cycle irreversibility values are between 28.44 and 34.23 mAh g^{-1}. When the temperature increases from 60 to 100 °C, the 1st cycle irreversibility systematically decreases. However, this reduction is more pronounced for the electrodes calendered using a gap between the rollers of 40 µm than those calendered using a gap between rollers of 70 µm.

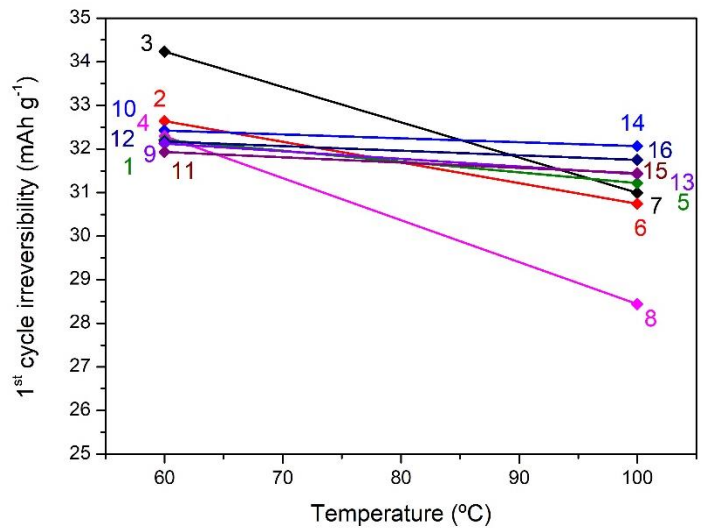

Figure 6.23. Effect of the calendering temperature in the 1st cycle irreversible capacity.

6.2.3 Reversible capacity

In the case of the reversible capacity, the most influencing factor is the interaction between the gap between rollers and the calendering temperature according to equation (6.4),

$$Q = 178.97 - 3.96A - 9.54B - 20.91C + 21.40D + 41.69AB - 19.53AC + 19.05AD - 25.21BC - 16.54BD + 2.21CD \quad (6.4)$$

According to **Figure 6.24**, for the electrodes calendered at 100 °C, when increasing the gap between rollers from 40 to 70 µm, the reversible capacity significantly increases in all the cases except from the 7-15 experiment pairs in which remains almost constant. On the other hand, for the electrodes calendered at 60 °C, when increasing the gap between rollers from 40 to 70 µm, the reversible capacity significantly decreases in all the cases except from the 2-10 experiment pairs in which remains almost constant.

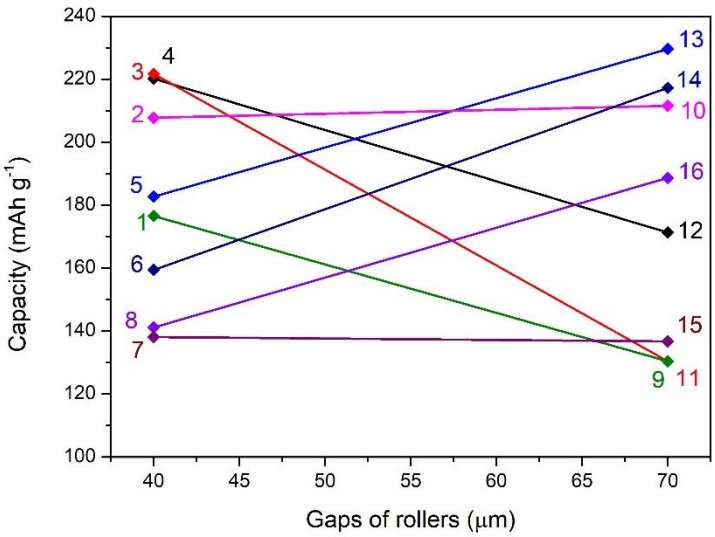

Figure 6.24. Effect of the gap between rollers in the reversible capacity.

The C-rate capability tests performed with the electrodes calendered using the conditions displayed in **Table 6.4** are represented in **Figure 6.25**. In order to visualize the effect of the gap between the rollers and the temperature, which are the most significant effects, each graph corresponds to two experiments in which only the gap between the rollers is modified and the other 3 parameters remain constant.

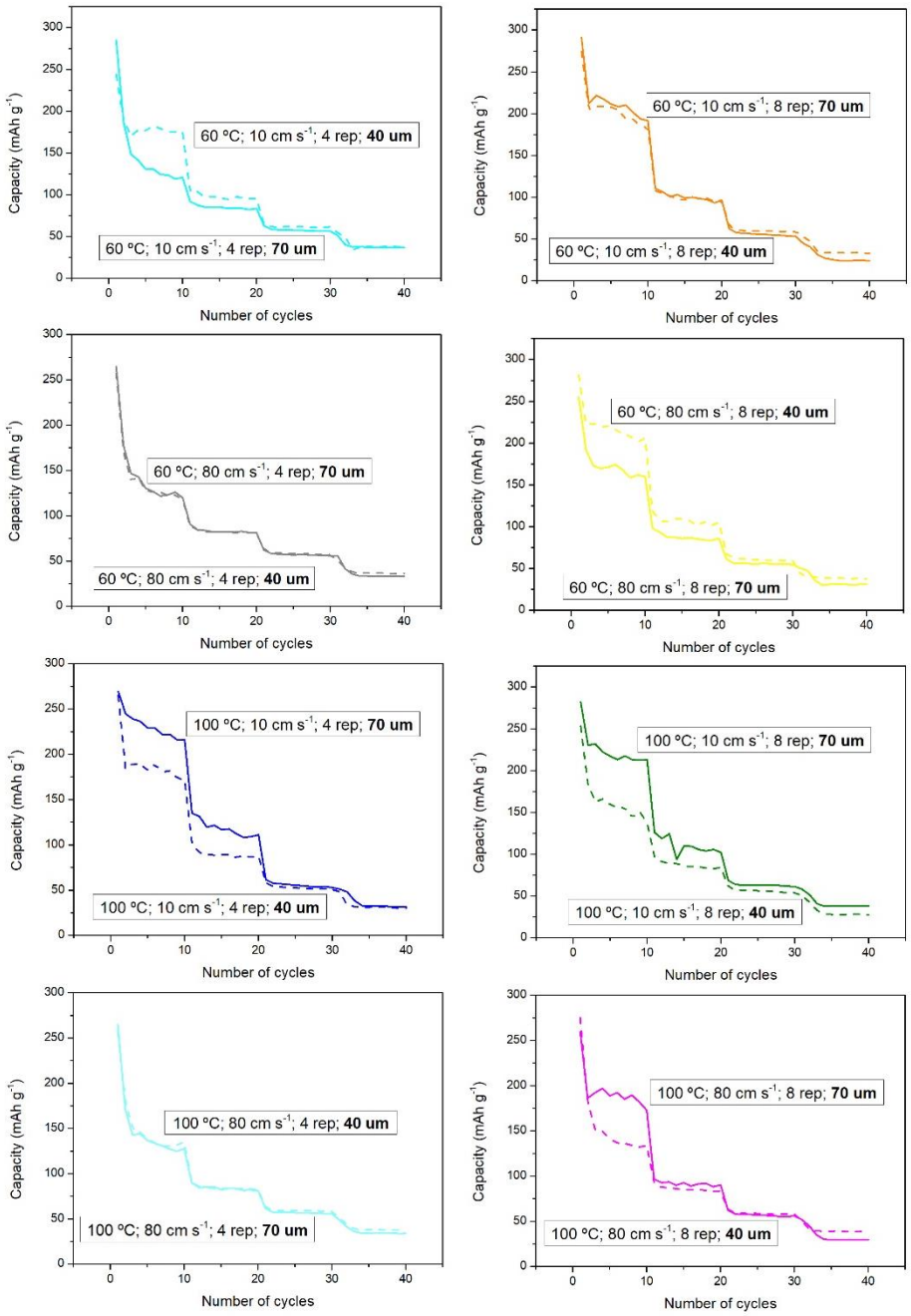

Figure 6.25 . C-rate performance of the anode half-cells calendered using different conditions.

The effect of the calendering conditions in the capacity at high C-rates (above 125 mA g^{-1}) is not significant due to the high active material loadings of the selected electrodes. At high rates, the plateau region of the voltage profile, which usually contributes to a larger extent to the total capacity, almost disappears and the total capacity corresponds to that delivered only in the sloping region.

The fact that the electrodes calendered at 100 °C and with a gap between rollers of 40 µm show poor electrochemical performance and the thickness/porosity of the electrodes calendered with a gap between rollers of 40 µm increases when increasing the temperature from 60 to 100 °C, is unexpected. Therefore, SEM analysis was performed in these electrodes. The images in **Figure 6.26** show that at these calendering conditions, the rollers damage the electrodes. In comparison with the non-calendered electrodes and the electrodes calendered at 100 °C and using a gap between rollers of 70 µm, which show an optimal microstructure, those electrodes calendered at 100 °C and using a gap between rollers of 40 µm show the presence of cracks and imperfections which can be the cause of poor electrochemical performance of these cells. Consequently the combination of low gaps between the rollers and high temperatures is considered too aggressive and intermediate calendering conditions (temperatures in the range of 60-80 °C and gaps between rollers higher than 40 µm) are suggested as the optimum ones.

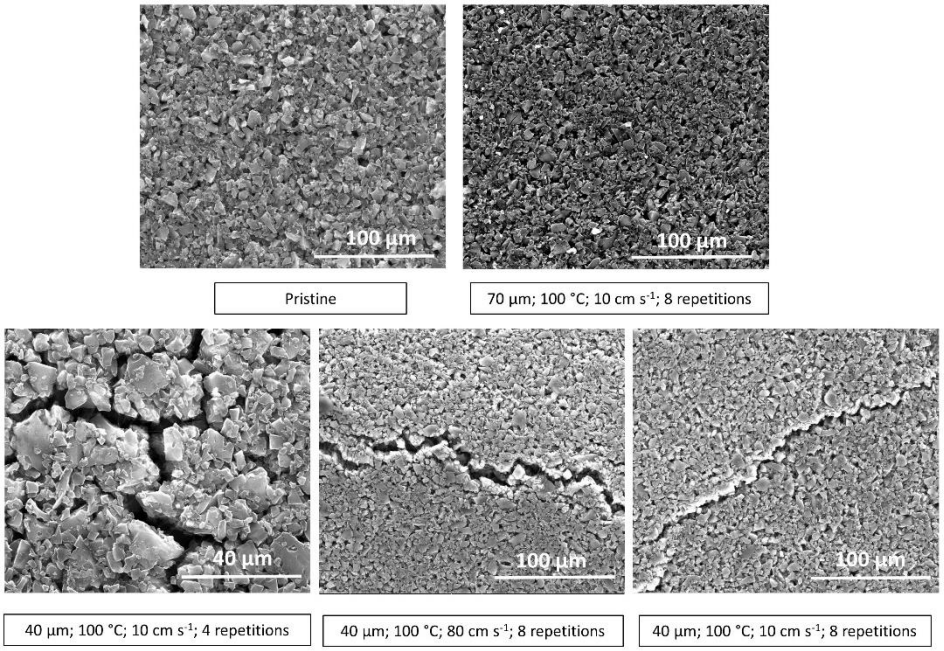

Figure 6.26. Surface SEM images of selected electrodes showing non-damaged microstructure (top images) and imperfections such as cracks and imperfections (bottom images).

With the aim to analyze the effect of the porosity in the electrochemical performance of the electrodes, the 1st cycle irreversibility and the reversible capacity, measured after 10 cycles is represented in **Figure 6.27** and **Figure 6.28**, respectively. Both graphs evidence that there is not a clear dependence between the porosity and the electrochemical performance in the range of studied porosities, and that other factors such as the pore size, the electrode microstructure, the mechanical integrity or the adhesion to the current collector also determine the electrochemical performance of the cells.

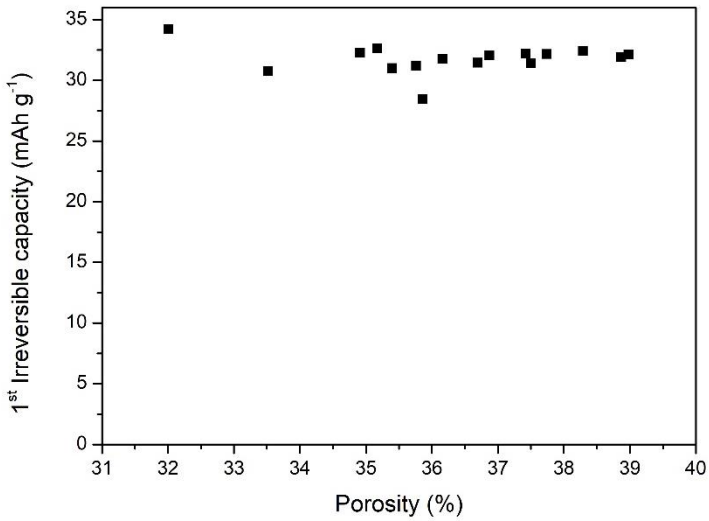

Figure 6.27. Influence of the electrode porosity in the 1st cycle irreversible capacity.

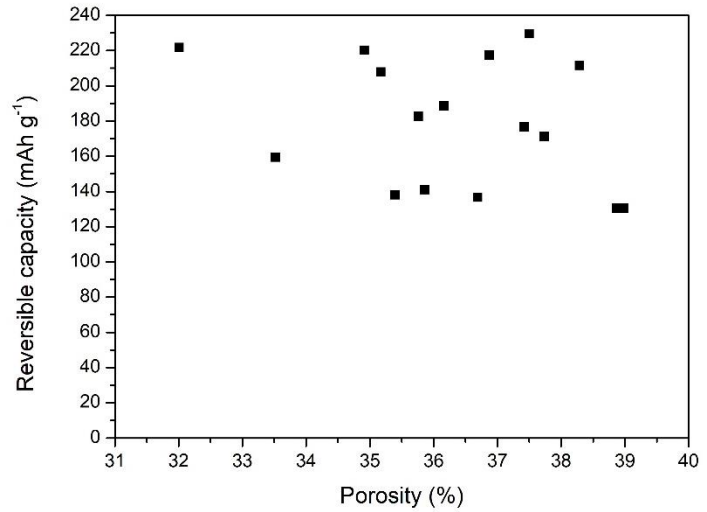

Figure 6.28. Influence of the electrode porosity in the reversible capacity.

6.3 Conclusions

The viscosity of the hard carbon anode formulations is determined by the amount of carbon black additive, being the slurries with 5% of C65 more viscous than those with 2.5% and no C65, especially at low shear rates. Due to the lower viscosity of the slurries with no C65, lower active material loading electrodes are obtained with this slurry despite its higher active material content for the same coating conditions. By increasing the active material loading of the electrodes, a detrimental effect in the adhesion strength of the coated foil to the current collector is observed independently of the active material content. Moreover, the cohesion properties of all the tested electrodes are better than the adhesion properties.

By increasing the carbon black content from 0% to 5% wt., the increment of the net of conductive agent around hard carbon particles is evident. However, the amount of C65 corresponding to 2.5% wt. is difficult to properly disperse using the planetary mixer and less homogeneous electrodes are obtained. One of the clearest effects of the presence of C65 as a conductive additive is an increment of the 1st cycle irreversible capacity values, which is also higher for low active material loading anodes. The diffusion coefficient values calculated using the Randles-Sevcik equation are lower for high active material loadings, while the effect of the active material content is not that clear.

By increasing the active material loading, there is an evident decrease of the reversible capacity for both the 95%AM and 90%AM formulations, which is in accordance with the increment of the resistance in the cell and the loss of adhesion properties. Moreover, at high C-rates, the small contribution of the capacity corresponding to the plateau region, significantly reduces the reversible capacity of the electrodes. This effect is more pronounced for high loading anodes in which the low contribution of the plateau region starts at lower C-rates. In spite of the lower specific capacities obtained for high loading anodes, the areal capacity increases with the active material loading and areal capacities of 1.2 mAh cm^{-2} at 25 mA g^{-1} (ca. 0.1C) are obtained for this material.

The effect of calendering conditions in the electrode properties was analyzed in this Thesis using Design of Experiments for the analysis of the effects of the individual factors and first order interactions. The studied parameters are the gap between the rollers, the calendering temperature, the speed of the rollers and the number of repetitions while the evaluated responses are the electrode thickness and porosity, the 1st cycle irreversible capacity and the reversible capacity.

Independent of the analyzed response, the most relevant parameters in the calendering process are the gap between the rollers, the calendering temperature and the interaction between these two parameters. Overall, lower electrode thicknesses and therefore lower porosities are obtained for low gaps between rollers (40 µm) and high temperatures (100 °C). However, the combination of these two conditions results in too aggressive calendering conditions and consequent damage of the electrode microstructure. Referring to the 1st cycle irreversibility, the calendering temperature is the parameter which presents the largest influence, being the 1st cycle irreversibility lower when increasing the temperature from 60 to 100 °C. Focusing in the reversible capacity, the interaction of the gap between the rollers and the temperature are the most significant factors.

Depending on the calendering conditions, porosity values in the range between 32 and 39% are obtained. However, no clear influence of this parameter in the 1st cycle irreversibility and reversible capacity is observed, which suggests that other parameters such as the pore size, the electrode microstructure, the mechanical integrity or the adhesion to the current collector also determine the electrochemical performance of the cells.

According to the obtained experimental data, no reasons which are determinant enough were identified that justify the use of C65 at this level of study. Therefore, the slurry with 95%AM was chosen for pouch cell preparation, based on slurry preparation easiness and time saving.

Chapter 7. Design, electrochemical characterization and thermal model of a Na-ion monolayer pouch-cell prototype

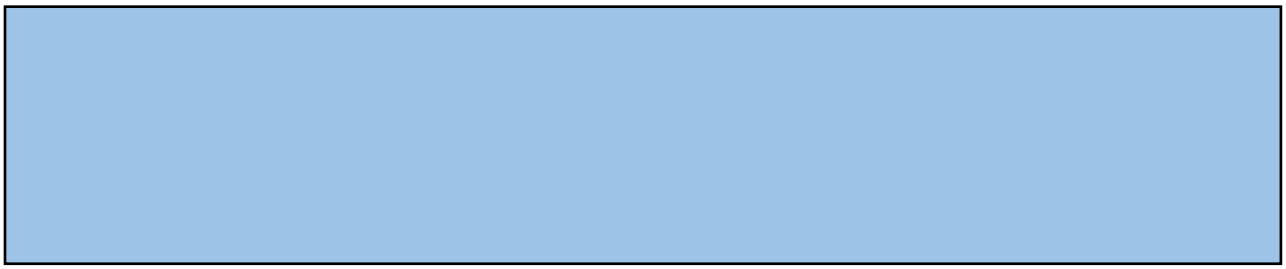

In this chapter, a hard carbon//O3-$NaFe_{0.4}Mn_{0.3}Ni_{0.3}O_2$ Na-ion monolayer pouch cell prototype is assembled and electrochemically and thermally characterized Cathode and anode fabrication procedures determined in Chapters 5 and Chapter 6, respectively are used for the full-cell assembly. The optimization of the Na-ion cell performance is done at coin and pouch cell level by varying parameters such as the electrode mass balance or cycling voltage range. The importance of preliminary work at small scale to settle the basis for further research at larger scale is highlighted. Finally, the thermal parameters for the Na-ion pouch cell prototype are determined to build a heat generation model.

7.1 Experimental procedure

Electrode fabrication procedure and characteristics were determined based on the conclusions extracted from Chapter 5 and Chapter 6, respectively for the cathode and the anode. $NaFe_{0.4}Mn_{0.3}Ni_{0.3}O_2$ with the original and spherical morphology as per the nomenclature previously described were used as the cathode active material and Kuranode hard carbon was used as the anode active material (see active material characteristics in Chapter 2, page 52). The cathode slurries with a AM:C65:PVDF = 87:5.7:7.3 composition were prepared using the disperser with the dissolver type impeller (see **Figure 5.31** for the cathode preparation procedure) and the anode slurries with a AM:PVDF = 95:5 composition was prepared using the planetary centrifugal vacuum mixer (see **Figure 6.1** for anode preparation procedure). The coin cell, 3-electrode Swagelok cell, 2-electrode monolayer pouch cells and 3-electrode pouch cells were assembled as described in Chapter 2, section 2.4.1, page 63, section 2.4.2, page 65, section 2.4.3, page 66 and section 2.4.4, page 69, respectively.

7.2 Full-cell assembly at coin cell level

7.2.1 Influence of the N/P ratio in 3-electrode cells

As it was previously described in Chapter 4, when assembling Na-ion batteries in full-cell configuration, the active material loading of the two electrodes needs to be carefully selected. Moreover, irreversible capacity of the two electrodes need to be compensated [276]. Concretely, in hard carbon anode full-cells, there is an irreversible sodium ion loss from the cathode that are used to create the SEI layer on the surface of the anode. In addition to the mass balance, it is also important to precisely adjust the operating voltage window to improve the cycling stability of the cells.

3-electrode cell configuration is used to monitor the voltage of the individual electrodes and the full-cell and analyze the properties of each electrode during the electrochemical charge/discharge cycles of the Na-ion cell. For example, by monitoring both the electrodes the state of charge of the individual electrodes can be monitored for different mass balances. In

these experiments, Swagelok cell configuration was used which is not the most suitable configuration for cycling stability tests. As an initial approach, 5 charge/discharge cycles were performed to evaluate the effect of the mass balance on the individual electrode voltage profiles. The full-cell voltage was limited between 4.0 V and 1.0 V and the cathode and anode voltage were not limited to replicate the cycling conditions of a 2-electrode full-cell in this first set of experiments.

The mass balances in this work are expressed as negative to positive ratio in terms of capacity ($R_{N/P}$ (Q)). For the calculation of this ratio, it has to be beard in mind the experimental data obtained for the electrochemical performance of both the anode and cathode half-cells as a function of the active material loadings. 110 mAh g^{-1} is considered as the reversible capacity for the cathode and for the anode, a capacity of 200 mAh g^{-1} is considered for the active material loading range of 5 and 6 mg cm^{-2}, respectively). The $R_{N/P}$ (Q) that are tested in the 3-electrode cell configuration in order to determine how this parameter is affecting to the electrochemical performance of the full-cell are: 1.8, 1.5, 1.2, 1.1 and 1.0. Cathode active material loading was fixed at ca. 6 mg cm^{-2} and corresponding anode material loadings were selected for the assembly of the cells with the selected mass balances.

Figure 7.1 to **Figure 7.5** show the voltage profiles of the cells with different mass balances and **Table 7.1** displays the specific capacity of the full-cell (same as that of the cathode since both are provided based on the mass of the cathode active material) and the anode, together with the lowest voltage value of the anode half-cell, representative of the risk of sodium plating which happens at voltages below 0 V and which can be a cause of serious safety issues.

The cell with $R_{N/P}$ (Q) = 1.8 (**Figure 7.1**), which is the one with the largest amount of anode active material (anode excess), and hence the highest anode capacity, shows low capacity and poor cycling stability (65 mAh g^{-1}_{AMCat} after 5 cycles). The irreversible capacity of this cell is as high as 100 mAh g^{-1}_{AMCat} which agrees with the high anode active material loading. $R_{N/P}$ (Q) values above the optimum, lead also to detrimental effects in the full-cell performance. For the high loading anode to be fully sodiated, overdesodiation of the cathode structure is needed which can cause irreversible structural changes and negatively affect to the cycle life of the cell [277]. In this cell, only the slopping region of the hard carbon is effective, and no contribution of the plateau region

is observed, leading to an anode capacity as low as 62 mAh g^{-1}_{AMAn}. However, similar to what observed in **Figure 7.1**, if the cathode polarization increases, an important capacity fade caused by the fact that the cell does not reach full charge can happen [278]. Moreover, as it was concluded in Chapter 6, high loading anodes also show worse cycling stability in half-cell configuration which contribute to the fast capacity fade of this full-cell.

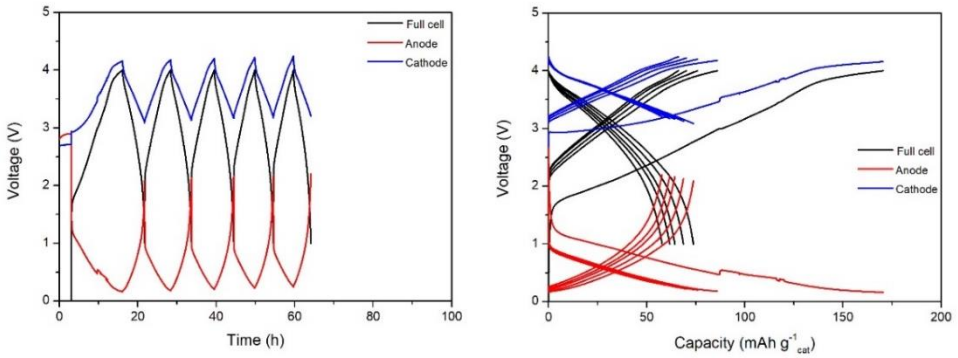

Figure 7.1. 3-electrode full-cell (Swagelok configuration) with $R_{N/P}$ (Q) = 1.8. Cycling rate = 13 mA g^{-1}_{AMCat} (ca. 0.1C); full-cell limited at 4.0-1.0 V.

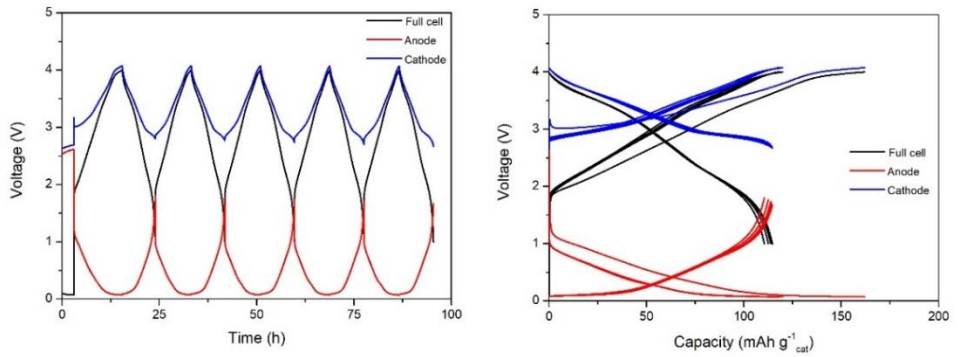

Figure 7.2. 3-electrode full-cell (Swagelok configuration) with $R_{N/P}$ (Q) = 1.5. Cycling rate = 13 mA g^{-1}_{AMCat} (ca. 0.1C); full-cell limited at 4.0-1.0 V.

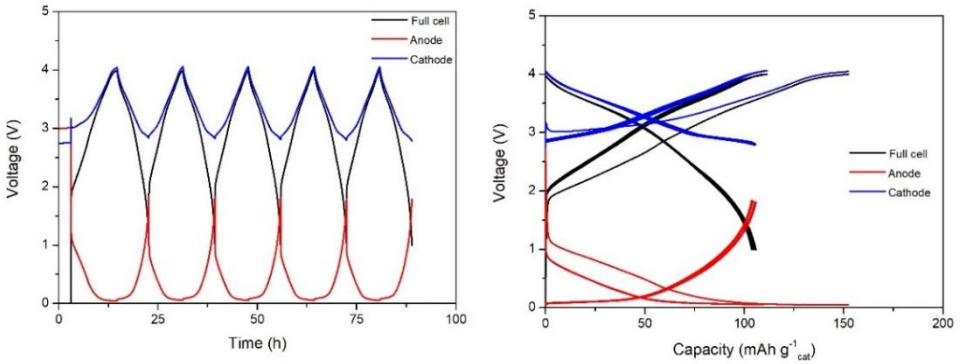

Figure 7.3. 3-electrode full-cell (Swagelok configuration) with $R_{N/P}$ (Q) = 1.2. Cycling rate = 13 mA g^{-1}_{AMCat} (ca. 0.1C); full-cell limited at 4.0-1.0 V.

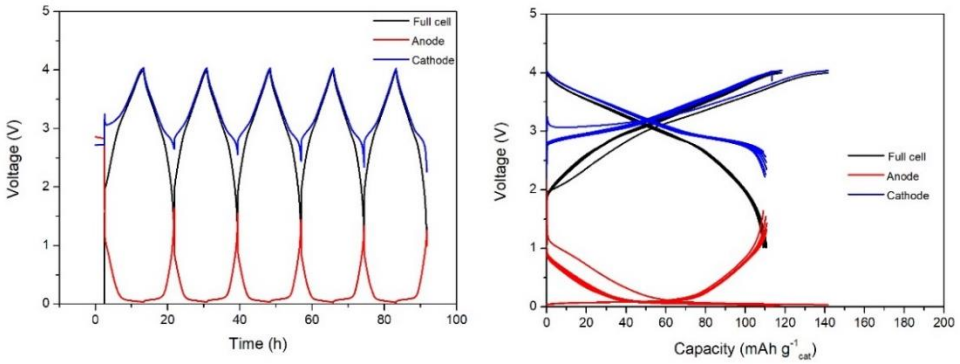

Figure 7.4. 3-electrode full-cell (Swagelok configuration) with $R_{N/P}$ (Q) = 1.1. Cycling rate = 13 mA g^{-1}_{AMCat} (ca. 0.1C); full-cell limited at 4.0-1.0 V.

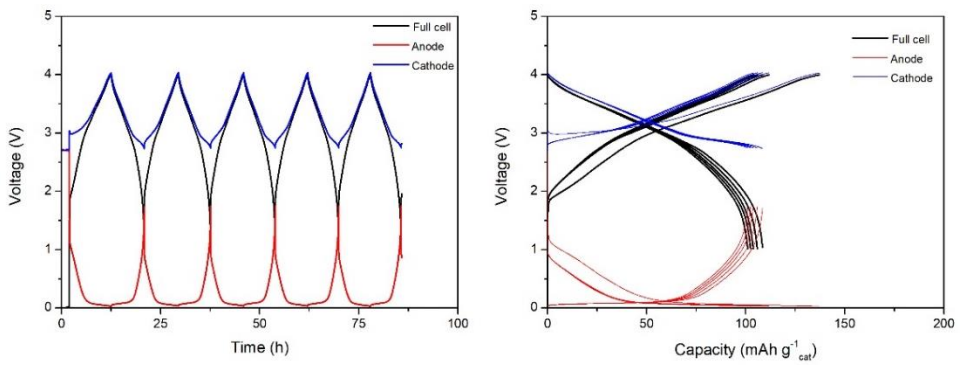

Figure 7.5. 3-electrode full-cell (Swagelok configuration) with $R_{N/P}$ (Q) = 1.0. Cycling rate = 13 mA g^{-1}_{AMCat} (ca. 0.1C); full-cell limited at 4.0-1.0 V.

Table 7.1. Summary of the capacity and voltage values for different $R_{N/P}$ (Q) 3-electrode full-cells.

$R_{N/P}$ (Q)	Anode reversible capacity in the 5th cycle (mAh g^{-1}_{AMAn})	Full-cell reversible capacity in the 5th cycle (mAh g^{-1}_{AMCat})	1st discharge V_{an} (V)	Minimum V_{an} (V)
1.8	62	65	0.17	0.16
1.5	144	113	0.07	0.07
1.2	163	105	0.05	0.05
1.1	214	110	0.06	0.06
1.0	203	105	0.04	0.02

As the $R_{N/P}$ (Q) decreases, the contribution of the plateau region in the anode is higher, the anode utilization is more effective and capacities above 200 mAh g^{-1}_{AMAn} are obtained. This should contribute to increase the energy density of the cells since the anode excess is reduced. The slightly higher 1st cycle irreversibility of the $R_{N/P}$ (Q) = 1.0 cell than that with $R_{N/P}$ (Q) = 1.1 is attributed to the higher 1st cycle irreversibility of low anode active material loading electrodes.

The reversible capacity in the 5th cycle is similar for $R_{N/P}$ (Q) = 1.5, 1.2, 1.1 and 1.0, with 113, 105, 110 and 105 mAh g^{-1}, respectively. However, the minimum anode voltage values tend to 0 V when decreasing the $R_{N/P}$ (Q), which can results in the presence of sodium plating. **Figure 7.6** shows the appearance of the anodes with $R_{N/P}$ (Q) = 1.0 and 1.1 after 5 cycles, in which sodium plating on the anode surface after cycling is clear, therefore, these ratios are below the optimum for stable cycling performance.

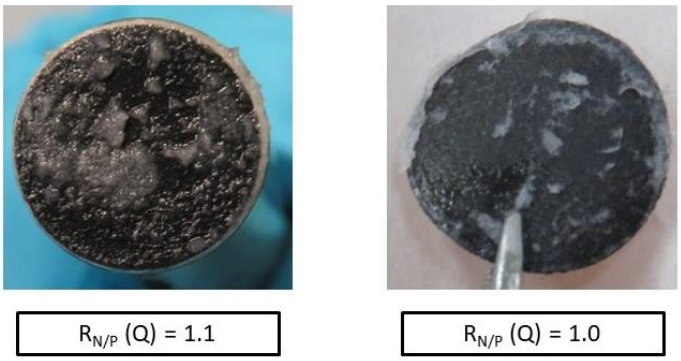

Figure 7.6. Sodium plating in the full-cells with $R_{N/P}$ (Q) = 1.1 and $R_{N/P}$ (Q) = 1.0 after 5 cycles at 13 mA g^{-1}_{AMCat} (ca. 0.1C).

A good mass balance should ensure the most effective anode sodiation, including the adsorption of Na^+ ions in the microporosity of the hard carbon, corresponding to the plateau region at low voltages, which is responsible of the main contribution to the reversible capacity. Another key point which determines the mass balance selection, is to maintain a consistent level of voltage polarization of both electrodes, which is a requirement to demonstrate a long cycle life in the sodium-ion battery [278]. In the case of $R_{N/P}$ (Q) = 1.5 and 1.2, at the fully charged state, full-cell voltage at 4.0 V, the cathode electrodes reach 4.07 V and 4.05 V vs. Na^+/Na, respectively which represents a well-balanced negative to positive ratio.

Based on the reversible capacity after several cycles for the full-cell, the anode utilization, the cathode polarization and the anode voltage when the cell is fully charged, the optimal $R_{N/P}$ (Q) range is selected between 1.5-1.2.

7.2.2 Influence of the N/P ratio in 2-electrode cells

After the electrochemical studies using a 3-electrode cell configuration, cycling stability tests were performed in 2-electrode cells (CR2032 coin cells). The $R_{N/P}$ (Q) = 1.0 and 1.8 were discarded based on the conclusions obtained from the experiments in the 3-electrode cell configuration. In the case of 3-electrode cells, parameters such as the sodium plating, or the individual cathode

and anode behavior were studied, while in the case of 2-electrode cells, parameters such as the reversible capacity and the capacity retention or cycling stability will be analyzed.

Figure 7.7 shows the cycling performance of the full-cells with $R_{N/P}$ (Q) = 1.1, 1.2 and 1.5. There is an important first cycle irreversibility, which is higher in the cell with $R_{N/P}$ (Q) = 1.5 due to the solid electrolyte interface formation at low voltages. On the other hand, the most stable cycling performance is obtained with $R_{N/P}$ (Q) = 1.2 which is consistent with the results obtained in 3-electrode configuration cells. The reason for the lower cycling stability of the cells with $R_{N/P}$ (Q) = 1.1 and 1.5 can be sodium plating in the anode and non-effective anode utilization, respectively.

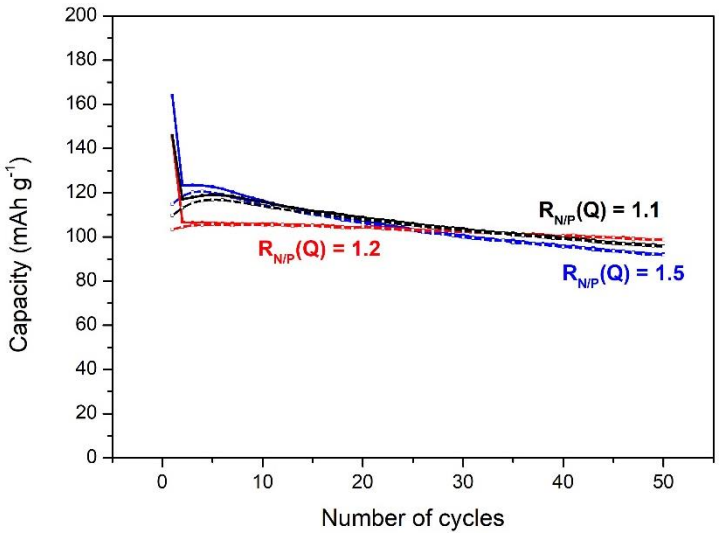

Figure 7.7. Cycling performance at 13 mA g^{-1}_{AMCat} (ca. 0.1C) of the full-cells with a different mass balances ($R_{N/P}$ (Q) = 1.1, 1.2, 1.5).

Table 7.2. Reversible capacity and capacity retention values for the full-cells (coin cell configuration) with different mass balances ($R_{N/P}$ (Q) = 1.1, 1.2, 1.5).

$R_{N/P}$ (Q)	Cell voltage (V)	Reversible capacity (50th cycle) (mAh g^{-1}_{AMcat})	Capacity retention (50th cycle) (%)
1.5	2.89	92	80
1.2	2.96	99	96
1.1	2.87	96	87

Based on the results in **Figure 7.7** (summarized in **Table 7.2**), the full-cell with a ratio of $R_{N/P}$ (Q) = 1.2 is the one which delivers the highest reversible capacities over cycling (99 mAh g^{-1}_{AMCat}), with a capacity retention of 96%. Although the full-cells with $R_{N/P}$(Q) = 1.5 and 1.1 deliver similar capacity values of 92 and 96 mAh g^{-1}_{AMCat} after 50 cycles, the capacity retention is lower, 80% and 87%, respectively. A simple extrapolation of these results forecasts capacity values of 23, 87 and 53 mAh g^{-1}_{AMCat} after 200 cycles for $R_{N/P}$ (Q) = 1.5, 1.2 and 1.1, respectively. Cell voltage for $R_{N/P}$ (Q) = 1.5, 1.2 and 1.1, are 2.89, 2.96 and 2.87 V respectively. This parameter will be used to calculate energy density values of each full-cell.

7.3 Full-cell assembly at pouch cell level

Going one step further in the development of a Na-ion battery prototype, the optimal mass balance in pouch cell level is determined in this section by assembling 3-electrode pouch cells. Moreover, the effect in the cycling stability of some design parameters such as the mass balance, the cathode morphology and the cycling voltage are analyzed.

7.3.1 3-electrode cell

7.3.1.1 Influence of the N/P ratio

In this section, $R_{N/P}$ (Q) = 1.0, 1.3 and 1.6 mass balances are tested, close to the ratios which are identified as the optimum in the coin cell configuration experiments. Since the 3-electrode cell configuration allows establishing the end of charge and end of discharge conditions based on the anode, cathode and/or full-cell voltage, as an initial approach, and with the aim to work on the safe side, all the cell components have been limited. This means that the cathode, anode and full-cell voltage ranges are limited between 2.5-4.0 V, 0.01-2.0 V and 2.0-4.0 V, respectively.

The Depth of Discharge (DOD) is one of the main factors limiting the cycle life of lithium-ion batteries. In fact, if the DOD of a battery is set at high values, the cycle life of the device is usually reduced [279]. As an example, it was reported by Omar et al., that if the maximum possible number of cycles is represented versus the DOD, the characteristic curve exponentially decreases [280]. Based on the fact that the capacity gain observed in **Figure 7.1- Figure 7.5** is limited in the

full-cell voltage range between 4 and 2 V, the full-cells were tested in this voltage range in the following tests.

Figure 7.8-Figure 7.10 present the voltage profiles of the 3-electrode cells with $R_{N/P}$ (Q) = 1.0, 1.3 and 1.6 and **Table 7.3** collects the principal results corresponding to the first 5 cycles.

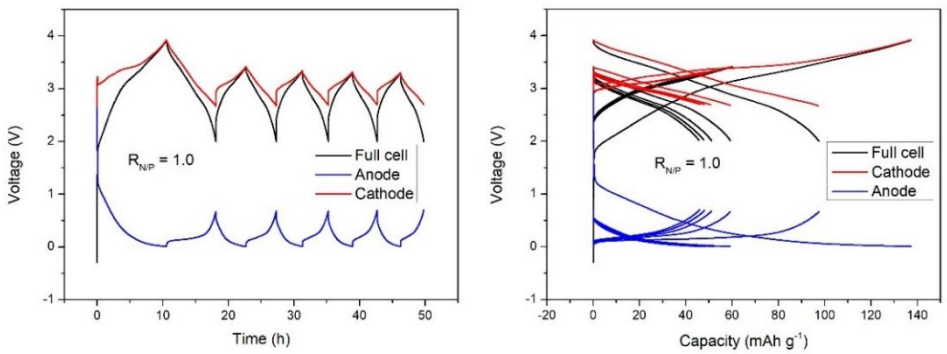

Figure 7.8. 3-electrode full-cell (pouch cell configuration) with $R_{N/P}$ (Q) = 1.0. Cycling rate = 13 mA g^{-1}_{AMCat} (ca. 0.1C); full-cell limited at 4.0-2.0 V, anode limited at 2-0.01 V and cathode limited at 4.0-2.5 V.

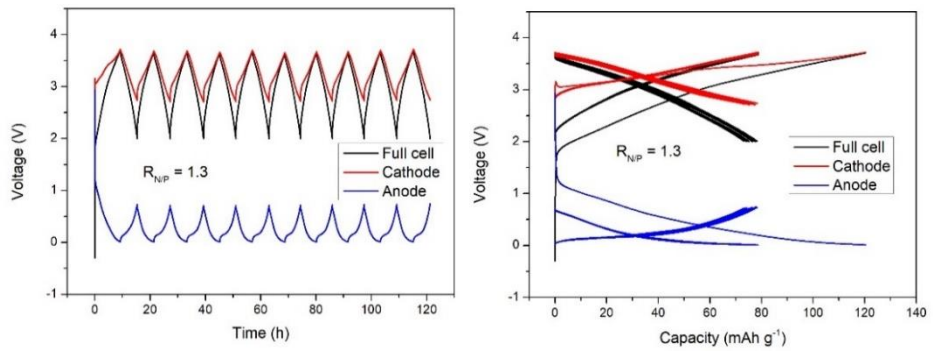

Figure 7.9. 3-electrode full-cell (pouch cell configuration) with $R_{N/P}$ (Q) = 1.3. Cycling rate = 13 mA g^{-1}_{AMCat} (ca. 0.1C); full-cell limited at 4.0-2.0 V, anode limited at 2-0.01 V and cathode limited at 4.0-2.5 V.

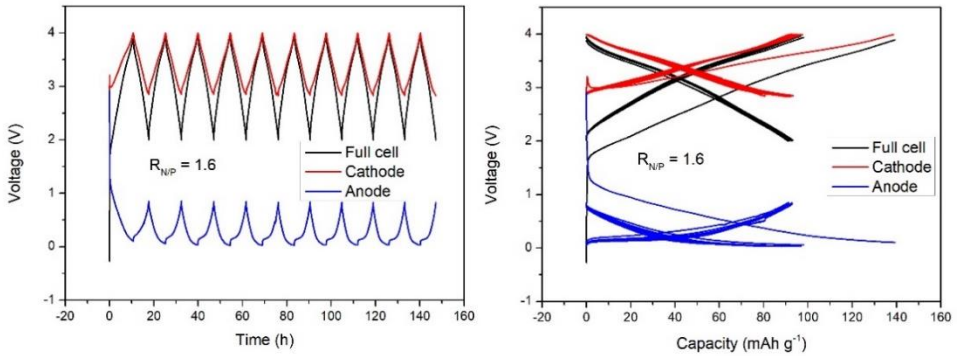

Figure 7.10. 3-electrode full-cell (pouch cell configuration) with $R_{N/P}$ (Q) = 1.6. Cycling rate = 13 mA g^{-1}_{AMCat} (ca. 0.1C); full-cell limited at 4.0-2.0 V, anode limited at 2-0.01 V and cathode limited at 4.0-2.5 V.

Table 7.3. Experimental data of three different 3-electrode pouch cells (all the cell components limited).

$R_{N/P}$ (Q)	1st capacity anode (mAh g_{anode}^{-1})	5th discharge capacity anode (mAh g_{anode}^{-1})	5th discharge capacity full-cell (mAh g^{-1})	Charge limited by
1.0	138	46	45	Anode
1.3	167	110	78	Anode
1.6	139	108	93	Cathode

In the case of $R_{N/P}$ (Q) = 1.0 (**Figure 7.8**), setting a limit for all the components has detrimental effects for the electrochemical performance of the cells since it limits the reversible capacity of the cathode and anode electrodes, and therefore, the full-cell reversible capacity. With this mass balance, the positive electrode was never fully desodiated. If for a given mass balance the end of charge of the cell is set by the anode, it means that voltage would go down to this value if no anode limitation would be set.

When the $R_{N/P}$ (Q) is increased from 1.3 to 1.6, the end of charge condition changes from anode to cathode limitation, which means that the optimal $R_{N/P}$ (Q) should be between these two values. Making the full-cell limited by the cathode provides an excess of negative capacity which would be able to intercalate more sodium ions in without having the risk of formation of reactive sodium metal on the electrode surface, as it was reported by Bennet et al., in the case of lithium-ion batteries [281]. However, it limits the electrochemical performance of the full-cell. The combination of the most effective anode utilization ($R_{N/P}$ (Q) = 1.3) and the minimization of the

sodium plating risk over cycling ($R_{N/P}$ (Q) = 1.6) will give to the pouch cell the optimum mass balance.

A second set of experiments was performed with cells with different mass balances setting the end of charge/discharge when the full-cell reaches 4 and 2 V, respectively. Anode and cathode voltages were monitored over cycling in these experiments but no limitation was established based on anode/cathode voltage; thus, this configuration is analogous of that used in 2-electrode cells. The voltage profiles for $R_{N/P}$ (Q) = 1.0, 1.3 and 1.6 are represented in **Figure 7.11-Figure 7.13** and some relevant capacity data are provided in **Table 7.4**.

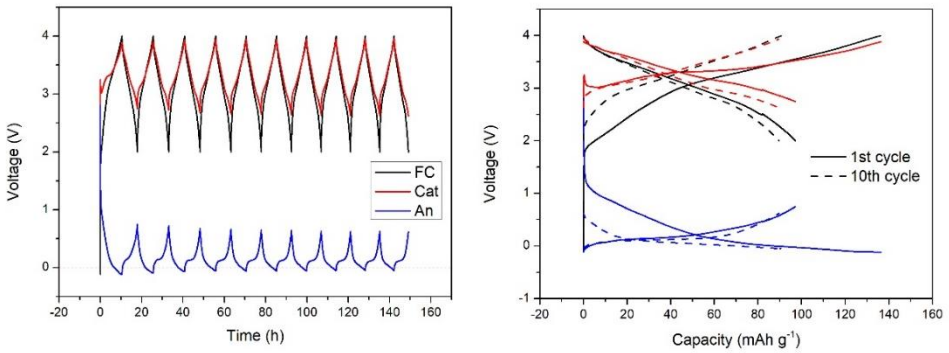

Figure 7.11. 3-electrode full-cell (pouch cell configuration) with $R_{N/P}$ (Q) = 1.0. Cycling rate = 13 mA g^{-1}_{AMCat} (ca. 0.1C), full-cell limited at 4.0-2.0 V.

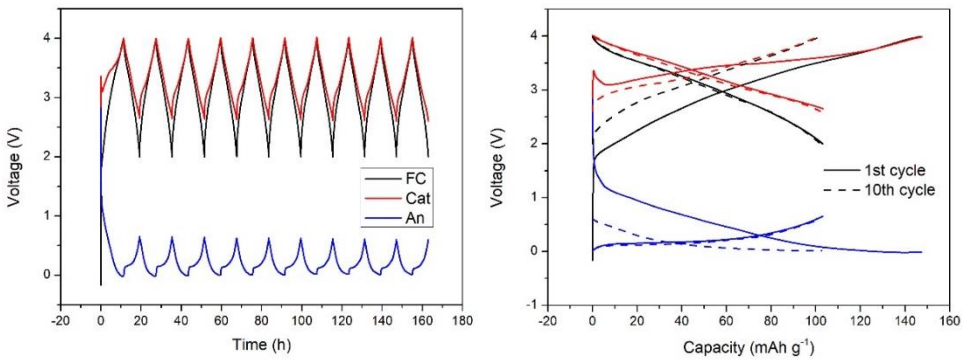

Figure 7.12. 3-electrode full-cell (pouch cell configuration) with $R_{N/P}$ (Q) = 1.3. Cycling rate = 13 mA g^{-1}_{AMCat} (ca. 0.1C), full-cell limited at 4.0-2.0 V.

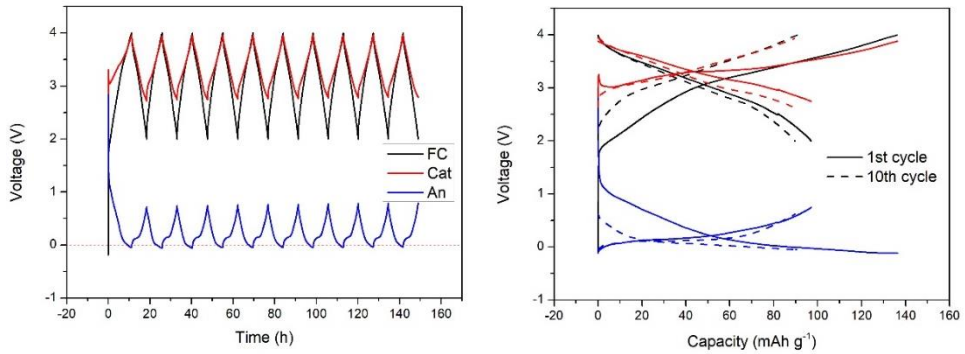

Figure 7.13. 3-electrode full-cell (pouch cell configuration) with $R_{N/P}$ (Q) = 1.6. Cycling rate = 13 mA g^{-1}_{AMCat} (ca. 0.1C), full-cell limited at 4.0-2.0 V.

Table 7.4. Experimental data of three different 3-electrode pouch cells (full cell limited).

$R_{N/P}$ (Q)	1st capacity anode (mAh g^{-1}_{AMAn})	10th discharge capacity anode (mAh g^{-1}_{AMAn})	10th discharge capacity full-cell (mAh g^{-1}_{AMCat})	Minimum V_{an} (V)
1.0	185	168	90	-0.1
1.3	208	145	102	-0.047
1.6	168	108	93	0

The cell with $R_{N/P}$ (Q) = 1.0 (**Figure 7.11**) presents the highest 1st and 10th cycle anode capacity values when the anode voltage is not limited. This causes a detrimental effect in the battery associated to the sodium plating on the surface of the anode. The cells with a mass balance of $R_{N/P}$ (Q) = 1.3 and 1.6 (**Figure 7.12** and **Figure 7.13**) present similar 10th cycle discharge capacity values, 102 and 93 mAh g^{-1}, respectively. However, in the case of $R_{N/P}$ (Q) = 1.3 the risk for sodium plating is also there since the anode voltage decreases below 0 V. In the case of $R_{N/P}$ (Q) = 1.6, anode voltage takes positive values during the first 10 cycles.

The detrimental effect of low $R_{N/P}$ (Q) mass balances is usually even more evident at higher C-rates. **Figure 7.14** shows that the cell with low $R_{N/P}$ (Q) = 1 has lower capacity retention, especially at 65 and 130 mA g^{-1} (ca. 0.5C and 1C, respectively). The cell with $R_{N/P}$ (Q) = 1.6 has higher and more stable capacity at high C-rates. The cell with $R_{N/P}$ (Q) = 1.3 also shows better electrochemical performance at higher C-rates than that with $R_{N/P}$ (Q) = 1.0, although the capacity fade is more evident than for $R_{N/P}$ (Q) = 1.6, as more undesired reactions happen. It is important to highlight

that the full-cell with $R_{N/P}$ (Q) = 1.3, is in the limit to avoid sodium plating; therefore, depending on the full-cell configuration (active material loadings, alignment of the electrodes, etc.) better electrochemical performances can potentially be achieved with this ratio.

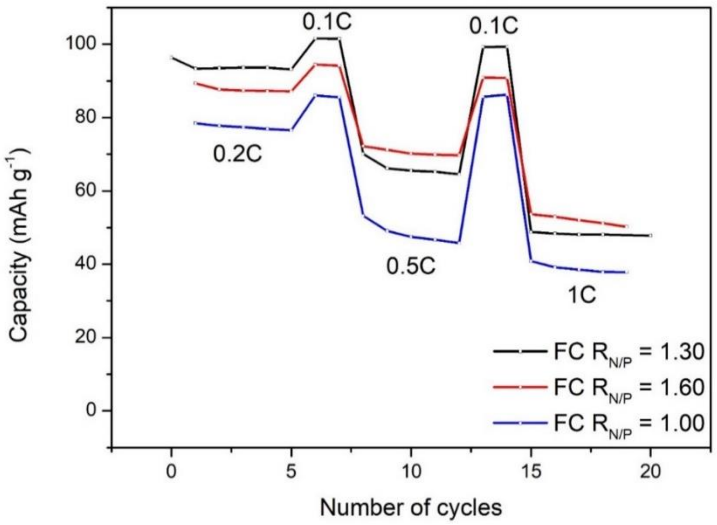

Figure 7.14. C-rate performance of the pouch cells with different $R_{N/P}$ (Q).

The conclusions extracted from **Figure 7.11**-**Figure 7.13** are corroborated by the images of the anodes shown in **Figure 7.15** after disassembly of the pouch cells, showing a significant increment of the amount of sodium plating when decreasing the $R_{N/P}$ (Q). As it was expected, the cell with $R_{N/P}$ (Q) = 1.0 presents a huge amount of sodium plating on the surface of the anode which appears, mainly in the area close to the tab of the reference electrode and the edges of the electrode.

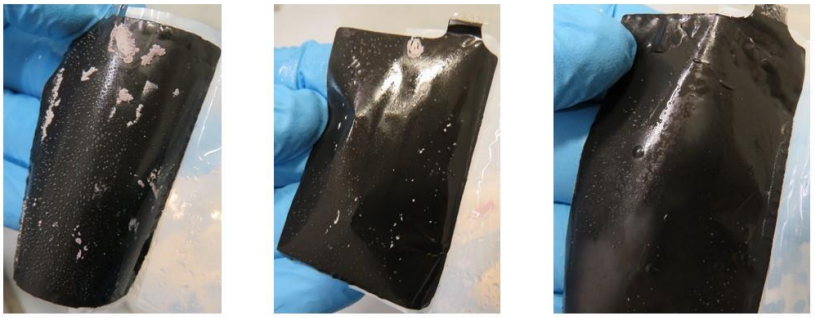

Figure 7.15. Images showing the anode aspect after 10 charge discharge cycles for the cells with different $R_{N/P}$ (Q).

In conclusion, $R_{N/P}$ (Q) = 1.0 is discarded because of the sodium plating on the surface of the anode, and consequent low reversible capacity especially at high C-rates. In the case of $R_{N/P}$ (Q) = 1.6, sodium plating risk is significantly reduced; however, the reversible capacity values are slightly lower than expected due to the smaller contribution of the plateau region of the negative electrode. According to these experiments, the $R_{N/P}$ (Q) = 1.3 represents a trade-off between these two effects and it becomes in the best option for the next experiments, showing good reversible capacity values of 100 mAh g^{-1}_{AMCat} at 13 mA g^{-1} and at higher current densities, as well as good capacity retention.

7.3.1.2 Influence of the cycling voltage range

It is expected that by decreasing the upper cut-off voltage from 4.0 V to 3.9 V, the risk of sodium plating should be reduced; therefore, pouch cells with $R_{N/P}$ (Q) = 1.3 were assembled and tested in 3 electrode configuration in two different voltage ranges, i.e. 2-4.0 V and 2-3.9 V. The voltage profiles corresponding to the 1st and 10th cycles and representative data of the cells are displayed in **Figure 7.16** and **Table 7.5**. The 1st charge anode capacities are 208 and 203 mAh g^{-1}_{AMAn} for the cells limited at 4.0 V and 3.9 V, respectively, and the reversible capacity is slightly reduced from 102 to 95 mAh g^{-1}_{AMCat}. Unexpectedly, no significant differences are observed in the cathode/anode voltage profiles and anode voltages < 0 V are observed in both cells. This fact

could be also related to small variations in cell resistance due to the nature of the 3-electrode cell itself.

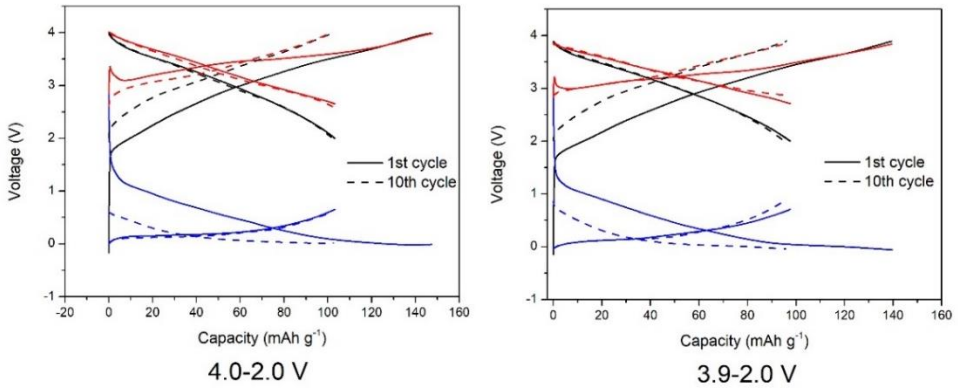

Figure 7.16. 3-electrode full-cell (pouch cell configuration) with $R_{N/P}$ (Q) = 1.3. Cycling rate = 13 mA g^{-1}_{AMCat} (ca. 0.1C), full-cell limited at 4.0-2.0 V and 3.9-2.0 V. The red, blue and black curves represent the cathode, anode and full-cell voltages, respectively.

Table 7.5. Experimental data of 3-electrode pouch cells limited at different upper cut-off voltages.

Voltage range (V)	1st capacity anode (mAh g^{-1}_{AMAn})	10th discharge capacity anode (mAh g^{-1}_{AMAn})	10th discharge capacity full cell (mAh g^{-1}_{AMCat})
4.0-2.0	208	145	102
3.9-2.0	203	140	95

7.3.1.3 Influence of the cathode morphology

As it was discussed in the Chapter 5 of this Thesis, with the aim to make possible the casting of cathode slurries using the continuous comma bar coating machine, the morphology of the active material had to be modified. **Figure 7.17** and **Table 7.6** show the voltage profiles and representative data of 3-electrode pouch cells assembled using the cathode with the original and spherical morphology, with $R_{N/P}$ (Q) = 1.3 in the voltage range between 2-3.9 V. Consequent with the results observed when the two cathode morphologies were tested at half-cell level, a reduction of the reversible capacity from 95 to 73 mAh g^{-1}_{AMCat} is observed when using the spherical morphology cathode.

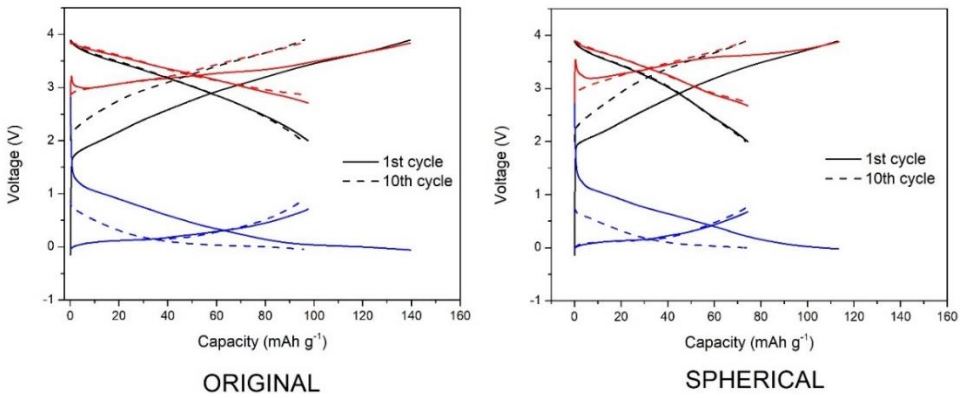

Figure 7.17. 3-electrode full-cell (pouch cell configuration) with $R_{N/P}$ (Q) = 1.3 with two different cathode active material morphologies, original and spherical. Cycling rate = 13 mA g^{-1}_{AMCat} (ca. 0.1C), full-cell limited at 3.9-2.0 V. The red, blue and black curves represent the cathode, anode and full-cell voltages, respectively.

Table 7.6. Experimental data two 3-electrode cells with different cathode active material morphologies.

Cathode morphology	1st capacity anode (mAh g_{anode}^{-1})	10th discharge capacity anode (mAh g_{anode}^{-1})	10th discharge capacity full cell (mAh g^{-1})
Original	203	140	95
Spherical	165	107	73

7.3.2 Cycling stability of monolayer pouch cells

Cycling stability experiments of monolayer Na-ion pouch cells are performed in this section. The effect of the parameters evaluated in the previous section using 3-electrode configuration are studied in this section. Concretely four Na-ion cells in which 3 different parameters are modified are studied: the negative to positive ratio, the cathode active material morphology and the cycling voltage range. **Table 7.7** displays the characteristics of the studied cells.

Table 7.7. Characteristics of the four Na-ion pouch cells subjected to cycling stability tests.

Cell	Voltage range (V)	Cathode morphology	$R_{N/P}$ (Q)
O1.3_2.0-3.9	2.0-3.9	Original	1.3
S1.3_2.0-4.0	2.0-4.0	Spherical	1.3
O1.6_2.0-3.9	2.0-3.9	Original	1.6
S1.3_2.0-3.9	2.0-3.9	Spherical	1.3

After the formation cycles, which consisted in 3 cycles at 13 mA g^{-1}_{AMCat} and the degassing process, the cells were cycled at 13 mA g^{-1}_{AMCat} for 100 cycles. After the cyclability test, the Na-ion pouch cells were disassembled to perform post-mortem analysis and elucidate the possible causes for different cell performances. **Figure 7.18** shows the evolution of the charge/discharge capacities of the tested cells.

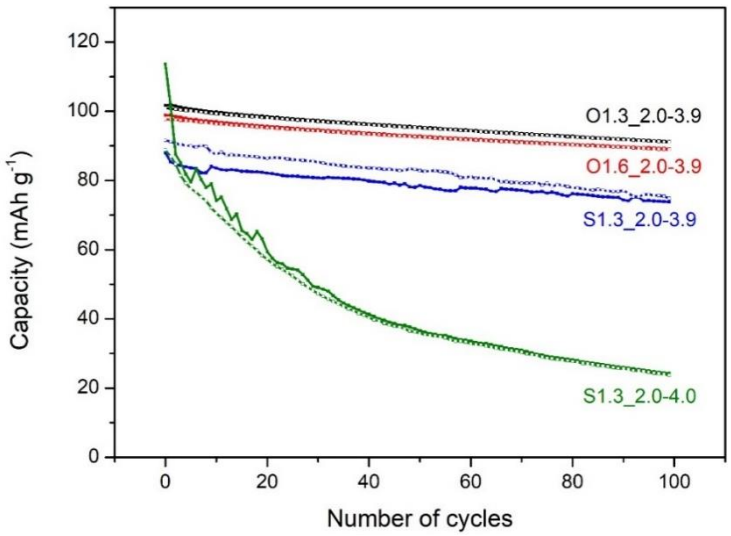

Figure 7.18. Cycling performance at 13 mA g^{-1}_{AMCat} of the cycled monolayer pouch cells: O1.3_2.0-3.9, O1.6_2.0-3.9, S1.3_2.0-3.9 and S1.3_2.0-4.0.

7.3.2.1 Influence of the mass balance

Firstly, the influence of $R_{N/P}$ (Q) is analyzed. Concretely, the analysis is focused on the O1.3_2.0-3.9 and O1.6_2.0-3.9 cells with $R_{N/P}$ (Q) = 1.3 and 1.6. The cycling voltage range is set at 2.0 to 3.9 V, and the cathode morphology is the original. Both cells present reversible capacities after 100 cycles close to 90 mAh g^{-1}_{AMCat}. As it can be observed in the **Figure 7.18** high capacity retention values close to 90% are obtained after 100 cycles.

A visual inspection of the anode electrodes of both cells (**Figure 7.19**) shows that in the case of $R_{N/P}$ (Q) = 1.3, there are small traces of sodium plating close to the top edges of the electrode. In addition to this, the anode part close to the tab and on the bottom edges can be easily detached from the current collector. In the case of $R_{N/P}$ (Q) = 1.6, sodium plating is not evident and no signs of delamination of the coated anode from the current collector are observed, which is a good signal for the cycle life of the battery.

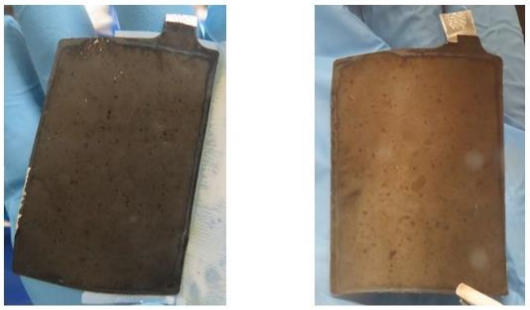

Figure 7.19. Visual aspect of the anode electrodes of O1.3_2.0-3.9 ($R_{N/P}$ (Q) = 1.3) and O1.6_2.0-3.9 ($R_{N/P}$ (Q) = 1.6) cells after cycling.

The microstructure of the electrodes after cycling is also analyzed by means of SEM (**Figure 7.20** and **Figure 7.21**). The microstructures of the cathodes (**Figure 7.20**) and the anodes (**Figure 7.21**) do not show evident changes compared to the pristine electrodes, independently of the ratio used to balance the cell. The presence of small particles on the surface of the anode are the only difference of the cycled anodes compared to the pristine electrode.

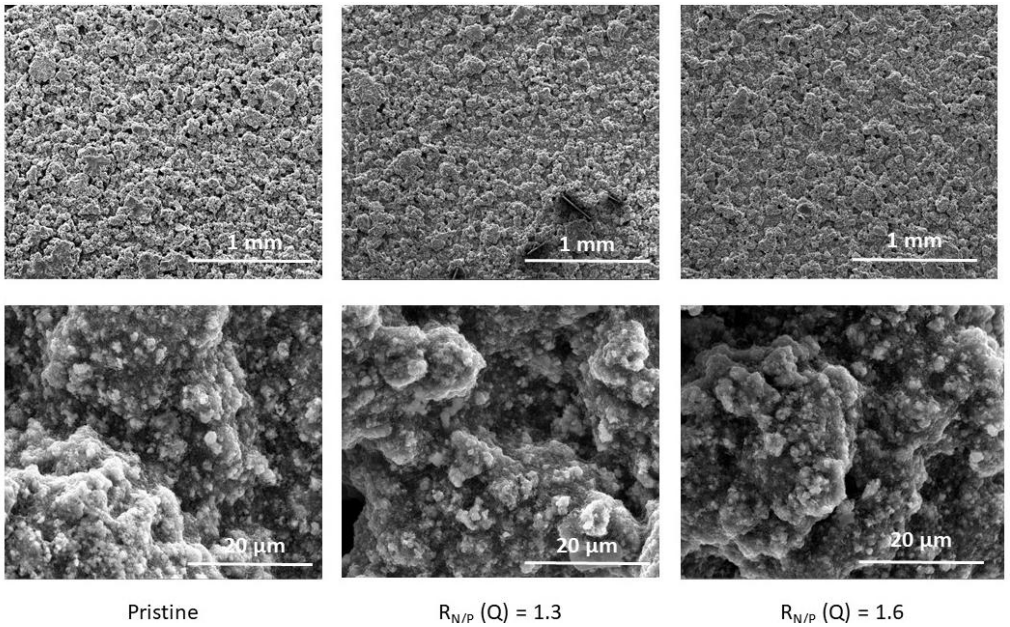

Figure 7.20. SEM images of the cycled cathode electrodes compared to the pristine cathode.

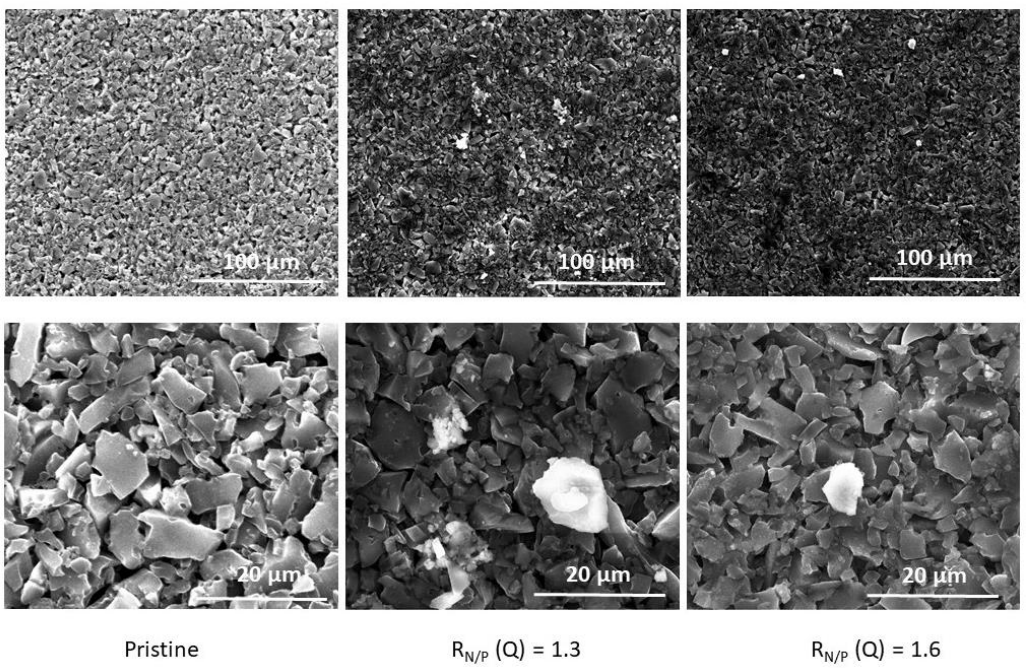

Figure 7.21 SEM images of the cycled anode electrodes compared to the pristine anode.

Cathode electrodes are analyzed by means of XRD (**Figure 7.22**) in order to detect structural changes as a consequence of the cycling process. The X-ray diffraction pattern of the pristine electrode is indexed to α-$NaFeO_2$ type crystal structure and cycled cathodes maintain similar crystalline structure. Minor changes in intensity of the reflection peaks are observed which can be caused by the differences on the crystallinity of the samples after cycling.

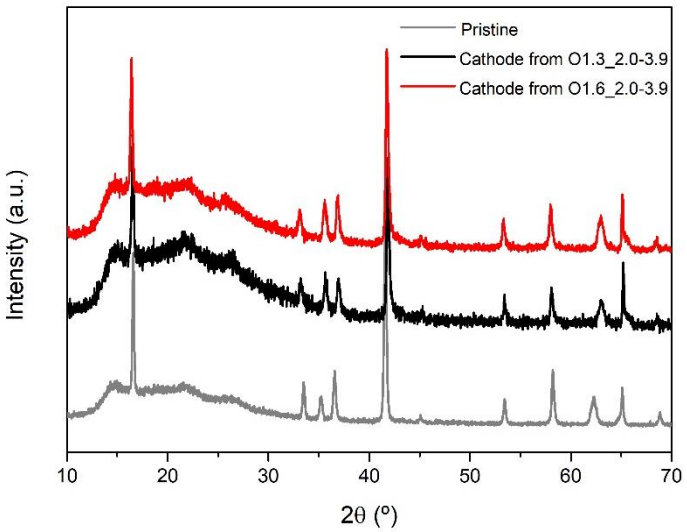

Figure 7.22. X-ray diffraction patterns from pristine cathode and O1.3_2.0-3.9 and O1.6_2.0-3.9 cathodes.

The cell parameters determined by Le Bail method are displayed in **Table 7.8**. If the *c* parameter increases while the *a* parameter decreases, as it happens in the case of the cycled electrodes, it suggests that the crystal structure of the cycled electrodes exhibit lower Na^+ content in comparison to the pristine one [80].

Table 7.8. Summary of the cell parameters from pristine and cycled O1.3_2.0-3.9 and O1.6_2.0-3.9 cathodes.

Cell parameter	Pristine cathode	$R_{N/P}$ (Q) = 1.3 cathode	$R_{N/P}$ (Q) = 1.6 cathode
***a* (Å)**	2.9799(1)	2.9572(3)	2.9600(4)
***b* (Å)**	2.9799(1)	2.9572(3)	2.9600(4)
***c* (Å)**	16.046(1)	16.089(4)	16.100(3)

The amount of sodium ions in the cathode per formula unit was estimated doing the following assumptions: (1) the amount of Na^+ per formula unit in $NaFe_{0.4}Mn_{0.3}Ni_{0.3}O_2$ at the beginning of the experiment is 1, (2) the sodium content in the subsequent cycles is calculated based on the charge/discharge capacity delivered by the cell, assuming that no secondary reactions happen upon cycling. For $R_{N/P}$ (Q) = 1.3 and 1.6, the final amount of sodium ions in the cathode structure are, 0.77 and 0.75 Na^+, respectively. The XRD diffraction patterns are in accordance with the estimations of the Na moles remaining in the cathode structure for both samples, which is less than the fully sodiated pristine cathode. All these facts derived from the post-mortem analysis are consistent with the electrochemical performances observed for the two cells with degradation over cycling.

7.3.2.2 Influence of the cathode morphology

This section is focused in the effect of the variation of the cathode morphology. The cycling performance of the cell with original cathode morphology (O1.3_2.0-3.9) and spherical cathode morphology (S1.3_2.0-3.9) are compared.

The cell with the original morphology cathode presents higher reversible capacity values after 100 cycles than the cell with spherical morphology, 91 mAh g^{-1}_{AMCat} (13.7 mAh) and 75 mAh g^{-1}_{AMCat} (10.8 mAh) respectively for O1.3_2.0-3.9 and S1.3_2.0-3.9 (**Figure 7.18**). The capacity retention is also different, being higher for the one with the original morphology cathode (90.3%) than for the one with spherical morphology cathode (81.7%). Surprisingly, the cell with the spherical cathode morphology presents coulombic efficiencies higher than 100% due to some secondary reactions happening in the cell.

The visual inspection of the anodes after 100 cycles in **Figure 7.23** shows that the spherical morphology cathode containing cell anode presents some Na traces in the edges of the anode electrode.

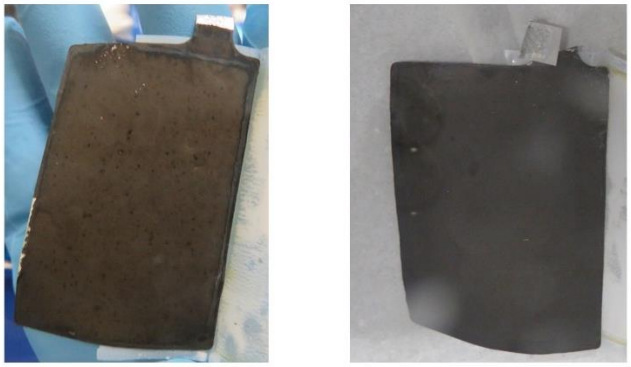

Figure 7.23. Visual aspect of the anode electrodes of O1.3_2.0-3.9 (original morphology) and S1.3_2.0-3.9 (spherical morphology) cells after cycling.

The SEM images of the cathodes show completely different microstructures (**Figure 7.24**) related to the morphology and the level of agglomeration of the particles. In the case of spherical morphology cathode, the size of the agglomerates is significantly lower. Moreover, the structure of this electrode seems to be more porous than the original morphology cathode. This fact might have enhanced the penetration of the electrolyte in the cathode microstructure and can be the cause of the secondary reactions and consequent low Coulombic efficiency.

Similar to what observed in the previous section, anodes present small particles on the surface of the electrode (**Figure 7.25**).

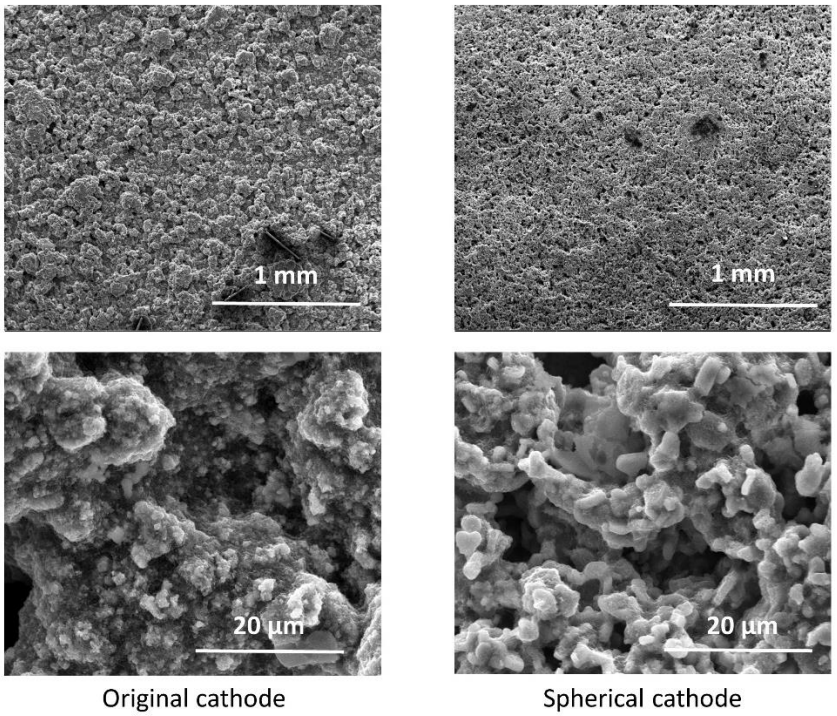

Figure 7.24. SEM images of the cycled original morphology cathode compared to the spherical morphology cathode.

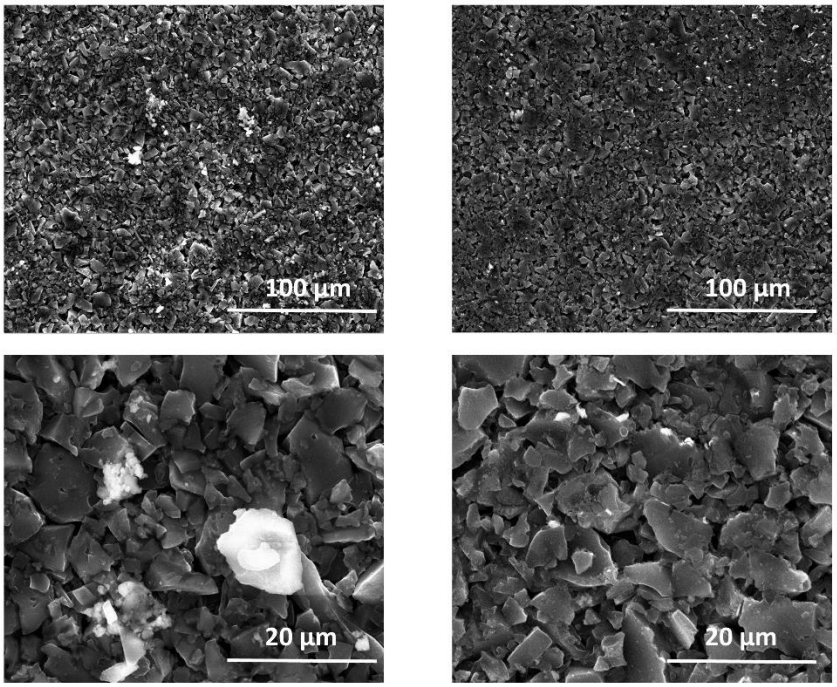

Figure 7.25. SEM images of the cycled anode coupled with a cathode with original morphology compared to the cycled anode coupled with a cathode with spherical morphology.

As it is shown in the X-ray diffraction patterns of the fully discharged cells in **Figure 7.26**, further structural changes occurred in the spherical type morphology cathode after cycling.

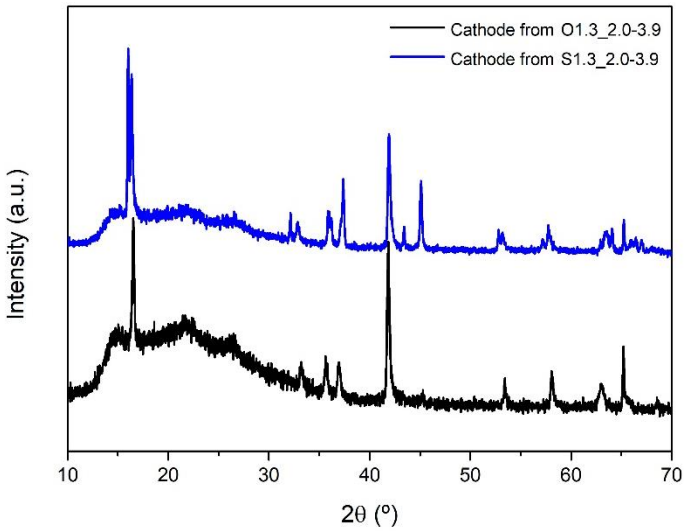

Figure 7.26. X-ray diffraction patterns from O1.3_2.0-3.9 and S1.3_2.0-3.9 cathodes.

Ex-situ X-ray diffraction analysis in the charge process of fresh spherical morphology cathode is performed in order to find out the reason for such a difference in the X-ray diffraction patterns between both cathode morphologies. Half-cells were assembled and charged up to 3.6, 3.9 and 4.0 V, dismantled and washed in DEC to be analyzed by XRD. The *ex-situ* XRD diffraction patterns in the charge process are collected in **Figure 7.27**.

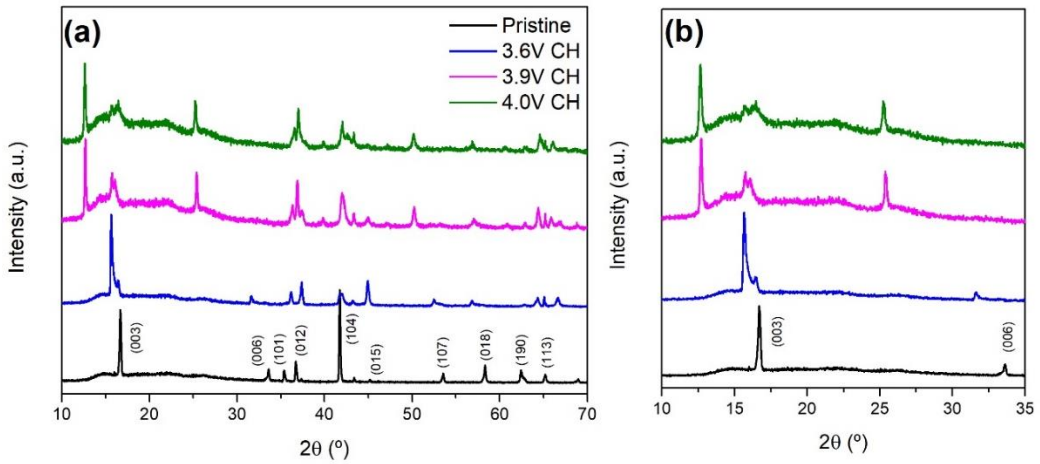

Figure 7.27. (a) *Ex-situ* XRD analysis of the $NaFe_{0.4}Mn_{0.3}Ni_{0.3}O_2$ cathode with spherical morphology in the charge process and (b) detail of the diffraction patterns in the range between 10 and 35°.

According to Xie et al., in the case of $Na_{1-x}Ni_{1/3}Fe_{1/3}Mn_{1/3}O_2$, which could be considered analogous as $NaFe_{0.4}Mn_{0.3}Ni_{0.3}O_2$, there is a reversible evolution of the O3-P3-P3-O3 hexagonal phase, in which a biphasic region formed by O3 and P3 is also observed. All the peaks are indexed to the *R-3m* space group with hexagonal layered structure during cycling as the pristine cathode [282].

In their case, when charging from 2.0 to 4.0 V, the (003) and (006) reflection peaks at 16° and 31°, which are the main diffraction peaks associated with the O3 phase, are shifted to lower angles. The same phase transformation is observed in our case at 3.6 V (**Figure 7.27** (b)). Moreover, at 3.9 V and 4.0 V, the (006) peaks starts to disappear, which is in accordance to what Xie et al. published. In addition to the (006) peak, (104) and (018) peaks also start to disappear at higher voltages.

The new peaks that can be assigned to a hexagonal P3 phase, start to appear at >3.5 V at 13, 25 and 50°, as in the case of 3.9 V and 4.0 V. (003) and (110) reflection peaks split into two during the charge process, which are an indicator of the two-phase reaction with the coexistence of O3 and P3 phases and then they merge into one again, when the cathode structure reaches the formation of the P3 phase. At the same time, the (101) and (012) peaks also split into two during the biphasic region.

According to the XRD patterns, the cathode structure undergoes a series of phase transition over the charge process, which is in accordance to what it is described in the literature. The differences in the X-ray patterns from between O1.3_2.0-3.9 and S1.3_2.0-3.9 can be derived from the changes in the amount of Na ions remaining in the cathode structure after cycling. **Table 7.9** collects the estimation of the amount of sodium ions remaining in the cathode structure as a function of the voltage from 3.6 V to 4.0 V, taking into account the same assumptions as those in section 7.3.2.1.

Table 7.9. Level of sodiation of the cathode during the charge process from 2.5 V to 4.0 V.

Ex-situ voltage (V)	Na moles in the cathode structure
Pristine	1
3.6	0.63
3.9	0.51
4.0	0.43

The S1.3_2.0-3.9 cathode diffraction pattern (**Figure 7.26**) presents a similar feature than the one done in the *ex-situ* XRD at 3.6 V. This fact could help to elucidate the quantification of sodium ions remaining in the cathode structure after cycling in the case of S1.3_2.0-3.9 pouch cell (**Table 7.9**) which should be in the range of 0.63. Contrarily, the amount of Na ions in remaining in the O1.3_2.0-3.9 cathode structure were quantified to be higher (0.77), corresponding to XRD patterns similar to the pristine electrode.

7.3.2.3 Influence of the cycling voltage range

In this section, the influence of the cycling voltage range is studied. Concretely, the analysis is focused in analyzing the effect of increasing the upper cut-off voltage from 3.9 V to 4.0 V. The $R_{N/P}$ (Q) is 1.3 and the cathode morphology is the spherical one in these tests.

When the cell is cycled within the voltage range from 2.0 V to 3.9 V, it presents significantly higher capacity retention and reversible capacity values after 100 cycles, 81.7% and 74.8 mAh g^{-1}_{AMCat} (10.8 mAh), respectively (**Figure 7.18**). When the cell is cycled in a wider voltage range, up to 4.0 V, there is a huge capacity fade over cycling of, approximately 70%, delivering a reversible capacity value of 24 mAh g^{-1}_{AMCat} (3.4 mAh) after 100 cycles.

The cell cycled between 2.0 V and 4.0 V presents low coulombic efficiency values during the first 20 cycles. This low Coulombic efficiency could be caused by multiple issues. For example, at high voltages, cathode structural changes and electrolyte decomposition reactions can happen in a larger extent.

In the case of the upper cut-off voltage limited at 3.9 V, there is some sodium plating in the area next to the negative tab. When the cell is limited at 4.0 V, the anode presents a huge amount of sodium plating in the interface between the coated material and the current collector (**Figure 7.28**). As a consequence of this sodium plating, there is a strong delamination of the coated foil from the current collector, which increases the cell resistance and is detrimental for the cycling performance of the cell.

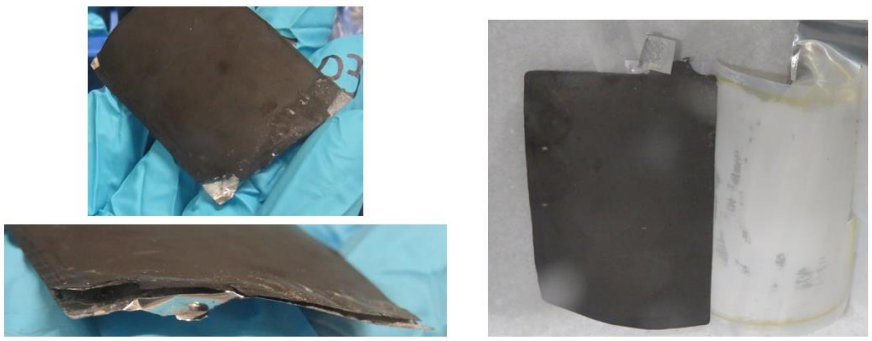

Figure 7.28. Visual aspect of the anode electrodes of S1.3_2.0-4.0 (upper cut-off voltage of 4.0 V) and S1.3_2.0-3.9 (upper cut-off voltage of 3.9 V) cells after cycling.

In the case of higher cut-off voltages, 2.0 V-4.0 V, the microstructure of the cathode looks less porous than the pristine cathode (**Figure 7.29**). On the other hand, the anode of the cell cycled in the voltage range between 2.0 V-4.0 V, presents evident cracks and voids. Moreover, there is a significant amount of secondary products deposited on the surface of the anode which can form an insulating layer (**Figure 7.30**).

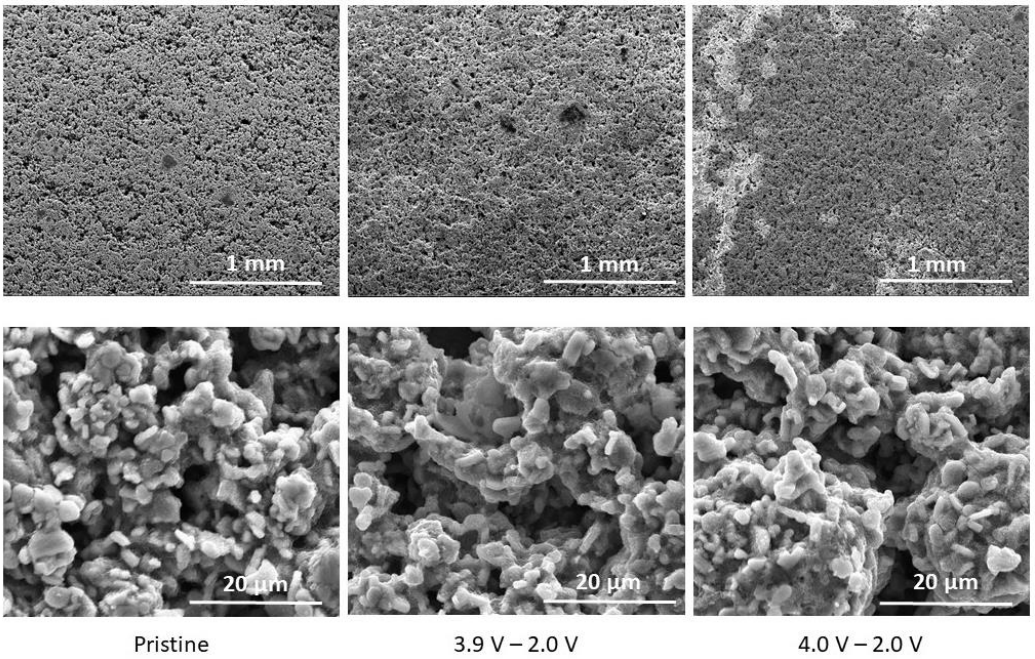

Figure 7.29. SEM images of the pristine and cycled cathodes with a upper cut-off voltage of 3.9 and 4.0 V.

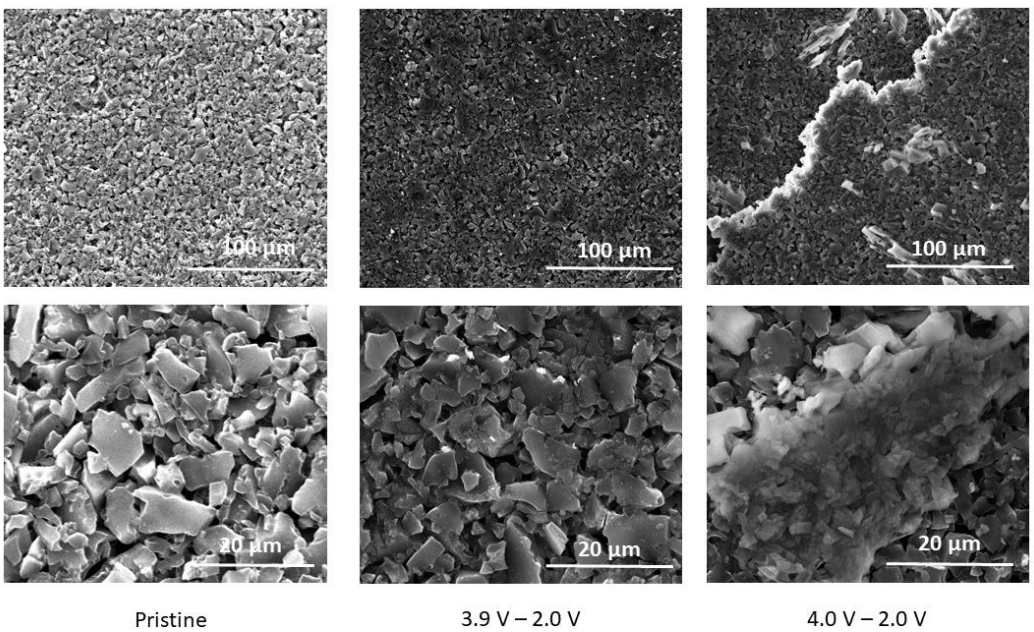

Figure 7.30. SEM images of the pristine and cycled anodes with an upper cut-off voltage of 3.9 and 4.0 V.

By means of the *ex-situ* analysis shown in the previous section, it can be concluded that, after 100 cycles, the spherical cathode structures from S1.3_2.0-3.9 and S1.3_2.0-4.0 can be indexed to a P3-type structure in the first case, and to a biphasic region of O3 + P3 in the second one (**Figure 7.31**).

It is also a fact that sodium ion amount in the cathode material structure after 100 cycles is not recovered to $X_{Na} = 1$. Bearing in mind the same assumptions than those in section 7.3.2.1, for the voltage range between 2.0-4.0 V, the final amount of sodium ions in the cathode structure is 0.27, while a final amount of sodium in the range of 0.63 was estimated for the cell tested in the voltage range between 2.0-3.9 V.

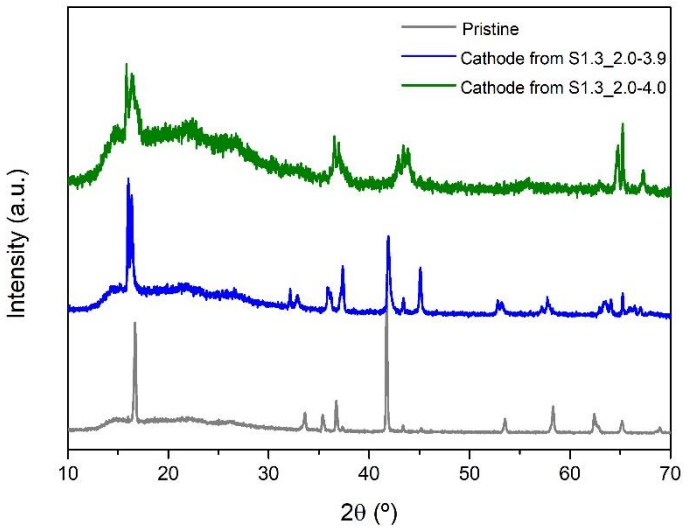

Figure 7.31. X-ray diffraction patterns from pristine cathode and S1.3_2.0-3.9 and S1.3_2.0-4.0 cathodes.

Electrochemical performance measurements of the cycled electrodes were done at half-cell configuration with sodium metal as reference in order to determine if the individual electrodes are able to recover the initial capacity of the corresponding electrodes after being cycled at pouch cell level. C-rate capability experiments were performed: 5 cycles at 0.1C, 5 cycles at 0.2C, 5 cycles at 0.5C, 5 cycles at 1C and 5 cycles at 0.1C. The lower and higher cut-off voltages were set at 2.5-3.9 V and 0.01-2 V, respectively for the cathode and the anode.

Figure 7.32 presents the rate performance of a pristine cathode at half-cell configuration as a reference cell and the half-cells made with the electrodes already cycled in pouch cell configuration.

In the case of O1.3_2.0-3.9 and O1.6_2.0-3.9 pouch cells, the amount of sodium ions remaining in the cathode structure were close to 0.75 and 0.77 Na^+, corresponding to 90 mAh g^{-1}_{AMCat}, in both cases (**Figure 7.32** (a) and (b)). In the pristine half-cell cathode, the initial reversible capacity is close to 120 mAh g^{-1} which is much higher than in the cycled electrodes of O1.3_2.0-3.9 and O1.6_2.0-3.9. As it was expected, the 1st charge capacities are different for each cell, depending on the level of sodiation at the end of the pouch cell cycling teste. However, in the case of the 1st discharge capacity due to the presence of the Na metal as an unlimited source of sodium ions, it was expected that the cathode structure could again be fully sodiated. However, this fully sodiation process is not happening due to some limitation in the cathode to reinsert Na ions up to x=1.

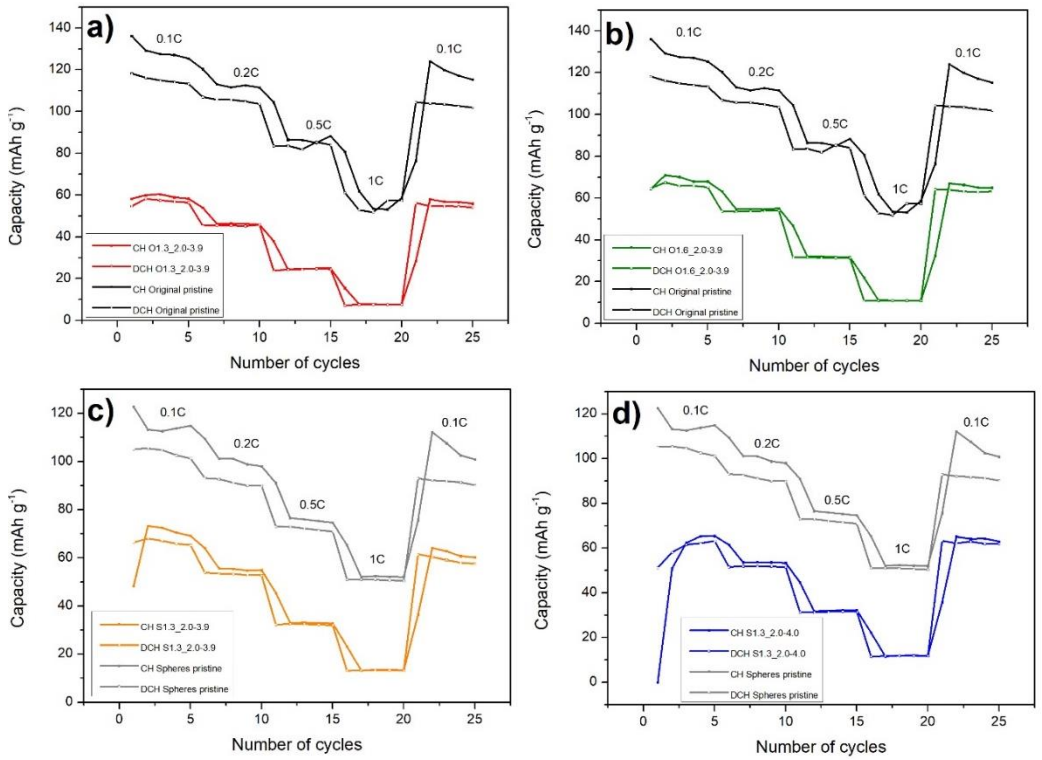

Figure 7.32. Rate performance of (a) O1.3_2.0-3.9, (b) O1.6_2.0-3.9, (c) S1.3_2.0-3.9 and (d) S1.3_2.0-4.0 compared to the pristine cathode electrode.

In the case of S1.3_2.0-3.9 and S1.3_2.0-4.0 pouch cells, estimated sodium ions remaining in the cathode structure were close to 0.63 and 0.27 Na^+, corresponding to 80 and 20 mAh g^{-1}_{AMCat}, respectively (**Figure 7.32** (c) and (d)). In the half-cell cathodes built from the cycled electrodes, it can be observed that in both cases, there is an initial recovery of the amount of Na ions in the 1st discharge process, which is due to the presence of a Na metal source. Especially in the case of S1.3_2.0-4.0, in which no Na ions are extracted during the 1st charge process. Therefore, the cathode structure can be recovered in some extent if a Na source is supplied. Again, there is a limitation to fully sodiate the cathode structure.

Regarding the anode electrodes, **Figure 7.33** presents the rate performance of the pristine anode electrode at half-cell and the half-cells made with the electrodes already cycled as a pouch cell. The cycling performance of all the anode half-cells is significantly lower than that of the pristine

electrode. As the cathode electrode is able to readmit Na ions in its structure, even if the pouch cell containing that specific cathode has shown significant degradation, it could be concluded that the anode is the most influencing component for the ageing of the cell. The formation of a thick insulating layer or the presence of Na plating that caused anode delamination are among the causes for cell degradation.

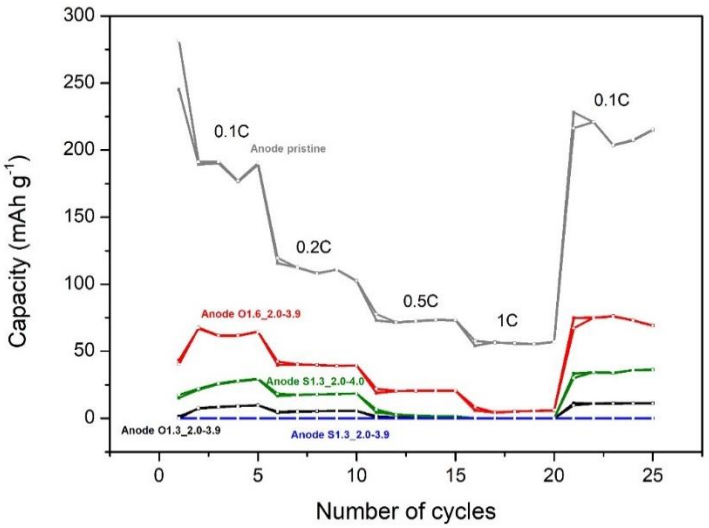

Figure 7.33 Rate performance of O1.3_2.0-3.9, O1.6_2.0-3.9, S1.3_2.0-3.9 and S1.3_2.0-4.0 anodes compared to the pristine anode electrode.

7.4 Thermal model for sodium-ion battery

There is a temperature range considered to be the safest for Li-ion batteries, in which capacity is maximized and safety risks are minimized [283]. Some researchers have already performed studies to determine the safety temperature limits for Li-ion technology. For example, Zhang, et al. [284] identified the safe temperature limits of the Li-ion battery in their research as −10 to 50 °C. Other sources state that Li-ion batteries are adversely affected when the ambient temperature is outside the range of 0 to 65 °C [219]. Many literature works have identified the ideal operating temperature of Li-ion batteries being in between 20 and 30 °C [285]. At this temperature, the electrochemistry of the Li-ion batteries is near its maximum capacity and the

degradation effects are minimized. As Waldmann et al. [286] reported, in the Li-ion cell, below 25 °C, the lithium plating phenomena is accelerated. However, at temperatures above 25 °C, an increment of the solid-electrolyte interphase (SEI) can happen leading to a capacity fade, growth of internal resistance (reported by Bloom et al. [287], Vetter et al. [288] and Troxler et al. [289]), or thermal runaway.

For each battery type, the heat generation rate depends on the initial state of charge, initial temperature, charge/discharge profile and surrounding cooling conditions [290]. Therefore, the internal heat generation is related to the variation of the temperature and the state of charge (SOC). In the case of the temperature, it is dependent on the overpotential heat generation which is caused by the internal resistance, kinetic aspects and mass transport related to the electrochemical reactions. On the other hand, the state of charge variation causes heat generation due to entropy changes attributed to the reversible electrochemical reactions within the battery [284]. As Manikandan et al. reported, in the case of Li-ion batteries, heat generation can be classified in two different categories, irreversible and reversible heat generation [291,292,293]. The irreversible heat generation is related to the internal resistance of each element of the battery and it can be measured by different methods such as electrochemical impedance spectroscopy, high power pulse tests or intermittent discharge methods [292], while the reversible heat generation is dependent on the nature of the electrode materials, and it is measured via entropic coefficient. The irreversible heat generation is related to the effects of the insertion reactions, ohmic resistance, the charge transfer and the diffusion of the electro-active species in the solid host material and the liquid electrolyte. These limitations cause an overpotential, also called Joule heat. According to Heubner et al., the reversible heat is more significant at low C-rates while irreversible heat is the dominating at higher current densities. They found out that the $NaFePO_4$ cells present larger heat generation rates than $LiFePO_4$ ones. This fact is related to the limitations in the case of sodium-ion cell of the charge transfer reaction and the solid-state diffusion.

Few reports have been published until date reporting the thermal model generation of Na-ion cells. They have been mainly focused on improving cathode, anode or electrolyte components,

separately [294,295,296,297]. Recently, Subasinghe et al. reported a study about the heat generation and internal resistance of 18650-type cells with sodium vanadium phosphate, $Na_3V_2(PO_4)_3$ as cathode and hard carbon anode using nonflammable 1 M $NaBF_4$ in tetraglyme electrolyte [298].

It is important to adequately manage the thermal behavior of the Na-ion cell. Concretely, the heat generation model of a Na-ion battery allows comparing heat generation rates for equivalent current levels and eventually, it is a tool to select the most suitable thermal management option. Wang et al. incised on how the analysis of the heat generation into the cell is essential to obtain the knowledge on how to enhance the processing and safety of batteries [299].

In this model, internal resistance and entropic heat coefficient are only considered to predict the heat generation, which according to some researchers, should be enough to adequately define our system [18]. As it was already done by Christen et al. [300], other parameters have also been beard in mind to develop the heat generation model, as the heat capacity (Cp), the amount of heat generated in the cell during a given load profile, etc. Other parameters that can be studied are the location of the heating or cooling source, which has a great impact on the efficiency of the cell. In order to perform the heat generation model of a sodium-ion cell, it is necessary to take into account the irreversible and reversible heat generation. This model can also provide valuable information to elucidate the favorable states of charge and discharge for battery operation and designing the management systems [301].

In this case, the heat generation in a range of temperatures from 10 °C to 40 °C is studied in a monolayer pouch cell. First, the thermal characterization of a Na-ion monolayer pouch cell prototype was performed, that is, the thermal parameters of the pouch cell were evaluated in the charge and discharge processes Secondly, a heat generation model was developed taking into account isotherm and cooled conditions.

7.4.1 Determination of thermal parameters

7.4.1.1 Heat capacity

For this sodium-ion battery, it is necessary to determine the average specific heat capacity for the complete cell taking into account the whole device, including different components (anode, cathode, separator, pouch encapsulation, etc.). That is, as the monolayer pouch cell is built from a variety of components, the calculated specific heat is an average specific heat. By definition, the specific sensible heat capacity is the amount of heat required to cool or heat 1 kg of a material by 1 °C [291]. The heat capacity can change depending on the state of charge and the temperature effects [291]. However, in this case, an average heat capacity is calculated, doing measurements in an adiabatic calorimeter at fully discharged state of the Na-ion cell.

A power of 0.3 W is supplied first to heat the resistance and a linear relationship between temperature and time is identified (**Figure 7.34**).

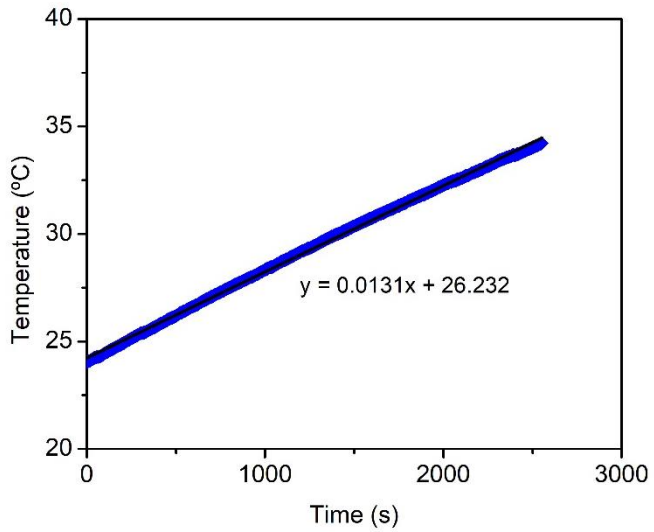

Figure 7.34. Evolution of the temperature measured at the ARC when 0.3 W is supplied. Blue points correspond to the measured values and the black line corresponds to the linear regression of the data.

As the temperature is evaluated by means of the ARC equipment and two external thermocouples, both responses are analysed in order to consider a range of the heat capacity

values. The Cp parameter is calculated from the slope of the linear regression of the relationship between the 3 measured temperatures and the time according to the formula (7.1) in which q is the supplied power, M is the mass of the cells, T is the temperature and t is the time.

$$q = Cp \times M \times \frac{dT}{dt} \qquad (7.1)$$

According to the Cp values displayed in **Table 7.10,** there are small variations for both different devices used to perform the temperature measurements. It is assumed that the Cp parameter for these cells is close to an average Cp value of approximately 2.30 J g^{-1} K^{-1}.

Table 7.10. Cp parameter as function of the equipment used for the measurements.

	Mass of the cells (g)	Power (W)	dT/dt	Cp (J g^{-1} K^{-1})
ARC thermocouple	10	0.3	0.0131	2.290
External thermocouple 1			0.0127	2.362
External thermocouple 2			0.0133	2.255

A different power was supplied in order to check the reproducibility of the measurement and the independency from the power supplied. When applying 0.1 W, the obtained Cp value is close to 2.5 J g^{-1} K^{-1}. Therefore, a range of Cp values in the range between 2.30 to 2.50 J g^{-1} K^{-1} can be considered for the analysed Na-ion pouch cells.

7.4.1.2 Thermal conductivity

The thermal conductivity (λ) is defined as the capability of a material to transfer heat. Therefore, it is the thermal energy transmitted through a length or a thickness, in-plane or cross-plane. Thermal conductivity values can go from ~ 0.015 W m^{-1} K^{-1} for aero-gels at the low end to ~2000 W m^{-1} K^{-1} for diamond and ~3000 W m^{-1} K^{-1} for single-layer graphene at the high end, at room temperature. This parameter has an orthotropic performance, meaning that it can be different depending on the considered Cartesian coordinate through the body of the cell. The reciprocal of this parameter is the thermal resistivity.

In this case, cross-plane thermal conductivity was measured, by means of 4 thermocouples. T01, located in the outer part of PCI; T02, located in the inner part of the PCI and close to the resistance; T03, located in the inner part of the PCII and T04, located in the outer part of the PCII.

Firstly, one set of measurement was performed, in which the cells were horizontally placed. 5 different supplied power values were tested (0.1 W, 0.3 W, 0.61 W, 1.22 W and 2.44 W) and the evolution of the temperatures is represented in **Figure 7.35** and **Figure 7.36**). However, as the objective of the power supply is to heat the resistance to reach stationary conditions inside the air tube, two power values were discarded because they were not fulfilling this requirement. At 0.1 W, the temperature is not stable over time and measured values are very close to room temperature (**Figure 7.35** (a)). In the case of 2.44 W, the temperature is not stable either over time and this temperature stability could only be reached at temperatures higher than 35 °C, which is above the safe temperature range that was stablished for these cells (> 35 °C) (**Figure 7.35** (b)).

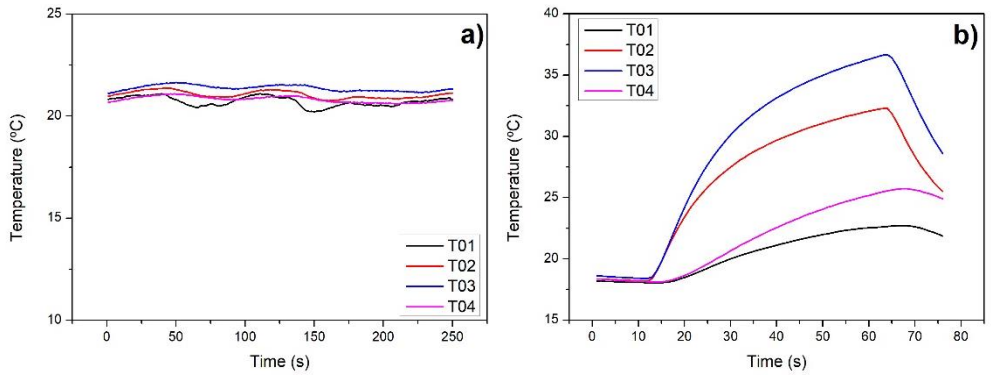

Figure 7.35. Evolution of the temperature with the time at (a) 0.1 W and (b) 2.44 W.

On the other hand, when 0.3 W, 0.6 W and 1.22 W are supplied, steady state conditions are reached, so the thermal conductivity can be calculated (**Figure 7.36** (a), (b) and (c)). However, it is important to bear in mind that initial temperature values are discarded because they correspond to a non-stable profile. The experiment with 1.22 W is considered to have the most stable temperature profile, while in the case of 0.3 W, T02 and T03 are closer, which can indicate that the heat flux, Q, is more homogeneously distributed in both sides (**Figure 7.36** (a)).

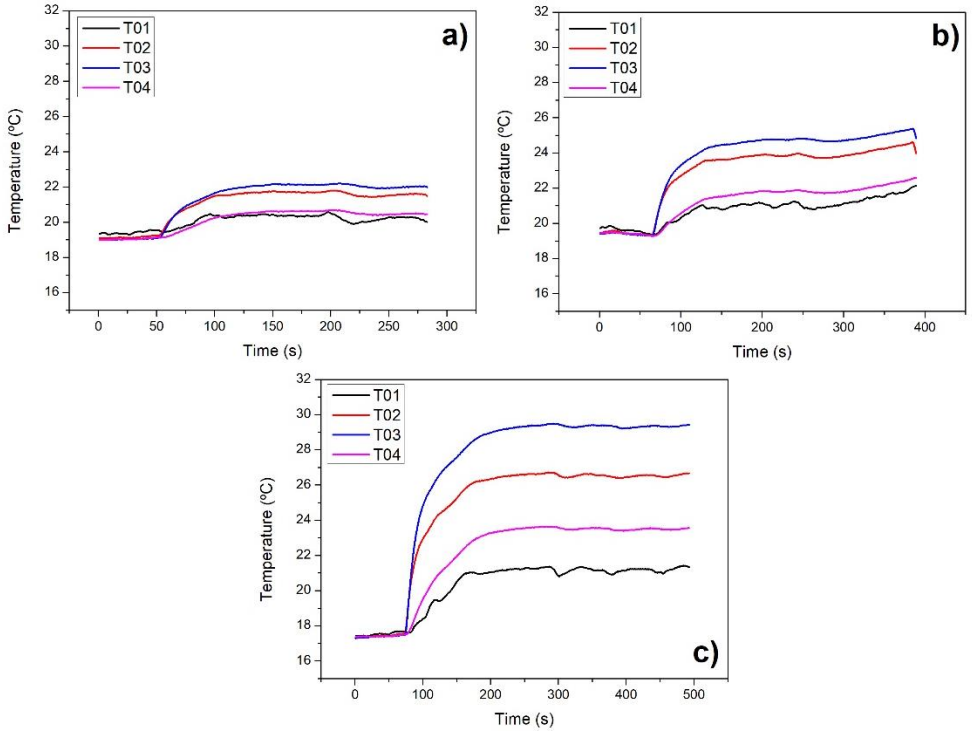

Figure 7.36. Evolution of the temperature with the time at (a) 0.3 W, (b) 0.6 W and (c) 1.22 W.

Table 7.11 shows the thermal conductivity values for PCI and PCII, when the cells are placed in both vertical and horizontal position during the measurements (**Figure 7.37**).

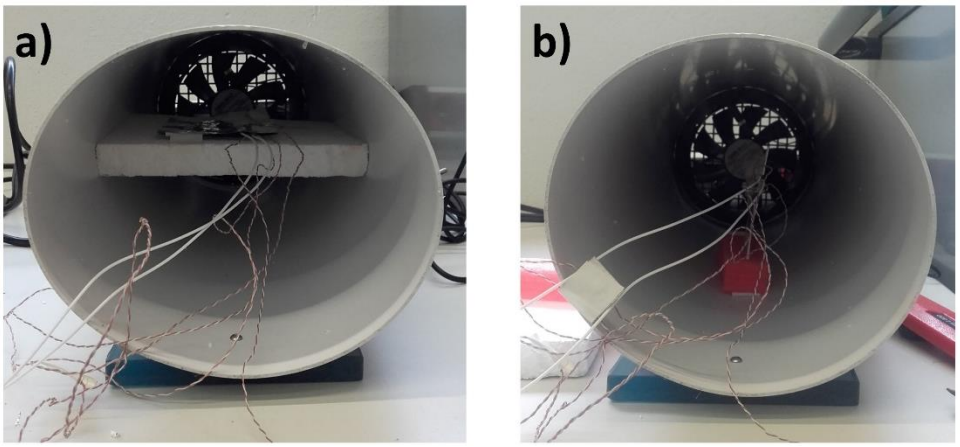

Figure 7.37. (a) Horizontally and (b) vertically placed monolayer pouch cells.

The thermal conductivity is obtained from the experimental data represented in **Figure 7.36** according to the equation (7.2).

$$Q = \lambda \times \frac{A}{L} \times \Delta T \qquad (7.2)$$

It is worth to mention that in the case of the horizontally placed cells, the standard deviation between PCI and PCII is 1.73 W $m^{-1}K^{-1}$, while the standard deviation between the results obtained at different supplied power (0.3, 0.6 and 1.22 W) is 0.62 W $m^{-1}K^{-1}$ (**Table 7.11**). An average value of 32.43 W m^{-1} K^{-1} is obtained from these experiments when the cells are placed in horizontal position.

Table 7.11. Thermal conductivity as a function of the power supplied to the resistance for both PCI and PCII (horizontally and vertically placed pouch cell).

Pouch cell	Power (W)	Thermal conductivity (W m^{-1} K^{-1}) (horizontally placed cell)	Thermal conductivity (W m^{-1} K^{-1}) (vertically placed cell)
PCI	0.3	34.2	39.66
	0.6	33.065	38.37
	1.22	35.225	37.2
PCII	0.3	30.25	22.25
	0.6	30.685	23.91
	1.22	31.135	24.23

A second batch of experiments was also performed which the cells were vertically placed. In this case, only 0.3 W, 0.61 W and 1.22 W were applied. This new experimental setup should allow improving the equalization of the air flow through the two faces of the pouch cell. As it can be observed in **Table 7.11**, the thermal conductivity values obtained for both PCI and PCII as a function of the power supplied, present more variability, with standard deviation between PCI and PCII of 7.47 W m^{-1} K^{-1}. So, further variations might be happening in this configuration

between both cells. As it has been already mentioned, in the case of 0.3 W, T02 and T03 are closer, which can indicate that the heat flux is more homogeneously distributed in both sides. An average thermal conductivity value of 30.94 W m^{-1} K^{-1} is obtained when the cells are located in the vertical position, however, the standard deviation is higher in this second case.

In general, taking into account these two type of measurement and the existence of two similar pouch cells in the measurement, thermal conductivity values of the Na-ion cells are between 22.25 and 39.66 W m^{-1} K^{-1}, approximately.

The differences between PCI and PCII can be derived from the thickness approximation, which was considered to be 477.8 µm for both the cells. In **Figure 7.38**, the influence of the variation of the thickness of the pouch cell (for the same experimental data obtained) () in the thermal conductivity value can be observed. Even small differences on the thickness (< 20 µm) have a large influence in the thermal conductivity estimation. It is also necessary to take into account that, in both types of measurements (horizontal and vertical configuration), the contact between both cells is not complete, and therefore, it is not possible to consider total symmetry spite of having same characteristic cells. Therefore, the heat flux is not being transmitted equally in both opposite directions.

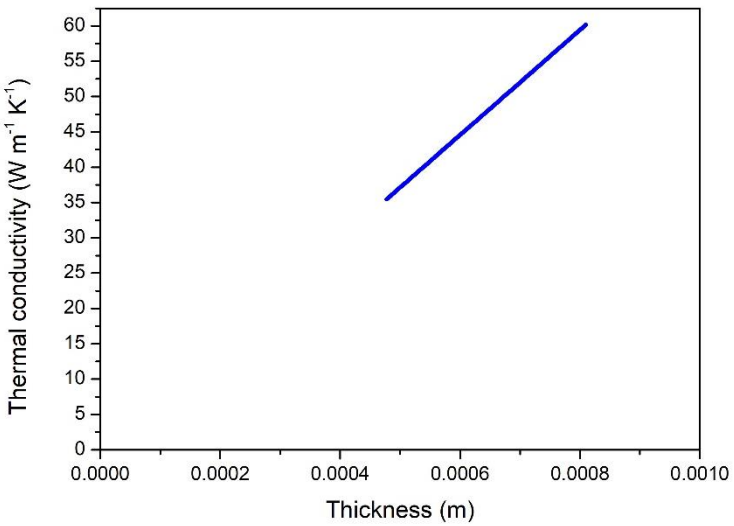

Figure 7.38. Influence of the thickness variation on the thermal conductivity.

7.4.1.3 Internal resistance

There is a requirement on the batteries to have a specific knowledge of the internal resistance in the cell. This parameter depends on the cell temperature and the SOC of the battery. As the internal resistance increases, the heat generation inside the cell increases too and this heat generation inside the cell can lead to negative exothermic reactions causing thermal runaway [302].

Constant current discharge pulses have been used in order to analyze the evolution of the R_{in} of the Na-ion cells at various SOC and temperatures. The selected constant current discharge pulses have a length of 18 s and a current rate of 1C. For the determination of the internal resistance at different SOC stages of ca. 20%, 40%, 60% and 80% during the charge and the discharge processes, three different cells at three different temperatures, 15, 25 and 35 °C, were analyzed.

In order to study the influence of relaxation times in the potential stabilization of the cells, two methodologies were followed. First experiments were performed 5 hours of relaxation time after the pulses at each SOC (Methodology I). The second batch of experiments was performed incorporating a relaxation time of 10 h after reaching each state of charge (Methodology II).

The real state of charge of the cells is calculated bearing in mind the total charge and discharge capacity values respectively for the steps in the charge and in the discharge process, respectively.

The Open Circuit Voltage after 1 h, 3 h and 5 h after the pulses was recorded in order to determine the differences between both methodologies. **Table 7.12** collects the values obtained for Methodology I.

Table 7.12. Difference in % with respect to the OCV measured after 5 hours after each SOC change during the internal resistance measurements for Na-ion cells at different temperatures (Methodology I).

15 °C								
	Charge				**Discharge**			
SOC (%)	21.7	40.9	60.1	79.3	79.6	58.6	37.5	16.5
Time								
1 h	0.4132	0.2274	0.1633	0.1953	0.0838	0.1500	0.3004	0.5959
3 h	0.1127	0.0325	0.0445	0.0558	0.0279	0.0300	0.0834	0.1589
25 °C								
	Charge				**Discharge**			
SOC (%)	19.0	38.2	57.4	76.5	79.8	58.8	38.0	17.0
Time								
1 h	0.6967	0.3626	0.2109	0.1436	0.0378	0.1445	0.9008	0.6604
3 h	0.1742	0.0898	0.0542	0.0479	0.0028	0.0391	0.7339	0.1801
35 °C								
	Charge				**Discharge**			
SOC (%)	18.8	37.8	56.6	75.4	79.5	58.1	36.7	15.4
Time								
1 h	0.7564	0.5577	0.2397	0.1971	0.0419	0.1497	0.2996	0.9145
3 h	0.1513	0.1969	0.0599	0.0563	0.0000	0.1048	0.0999	0.2783

The change of the OCV after 1 hour compared to 5 hours is not higher than 1% for any state of charge and temperature when using Methodology I. Moreover, 3 hours of relaxation time supposes no more than 0.2% of difference with respect to the values measured after 5 hours, except for the experiment at 25 °C, at which the difference is < 0.8%.

The time needed for OCV stabilization depends on the temperature, the SOC and the charge/discharge process (**Figure 7.39** (a), (b) and (c)). For example, at low state of charge, ca. 20% and 40%, both during the charge and discharge processes, longer times are needed for voltage stabilization than at 80% of state of charge. Moreover, at 15 and 35 °C minimum variation of the OCV with respect to that recorded after 5 hours of stabilization are observed compared to 25 °C measurements. In addition to this, the time needed for potential stabilization varies

depending on charge or discharge process, i.e. in the case of discharge process, slightly longer times are required.

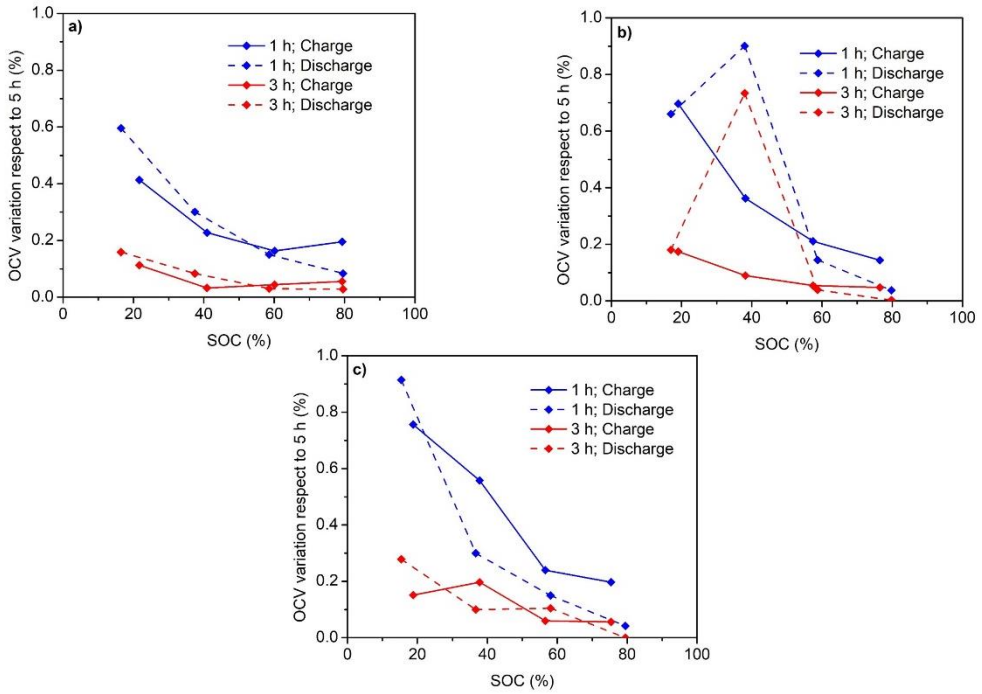

Figure 7.39. Variation of the OCV respect to that measured after 5 h as a function of the state of charge at (a) 15 °C, (b) 25 °C and (c) 35 °C (Methodology I).

As it has been stated a previous paragraph, a second set of experiments was also performed in which a relaxation time of 10 h was set after reaching each state of charge target (Methodology II). Similar to what recorded for Methodology I, Open Circuit Voltage was recorded after 1 h, 3 h and 5 h after the pulses, in order to determine if differences are detected in the time needed for stabilization (**Table 7.13**).

Table 7.13. Difference in % with respect to the OCV measured after 5 hours after each SOC change during the internal resistance measurements for Na-ion cells at different temperatures (Methodology II).

15 °C								
	Charge				**Discharge**			
SOC (%)	19.8	39.7	59.5	79.3	79.4	58.1	36.8	15.5
Time								
1 h	0.0076	0.0353	0.0208	0.0215	0.0219	0.0454	0.0466	0.1391
3 h	0.0201	0.0176	0.0104	0.0171	0.0053	0.0150	0.0131	0.1391
25 °C								
	Charge				**Discharge**			
SOC (%)	19.1	38.3	57.4	76.5	79.3	57.9	36.3	15.0
Time								
1 h	0.0118	0.0442	0.0240	0.0360	0.0141	0.0330	0.0879	0.2729
3 h	0.0212	0.0254	0.0105	0.0215	0.0037	0.0121	0.0338	0.2729
35 °C								
	Charge				**Discharge**			
SOC (%)	19.1	38.2	57.3	76.4	79.0	57.2	35.2	13.4
Time								
1 h	0.0540	0.0661	0.0420	0.0422	0.0113	0.0319	0.0820	0.2438
3 h	0.0463	0.0396	0.0240	0.0253	0.0023	0.0106	0.0275	0.0873

In the case of Methodology II, the change of the OCV after 1 hour compared to 5 hours is not higher than 0.3% irrespective of the state of charge and temperature, while after 3 hours of relaxation time, the maximum variation is less than 0.1%, except for the experiments performed at 25 °C. As observed when applying Methodology I, higher differences (< 0.3%) are observed at 25 °C also for Methodology II.

As it was happening in the previous case of study (Methodology I), voltage stabilization depends on the temperature, the SOC and the charge/discharge processes (**Figure 7.40** (a), (b) and (c)).

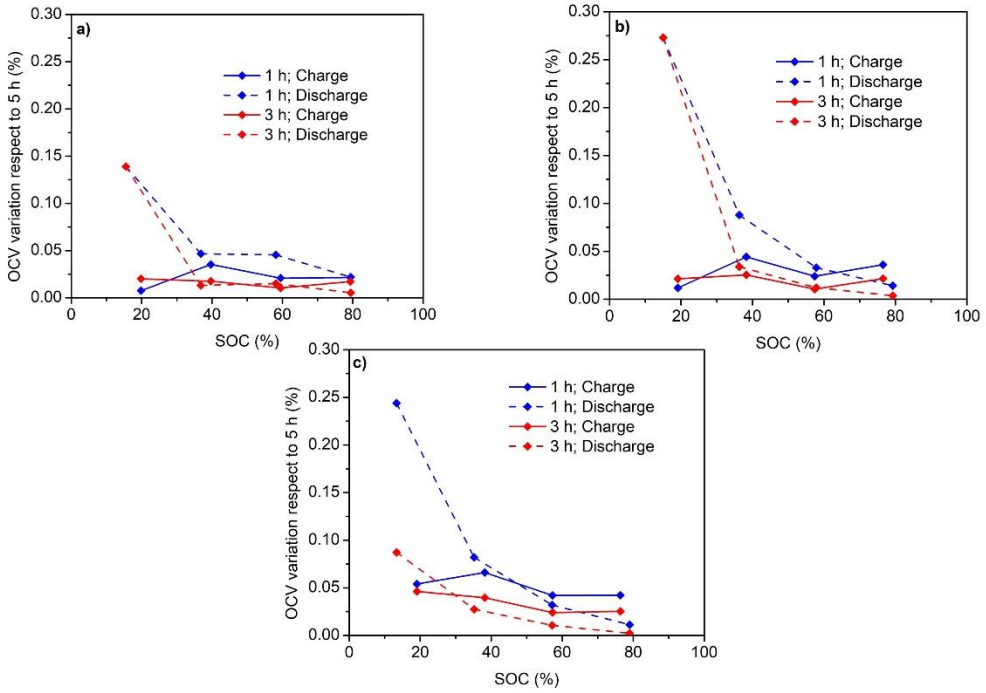

Figure 7.40. Variation of the OCV respect to that measured after 5 h as a function of the state of charge at (a) 15 °C, (b) 25 °C and (c) 35 °C (Methodology II).

The differences of the OCV variation at 3 hours with respect to 5 hours between the two methodologies, without relaxation time when reaching each SOC and with 10 hours of relaxation time after reaching each SOC are compared in the charge process, as an example in **Figure 7.41**. It is observed, that the OCV stabilization is much more evident in the second methodology, which includes the 10 hours of relaxation time after reaching each SOC. Therefore, it was concluded that the first methodology did not avoid the interferences created by the insufficient relaxation time after SOC variation.

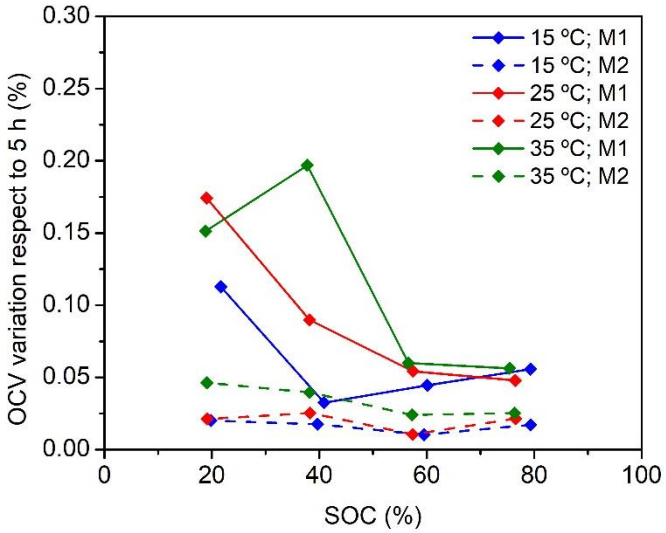

Figure 7.41. Comparative of the variation of OCV at 3 hours with respect to 5 hours for Methodologies I and II.

As it has been observed, there is requirement for the stabilization of the OCV after reaching each SOC. The variation of the OCV after 2 h, 4 h, 6 h and 8 h with respect to the value recorded after 10 hours is represented in **Figure 7.42** (a), (b) and (c), respectively for the experiments performed at 15, 25 and 35 °C. Maximum differences of approximately 1% are detected with respect to the voltage values measured after 10 hours. After 6 and 8 hours, it can be considered that the OCV is stabilized with a maximum variation of 0.3% with respect to the values measured after 10 hours, independently of charge and discharge processes, the temperature and the SOC. Another remarkable fact is that the variation of the OCV with respect to the values measured after 10 hours is higher 35 °C than at the rest of temperatures. Similar to what happened when applying Methodology I, it is also observed that longer times are required for voltage stabilization in the case of low SOCs, ca 20% and 40%.

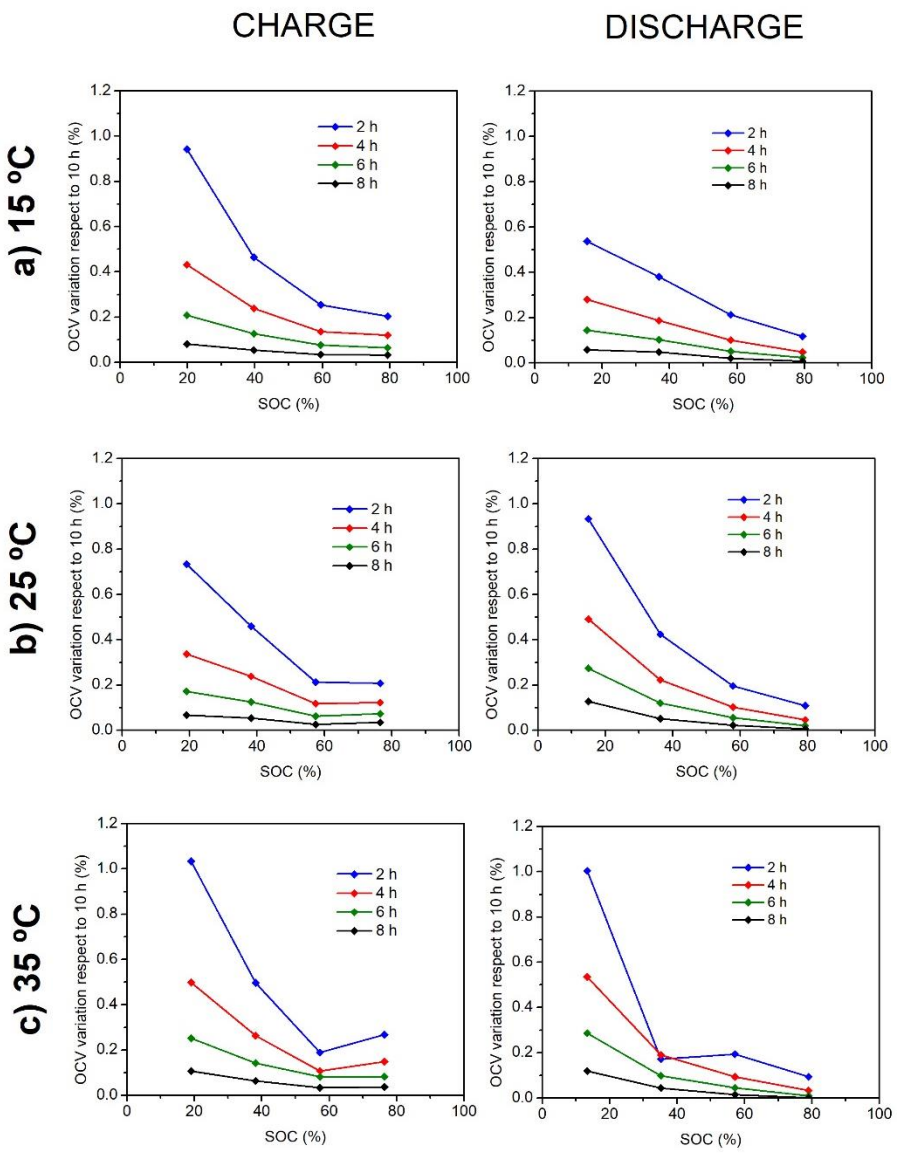

Figure 7.42. Variation of the OCV in % with respect to that measured after 10 hours applying Methodology II for internal resistance determination at (a) 15 °C, (b) 25 °C and (c) 35 °C. Data measured during the charge and the discharge.

It is noticeable that the internal resistance shows slightly higher values when measured during the charge process than during the discharge process. As an example, maximum internal resistance values measured in the charge and discharge processes are 28.93 and 27.54 Ω,

respectively (data obtained at a SOC of ca. 20% at 15 °C). However, these small differences in the internal resistance values could be related to the experimental methodology used to determine it. The effective value of the internal resistance should not be dependent on the charge and discharge processes, as it is not possible to model it assuming a discontinuous process. Therefore, for the heat generation model, an average internal resistance value is used.

Figure 7.43 and **Figure 7.44** represent the variation of the internal resistance as a function of the SOC and the temperature measured in the charge and the discharge, respectively.

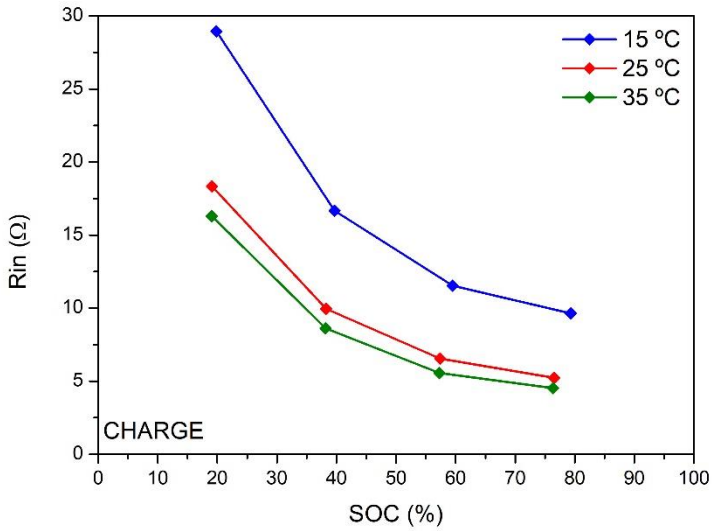

Figure 7.43. Variation of the average internal resistance with the SOC and the temperature measured during the charge process.

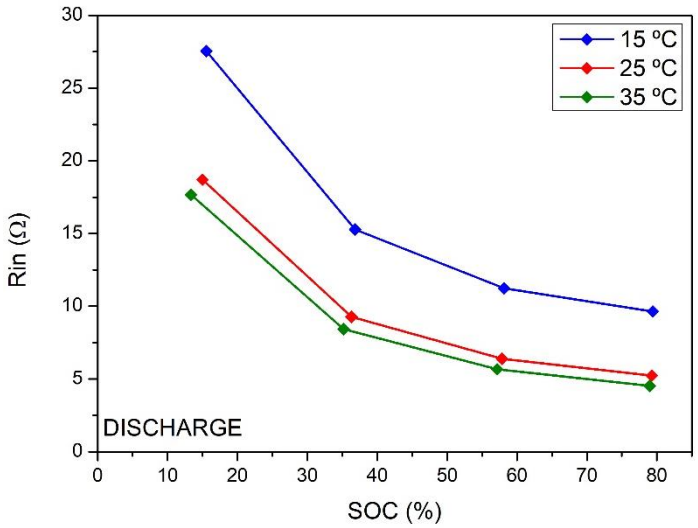

Figure 7.44. Variation of the internal resistance with the SOC and the temperature measured during the discharge process.

By increasing the temperature, the internal resistance decreases due to the reduced concentration overpotential at higher temperatures [223]. In addition to the temperature, the internal resistance is also influenced by the state of charge, the effect of the latter being more pronounced. The state of charge of the Na-ion cell significantly affects to the internal resistance of the cell, which decreases when increasing the state of charge. This fact is related to the build-up of concentration polarization at the end of discharge, which usually increases with the depth of discharge [223].

There is not exactly a linear relationship between the temperature and the internal resistance, as the differences in the internal resistance values between 15 °C and the other two temperatures are more evident than between 25 °C and 35 °C.

As it was stated by Heubner et al. the contributions of the irreversible and reversible heat are affected by the chemical and physical properties of the active material and the design of the cell. Therefore, the internal resistance can be minimized from the first steps of the electrode processing. As an example, the particle size variation can affect to the charge transfer resistance and the path for the diffusion of sodium ions, and thus to the internal resistance [298].

In order to reduce the internal resistance of the Na-ion batteries, and hence the heat generation over cycling, some improvement could be done in the battery design as it was proposed by Heubner et al., such as targeted nanostructuring, highly conductive catalytic coatings, and doping of the material with supervalent cations to increase the rate constant and the diffusivity.

The internal resistance can also be used to determine the degradation factor of a cell, as the internal resistance value increases as the cells are degraded [303]. This effect could be analyzed by means of the application of aging tests at monolayer pouch cell.

7.4.1.4 Entropic heat coefficient

The EHC, also referred as the temperature coefficient, describes the potential derivative with respect to the temperature and is determined in order to calculate the reversible heat generation within the cell [304]. In spite of the fact that battery pack designers are not taking into account extreme battery operation conditions in order to maximize its cycle life, it is important bear in mind these conditions, i.e. fully discharged and fully charged state, to calculate the heat generation [305].

Caused by the insertion and deinsertion process of the sodium ions, there can be some changes in the crystal structure of the cathode material and interactions among the sodium ions. This fact produces a heat increment, reversible heat, within the cell. The entropic heat parameter is principle characteristic of the active material of the cathode [306].

Figure 7.45 represents the voltage measured at the end of the 5 hours resting period at 15, 25 and 35 °C at a SOC of ca. 60% (data measured during the cell charging process). Similar to what observed in **Figure 7.45**, the relationship between the voltage and temperature should be almost linear and the slope of this line corresponds to the entropic heat coefficient, which should be similar to the B coefficient of the fitting to the function (2.13). Before starting the temperature sequence at each SOC, it is necessary to leave the cell at 25 °C for 10 hours, in order to reach thermodynamic stability. Once the SOC target is reached, a resting time between 5 and 10 hours is needed in order to have enough potential stability. However, at high SOC values, high resting

times can lead to self-discharge and it is necessary to check if the cell is affected by the influence of this high-self-discharge [305].

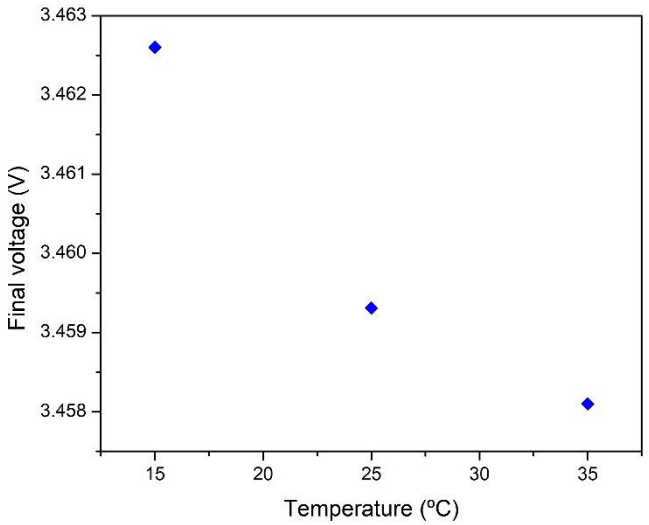

Figure 7.45.The relation between voltage and temperature at 60% of charge process.

The entropic heat coefficient is calculated as a function of the SOC. The real state of charge of the cells is calculated bearing in mind the total charge and discharge capacity values respectively for the steps in the charge and in the discharge process, respectively. The OCV evolution with the temperature is represented at different SOC in visible in **Figure 7.46**. The fitting for each SOC, ca. 0%, 20%, 40%, 60%, 80% and 100% in charge and discharge processes is also provided in **Figure 7.46**.

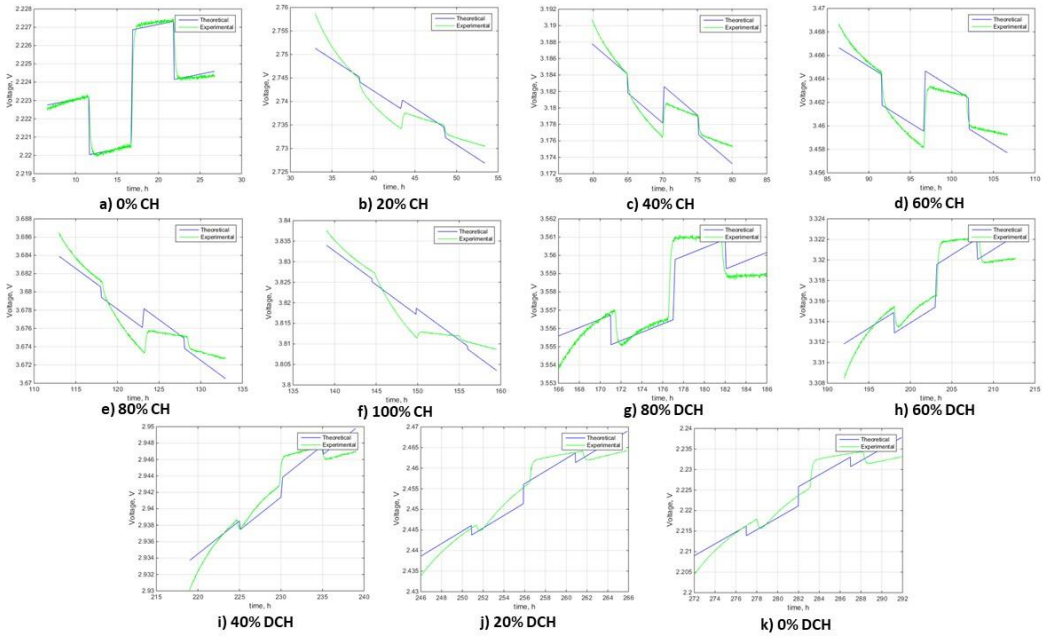

Figure 7.46. Voltage profile during the thermal sequence to calculate the EHC at different SOCs. (a) 0%, (b) 20%, (c) 40%, (d) 60%, (e) 80% and (f) 100% measured during the charge process and (g) 80%, (h) 60%, (i) 40%, (j) 20% and (k) 0% during the discharge process.

If it is observed the difference between the initial voltages at 25 °C, and then, after the temperature sequence, which is as low as 0.03 mV, it can be assumed that there is no important self-discharge issue for any SOC. The maximum difference between these two values is obtained at low SOC values, ca. 0 and 20%, and at high SOC values, ca. 100%. These SOC ranges would be more susceptible to suffer from self-discharge. **Figure 7.47** shows the data corresponding to this difference.

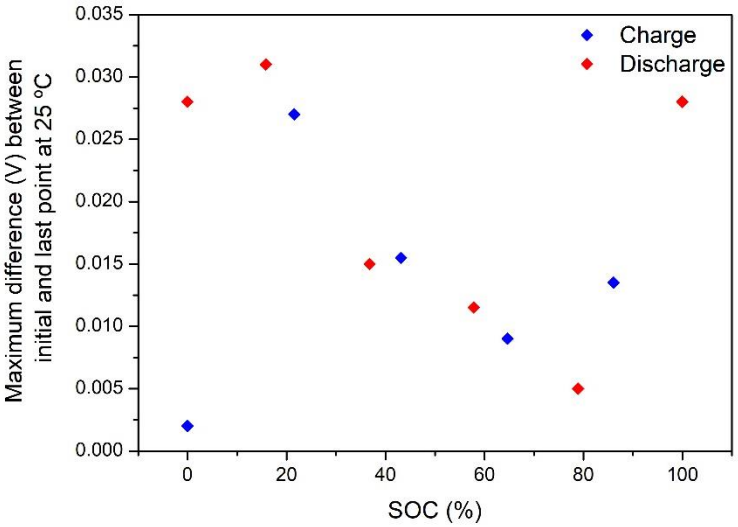

Figure 7.47. Maximum difference between the initial and final voltage at 25 °C.

If the voltage is inversely proportional to the temperature, i.e. the voltage decreases while the temperature increases, the entropic heat coefficient value is negative (**Figure 7.48**). If the EHC of the studied Na-ion cell has negative values in the whole SOC range, the voltage is inversely proportional to the temperature for the whole SOC range in the charge and discharge processes. A lack of significant changes in the cell chemistry all over the charge and discharge processes could be the reason for the EHC to keep negative values. Therefore, it could be assumed that there are not relevant crystalline phase changes [307].

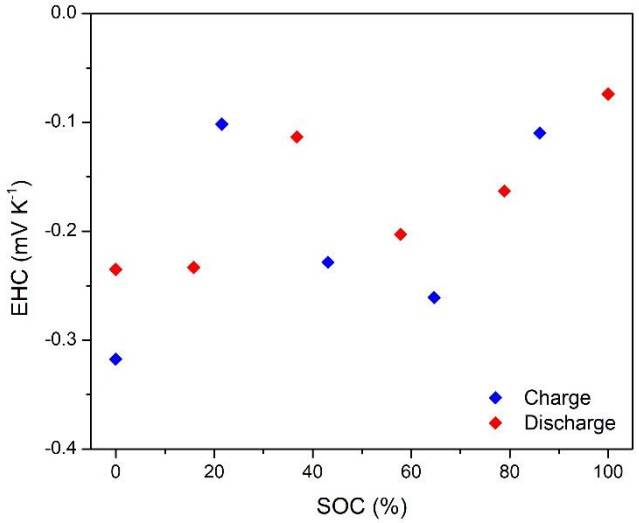

Figure 7.48. Entropic heat coefficient as a function of the SOC measured during the charge and discharge processes.

The maximum standard deviation between the entropic heat coefficient measured during the charge and the discharge processes is less than 0.06 mV, which is considered as low enough to assume a similar behavior in the insertion and de-insertion processes of the sodium ions. Taking into account that the error expected in the measurements is, approximately ± 1 mV, this could suggest that the reaction taking place in the Na-ion cell is highly reversible.

In general, low entropic heat coefficient values are obtained. As it was said by Abdul-Quadir et al. the magnitude of the entropy is small, but it cannot be neglected because the heat generated by this parameter could be significant [308]. According to Lu et al., small entropy coefficient values mean that the particular cathode material is thermally stable [309].

As well, as the values of the EHC are negative, it suggests that the effect of the entropic heat is exothermic during the discharge and endothermic during charging process, independent on the battery cycling rate [305]. As Manikandan et al. exposed in their work, negative entropic heat coefficient throughout the charge or discharge cycle at any given SOC, indicate that there is a dominant role of exothermic reactions, which could be evident from the increase of the temperature of the cell surface during slow discharge of the studied cell [310]. Manikandan et al.

also studied both the cathode and the anode in a separate way. While the anode maintained its entropic coefficient on negative values, the cathode reached positive values at, approximately, 85% of SOC. Further studies could be developed by analyzing both electrodes of the Na-ion cell, in order to know which is contributing in a more important way to the reversible heat generation measured from the entropic coefficients. For instance, when the negative electrode is a carbon, it could affect to the entropic heat coefficient. Choi et Lim et al., concluded that the entropic heat coefficient varies with the structural changes of the graphite anode and $LiCoO_2$ cathode [285]. For example, according to Bai et al., the anode material is greatly affecting to the entropic heat coefficient [310]. As Hong et al. proved, coke-based carbon negative electrodes had primarily negative coefficients, while other authors could switch from negative to positive by changing the negative electrode [311]. It was stated by Yun et al. that the anode is usually the dominant contributor, for both, degradation factor and entropic heat coefficient of the battery [312].

Related to the degradation factor and the influence of the entropic heat coefficient, according to Stanciu et al., at degraded cells, entropic heat coefficient slightly varyies from medium to high SOC range values [313].

The determination of the entropic heat coefficient also allows determining the best possible application for the studied cells. For example, in the case of having positive values of the entropic heat coefficient for a battery in the charge process, i.e. endothermic process, the battery could be used for fast charge type applications, if in a complementary way, the generated irreversible heat is not very pronounced as well.

7.4.2 Heat generation model

In the **Figure 7.49**, the electrochemical performance of the monolayer Na-ion pouch cell at 3 different temperatures and C-rates can be observed.

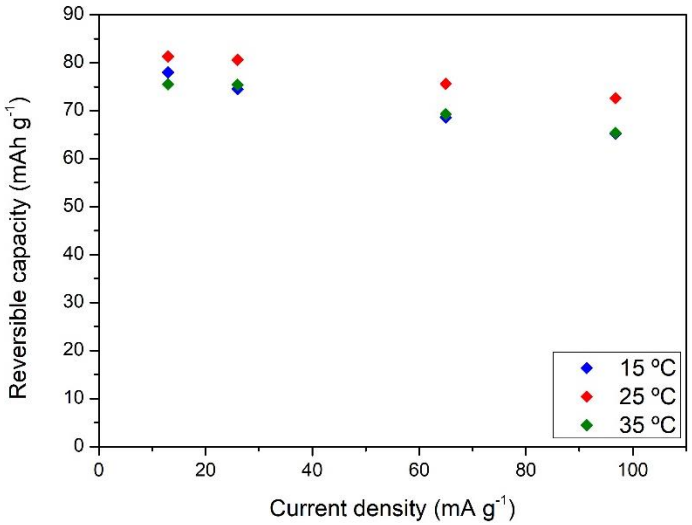

Figure 7.49. C-rate performance of the pouch cells at different temperatures.

According to the equation already mentioned in the Chapter 2 (7.3), based on the values of the internal resistance and the entropic heat coefficient as a function of the SOC and the temperature, the heat generation model is calculated, following the procedure described below (**Figure 7.50**).

$$\dot{q}_t = (I^2 \times R_{in}) + \left(I \times T \times \frac{dU}{dT}\right) \qquad (7.3)$$

From the experimental data of the internal resistance, the heat generation model makes a double linear interpolation of the values to obtain the internal resistance at any SOC and temperature. The same procedure is done with the entropic heat coefficient for the whole SOC range. The inputs for the heat generation model are the interpolated points of the internal resistance and the entropic heat coefficient, the current per time and the temperature per time in one known cycle of the Na-ion pouch cell.

For the heat generation model, two paths are followed. In one of the cases, constant temperature input is inserted in the system, which represents an isotherm model. Depending on the temperature input, the heat generation is calculated. In the second case, a predictive thermal model of the temperature is generated from which the heat generation is calculated. The temperature is calculated by means of an electrical circuit combining the battery equivalent

circuit with the polycarbonate blocks used to press the Na-ion monolayer pouch cell to obtain an optimal electrochemical performance. In this second case, cell is able to store and dissipate the heat during the experimental procedures, so it is a non-adiabatic cooled model.

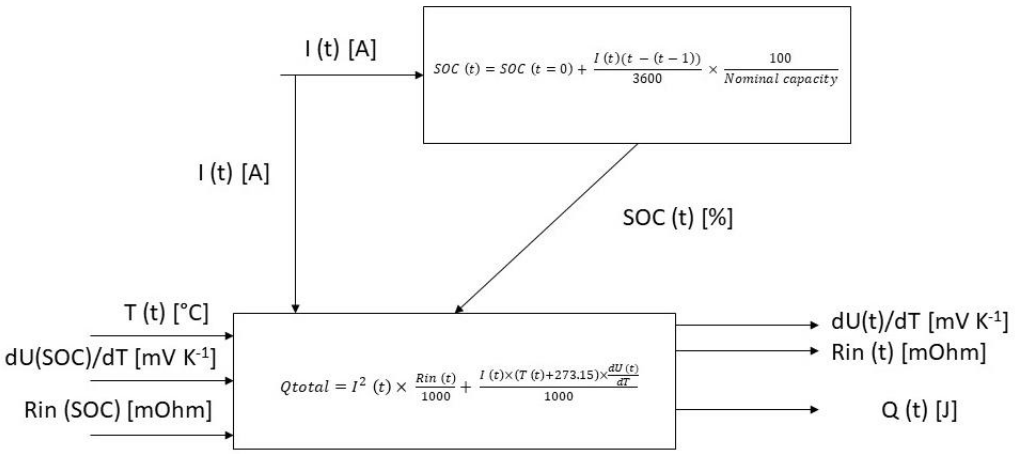

Figure 7.50. Procedure to determine the heat generated within Na-ion cells.

The input of the current for the Na-ion cell heat generation model is represented as **Figure 7.51**, in which the SOC over time is also represented for one cycle.

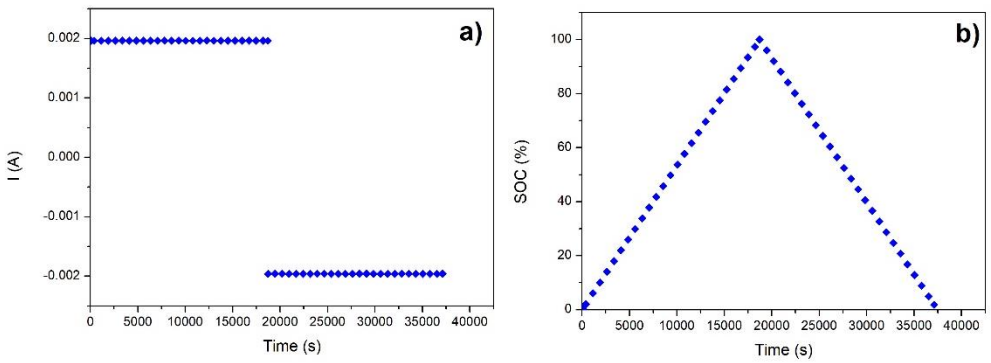

Figure 7.51. Heat generation model for the Na-ion cell (a) Current per time (b) SOC per time.

The heat generation of the Na-ion cell is evaluated at seven different temperatures, taking into account this input range of temperatures: 10, 15, 20, 25, 30, 35 and 40 °C. The interpolation of the internal resistance and the entropic heat coefficient values for the whole SOC range results

is shown in **Figure 7.53**. For the heat generation model, the internal resistance values for each SOC are calculated by means of an average value of the ones obtained in the charge and discharge processes. The internal resistance data was extrapolated to 0 and 100%, in the case of 15, 25 and 35 °C. **Figure 7.52** shows the example of the extrapolation performed for 25 °C. The equation derived from the linear fitting is used to calculate the increment and reduction in % of the internal resistance with respect to the value of consecutive SOC.

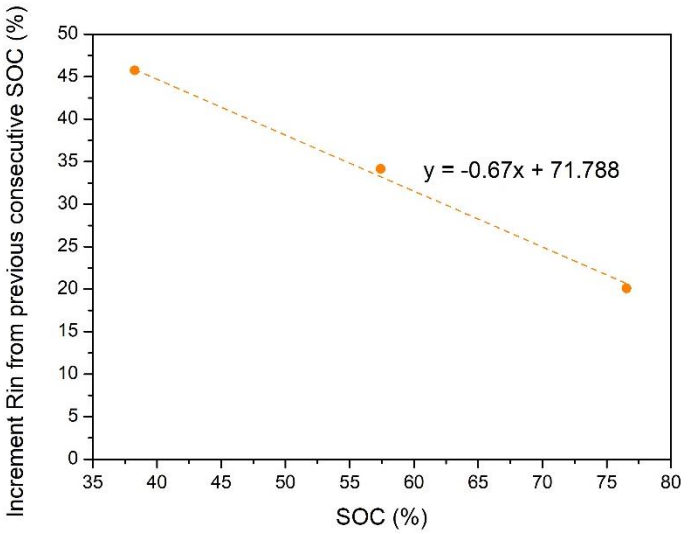

Figure 7.52. Data interpolation for 0% and 100% of the internal resistance.

The entropic heat coefficient should be valid for all the evaluated temperature range and it changes with the SOC, while the internal resistance varies with both the temperature and the SOC (**Figure 7.53**).

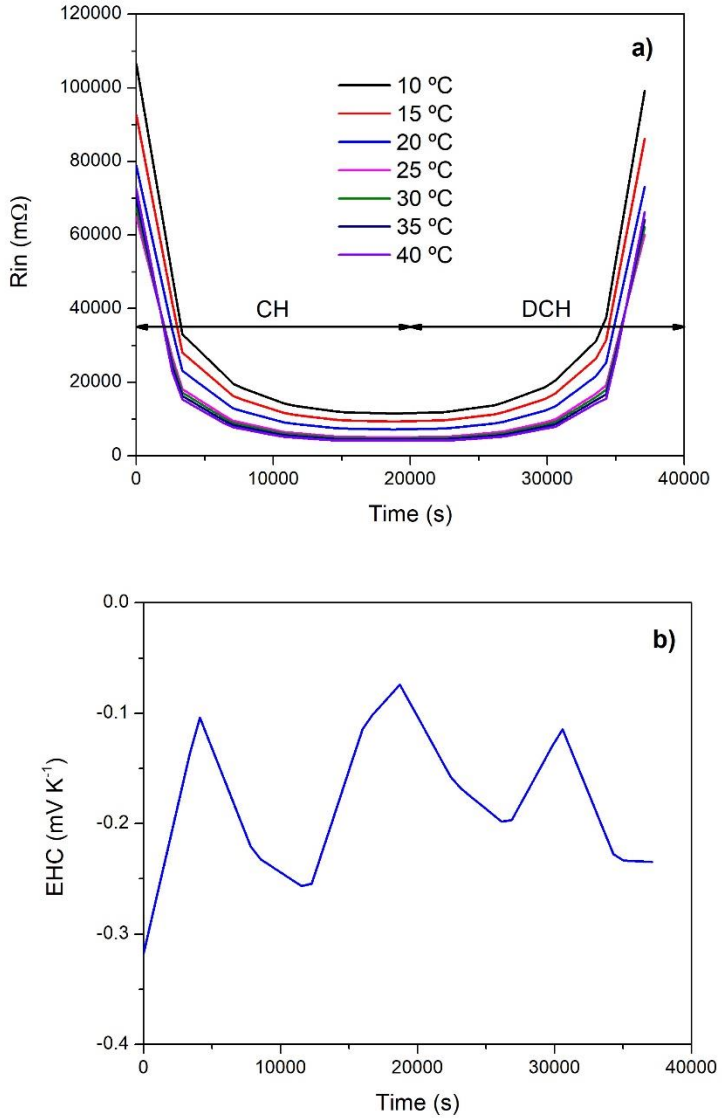

Figure 7.53. Heat generation model for the Na-ion cell. Evolution of the (a) internal resistance and (b) the entropic heat coefficient with the time.

The calculation of the heat generation in the Na-ion monolayer pouch cell is divided between two contributions, the reversible and the irreversible heat. The reversible heat corresponds to the influence of the entropic heat (7.4), while the irreversible heat corresponds to the internal resistance contribution (7.5). These two equations explain both terms,

$$\text{Preversible} = \text{I} \times (\text{T} + 273) \times \left(\frac{\text{Rin}}{1000}\right) \quad (7.4)$$

$$\text{Pirreversible} = \text{I}^2 \times \left(\frac{\text{Rin}}{1000}\right) \quad (7.5)$$

Figure 7.54 shows the contribution from both the sources of heat to the total heat generation in one cycle of the monolayer Na-ion pouch cell when the initial temperature is 15 °C.

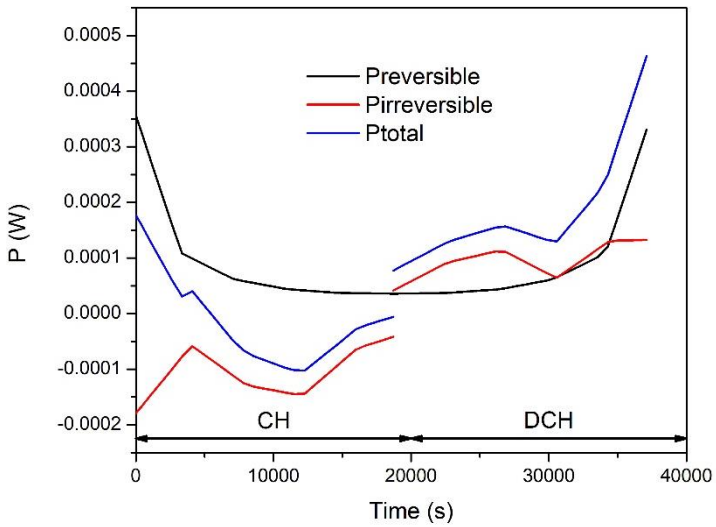

Figure 7.54. Evolution of the Preversible, Pirreversible and Ptotal with the time when the initial temperature is set at 15 °C. Isothermal model.

The total heat generation increases at the end of the discharge processes which could be attributed to the increase of the resistance of the cell. It is observed that the heat generated in the discharge process is higher than in the case of charge process [314].

Bai et al. studied the heat generation in a lithium ion battery, analyzing separately the effect of the reversible and the irreversible heat contribution to the total heat. The irreversible heat is affected by the ohmic resistance, as it is calculated from the internal resistance data, and it contributes dominantly to the overall heat generation. The irreversible heat is calculated from the internal resistance experimental data, which is considered as the major contribution. The internal resistance decreases with the increment of the temperature, which is a consequence of the higher chemical reaction activity at higher temperature and leads to better sodium-ion

diffusion. The reversible heat is calculated from the entropic variation, which is caused by the charge and discharge processes, and consequently the reversible heat is depending on the electrode materials.

As the total heat generation is divided in both reversible and irreversible heats, it reflects the contribution of both of them, depending on the charge or discharge processes. It is necessary to observe which the most predominant heat contribution is, in order to control the properties affecting to each one. In this case, the major contribution is given by the irreversible heat in the case of the charge process, while the reversible heat apparently dominates the discharge process. However, in the discharge process, the average heat generated by the reversible and irreversible heat are $8.6 \cdot 10^{-5}$ and $9.5 \cdot 10^{-5}$ W, respectively, which can be considered as very similar values. Overall, the irreversible heat could be dominating the charge and discharge processes. If the reversible heat is lower than the irreversible heat, it means that the chemical reaction affect in a lower extent than the polarization and the ohmic resistance [313].

The total heat generation increases at the end of the discharge which could be attributed to the increase of the resistance of the cell. Overall, it is observed that the heat generated in the discharge process is higher than that in the charge process. As Heubner et al. also assessed, the heat generation is higher for the discharge processes than for the charging process due to the exothermic and endothermic contribution of the reversible heat, respectively [297]. This endothermic contribution, at the charge process, it is derived from the fact that the dissipation of the heat, at that point, is higher than the heat generation in the cell. By increasing the current applied to the cell, this effect is expected to be reduced.

The average value of the generated total heat $(Q_{tota})_I$ is calculated according to **Figure 7.54**, and their values are displayed in **Table 7.14** according to the initial temperatures analyzed for isotherm conditions. As it can be observed in the **Table 7.14**, there is a tendency to decrease the Q_{total} in the Na-ion cell by increasing the initial input temperature of the cell, thus more heat should be dissipated in the case of lower temperature inputs. The calculation of the average value of the Q_{total} generated from different temperature inputs could be used to design the implementation of the thermal management of a battery pack (**Table 7.14**).

Table 7.14.Total heat generated in the Na-ion monolayer pouch-cell depending on the temperature input.

Temperature input (°C)	Q_{total} (W)
10	1.12×10^{-4}
15	9.26×10^{-5}
20	7.21×10^{-5}
25	5.17×10^{-5}
30	5.11×10^{-5}
35	5.05×10^{-5}
40	4.98×10^{-5}

As the calculated values of Q_{total} are not high enough, the evaluation of the evolution of the temperature in non-adiabatic cooled situations was not possible, as the margin of error associated to thermocouples is higher than the percentage of expected increment of the temperatures. For this reason, the experimental validation of these calculated data for a monolayer Na-ion pouch cell was not possible. Therefore, further studies can be developed in multilayer Na-ion pouch cells in order to corroborate this heat generation model. In addition, the endothermic behavior already observed in the charge process could also be validated and the effect of the current applied to the cell could be tested.

In the second case, mentioned at the beginning of the chapter, a predictive thermal model of the temperature is generated. If the temperature is not being inserted in the heat generation model as a constant, an equivalent electric circuit is inserted, representing the Na-ion monolayer pouch cell with the polycarbonate blocks (**Figure 7.6**).

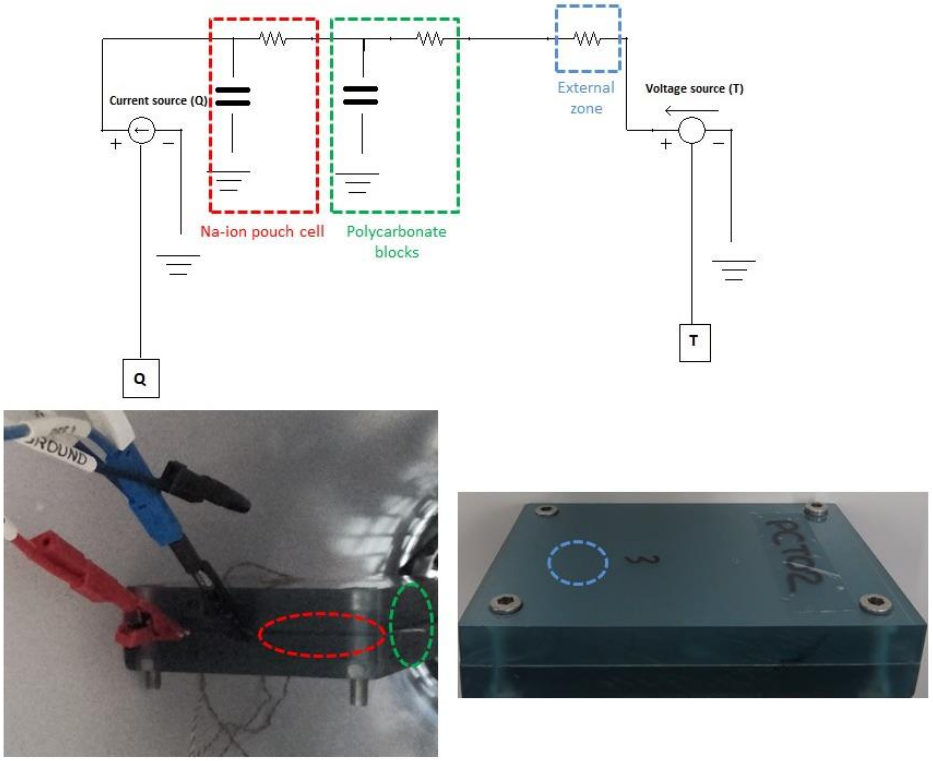

Figure 7.55. Detail of the equivalent electric circuit of the battery assembly

In the case of the equivalent electric circuit, the voltage corresponds to the temperature and the current is the heat flux. In this model, the temperature is changing due to the heat production and dissipation in the cell in each time step, and therefore, the input temperature in the consequent cycles will be varying integrated in a constant loop. This model represents a non-adiabatic cooled situation, as the cell is able to store and dissipate the heat during the experimental procedures.

In order to extract the equivalent circuit in the Simulink block diagram, thermal conductivity and heat capacity parameters already determined based on experimental measurements in the previous sections are considered. Taking into account that the Na-ion pouch cell is placed inside a polycarbonate holder in order to ensure enough pressure to obtain good cycle performance, both data considering the Na-ion monolayer cell and the polycarbonate blocks are taken into consideration to develop de equivalent circuit in the Simulink block diagram. The equations and

data displayed below (**Table 7.15**) are used in order to extract the thermal conductivity and Cp values.

For rectangular coordinates, the resistance for conduction, in the case of the Na-ion pouch cell and the polycarbonate blocks, corresponds to the following equation (7.6),

$$R = \frac{\Delta x}{k\,A} \qquad (7.6)$$

where, Δx (m) is the thickness of the cell and the blocks respectively, k is the thermal conductivity (W m^{-2} K^{-1}) and the A (m^2) is the area.

In the case of the last resistance placed in the circuit, it corresponds to the air temperature zone, out of the edges of the polycarbonate blocks. In this case, the resistance is due to the convection forces, so the equation corresponding to this resistance (7.7) is,

$$R = \frac{1}{hA} \qquad (7.7)$$

where, h (W m^{-1} K^{-1}) is the thermal conductivity for convection and the A (m^2) corresponds to the area exposed to the air temperature. In this case, h corresponds to an usual value of 5 W m^{-1} K^{-1} [315].

Table 7.15 summarizes the data for the circuit. In the **Table 7.15**, it is assumed that the values of the Na-ion pouch cell correspond to a unique cell, while the values of the polycarbonate blocks correspond to two blocks, as two blocks are required to cycle the Na ion monolayer pouch cell.

Table 7.15. Experimental data for the Simulink electric circuit

	Cp ($J\ g^{-1}\ k^{-1}$)	Thermal conductivity ($W\ m^{-1}\ k^{-1}$)	Convection heat transference coefficient ($W\ m^{-2}\ k^{-1}$)	Individual mass (g)	Individual thickness (m)	Area (m^2)	R (Ω)	Capacitance (F)
Na-ion pouch cell	2.5	32	-	5	0.000478	0	0.007	12.5
Polycarbonate block	1.25	0.2 [316]	-	122.5	0.011	0.01	6.268	306.25
External zone	-	-	5				11.4	-

In this case, and taking as initial temperature 25 °C, the evolution of the temperature represented in **Figure 7.56** is obtained (), according to the thermal model prediction of the temperature. Again, as it was shown in the isotherm model, there is an endothermic contribution in the charge process, and the temperature goes down below initial value of 25 °C. This remarkable fact is due to the dissipation effect that is higher than the generation effect of the heat, which is also related to the applied current.

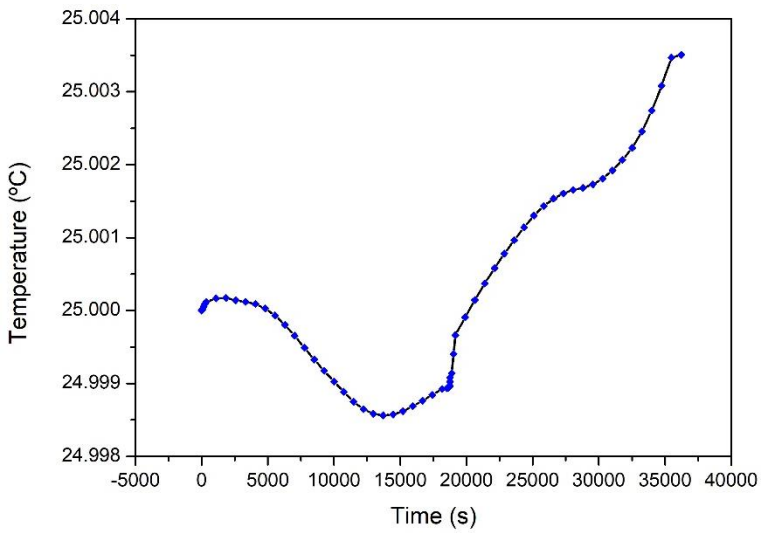

Figure 7.56. Evolution of the temperature in the cell starting at 25 °C.

The evolution of the temperature takes into account the dissipation and generation effects of the heat along one charge and discharge cycle. Again, as it can be observed in **Figure 7.57**, which represents the total heat generation taking into account the contributions from reversible and irreversible heat, it is observed that the experimental heat generation model validation is not possible due to the small size and thickness of the monolayer Na-ion pouch cell and the low amount of heat generated by the cell.

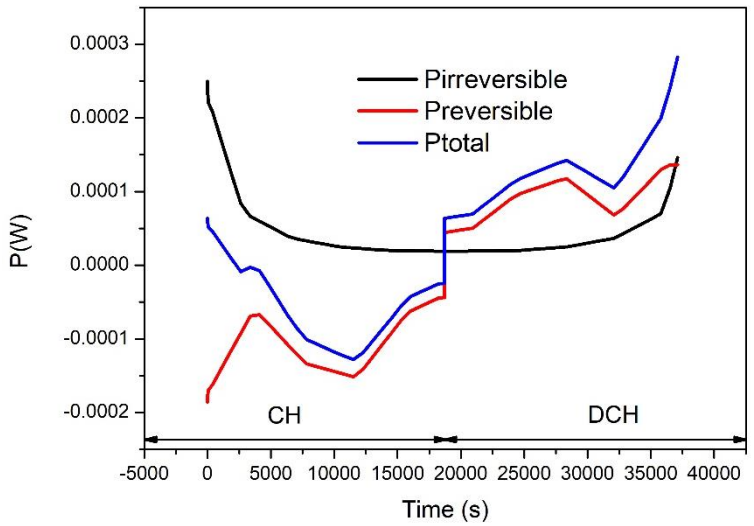

Figure 7.57. Evolution of the Preversible, Pirreversible and Ptotal with the time. Predictive model.

7.5 Conclusions

Based on the studies performed at small scale (2-electrode coin cell and 3- electrode Swagelok cell) an optimum $R_{N/P}$ (Q) range is selected between 1.5-1.2. The reversible capacity delivered after several cycles, the voltage profiles of the cathode, the anode and the full-cell, or the safety issues derived from the operation below or above the optimum voltage ranges have determined this initial range.

The negative to positive capacity ratio should be defined correctly when configuring a new full-cell. Essentially, the optimization of this ratio will help to enhance cycling performance and the safety design of these sodium-ion cells. $R_{N/P}$ (Q) = 1 is discarded because of the sodium plating

on the surface of the anode, the low reversible capacity values along cycling associated to the previous fact and the especially bad performance at higher rates. In the case of $R_{N/P}$ (Q) = 1.6, there is not sodium plating risk associated but, the reversible capacity values are reduced due to the short plateau region of the negative electrode which is effective. The negative to positive ratio of 1.3 represents the trade-off between these two ratios and it becomes in the best option for the subsequent experiments, showing good reversible capacity values at 13 mA g^{-1}_{AMCat} and higher current densities, as well as good capacity retention.

In addition to this, limiting the upper cut-off voltage to 3.9 V allows to reduce the amount of metallic sodium deposited on the surface of the anode by limiting the low voltage zone in the anode side when cycled for larger number of cycles. Moreover, this affirmation will be complemented by the positive effect in the capacity retention observed over cycling. Although, spherical type morphology in the cathode half-cell configuration presents slightly lower reversible capacities and slightly worse electrochemical performance at higher C-rates, it allows to perform the electrode coating process at large scale using the continuous coating machine, since the size of the agglomerates is significantly reduced.

The increment of the cycling voltage range up to 4 V affects to the cycle performance of the pouch cells. Comparing two pouch cells done with the same $R_{N/P}$ (Q) = 1.3, if the upper cut-off voltage is established at 4 V instead of 3.9 V,, the sodium plating in the cell increases, as the anode operates at voltages closer or lower than 0 V. Because of this reason, further deposition of sodium metal is happening in the anode side, so there is a significant loss of sodium ions which are not recovered over cycling. Moreover, the anode presents severe delamination after 100 cycles, also related to the sodium ion deposition in the interface between current collector and the coated foil, especially at the edges of the anode electrode.

It was concluded that the degradation of the anode is the main contributor to the cell degradation. On the other hand, it has been shown that cathodes partially recover initial capacity when tested as half cells after the cycling stability tests at pouch cell level.

Regarding the conclusions corresponding to the generation of the thermal generation model, the internal resistance increases by decreasing the temperature, so those parameters have an

inversely proportional relationship. However, the internal resistance is more influenced by the variation of the SOC than by the variation of the temperature, i.e. the internal resistance values are increased almost in one order of magnitude when decreasing the SOC from 80 to 20%. As the internal resistance increases, the expected heat generation is higher. Moreover, it has been proved the importance of the stabilization time after every SOC variation to improve the quality of the calculated internal resistance values, being a resting time of 10 hours selected as the optimum.

The entropic heat coefficient maintains negative values for all the studied SOC range, irrespective of the data being calculated during the charge or discharge processes. Based on this result, the optimum SOC range for the Na-ion pouch cell utilization could be determined, as small absolute values of the entropic heat coefficient are related to heat generation and stability of the electrode materials.

By modelling the heat generation over cycling of the Na-ion monolayer pouch cell it has been concluded that the irreversible heat is the main contribution to the total heat generation, which is related to the polarization and the ohmic resistance.

However, a validation of the heat generation model could not be performed because of the small size and thickness of the monolayer Na-ion cell, being the total heat generated too small. The proposed Na-ion heat generation model provides an idea of the heat generated during the charge and discharge processes of this type of technology, taking into account specific cathode and anode materials and both isotherm and non-adiabatic cooled conditions.

This model can help to identify further improvements that could be done in the Na-ion technology, with a sodium layered oxide as the cathode active material and hard carbon as the anode active material, and the implementation to a multilayer Na-ion pouch cell, in which the heat generation model validation could be done.

Chapter 8. General conclusions and future work

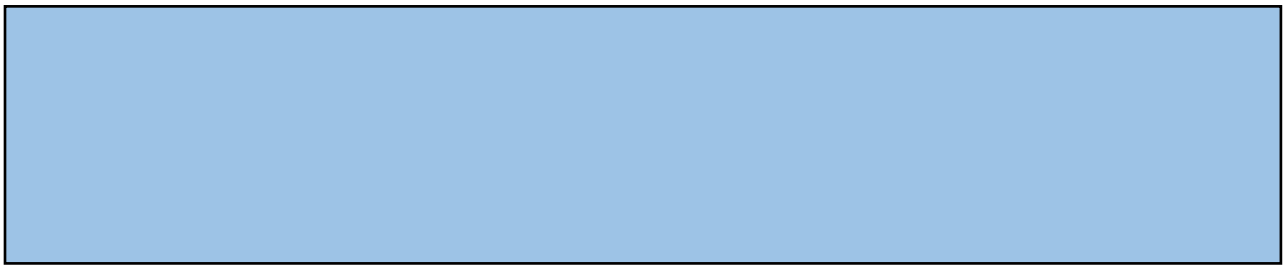

8.1 General conclusions

Following conclusions have been extracted from the results obtained in this Thesis.

Firstly, $Na_2C_4O_4$ sacrificial salt represents a more stable, safer and more cost effective solution than the use of NaN_3 to compensate for the Na deficiency of P2-type layered oxides. The electrochemical performance of the P2-type layered oxide with 31% of $Na_2C_4O_4$ sacrificial salt outperforms the cathode with 20% of NaN_3 with improved cycling stability, delivering a reversible capacity of 155 mAh g^{-1} and an energy density of 165 Wh kg^{-1}.

Regarding to the optimization of the synthesis of O3-$Na_{1-\delta}Ni_{0.32}Ti_{0.32}Mg_{0.16}Mn_{0.20}O_2$ cathode active material by solid state synthesis route, with the aim to minimizing the formation of $Mg_{1-x}Ni_xO$ impurity, avoid reactivity issues with the crucibles, minimize energy consumption and improve costs savings, optimum synthesis conditions were set as: calcination temperature = 900 °C; calcination time = 8 hours; precursors mixing by wet-ball-milling in ethanol.

Focusing on the cathode formulation studies, it was concluded that depending on the active material composition the optimal C65:PVDF ratio varies. The highest values for the reversible capacity and capacity retention over cycling, 91 mAh g^{-1} and 82.3%, respectively, are obtained for the $NaFe_{0.4}Mn_{0.3}Ni_{0.3}O_2$ containing cathode with a C65:PVDF = 0.8:1, while in the case of $Na_{1-\delta}Ni_{0.32}Ti_{0.32}Mg_{0.16}Mn_{0.20}O_2$, C65:PVDF = 0.6:1 represents the best ratio between these two inactive components for similar active material contents, with a reversible capacity of ca. 100 mAh g^{-1} after 40 cycles and a capacity retention close to 70%.

In addition to the optimal cooperation between the carbon black and the binder, the active material content must also be balanced. With the aim of maximizing the active material loading of the electrodes, and hence, increase the capacity and energy density of resulting cells, the active material content of $NaFe_{0.4}Mn_{0.3}Ni_{0.3}O_2$ and $Na_{1-\delta}Ni_{0.32}Ti_{0.32}Mg_{0.16}Mn_{0.20}O_2$ containing cathodes was increased to 87% and 88% of AM, respectively. The $NaFe_{0.4}Mn_{0.3}Ni_{0.3}O_2$ half-cells with 87% of active material present good electrochemical performance at low and high cycling

rates with a good capacity retention up to 9 mg cm^{-2} of active material loading. Specific energy densities of 105 Wh kg^{-1} at full-cell level are calculated for this cell.

A dissolver with disperser type impeller is considered as the best option when preparing the cathode slurry, presenting the most homogeneous components mixture as well as the best electrochemical performance. Moreover, a modification of the active material morphology provides a solution in terms of reducing the size of the agglomerates and enabling the fabrication of electrodes using the continuous comma bar coating machine. It was also identified that improved electrochemical performances are achieved when the electrodes are dried at a drying temperature of 60-80 °C.

Focusing on the anode side, it is shown that the viscosity varies as a function of the carbon black content of the slurry. Besides, the carbon black content also affects to the 1st cycle irreversibility of the anodes when tested as half-cells.

The most relevant parameters in the calendering process are also identified. The gap between the rollers, the temperature of the rollers and the interaction between these two parameters significantly affect to the thickness, porosity, 1st cycle irreversibility and reversible capacity of the hard carbon anodes. However, no clear effect of the porosity in the electrochemical performance is identified. Moreover, it has to be taken into account that determined calendering conditions can promote the formation of cracks and electrode inhomogeneities that limit the electrochemical performance of the cells, as happened when the electrodes were calendered at 100 °C and using a gap between rollers of 40 µm.

Referring to the development of hard carbon containing full-cells, $Na_{1-\delta}Ni_{0.32}Ti_{0.32}Mg_{0.16}Mn_{0.20}O_2$ and $NaFe_{0.4}Mn_{0.3}Ni_{0.3}O_2$ have been used as the cathode active materials. In the case of $Na_{1-\delta}Ni_{0.32}Ti_{0.32}Mg_{0.16}Mn_{0.20}O_2$, the full-cells were assembled at coin cell level, showing an energy density 111 Wh kg^{-1}.

In the case of $NaFe_{0.4}Mn_{0.3}Ni_{0.3}O_2$, the studies went one step further and a monolayer pouch cell was assembled. The final design of the pouch cell was supported by the studies at small scale (2-electrode coin cell and 3-electrode Swagelok type cells) and at larger scale (3-electrode cell at

pouch cell level). On the one hand, the optimum $R_{N/P}$ (Q) is in the range between 1.3 and 1.6, as a trade-off between the maximization of the anode utilization and the limitation of the low voltage zone in order to avoid sodium plating risk.

The cycling stability tests and subsequent post-mortem analysis at monolayer Na-ion pouch cell level, indicate that the anode is the main contributor to the degradation of the cell. Moreover, limiting the end of charge voltage to 3.9 V instead of 4.0 V, significantly improved the cycling stability of these cells. Independent of the mass balance, the cycling voltage range and the cathode active material morphology, the cathode electrodes partially recover the ability to insert Na ions when cycled versus metallic Na using fresh electrolyte.

The thermal properties of a Na-ion pouch cell are determined for the first time in a Na-ion full cell monolayer configuration at pouch cell level. The internal resistance increases by decreasing the temperature, so they have an inversely proportional relationship. However, the internal resistance is more influenced by the SOC than by the temperature. The entropic heat coefficient maintains negative values for the whole studied SOC range, both in the charge and the discharge processes. By modelling the heat generation over cycling of the Na-ion monolayer pouch cell it has been concluded that the irreversible heat is the main contribution to the total heat generation, which is related to the polarization and ohmic resistance.

Although, the experimental validation of the heat generation model could be performed because of the small size and thickness of monolayer Na-ion cell, the calculated Na-ion heat generation model provides an idea about the temperature increment during the charge and discharge processes for this type of technology, taking into account specific cathode and anode materials. This model helps to identify further improvements that should be done in the Na-ion technology, with sodium layered oxide as cathode active material and hard carbon as anode active material and the implementation to a multilayer Na-ion pouch cell, in which adiabatic model validation could be done in a calorimeter.

8.2 Future work

- Implementation of $Na_2C_4O_4$ as sacrificial salt in P2-type sodium layered oxides when using non-sodium containing anodes at pouch cell configuration in order to develop high energy density Na-ion multilayer pouch cells.
- Based on the conclusions obtained from small scale $Na_{1-\delta}Ni_{0.32}Ti_{0.32}Mg_{0.16}Mn_{0.20}O_2$ synthesis conditions, electrode formulation and full-cell assembly, scale-up of the slurry/electrode preparation and cell assembly processes towards pouch cell fabrication.
- Improvement of the cathode active material morphology through new synthesis routes and/or post-processing steps as a strategy to enhance cathode electrode microstructure and its electrochemical performance. Realization of comparative studies on the effect of different cathode morphologies in the electrode properties.
- Development of deeper cathode and anode slurry rheological properties characterization. In addition to steady state flow measurements for the detection of viscosity and shear thinning behavior, dynamic oscillatory shear measurements could be made in order to determine dynamic viscoelastic properties. These tests are oriented to provide information about the slurry stability and the strength of the aggregated state (transport stability, segregation characteristics, long time storage behavior of dispersions, etc.).
- Calendering process becomes in a critical step used to reduce thickness, increase electrode density and enhance mechanical properties of the electrodes, such as the adhesion and cohesion parameters. The presence of big agglomerates in the cathode prevented the realization of detailed studies to determine of the optimal calendering conditions. Therefore, cathode calendering studies should also be performed for optimized cell performance.
- Development of drying studies for deeper understanding of this process in both cathode and anode electrodes.

- Understand the degradation mechanisms of the monolayer pouch cells (SEI formation, impact of fast cycling, effect of temperature, self-discharge...).
- Scale-up of Na-ion monolayer pouch cell to multilayer pouch cell, in order to analyze its electrochemical performance and the impact of the scale-up process.
- Implementation of the heat generation model of the Na-ion monolayer pouch cell to a multilayer pouch cell. Validation of the heat generation model and its possible extrapolation to a battery pack.

Chapter 9. BIBLIOGRAPHY

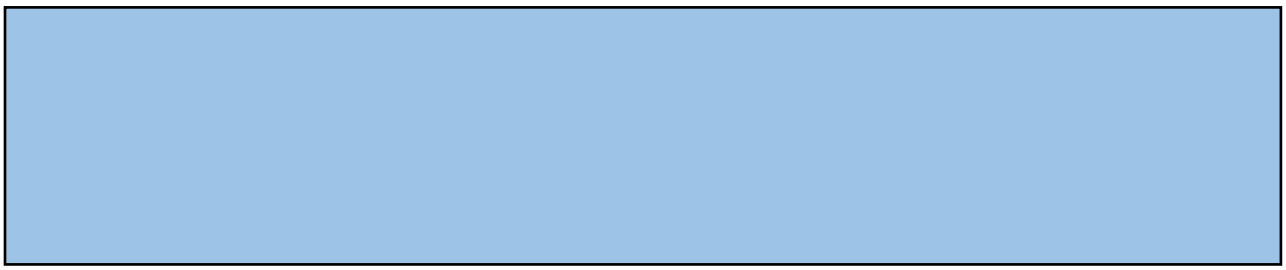

1. Global Energy Transformation: A Roadmap to 2050, International Renewable Energy Agency, 2018.
2. Global Climate change, Vital Signs of the Planet, “A blanket around the Earth”, https://climate.nasa.gov/causes/ (acceded January 2019).
3. Paris Agreement, United Nations Climate Change, https://unfccc.int/process/the-paris-agreement/what-is-the-paris-agreement (acceded January 2019).
4. Our World in Data, https://ourworldindata.org/grapher/cumulative-co-emissions (acceded January 2019).
5. International Energy Agency, https://www.iea.org/ (acceded January 2019).
6. DOE Global Energy Storage Database, Office of Electricity Delivery & Energy Reliability, https://www.energystorageexchange.org/ (acceded January 2019).
7. World Energy Resources E-Storage, 2016, World Energy Council, https://www.worldenergy.org/ (acceded January 2019).
8. Energy Storage Basque Country. Cluster Energy of Basque Country, http://www.clusterenergia.com/ (acceded January 2019).
9. Estrategia del cambio climático 2050 del País Vasco, Gobierno Vasco, https://www.euskadi.eus/ (acceded January 2019).
10. Electrical Energy Storage, International Electrotechnical Comission, https://www.iec.ch/index.htm (acceded January 2019).
11. G. J.May, A. Davidson and B. Monahov, J. Energy Storage, 2018, 15, 145-157.
12. L. Medenbach and P. Adelhelm, Top. Curr. Chem., 2017, 375.
13. R. H. Newman, J. Power Sources, 1994, 52, 149-153.
14. Lead acid batteries, https://batteryuniversity.com (acceded January 2019).
15. Battery University, Nickel based batteries, https://batteryuniversity.com/learn/article/nickel_based_batteries (acceded December 2018).

16. N. Omar, Y. Firouz, M. Abdel Monem, A. Samba, H. Gualous, T. C. Coosemans and J. Van Mierlo, 2014, 'Analysis of Nickel-Based Battery Technologies for Hybrid and Electric Vehicles'. In Reference Module in Chemistry, Molecular Sciences and Chemical Engineering, Elsevier.

17. Nickel-Cadmium Battery Advantages, Philips Bodine, https://www.bodine.com (acceded January 2019).

18. Nickel Metal Hydride (NiMH), Handbook and Application Manual, Energizer, https://energizer.com/ (acceded December 2018).

19. Young, K.-H., Batteries, 2016, 2, 31.

20. J. Tarabay and N. Karami, Third International Conference on Technological Advances in Electrical, Electronics and Computer Engineering, 2015.

21. Electropaedia, Battery and Energy Technologies, https://www.mpoweruk.com/nimh.htm/ (acceded December 2018).

22. R. Chen, S. Kim and Z. Chang, Chapter 5. 'Redox Flow Batteries: Fundamentals and Applications', (ed. Khalid, M. A. A., InTech, 2017).

23. M. Skyllas-Kazacos, M. Rychcik, R. G. Robins, A. G. Fane and M. A. Green, J. Electrochem. Soc., 1986, 1057.

24. D. Akinyele, J. Belikov and Y. Levron, Energies, 2017, 10, 1760.

25. X. Luo, J. Wang, M. Dooner, J. Clarke, Appl. Energy, 2015, 137, 511–536.

26. N. P. Dugos, R. M. U. Cua, 2016, 'Redox Flow Batteries'.

27. Sodium Sulfur Battery Energy Storage and its Potential to Enable Further Integration of Wind, Energy Storage Association, http://energystorage.org/ (acceded December 2018).

28. D. Kumar, S. K. Rajouria, S. B. Kuhar and D. K. Kanchan, Solid State Ion., 2017, 312, 8–16.

29. R. Carter, L. Oakes, A. Douglas, N. Muralidharan, A. P. Cohn and C. L. Pint, Nano Lett., 2017, 17(3), 1863–1869.

30. D. Kumar, M. Suleman and S. A. Hashmi, Solid State Ion., 2011, 202(1), 45–53.

31. NAS, Sodium Sulfur Battery, Energy Storage System, https://www.ngk.co.jp/nas/ (acceded February 2019).

32. V. S. Kolosnitsyn and E. V. Karaseva,. J. Electrochem., 2008, 44, 5, 506–509.

33. E. K. Heidari, A. Kamyabi-Gol, M. H. Sohi, A. Ataie, J. Ultrafine Grained Nanostructured Mater., 2018, 51, 1, 1-12.

34. J.-M. Tarascon and M. Armand, Nature, 2001, 414.

35. N. Nitta, F. Wu, J. Tae Lee, G. Yushin, Mater. Today, 2015, 18, 5.

36. J. Gustavsson, KTH School of Industrial Engineering and Management of Sweeden, Bachelor Thesis 'Energy Storage Technology Comparison'.

37. K. Mizushima, P.C. Jones, P.J. Wiseman and J.B. Goodenough, Solid State Ion., 1981, 171-174.

38. G. Ceder, Y.-M. Chiang, D. R. Sadoway, M. K. Aydinol, Y.-I. Jang and B. Huang, Nature, 1998, 392.

39. C.H. Chen, J. Liu, M. E. Stoll, G. Henriksen, D.R. Vissers, K. Amine, J. Power Sources, 2004, 128, 278–285.

40. A. Yamada, S. C. Chung and K. Hinokuma, J. Electrochem. Soc. 2001,148, A224-A229.

41. C. Delacourt, L. Laffont, R. Bouchet, C. Wurm, J.-B. Leriche, M. Morcrette, J.-M. Tarascon and C. Masquelier, J. Electrochem. Soc., 2015, 152 (5), A913-A921.

42. J. Barker, M. Y. Saidi, R. K. B. Gover, P. Burns and A. Bryan, J. Power Sources, 2007, 174, 927-931.

43. G.Che, K. B. Jirage, E. R. Fisher, C. R. Martin and H. Yoneyama, J. Electrochem. Soc, 1997, 144, 12, 4296-4302.

44. J. Cho, Y.-W. Kim, B. Kim, J.-G. Lee, and B. Park, 2003, Angew. Chem. Int., 42, 1618–1621.

45. T. Ohzuku, A. Ueda, and M. Nagayama, J. Electrochem. Soc., 1993, 140, 7.

46. P. G. Bruce, A. R. Armstrong and R. L. Gitzendanner, J. Mater. Chem., 1999, 9, 193–198.

47. F. Lin, I. M. Markus, D. Nordlund, T.-C. Weng, M. D. Asta, H. L. Xin and M. M. Doeff, Nat. Commun., 2014, 5, 3529.

48. S. K. Martha, O. Haik, E. Zinigrad, I. Exnar, T. Drezen, J. H. Miners and D. Aurbach, J. Electrochem. Soc., 2011,158, A1115-A1122.

49. R. Wang, X. He, L. He , F. Wang , R. Xiao , L. Gu , H. Li and L. Chen, Adv. Energy Mater. 2013.

50. M.-J. Lee, S. Lee, P. Oh, Y. Kim and J. Cho, Nano Lett. 2014, 14, 993−999.

51. D. Choi, D. Wang, In-T. Bae, J. Xiao, Z. Nie, W. Wang, V. V. Viswanathan, Y. Jung Lee, J.-G. Zhang, G. L. Graff, Z. Yang and J. Liu, Nano Lett. 2010, 10, 2799–2805.

52. J. M. Lloris, C. Pérez Vicente and J. L. Tirado, Electrochem. Solid-State Lett., 2002, 5, A234-A237.

53. A. Sobkowiak, M. R. Roberts, R. Younesi, T. Ericsson, L. Häggström, C.-W. Tai, A. M. Andersson, K. Edström, T. Gustafsson and F. Björefors, Chem. Mater., 2013.

54. N. A. Kaskhedikar, J. Maier, Adv. Mater. 2009, 21, 2664–2680. 55.

55. G.-N. Zhu, Y.-G. Wang and Y.-Y. Xia, Energy Environ. Sci., 2012, 5, 6652-6667.

56. S.-H. Yu, X. Feng, N. Zhang, J. Seok and H.D. Abrun, Acc. Chem. Res., 2018, 51, 273−28.

57. Y. Li and J. Lu, ACS Energy Lett. 2017, 2, 1370−1377.

58. W. N. Carson, C. E. Kent, 'The Magnesium-Air Cell' (In Power Sources; Collins, D. H., Ed.; Pergamon Press: Oxford, U.K., 1966).

59. L. Ojefors and L. Carlsson, J. Power Sources, 1978, 2, 287−296.

60. K. M. Abraham and Z. Jiang, Electrochem. Soc., 1996, 143.

61. P. Hartmann, C. L.Bender,M. Vracar,A. K. Dürr, A. Garsuch, J. Janek and P. Adelhelm, Nat. Mater., 2013, 12, 228-260.

62. P. G. Bruce, S. A. Freunberger, L. J. Hardwick and J.-M. Tarascon, Nat. Mat. 2012, 11, 172.

63. Metal-Air Battery, European Association for Storage of Energy (EASE), http://ease-storage.eu/energy-storage/technologies/ (acceded February 2019).

64. X. Zhang, X.-G. Wang, Z. Xie and Z. Zhou, Green Energy and Environment, 2016, 1, 4-17.

65. S. K. Das, S. Lau and L. A. Archer, J. Mater. Chem. A, 2014, 2, 12623.

66. E. Peleda, D. Golodnitsky, H. Mazor, M. Goor, S. Avshalomova, J. Power Sources, 2011, 196, 6835-6840.

67. A. Fotouhi, D. J. Auger, L. O'Neill, T. Cleaver and S. Walus, Energies, 2017, 10, 1937.

68. K. Kubota and S. Komaba, J. Electrochem. Soc., 2015,162 (14), A2538-A2550.

69. J.-J. Braconnier, C. Delmas, C. Fouassier and P. Hagenmuller, Mat. Res. Bull., 1980, 15, 1797-1804.

70. J. M. Tarascon, Nat. Chem., 201, 2, 510.

71. P. K. Nayak,L. Yang, W. Brehm and P. Adelhelm, Angew.Chem. Int. Ed. 2018, 57,102–120.

72. J.-Y. Hwang, S.-Taek Myung and Y.-K. Sun, Chem. Soc. Rev., 2017, 46, 3529.

73. World Lithium Supply, Eric Eason, Stanford University, 2010, http://large.stanford.edu/courses/2010/ph240/eason2 (acceded January 2019).

74. Abundance in Earth's Crust of elements, http://periodictable.com/Properties/A/CrustAbundance.an.html (acceded December 2018).

75. Z. Dai, U. Mani, H. Teng Tan and Q. Yan, Small Methods 2017, 1, 1700098.

76. S. Kuze, J.-I. Kageura, S. Matsumoto,T. Nakayama, M. Makidera, M. Saka, T. Yamaguchi,T. Yamamoto, K. Nakane, Sumitomo Chemical Co., Ltd.

77. M. Huan Han, E. Gonzalo, G. Singh and T. Rojo, Energy Environ. Sci., 2015, 8, 81.

78. C. Delmas, J.-J. Braconnier, C. Fouassier and P. Hagenmuller, Solid State Ion., 1981, 3-4, 165-169.

79. T. Ma, G.-L. Xu, X. Zeng, Y. Li, Y. Ren, C. Sun, S. M. Heald, J. Jorne, K. Amine and Z. Chen, J. Power Sources, 2017, 341,114-121.

80. M. Keller, D. Buchholz, S. Passerini, Adv. Energy Mater. 2016, 6, 1501555.

81. N. Yabuuchi, K. Kubota, M. Dahbi and S. Komaba, Chem. Rev. 2014, 114, 11636−11682.

82. S. Okada, Y. Takahashi, T. Kiyabu, T. Doi, J. Yamaki, and T. Nishida, ECS Meeting Abstracts, 2006, 602, 201.

83. N.-A. Nguyen,K. Kim,K. H. Choi,H. Jeon, K. Lee,M.-H. M. Ryou, Y. M. Lee, J. Electrochem. Soc., 2017, 164 (1), A6308-A6314.

84. N. Yabuuchi, M. Kajiyama, J. Iwatate, H. Nishikawa, S. Hitomi, T. Okuyama, R. Usui, Y. Yamada, S. Komaba, Nat. Materials, 2012, 11.

85. Park, J., Park, G., Kwak, H. H., Hong, S.-T. and Lee, J. ACS Omega, 2018, 3, 361–368.

86. H. Zhu, KT. Lee, GT. Hitz, X. Han, Y. Li, J. Wan, S. Lacey, A. Cresce, K. Xu, E. Wachsman and L. Hu, ACS Appl. Mater. Interfaces, 2014, 6, 4242–4247.

87. Y. Bai, L. Zhao, C. Wu, H. Li, Y. Li, F. Wu, ACS Appl. Mater. Interfaces, 2016, 8, 2857–2865.

88. E. Talaie, V. Duffort, H. L. Smith, B. Fultz and L. Nazar, Energy Environ. Sci., 2015, 8, 2512-2523.

89. P.-F. Wang, Y. You, Y.-X. Yin and Y.-G. Guo, Adv. Energy Mater. 2018, 8, 1701912.

90. Konarov, A., Choi, J. U., Bakenov, Z. and Myung, S. T, J. Mater. Chem. A, 2018, 6, 8558-8567

91. J. Molenda and A. Stoklosa, Solid State Ion., 1990, 38, 1-4.

92. S. Komaba, N. Yabuuchi, T. Nakayama, A. Ogata, T. Ishikawa, and I. Nakai, Inorg. Chem. 2012, 51, 6211−6220.

93. Gotoh, K. and Na, E. J. Barker, et al., EP 2872450 B1.

94. N. Yabuuchi, H. Yoshida and S. Komaba, Electrochem., 2012, 80(10), 716–719.

95. D. D. Yuan, Y. X. Wang, Y. L. Cao, X. P. Ai, and H. X. Yang, ACS Appl. Mater. Interfaces, 2015, 7, 8585−8591.

96. D. Kim, E. Lee, M. Slater, W. Lu, S. Rood, C. S. Johnson. Electrochem. Commun., 2012, 18, 66–69.

97. P. Barpanda, L. Lander, S.-I. Nishimura, and A. Yamada, Adv. Energy Mater. 2018, 1703055.

98. X. Xiang, K. Zhang and J. Chen, Adv. Mater. 2015, 27, 5343–5364.

99. M. Casas-Cabanas, V. V. Roddatis, D. Saurel, P. Kubiak, J. Carretero-Gonzalez, V. Palomares, P. Serras and T. Rojo, J. Mater. Chem., 2012, 22, 17421.

100. J. Kim, D.-H. Seo, H. Kim, I. Park, J.-K. Yoo,S.-K. Jung, Y.-U. Park, W. A. Goddard IIIe and K. Kang, Energy Environ. Sci., 2014.

101. C. Li, X. Miao, W. Chu, P. Wu and D. G. Tong, J. Mater. Chem. A, 2015, 3, 8265-8271.

102. Z. Jian, C. Yuan, W. Han, X. Lu, L. Gu, X. Xi, Y.-S. Hu, H. Li, W. Chen, D. Chen, Y. Ikuhara and L. Chen, Adv. Funct. Mater., 2014.

103. Z. Jian, L. Zhao, H. Pan, Y.-S. Hu, H. Li, W. Chen, L. Chen, Electrochem. Commun., 2012, 14, 86–89.

104. W. Duan, Z. Zhu, H. Li, Z. Hu, K. Zhang, F. Cheng and Jun Chen, J. Mater. Chem. A, 2014, 2, 8668-8675.

105. K. Saravanan, C. W. Mason, A. Rudola K. H. Wong and P. Balaya, Adv. Energy Mater., 2013, 3, 444-450.

106. M. J. Aragon, P. Lavela, G. F. Ortiz, and J. L. Tirado, J. Electrochem. Soc., 2015, 162, A3077-A3083.

107. Z. Jian, Y. Sun and X. Ji, Chem. Commun., 2015, 5129, 6381-6384.

108. P. Barpanda, S.-I. Nishimura and A. Yamada, Adv. Energy Mater. 2012, 2, 841–859.

109. P. Barpanda,T. Ye, S.-I. Nishimura, S.-C. Chung, Y. Yamada, M. Okubo, H. Zhou, A. Yamada, Electrochem. Commun., 2012, 24,116–119.

110. S. Park, H. Kim, R. A. Shakoor, E. Yang, S. Y. Lim, R. Kahraman, Y. Jung and J. W. Choi, J. Am. Chem. Soc. 2013, 135, 2787−2792.

111. A. Langrock, Y. Xu, Y. Liu, S. Ehrman, A. Manivannan, C. Wang, J. of Power Sources, 2013, 223, 62-67.

112. K. Kubota, K. Yokoh, N. Yabuuchi and S. Komaba, Electrochem., 2014, 82(10), 909–911.

113. Y. Zhong, Z. Wu, Y. Tang, W. Xiang, X. Guo, B. Zhong, Mater. Lett., 2015.

114. P. Barpanda, G. Oyama, S.-I. Nishimura, S.-C. Chung, A. Yamada, Nat. Commun., 2014, 5 (1), 4358.

115. P. Barpanda, G. Oyama, C. D. Ling and A. Yamada, Chem. Mater. 2014, 26, 1297−1299.

116. X. Zheng, C. Bommier, W. Luo, L. Jiang, Y. Hao, Y. Huang, Energy Storage Mater., 2019, 16, 6–23.

117. P. Thomas, D. Billaud, Electrochim. Acta, 2000, 46, 39–47.

118. Y. Wen, K. He, Y. Zhu, F. Han, Y. Xu, I. Matsuda, Y. Ishii, J. Cumings, C. Wang, Nat. Commun., 2014.

119. B. Jache, P. Adelhelm, 2015 ECS, The Electrochem. Soc., Abstract.

120. G. Gao, L.-Z. Cheong, D. Wang, C. Shen, Carbon Resour. Convers., 2018, 1, 104-108.

121. H. Zhu, F. Shen, W. Luo, S. Zh, M. Zhao, B. Natarajan, J. Dai, L. Zhou, X. Ji, R. S. Yassar, T. Li, L. Hu, Nano Energy, 2017, 33, 37–44.

122. Y. Pan, Y. Zhang, B. S. Parimalam, C. C. Nguyen, G. Wang, B. L. Lucht, J. Electroanal. Chem., 2017, 799, 181-186.

123. Y. Zheng, Y. Wang, Y. Lu, Y.-S. Hub, J. Li, Nano Energy, 2017, 39, 489-498.

124. H. Che, J. Liu, H. Wang, X. Wang, S. S. Zhang, X.-Z. Liao, Z.-F. Ma, Electrochem. Commun., 2017, 83, 20-23.

125. C. Bommier, W. Luo, W.-Y. Gao, A. Greaney, S. Ma, X. Ji, Carbon, 2014, 76,165-174.

126. B. Mortemard de Boisse, D. Carlier, M. Guignard, C. Delmas, J. Electrochem. Soc., 2013, 160, A569-A574.

127. C. Yu, H. Hou, X. Liu, Y. Yao, Q. Liao, Z. Dai, D. Li, Int. J. Hydrog., 43, 6, 2018, 3253-3260.

128. L. Cao, W. Hui, Z. Xu, J. Huang, P. Zheng, J. Li, Q. Sun, J. Alloys Compd., 2017, 695, 632-637.

129. G. Yasin, M. Abubaker Khan, W. Qamar Khan, T. Mehtab, R. Mustafa Korai, X. Lua, M. Tariq Nazir, M. Noaman Zahid, Results Phys., 2019, 14, 102404.

130. E. Irisarri, A. Ponrouch, and M. R. Palacin, J. Electrochem. Soc., 2015,162 (14), A2476-A2482.

131. Y. Li, S. Y. Hu, H. Li, L. Chen, X. Huang, X., J. Mater. Chem. A, 2016, 4, 96–104.

132. Dahn, J.R.; Sleigh, A.K.; Shi, H.; Reimers, J.N.; Zhong, Q.; Way, B.M., Electrochim. Acta 1993, 38, 1179–1191.

133. Liu, Y.; Xue, J.S.; Zheng, T.; Dahn, J.R., Carbon 1996, 34, 193–200.

134. Jin, J.; Shi, Z.-Q.; Wang, C.-Y., Electrochim. Acta 2014, 141, 302–310.

135. V. Aravindan, Y. S. Lee, R. Yazami, S. Madhavi, Mater. Today, 2015, 18, 345–351.

136. S.-P. Guo , J.-C. Li, Q.-T. Xu, Z. Ma, H.-Guo Xue, J. Power Sources, 2017, 361, 285-299.

137. H.-G. Jung, S.-T. Myung, C. Seung Yoon, S.-B. Son, K. Hwan Oh, K. Amine, B. Scrosati and Y.-K. Sun, Energy Environ. Sci., 2011, 4, 1345.

138. J. Xu, C. Ma, M. Balasubramanian, Y. S. Meng, Chem. Commun., 2014, 50, 12564.

139. S. Lunell, A. Stashans, L. Ojama, H. Lindstro and A. Hagfeldt, J. Am. Chem. Soc. 1997, 119, 7374-7380.

140. Y. Xu,E. Memarzadeh Lotfabad, H. Wang, B. Farbod, Z. Xu, A. Kohandehghanab and D. Mitlin, Chem. Commun., 2013, 49, 8973.

141. L. Wu, D. Bresser, D. Buchholz, G.Giffi, C. Ramirez Castro, A. Ochel and S. Passerini, Adv. Energy Mater. 2014, 1401142.

142. Y. Zhang, X. Pu, Y. Yang, Y. Zhu,H. Hou, M. Jing, X. Yang, J. Chen, X. Ji, Phys. Chem. Chem. Phys., 2015, 17(24), 15764-70.

143. A. Ponrouch, D. Monti, A. Boschin, B. Steen, P. Johansson and M. R. Palacín, J. Mater. Chem. A, 2015, 3, 22-42.

144. R. Mogensen, D. Brandell and R. Younesi, ACS Energy Lett. 2016, 1, 6, 1173-1178.

145. N. Weadock, N. Varongchayakul, J. Wan, S. Lee, J. Seog, L. Hun, Nano Energy, 2013, 2, 713–719.

146. L. Otaegui, E. Goikolea, F. Aguesse, M. Armand, T. Rojo, G. Singh, J. Power Sources, 2015, 297,168-173.

147. R. Hagiwara, K. Matsumoto, J. Hwang and T. Nohira, Chem. Rec. 2018, 18, 1–14.

148. A. Ponrouch, E. Marchante, M. Courty, J.-M. Tarascon and M. R. Palacín, Energy Environ. Sci., 2012, 5, 8572.

149. A. Raj K, M. R. Panda, D. P. Dutta and S. Mitra, Carbon, 2019, 143, 402-412.

150. Y.-N. Zhou, P.-F. Wang, Y.-B. Niu, Q. Li, X. Yu, Y. X. Yin, S. Xu and Y.-G. Guo, Nano Energy, 2019, 55, 143-150.

151. J. Barker, M. Y. Saidi and J. L. Swoyer, Electrochem. SolidState Lett., 2003, 6, Al–A4.

152. M. Nose, H. Nakayama, K. Nobuhara, H. Yamaguchi, S. Nakanishi and H. Iba, J. Power Sources, 2013, 234, 175–179.

153. S. Komaba, W. Murata, T. Ishikawa, N. Yabuuchi, T. Ozeki, T. Nakayama, A. Ogata, K. Gotoh and K. Fujiwara, Adv. Funct. Mater., 2011, 21, 3859–3867.

154. D. Kim, E. Lee, M. Slater, W. Lu, S. Rood and C. S. Johnson, Electrochem. Commun., 2012, 18, 66–69.

155. M. Keller, C. Vaalma, D. Buchholz and S. Passerini, ChemElectroChem, 2016, 3, 1124–1132.

156. H. Li, L. Peng, Y. Zhu, D. Chen, X. Zhang and G. Yu, Energy Environ. Sci., 2016, 9, 3399–3405.

157. Y. Wang, R. Xiao, Y. S. Hu, M. Avdeev and L. Chen, Nat. Commun., 2015, 6, 6954.

158. Green Car Congress, Energy, Technologies, Issues and Policies for sustainable mobility, 2015, https://www.greencarcongress.com/2015/11/20151127-rs2e.html (acceded January 2019).

159. A. Bauer, J. Song, S. Vail, W. Pan, J. Barker and Y. Lu, Adv. Energy Mater. 2018, 1702869.

160. J.-Y. Hwang,S.-T. Myung, Y.-K. Sun, Chem. Soc. Rev., 2017, 46, 3529.

161. M. Wolter, D. Leiva, M. Fritsch, S. Börner, The 27th International Electric Vehicle Symposium and Exhibition, 2013, Fraunhofer IKTS. 'Process development and optimization for Li-ion battery production'.

162. D. Liu, L.-C. Chen, T.-J. Liu, T. Fan, E.-Y. Tsou, C. Tiu, Adv. Chem. Eng. Sci., 2014, 4, 515-528.

163. A. Spillmann, SCCER Symposium, 2017, BUHLER. 'From Coin Cell to Gigafactory – Scale-Up of LIB Slurry Processing'.

164. E. Ligneel, B. Lestriez, A. Hudhomme and D. Guyomard, J. Electrochem. Soc., 2007, 154 (3), A235-A241.

165. W. Bauer, D. Nötzel, Ceram. Int., 2014, 40(3), 4591-4598.

166. Y. I. Kwon, J. D. Kim, and Y. S. Song, J. Electron. Mater., 2015, 44 (1).

167. G. Liu, H. Zheng, S. Kim, Y. Deng, A. M. Minor, X. Song, and Vincent S. Battaglia, J. Electrochem. Soc., 2008, 155 (12) A887-A892.

168. A. M. Gaikwad and A. C. Arias, ACS Appl. Mater. Interfaces, 2017, 9, 6390−6400.

169. M. Despotopoulou, M. T. Burchill, Prog. Org. Coat., 2002, 45, 119–126.

170. W. Zhang, X. He, W. Pu, J. Li, C. Wan, Ionics, 2011, 17, 473–477.

171. V. Wenzel, H. Nirschl D. Nçtzel, Energy Technol. 2015, 3, 692–698.

172. A. Ponrouch, M. R. Palacín, J. Power Sources, 2011, 196, 9682-9688.

173. G.W. Lee, J. H. Ryu, W. Han, K. Hyun Ahn, S. M. Oh, J. Power Sources, 2010, 195, 6049-6054.

174. A. Kraytsberg and Y. Ein-Eli, Adv. Energy Mater. 2016, 1600655.

175. C. Schilde, C. Mages-Sauter, A. Kwade, H.P. Schuchmann, Powder Technol., 2011, 207, 353–361.

176. C. F. Burmeister and A. Kwade, Chem. Soc. Rev., 2013, 42, 7660.

177. R. Schmidt, H. M. Scholze, A. Stolle, Int. J. Ind. Chem., 2016, 7, 181–186.

178. H. Dreger, H. Bockholt, W. Haselrieder and A. Kwade, J. of Electron. Mater., 2015, 44, 4434–4443.

179. O. El Baradai, D. Beneventi, F. Alloin, Y. Bultel, M. Party, D. Chaussy, Int. J. Innov. Res. Sci. Eng. Technol., 2008, 9001, 2277 - 3754.

180. A. G. King and S. T. Keswani, J. of the Am. Ceram. Soc., 77, 3, 769-777.

181. M. Schmidt, KIT Scientific Publishing, 2015. 'Slot die coating of lithium-ion battery electrodes'.

182. Cohen, E.D. and Gutoff, E.B., John Wiley & Sons, 1992. 'Modern Coating and Drying Technology'.

183. S.F. Kistler, P.M. Schweizer, (Eds. Chapman & Hall.), 1997, 'Liquid film coating: scientific principles and their technological implications'.

184. Yoshio, M., Brodd, R.J., Kozawa, A., Springer, 2009. 'Lithium-ion batteries: science and technologies'.

185. E. Briec, B. Müller, 2015th ed. Springer International Publishing, Cham. 2015, 'Electric Vehicle Batteries: Moving from Research towards Innovation: Reports of the PPP European Green Vehicles Initiative'.

186. S. Maenosono, T. Okubo and Y. Yamaguchi, J. Nanoparticle Research, 2003, 5, 5–15.

187. J. Kurfer, M. Westermeier, C. Tammer, G. Reinhart, Manuf. Technol., 2012, 61, 1-4.

188. Battery University, https://batteryuniversity.com/ (acceded December 2018).

189. Prismatic cell, DNK power, https://www.dnkpower.com/ (acceded January 2019).

190. KOK battery, http://www.kokpower.com (acceded January 2019).

191. S. Ahn, H.-M. Lee, S.-J. Lee, Y. Park, C.-Hu. Ku, J. Young Kim, J.-H. Lee, S. K. Kim and J. Yeon Cho, Batteries R&D, LG Chemical Ltd., Electrochem. Soc.

192. G. Singh, J. Miguel López del Amo, M. Galceran, S. Pérez-Villar, and T. Rojo, J. Mater. Chem. A, 2015, 3, 6954.

193. G. Singh, B. Acebedo, M. Casas Cabanas, D. Shanmukaraj, M. Armand, T. Rojo, Elect. Com., 2013, 37, 61-63.

194. Doped Nickelate Compounds, International Application Published under the Patent Cooperation Treaty (PCT), 2014.

195. An introduction to Planetary Centrifugal Mixers. Thinky Corporation, 2011, https://www.intertronics.co.uk/ (acceded September 2019).

196. N. Adachi, M. Hashiba, O. Sakurada, Ceram. Int., 2004, 30, 1055–1058.

197. VMA-Getzmann GMBH. Introduction to dispersion technology with the DISPERMAT dissolver, http://www.vma-getzmann.com (acceded July 2019).

198. A. Kayyar, J. Huang, M. Samiee, and J. Luo, J. Vis Exp., 2012, 66, 4104.

199. S.-I. Pyun, H.-C., Shin, J.W. Lee, J.-Y- Go, 2012, Ed. Springer, 'Electrochemistry of Insertion Materials for Hydrogen and Lithium'.

200. A. Goren, D. Cintora Juárez, P. Martins, S. Ferdov, M. Silva, J. L. Tirado, C. M. Costa, S. Lanceros. Energy Technol. 2016, 4, 573–582.

201. Viscous fluids monography, http://jpdb.nihs.go.jp/ (acceded September 2019).

202. M. Ochowiak, L. Broniarz-Press and J. Rozanski, J. Disper. Sci. and Technol., 2013, 332, 177-184.

203. Understanding Rheology of Structured Fluids, TA Instruments, http://www.tainstruments.com/ (acceded March 2019).

204. Understanding yield stress measurements, Malvern Panalytical (https://www.malvernpanalytical.com/ (acceded September 2019).

205. A. H. Khalili Garakani, N. Mostoufi, F. Sadeghi, M. Hosseinzadeh, H. Fatourechi, M. H. Sarrafzadeh, M. R. Mehrnia, Iran. J. Environ. Health. Sci. Eng., 2011, 8, 3, 255-264. **8**, 10 (2011).

206. Folayan J. Adewale, Anawe P. Lucky, Abioye P. Oluwabunmi and Elehinafe F. Boluwaji, Int. J. Appl. Eng., 2017, 12, 18, 7614-7629.

207. Mitsoulis, E. E. Mitsoulis, Rheology Reviews, 2007, 135 - 178. 44 (2007).

208. Reómetro rotacional HAAKE, ThermoFisher Scientific, https://www.thermofisher.com/ (acceded September 2019).

209. J.Anthony von Fraunhofer, Int. J. Dent., 2012, ID 951324, 8.

210. B. Ludwig, Z. Zheng, W. Shou, Y. Wang, H. Pan, Nature, Sci. Rep., 2016, 6, 23150.

211. W. Zhou, R. P. Apkarian, Z. Lin Wang and D. Joy, Elsevier, Chapter 1: Fundamentals of Scanning Electron Microscopy, 'Scanning Microscopy for Nanotechnology'.

212. R. Kaur, International Journal of IT, Engineering and Applied Sciences Research (IJIEASR), 2015, 4, 7.

213. X-ray diffraction (XRD), https://serc.carleton.edu/research_education (acceded September 2019).

214. Determining the Specific Heat Capacity of a Battery Pack. Thermal Hazard Technology, http://www.thermalhazardtechnology.com/ (acceded March 2019).

215. H. Maleki, S. A. Hallaj, J. R. Selman, R. B. Dinwiddie and H. Wang, J. Electrochem. Soc., 1999, 146, 947-954.

216. M. Shadman Rada, D.L. Danilova, M. Baghalha, M. Kazemeini, P.H.L. Nottena, Electrochim. Acta, 2013, 102, 183–195.

217. D. Zhao, X. Qian, X. Gu, S. Ayub and R. Yang, J. Electron Packaging, 2016, 138.

218. Thermal conductivity, https://thermtest.com/ (acceded March 2019).

219. S. Al Hallaj, J. Prakash, J.R. Selman, J. Power Sources, 2000, 87,186–194.

220. C. Forgez, D. V. Do, G. Friedrich, M. Morcrette, C. Delacourt, J. Power Sources, 2010, 195, 9, 2961-2968.

221. C. Veth, D. Dragicevic and C. Merten, J. Power Sources, 2014.

222. N. Nieto, Doctoral Thesis, 2014, 'A Model Based Design of a Thermal Management System for a High Power Lithium-Ion Battery Pack'.

223. B. Manikandan, C. Yap, and P. Balaya, J. Electrochem. Soc., 2017, 164 (12), A2794-A2800.

224. G. Singh, J. Miguel López del Amo, M. Galceran, S. Pérez-Villar, and T. Rojo, J. Mater. Chem. A, 2015, 3, 6954.

225. M. H. Han, B. Acebedo, E. Gonzalo, P. Sánchez Fontecoba, S. Clarke, D. Saurel, and T. Rojo, Electrochim. Acta, 2015, 182, 1029-1036.

226. H. Wang, Y. Xiao, C. Sun, C. Lai, X. Ai, RSC Adv., 2015, 5, 106519.

227. B. Zhang, R. Dugas, G. Rousse, P. Rozier, A. M. Abakumov, J. M. Tarascon, Natur. Communic., 2016, 7, 10308.

228. C.-H. Jo, J. U. Choi, H. Yashiro, S.-T. Myung, J. Mater. Chem. A, 2019,7, 3903-3909.

229. D. Shanmukaraj, S. Grugeon, S. Laruelle, G. Douglade, J.-M. Tarascon, M. Armand, Electrochem. Commun., 2010, 12, 1344–1347.

230. K. Chihara, M. Ito, A. Kitajou, S. Okada, Evergreen, 2017, 04, 1-5.

231. S. Okada, K. Chihara, K. Nakamoto, Y. Kano, M. Ito, Abstract ABAA7, 'Disodium Rhodizonate and the Derivatives as Organic Electrode Active Materials for Sodium-ion Battery'.

232. K. Chihara, N. Chujo, A. Kitajouc, S. Okada, Electrochim. Acta 110 (2013) 240–246.

233. D. Shanmukaraj, K. Kretschmer, T. Sahu, W. Bao, T. Rojo, G. Wang and M. Armand, Chem. Sus. Chem., 2018, 11(18), 3286-3291.

234. J. Martínez De Ilarduya, L. Otaegui, M. Galcerán, L. Acebo, D. Shanmukaraj, T. Rojo, M. Armand, Electrochim. Acta, 2019, 321, 134693.

235. R. Dugas, B. Zhang, P. Rozier, J.M. Tarascon, J. of Electr. Socie., 2016, 163 (6), A867-A874.

236. E. Gonzalo, M.H. Han, J.M. López del Amo, B. Acebedo, M. Casas-Cabanas, T. Rojo, J. Mater. Chem. A, 2014, 2, 18523.

237. M.H. Han, E. Gonzalo, N. Sharma, J.M. López del Amo, M. Armand, M. Avdeev, J. J. Saiz Garitaonandia, T. Rojo, Chem. Mater., 2016, 28, 106-116.

238. M. Xie, R. Luo, J. Lu, R. Chen, F. Wu, X. Wang, C. Zhan, H. Wu, H. M. Albishri, A. S. Al-Bogami, D. Abd El-Hady, K. Amine, ACS Appl. Mater. Interfaces, 2014, 6, 17176−17183.

239. F. Fiévet, P. Germi, F. de Bergevin and M. Figlarz, J. Appl. Cryst., 1979, 12, 387-394.

240. A.M. Salem, M. Mokhtar, G.A. El-Shobaky, Solid State Ion., 2004, 170, 33 – 42.

241. J. Barker, R. J. Heap, N. Roche, C. Tan, R. Sayers and Y. Liu, International Meeting on Lithium batteries, 2014, 'Low Cost Na-ion Battery Technology'.

242. S. E.Trask, Y. Lia, J. J.Kubal,M. Bettge,B. J.Polzin,Y. Zhu,A. N. Jansen,D. P.Abraham, J. Power Sources, 2014, 259, 233-244.

243. Y. K. Lee, Energies, 2019, 12, 658.

244. H. Kondo, H. Sawada, C. Okuda and T. Sasaki, J. Electrochem. Soc., 2019, 166 (8), A1285-A1290.

245. H. Zheng, R. Yang, G. Liu, X. Song, V. S. Battaglia, J. Phys. Chem., 2012, 116, 4875−4882.

246. J. Kasnatscheew, T. Placke, B. Streipert, S. Rothermel, R. Wagner, P. Meister, I. C. Laskovic, M. Winter, J. Electrochem. Soc., 2017, 164 (12), A2479-A2486.

247. R. Hausbrand, G. Cherkashinin, H. Ehrenberg, M. Gröting, K. Albe, C. Hess, W. Jaegermann, Mater. Sci. Eng B, 2015, 192, 3–25.

248. D. Liu, L.-C. Chen, T.-J. Liu,T. Fan, E.-Y. Tsou, C. Tiu, Adv. Chem. Eng. Sci., 2014, 4, 515-528.

249. Y.K. Lee, Energies, 2019, 12, 658.

250. NEI Corporation, Nanomyte cathode and anode tapes, https://www.neicorporation.com/products/batteries (acceded June 2019).

251. A. Kwade and W. Haselrieder, 'Effect of electrode and cell production on Li-ion performance and cost', IPAT and BLB presentation.

252. J. Deng, W.-B. Luo, X. Lu, Q. Yao, Z. Wang, H.-K. Liu, H. Zhou, and S.-X. Dou, Adv. Energy Mater. 2017, 1701610.

253. R. Yazami, Pan Standford publishing, 2014, 'Nanomaterials for Lithium ion Batteries-Fundamentals and Applications'.

254. B.E.A Jacobs, Elsevier Applied Science, 'Design of slurry transport systems'.

255. D. Bresser, D. Buchholz, A. Moretti, A. Varzi and S. Passerini, Energy Environ. Sci., 2018, 11, 3096.

256. B. Vertruyen, N. Eshraghi, C. Piffet, J. Bodart, A. Mahmoud and F. Boschini, Materials, 2018, 11, 1076.

257. N. Bucher, S. Hartung, A. Nagasubramanian, Y. Ling Cheah, H. Ernst Hoster, and S. Madhavi, ACS Appl. Mater. Interfaces, 2014, 6, 8059–8065.

258. S. Jaiser, N. Sanchez Salaz, M. Baunach, P. Scharfer, W. Schabel. Dry. Technol., 2017.

259. F. Soergel, Thermo Fisher Scientific. 'Understanding Flow Behavior of Paints and Coatings'.

260. D. Liu, L.-C. Chen, T.-J. Liu, T. Fan, E.-Y. Tsou, C. Tiu, Adv. Chem. Eng. Sci., 2014, 4, 515-528.

261. H. Bockholt, M. Indrikova, A. Netz, F. Golks, A. Kwade, J. Power Sources, 2016, 325, 140-151.

262. W. Haselrieder, B. Westphal, H. Bockholt, A. Diener, S. Höft, A. Kwade, Int. J. Adhes. Adhes., 2015, 60, 1–8.

263. B. Son, M.-H. Ryou, J. Choi,T. Lee, H. Kyun Yu, J. Hun Kim, Y. Min Lee, ACS Appl. Mater. Interfaces 2014, 6, 526−531.

264. B. Son,M.-H. Ryou, J. Choi,T. Lee, H. Kyun Yu, J. Hun Kim, Y. Min Lee, ACS Appl. Mater. Interfaces 2014, 6, 526−531.

265. R. Alcántara, Juan M. Jiménez-Mateos, P. Lavela, J. L. Tirado, Electrochem. Comm., 2001, 3, 639-642.

266. L. Fransson, T. Eriksson, K. Edström, T. Gustafsson, J.O. Thomas, J. Power Sources, 2001, 101, 1-9.

267. N. Zhang, Q. Liu, W. Chen, M. Wan, X. Li, L. Wang, L. Xu, W. Zhang, J. Power Sources, 2018, 378, 331-337.

268. Y. Pan, Y. Zhang, B. S. Parimalam, C. C. Nguyen, G. Wang, B. L. Lucht, Journal of Elect. Chem., 2017, 799, 181–186.

269. C. Yu, H. Hou, X. Liu, Y. Yao, Q. Liao, Z. Dai, D. Li, Int. J. Hydrog., 43, 6, 2018, 3253-3260.

270. Y. Zhu, M. Cheng, Q. Li, C. Yuan, C. Wang, Carbon, 2017,123, 727-743.

271. B. R. Long, S. G. Rinaldo, K. G. Gallagher, D. W. Dees, S. E. Trask, B. J. Polzin, A. N. Jansen, D. P. Abraham, I. Bloom, J. Bareño, and J. R. Croy, J. Electrochem. Soc., 2016, 163, 14, A2999-A3009.

272. W. Haselrieder, S. Ivanov, D. K. Christen, H. Bockholt and A. Kwade, ECS Transactions, 2013, 50 (26), 59-70.

273. J. Shim and K. A. Striebel, 2018, IMLB, Japan.

274. J.S. Gnanaraj, Yaron S. Cohen, M.D. Levi, D. Aurbach, J. Electroanal. Chem., 2001, 516, 89–102.

275. C.-C. Li, Y.-W. Wang, J. Power Sources, 2013, 227, 204-210.

276. S. Roberts E. Kendrick, Nanotechnol. Sci. Appl., 2018, 11, 23–33.

277. J. Kasnatscheew, T. Placke, B. Streipert,S. Rothermel,R. Wagner, P. Meister, I. C. Laskovic, M. Winter, J. Electrochem. Soc., 2017, 164 (12), A2479-A2486.

278. A. Bauer, J. Song, S. Vail, W. Pan, J. Barker and Y. Lu, Adv. Energy Mater. 2018, 1702869.

279. Y. Wang, Z. Zhou, A. Botterud, K. Zhang, Q. Ding, J. Mod. Power Syst. Clean Energy, 2016.

280. N. Omar, M. A. Monem, Y. Firouz, J. Salminen, J. Smekens, O. Hegazy, H. Gaulous, G. Mulder, P. Van den Bossche, T. Coosemans, J. Van Mierlo, Applied Energy, 2014, 113, 1575-1585.

281. W. R. Bennett, NASA, 'Considerations for Estimating Electrode Performance in Li-Ion Cells'.

282. Y. Xie, H. Wang, G. Xu, J. Wang, H. Sheng, Z. Chen, Y. Ren, C.-J. Sun, J.Wen, Jun Wang, D. J. Miller, J. Lu, K. Amine and Z.-F. Ma, Adv. Energy Mater. 2016, 1601306.

283. B. Shabani and M. Biju, Energies, 2015, 8, 10153-10177.

284. J. Zhang, B. Wu, B. Wu, Z. Li, J. Huang, J. Power Sources, 2014, 259, 106-116.

285. S. S. Choi, H. S. Lim, J. Power Sources, 2002, 111,130–136.

286. T. Waldmann, M. Wilka, M. Kasper, M. Fleischhammer, M. Wohlfahrt-Mehrens, J. Power Sources, 2014, 262, 129-135.

287. I. Bloom, S. A. Jones, E. G. Polzin, V. S. Battaglia, G. L. Henriksen, C. G. Motloch, R. B. Wright, R. G. Jungst, H. L. Case, D. H. Doughty, J. Power Sources, 2002, 111, 152–159.

288. J. Vetter, P. Novák, M. R. Wagner, C. Veit, K.-C. Möller, J. O. Besenhard, M. Winter, M.Wohlfahrt-Mehrens, C.Vogler, A.Hammouche, J. Power Sources, 2005,147, 269-281.

289. Y. Troxler, B. Wu, M. Marinescu, V. Yufit, Y. Patel, A. J. Marquis, N. P. Brandon, G. J. Offer, J. Power Sources, 2014, 247, 1018-1025.

290. A. A. Pesaran and M. Keyser, 2001, Annual Battery Conference: Advances and Applications.

291. Lu, W. & Prakash, J. W. Lu and J. Prakash, J. Electrochem. Soci., 2003, 150, A262-A266.

292. K. Onda, H. Kameyama, T. HAMAnoto and K. Ito, J. Electrochem. Soc., 2003, 150, 3, A285-A291.

293. K. Chen, G. Unsworth, X. Li, J. Power Sources, 2014, 261, 28-37.

294. X. Xia and J. R. Dahn, Electrochem. Solid-State Lett., 2012, 15 (1), A1-A4.

295. J. Zhao, L. Zhao, K. Chihara, S. Okada, J.-I. Yamaki, S. Matsumoto, S. Kuze, K. Nakane, J. Power Sources, 2013, 244, 752-757.

296. A. Rudola, K. Du and Palani Balaya, J. Electrochem. Soc., 2017, 164 (6), A1098-A1109.

297. C. Heubner, M. Schneider and A. Michaelis, J. Solid State Electrochem., 2017.

298. L. U. Subasinghe, W. Chen, M. Law, S. Reddy Gajjela, M. Balasundaram and P. Balaya, 2018.

299. S. Wang, Chin. Phys. B, 2016, 25(1), 010509.

300. R. Christen, G. Rizzo, A. Gadola, M. Stöcke, Batteries 2017, 3, 3.

301. R. Amin, J. Maier, P. Balaya, D.P. Chen, C. T. Lin, Solid State Ion., 2008, 179, 1983-1987.

302. R. Spotnitz, J. Franklin, J. Power Sources, 2003,113, 81–100.

303. J. Remmlinger, M. Buchholz, M. Meiler, P. Bernreuter and K. Dietmayer, J. Power Sources, 2011, 196, 5357–5363.

304. D.-I. Stroe, V. Knap, M. Swierczynski and E. Schaltz, ECS Transactions, 2017, 77 (11) 467-476.

305. S. J. Bazinski and X. Wang, J. Power Sources, 2015, 2932015, 283-291.

306. B. Manikandan, C. Yap, and P. Balaya, J. Electrochem. Soc., 2017, 164 (12), A2794-A2800.

307. Linden's Handbook of Batteries, Fourth Edition (2011), edited by Thomas B. Reddy.

308. Y. Abdul-Quadir, T. Laurila, J. Karppinen, K. Valkanen, K. Vuorilehto, L. Skogström and M. Paulasto-Kröckel, Int. J. Energy Res., 2014, 1424–1437.

309. W. Lu, I. Belharouak, D. Vissers and K. Amine, J. Electrochem. Soc., 2006, 153, 11, A2147-A2151.

310. Y. Bai, L. Li, Y. Li, G. Chen, H. Zhao, Z. Wang, C. Wu, H. Ma, X. Wang, H. Cui, J. Zhou, J. Energy Chem., 2018, 13-17.

311. Jong-Sung Hong, H. Maleki, S. Al Hallaj, L. Redey and J. R. Selman, J. Electrochem. Soc., 1998,145, 5.

312. F.-L.Yun, W.-R. Jin, L. Tang, W. Li, J. Pang and S.-G. Lu, J. Electrochem. Soc., 2016, 163(5), A639-A643.

313. T. M. Stanciu, D.-I. Stroe, M. Swierczynski. R. Teodorescu, N. Nieto, J. Gastelurrutia, Jean-Marc Timmermans, IEEE, 2016, IEEE Energy Conversion Congress and Exposition.

314. M. Balasundaram, V. Ramar, C. Yap, L. Li, A. A. O Tay, P. Balaya, J. Power Sources, 2016, 413-421.

315. Thermopedia, A-to-Z Guide to Thermodynamics, http://thermopedia.com/ (acceded January 2019).

316. Thermal properties of plastic materials, Professional Plastics Datasheet, https://www.professionalplastics.com/ (acceded March 2019).

APPENDIX

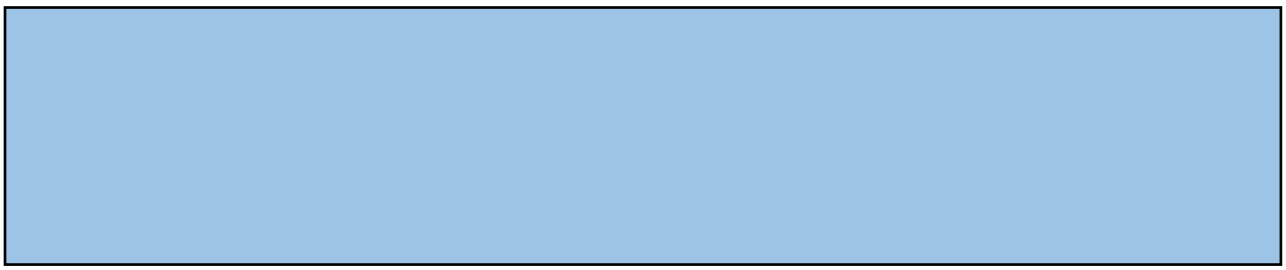

A.1. List of abbreviations and symbols

A	Area of pouch cell
AM	Active Material
AMAn	Anode active material
AMCat	Cathode active material
ARC	Accelerating Rate Calorimeter
BM	Planetary ball milling
CAES	Compressed Air Energy Storage
CB	Carbon Black
CEA	French Alternative Energies and Atomic Energy Commission
CH	Charge process
CNRS	French National Center for Scientific Research
Cp	Specific heat capacity
C-rate	Current rate
CV	Cyclic Voltammetry
DCH	Discharge process
DEC	Diethyl Carbonate
DMC	Dimethyl Carbonate
DOD	Depth of discharge
DOE	Department Of Energy (United States)
DTI	Disperser with the dissolver type impeller
dV/dT	Entropic heat coefficient
EC	Ethylene Carbonate
F	Faraday's constant
FEC	Fluoroethylene carbonate

h	Thermal conductivity for convection
HC	Hard Carbon
I	Intensity
IRENA	International Renewable Energy Agency
k	Thermal conductivity
LCO	Abbreviation for $LiCoO_2$ active material
LFP	Abbreviation for $LiFePO_4$ active material
M	Mass
MAS	Magic Angle Spinning
MW	Molecular weight
NCA	Abbreviation for $LiNi_{0.8}Co_{0.15}Al_{0.05}O_2$ active material
NMP	N-Methyl-2-Pyrrolidone
NMR	Nuclear Magnetic Resonance
OCP	Open Circuit Potential
OCV	Open Circuit Voltage
OER	Oxygen Evolution Reaction
ORR	Oxygen Reduction Reaction
P	Power
PC	Propylene carbonate
PC	Pouch cell
Pirreversible	Irreversible power
PM	Planetary centrifugal vacuum mixer
ppm	parts per million
Preversible	Reversible power
PTI	Overhead stirrer with the paddle type impeller
Ptotal	Total power

PVDF	Polyvinylidene fluoride
PVP	Polyvinylpyrrolidone
Q	Heat flux
q	Power
R	Resistance
R_{in}	Internal Resistance
$R_{N/P}$ (AM)	Negative to positive ratio in terms of active material mass
$R_{N/P}$ (Q)	Negative to positive ratio in terms of capacity
RT	Room Temperature
SDS	Sodium Dodecyl Sulfate
SEI	Solid Electrolyte Interface
SEM	Scanning Electron Microscopy
SIB	Sodium-ion batteries
SMES	Superconducting Magnetic Energy Storage
SOC	State Of Charge
T	Temperature
t	Time
V	Volume
W	Power
W	Weight
x	Na moles in the sodium layered oxide structures
XRD	X-ray Diffraction
Δx	Thickness of the pouch cell
λ	Thermal conductivity
τ	Shear stress
τ_0	Yield stress

γ	Shear rate
η_p	Constant plastic viscosity
η_p	Bingham viscosity

A.2 List of contributions

A.2.1 Publications

- Gurpreet Singh, Nuria Tapia-Ruiz, Juan Miguel López del Amo, Urmimala Maitra, James W. Somerville, A. Robert Amstrong, **Jaione Martínez de Ilarduya**, Téofilo Rojo, Peter G. Bruce, Chem. Mater., 2016, 28 (14), 5087-5094. 'High Voltage Mg-Doped $Na_{0.67}Ni_{0.3-x}Mg_xMn_{0.7}O_2$ (x = 0.05, 0.1) Na-Ion Cathodes with Enhanced Stability and Rate Capability'.

- **Jaione Martínez De Ilarduya**, Laida Otaegui, Juan Miguel López del Amo, Michel Armand, Gurpreet Singh, J. Power Sources, 2017, 337, 197-203. 'NaN_3 addition, a strategy to overcome the problem of sodium deficiency in P2-$Na_{0.67}[Fe_{0.5}Mn_{0.5}]O_2$ cathode for sodium-ion battery'.

- **Jaione Martínez De Ilarduya**, Laida Otaegui, Montserrat Galcerán, Laura Acebo, Devaraj Shanmukaraj, Teófilo Rojo, Michel Armand, Electrochimica Acta, 2019, 321, 1346932. 'Towards high energy density, low cost and safe Na-ion full-cell using P2-$Na_{0.67}[Fe_{0.5}Mn_{0.5}]O_2$ and $Na_2C_4O_4$ sacrificial salt'.

- **Jaione Martínez De Ilarduya**, Laida Otaegui, Guillermo Liendo, Jon Gastelurrutia, Aitor Villaverde. 'Thermal parameters determination and heat generation model for a monolayer sodium-ion pouch cell'. Under preparation.

A.2.2 Conferences

- **Jaione Martínez de Ilarduya**, Laida Otaegui, 'Cathode processing studies towards improved sodium ion batteries', 2018, e-MRS Fall Meeting, Warsaw, Poland (Oral).

- **Jaione Martínez de Ilarduya**, Laida Otaegui, Juan Miguel López del Amo, Michel Armand, Gurpreet Singh, 'Morphological, structural and electrochemical analysis of NaN_3 sacrificial salt containing P2-$Na_{0.67}[Fe_{0.5}Mn_{0.5}]O_2$ cathode and hard carbon anode sodium-ion battery', 2017, 231st ECS, New Orleans, USA (Oral).

- **Jaione Martínez De Ilarduya**, Laida Otaegui, Juan Miguel López del Amo, Michel Armand, Gurpreet Singh, 'NaN_3 addition, a strategy to overcome the problem of sodium deficiency', 2016, 3rd International Conference on Sodium Batteries, Geelong, Australia (Oral and Poster).

- **Jaione Martínez De Ilarduya**, Laida Otaegui, Lide M. Rodriguez, Gurpreet Singh, 'Sodium ion battery – a full cell study', 2016, Ulm ElectroChemical Talks (UECT), Ulm, Germany (Poster).

- **Jaione Martínez de Ilarduya**, Laida Otaegui, Monika Ortueta, Gurpreet Singh, 'Sodium ion battery – a full cell study', 2016, V Jornadas de Investigación de Facultad de Ciencia y Tecnología, Leioa, Spain (Poster).

- Laida Otaegui, **Jaione Martínez de Ilarduya**, Gurpreet Singh, 'Electrochemical characterization of a Hard Carbon / $Na_{1-\delta}Ni_{0.32}Ti_{0.32}Mg_{0.16}Mn_{0.2}O_2$ sodium-ion battery', 2016, Materials Science and Engineering, Darmstadt, Germany (Oral).

- Laida Otaegui, **Jaione Martínez de Ilarduya**, Guillermo Liendo and Aitor Villaverde, 'Cathode processing towards high energy density sodium-ion batteries', 2018, AMPT, Dublin, Ireland (Oral).

PERSONAL DETAILS

Date of birth: 21/02/1990

Address: c/Carta de Aalborg, 35 (01003), Vitoria (Álava-Spain)

Phone: 0034 616898973

Email: jaione0048@gmail.com

EDUCATION

2016-Present	**PhD in Chemical Engineering** (University of the Basque Country, Leioa, Spain) *'Na-ion battery development: from electrode processing studies to heat generation model of a monolayer pouch cell'*
2014-2015	**Master in Chemical Engineering** (University of the Basque Country, Leioa, Spain) - Specialization in chemical processes and sustainable development
2013	**Chemical Engineering Degree - Erasmus program** (Southern Denmark University, Odense, Denmark)
2008-2014	**Chemical Engineering** (University of the Basque Country, Bilbao, Spain) -Specialization in environmental area

WORK EXPERIENCE

2019 – Present	**BCARE** (Miñano, Spain) Project Manager
2018 - Present	**AQU Catalunya** (Barcelona, Spain) Vocal student in specific Commission of evaluation of Engineering and Architecture Degrees and Masters Vocal student of External Committee for the Accreditation of PhD Programs
2016 - 2019	**CIC energiGUNE** (Miñano, Spain) PhD student in Electrochemical Energy Storage Area (Fabrication & Processing, Proof of concept, Prototyping group): development of Na-ion pouch cell assembly, optimization of pouch cell design parameters, electrode processing optimization and post-mortem analysis.
2018	**IK4-Ikerlan** (Hernani, Spain) Visiting PhD student – Heat generation model of Na-ion pouch cell developed
2017	**Lawrence Berkeley National Laboratory** (Berkeley, USA) Visiting PhD student – 3 electrode pouch cell development
2015	**CIC energiGUNE** (Miñano, Spain) Master Internship in Electrochemical Energy Storage Area (Fabrication & Processing, Proof of concept, Prototyping group): *'From material to cell – case of sodium ion battery using layered oxides as cathode'*
2014	SuPrEn- SUstainable PRocess Engineering, Chemical Engineering and Environment department of Escuela Superior de Ingeniería de Bilbao (Bilbao, Spain) Final project degree: 'Hydrogen production by steam reforming of bio-oil compounds'

TRAININGS

Tutorial on Lithium-ion batteries, 2016 (ZSW, Germany)

Fullprof Suite Training, 2016, (CIC energiGUNE, Spain)

UPPA-UPV/EHU Cross-Border Doctorials, 40 hours, 2016, UPV/EHU and UPPA, France

NMR Workshop, 2017 (CIC energiGUNE, Spain)

Training session: Framework of the program of verification, monitoring, modification and accreditation of the proposals for the PhD program (AQU Catalunya, Spain)

1st School of Impedance Spectroscopy, 2018, (CIC energiGUNE, Spain)

Shmuel De-Leon, Batteries, Supercapacitors, Fuel Cells & EV's Seminar (CIC energiGUNE, Spain)

CONFERENCE CONTRIBUTIONS

- 'Cathode processing studies towards improved sodium ion batteries', **Jaione Martínez de Ilarduya**, Laida Otaegui, 2018, e-MRS Fall Meeting, Warsaw, Poland (Oral contribution).

- 'Morphological, structural and electrochemical analysis of NaN_3 sacrificial salt containing P2-$Na_{0.67}[Fe_{0.5}Mn_{0.5}]O_2$ cathode and hard carbon anode sodium-ion battery', **Jaione Martínez de Ilarduya**, Laida Otaegui, Juan Miguel López del Amo, Michel Armand, Gurpreet Singh, 2017, 231st ECS meeting, New Orleans, USA (Oral contribution).

- 'NaN_3 addition, a strategy to overcome the problem of sodium deficiency', **Jaione Martínez De Ilarduya**, Laida Otaegui, Juan Miguel López del Amo, Michel Armand, Gurpreet Singh, 2016, 3rd International Conference on Sodium Batteries, Geelong, Australia (Poster contribution selected for Burster presentation).

- ‘Sodium ion battery – a full cell study’, **Jaione Martínez De Ilarduya**, Laida Otaegui, Lide M. Rodriguez, Gurpreet Singh, 2016, Ulm ElectroChemical Talks (UECT), Ulm, Germany (Poster contribution).

- ‘Sodium ion battery – a full cell study’, **Jaione Martínez de Ilarduya**, Laida Otaegui, Monika Ortueta, Gurpreet Singh, 2016, V Jornadas de Investigación de Facultad de Ciencia y Tecnología, Leioa, Spain (Poster contribution).

- ‘Electrochemical characterization of a Hard Carbon / $Na_{1-\delta}Ni_{0.32}Ti_{0.32}Mg_{0.16}Mn_{0.20}O_2$ sodium-ion battery’, **Laida Otaegui**, Jaione Martínez de Ilarduya, Gurpreet Singh, 2016, Materials Science and Engineering, Darmstadt, Germany (Oral).

- ‘Cathode processing towards high energy density sodium-ion batteries’, **Laida Otaegui**, Jaione Martínez de Ilarduya, Guillermo Liendo and Aitor Villaverde, 2018, AMPT, Dublin, Ireland (Oral contribution).

PUBLICATIONS

- Iker García – García, Esther Acha, Kepa Bizkarra, **Jaione Martínez de Ilarduya**, Jesús Requies, José Francisco Cambra, Int. J. Hydrog. Energy, 2015, 40, 1444514455. ‘Hydrogen production by steam reforming of m-cresol, a bio-oil model compound, using catalysts supported on conventional and unconventional supports’.

- Gurpreet Singh, Nuria Tapia-Ruiz, Juan Miguel López del Amo, Urmimala Maitra, James W. Somerville, A. Robert Amstrong, **Jaione Martínez de Ilarduya**, Téofilo Rojo, Peter G. Bruce, Chem. Mater., 2016, 28 (14), 5087-5094. ‘High Voltage Mg-Doped $Na_{0.67}Ni_{0.3-x}Mg_xMn_{0.7}O_2$ (x = 0.05, 0.1) Na-Ion Cathodes with Enhanced Stability and Rate Capability’.

- **Jaione Martínez De Ilarduya**, Laida Otaegui, Juan Miguel López del Amo, Michel Armand, Gurpreet Singh, J. Power Sources, 2017, 337, 197-203. 'NaN$_3$ addition, a strategy to overcome the problem of sodium deficiency in P2-Na$_{0.67}$[Fe$_{0.5}$Mn$_{0.5}$]O$_2$ cathode for sodium-ion battery'.

- **Jaione Martínez De Ilarduya**, Laida Otaegui, Montserrat Galcerán, Laura Acebo, Devaraj Shanmukaraj, Teófilo Rojo, Michel Armand, Electrochimica Acta, 2019, 321, 1346932. 'Towards high energy density, low cost and safe Na-ion full-cell using P2-Na$_{0.67}$[Fe$_{0.5}$Mn$_{0.5}$]O$_2$ and Na$_2$C$_4$O$_4$ sacrificial salt'.

- **Jaione Martínez De Ilarduya**, Laida Otaegui, Guillermo Liendo, Jon Gastelurrutia, Aitor Villaverde. 'Thermal parameters determination and heat generation model for a monolayer sodium-ion pouch cell'. Under preparation.

COMPETENCES

- **Experimental techniques**

Structural and morphological characterization (SEM, XRD, NMR)

Electrochemical characterization (Cyclic voltammetry, electrochemical impedance spectroscopy)

Electrode processing optimization (slurry formulation, coating, calendering, drying)

Mechanical tests

Rheological tests

- **Software skills**

Aspentech, Ansys, Matlab, Origin, Fullprof Suite (Le Bail method), Electrochemical testing software (Maccor, VMP3, BT-Lab)